Constitutive Modeling and Life Prediction in Ni-Base Superalloys

A Dissertation
Presented to
The Academic Faculty

By

Mahesh M Shenoy

In Partial Fulfillment
of the Requirements for the Degree
Doctor of Philosophy in the
George W. Woodruff School of Mechanical Engineering

Georgia Institute of Technology
Aug 2006

Crack Initiation and Life Prediction in Ni-Base Superalloys

Approved By:

Dr David McDowell
George W. Woodruff School of Mechanical Engineering
Georgia Institute of Technology

Dr Richard Neu
George W. Woodruff School of Mechanical Engineering
Georgia Institute of Technology

Dr Thomas Sanders
School of Materials Science and Engineering
Georgia Institute of Technology

Dr Naresh Thadani
School of Materials Science and Engineering
Georgia Institute of Technology

Dr Min Zhou
George W. Woodruff School of Mechanical Engineering
Georgia Institute of Technology

Date Approved: 05/30/2006

Acknowledgements

I would like to thank my advisors, Dr David McDowell and Dr Richard Neu, who have helped me throughout my stay at Georgia Tech with their knowledge, support, encouragement, and guidance. I will always be grateful for their technical and editorial advice which was essential to the completion of this dissertation. They have also taught me innumerable lessons and insights on the workings of academic research in general. I would also like to thank my dissertation reading committee; Dr Thomas Sanders, Dr Naresh Thadani and Dr Min Zhou for reviewing my thesis and providing several useful suggestions.

This thesis would not have been possible without the support from a number of people during my graduate studies. For their substantial aid, I would like to express my sincere gratitude to those listed below as well as many others I have failed to mention. I would like to acknowledge the assistance provided by Dr Ali Gordon and Matt Trexler in both the technical and non-technical aspects of my research and Alejandro Ibanez for the experiment data inputs. The help from Dr Rajesh Kumar, Dr Aijun Wang, Dr Jixi Zhang and Yustianto Tjiptowidjojo, in collaborative research are much appreciated. I would also like to thank my friends who helped make my stay at Georgia Tech a memorable one: Jason Mayeur, Dr Vikas Tomar, Ambarish Kulkarni, R Vijaywargiya and Prahlad Fogla. I sincerely appreciate the support and funding from General Electric Energy and Pratt and Whitney towards my research activities.

Last and most importantly, I would like to thank my family members; my parents and my brother, who have backed me throughout the course of my PhD. They receive my

deepest gratitude for their patience and understanding and the many years of encouragement during my studies.

Table of Contents

List of Tables

List of Figures

Summary

Microstructural features at different scales affect the constitutive stress-strain response and the fatigue crack initiation life in Ni-base superalloys. While numerous efforts have been made in the past to experimentally characterize the effects of these features on the stress-strain response and/or the crack initiation life, there is a significant variability in the data with sometimes contradictory conclusions, in addition to the substantial costs involved in experimental testing. Computational techniques can be useful tools to better understand these effects since they are relatively inexpensive and are not restricted by the limitations in processing techniques. This research investigated the microstructure-dependence of the stress-strain response and the fatigue crack initiation life of two Ni-base superalloys; DS GTD111, which has been developed by GE Energy for use in gas turbine blades, and IN100, developed by Pratt and Whitney, which is used in turbine discs. The focus was on developing multiscale constitutive models and computational frameworks for life prediction.

Physically-based constitutive models were formulated and implemented as user material subroutines in ABAQUS using the single crystal plasticity framework which can predict the material stress-strain response with the microstructure-dependence embedded into them. The model parameters were calibrated using experimental cyclic stress-strain histories. A computational exercise was then employed to quantify the influence of idealized microstructural variables on fatigue crack initiation life. Understanding was sought on the influence of inclusion shape, size, and spacing and the primary and neighboring grain orientations on the variability in fatigue crack incubation life in DS

GTD111. A computational scheme was also formulated to predict the fatigue crack initiation life in IN100 for slip band based crack initiation and a material design framework was developed and used for the preliminary design of fatigue resistant microstructures. Lastly, it is noted that crystal plasticity models are often too computationally intensive if the objective is to model the macroscopic behavior of a textured or randomly oriented 3-D polycrystal in an engineering component. Homogenized constitutive models were formulated and implemented as user material subroutines in ABAQUS, which can capture the macroscale stress-strain response in both DS GTD111 and IN100. Even though the study was conducted on two specific Ni-base superalloys; DS GTD111 and IN100, the objective was to develop generic frameworks which should also be applicable to other alloy systems.

CHAPTER I

Introduction

1.1 Introduction

Ni-base superalloys are extensively used in applications that require a material with high strength and good creep, fatigue, and corrosion resistance, even at elevated temperatures. Some of the applications include turbine blades, turbine discs, burner cans and vanes (Antolovich, 1996). The operating temperatures of these components can range from room temperature (RT) to very high temperatures ($>1000°C$) and they are exposed to complex mechanical loading superimposed with thermal transient; for example, creep interacts with thermal and/or mechanical fatigue. Other uses for Ni-base superalloys include cryogenic applications, aircraft skins and superconducting applications. The material microstructure has a profound effect on performance of Ni-base superalloys. Various experimental techniques have been employed to improve their mechanical behavior by tailoring of relevant microstructural variables such as the γ'-precipitate size, morphology and grain size (Merrick and Floreen, 1978; Mughrabi et al., 1997; Kakehi, 1999a; Kakehi, 1999b; Antolovich, 2003). Specialized processing techniques are employed to maximize their mechanical properties for specific applications, such as elimination of grain boundaries by directional solidification for turbine blades (Antolovich, 2003).

Ni-base superalloys display an anomalous yield behavior (in which the yield strength increases with temperature, which makes them a natural choice for use in high temperature applications. However, this leads to additional complexities in predicting their constitutive response (Antolovich, 2003). A physically-based constitutive relation that can simulate the structural response in order to facilitate component life prediction should incorporate the active deformation mechanisms which change with varying loads, temperatures and material microstructure. This is essential since an accurate life prediction can ease the component inspection frequency, thus leading to substantial savings in cost. The total component life depends on the temperature, environment and loading history (i.e. fatigue, creep) and the coupling between these mechanisms. However an all-inclusive model has proved to be impossible; instead, empirical or phenomenological models are typically used for life prediction(Antolovich, 1996).

This research focuses on fatigue loading to which more attention will be devoted to in the sections that follow. Fatigue is the process of progressive damage accumulation in engineering components subjected to repeated cyclic loading. The fatigue life is composed of two parts; crack initiation life and crack propagation life. Crack initiation can be further decomposed into crack formation or incubation, microstructurally small crack (MSC) growth and physically small crack (PSC) growth. In Ni-base superalloys, crack initiation accounts for a significant part of the fatigue life (Chen et al., 1997). Microstructural features at different scales such as inclusions, the grain size distribution, and the γ'- precipitate size distribution and volume fraction often play an important role in determining the crack initiation life in both low cycle fatigue (LCF) and high cycle fatigue (HCF) in directionally solidified (DS) and polycrystalline (PC) Ni-base

superalloys (Jablonski, 1981; Gayda and Miner, 1983) . While numerous efforts have been made in the past to experimentally characterize the effects of these features on the stress-strain response and/or the crack initiation life, there is significant variability in the data with sometimes not very clear conclusions. This is probably due to the inherent variability in processing techniques and the inability to isolate interactive effects in complex microstructures, which might also change with the temperature and loading conditions. In addition to this, the costs involved in experimental testing can be substantial. Computational techniques can be useful tools to better understand these effects since they are relatively inexpensive and are not restricted by the limitations in processing techniques. However, a big challenge in using computational techniques is that the results are only as good as the model that is used to simulate the material stress-strain response.

Inclusions play an important role on fatigue crack initiation in DS Ni-base superalloys. Macroscopic J_2 nonlinear kinematic hardening models are typical of the continuum plasticity models used to study the role of inclusions in fatigue crack initiation(Melander and Gustavsson, 1996; McDowell et al., 2003). However, these models cannot capture the inherent material anisotropy in single crystal (SC)/ directionally solidified (DS) superalloys and the local anisotropy at the scale of the grains in polycrystalline (PC) superalloys. The crystal plasticity framework is suitable for modeling the directional dependence of the yield surface in SC/DS superalloys. Other microstructural features such as the γ' precipitate size distribution and the γ' precipitate volume fraction affect the local and macroscopic stress-strain response and the crack initiation life in both the DS and PC Ni base superalloys. It is essential to incorporate this microstructure-dependence

into the constitutive models in order to investigate their effect on the fatigue crack initiation life. Lastly, even though it is much easier and probably more accurate to incorporate the physics of the deformation process in the crystal plasticity based models; it is currently not feasible to use them in industry based applications due to the high computational burden involved. In this regard, it would be immensely beneficial if macroscopic models were available that can capture the essential characteristics of the deformation response and have clear connection to key microstructure attributes.

1.2 Scope of Thesis

Material modeling is crucial for obtaining accurate results in simulations of manufacturing processes in the industry. The desired features of a model also include the possibility to obtain model parameters from conventional test data and the feasibility in terms of time, money, and/or computational resources. A large number of constitutive models of the plastic behavior of metals are available for finite element modeling. Existing commercial finite element codes have quite advanced features, which can be further extended by means of user subroutines. However, the applicability of commonly used constitutive models is usually limited in terms of varying strain, strain rate and temperature, and sometimes also by changing microstructure or texture evolution (in polycrystalline materials). Material models based on consideration of the underlying physical processes are expected to have a larger range of usability and validity than the more commonly used empirical models. The material models can be formulated at different length scales represented in the Figure 1.1, which can be broadly classified into the following:

(1) Macroscale Level Models: These models are developed at the macroscale where the material response is treated in an average sense. The material microstructure at lower scales is not explicitly modeled and the response is homogenized. Most industry components are analyzed by finite element simulations using macroscale models since they are computationally feasible (Chaboche, 1989; Freed and Walker, 1989; Moosbrugger and McDowell, 1989; Nouailhas, 1989; Ohno and Wang, 1991; McDowell, 1992).

(2). Mesoscale Level Models: These include the material microstructure that include the microstructural features such as the grain structure in polycrystalline metals, precipitates in Ni-base superalloys, etc. However, most of these analyses are only used to guide the understanding of material behavior and are rarely used in actual component analysis (Pollock and Argon, 1992; Nouailhas and Cailletaud, 1996; Busso et al., 2000).

(3). Microscale Level Models: TEM studies of dislocation networks have provided the experimental evidence to support the classical principles of plastic deformation. Discrete dislocation dynamics can be applied to directly simulate material behavior at the micro and nano scale. Although some success has been achieved in representing hardening curves by this method, it remains far too costly to compute.

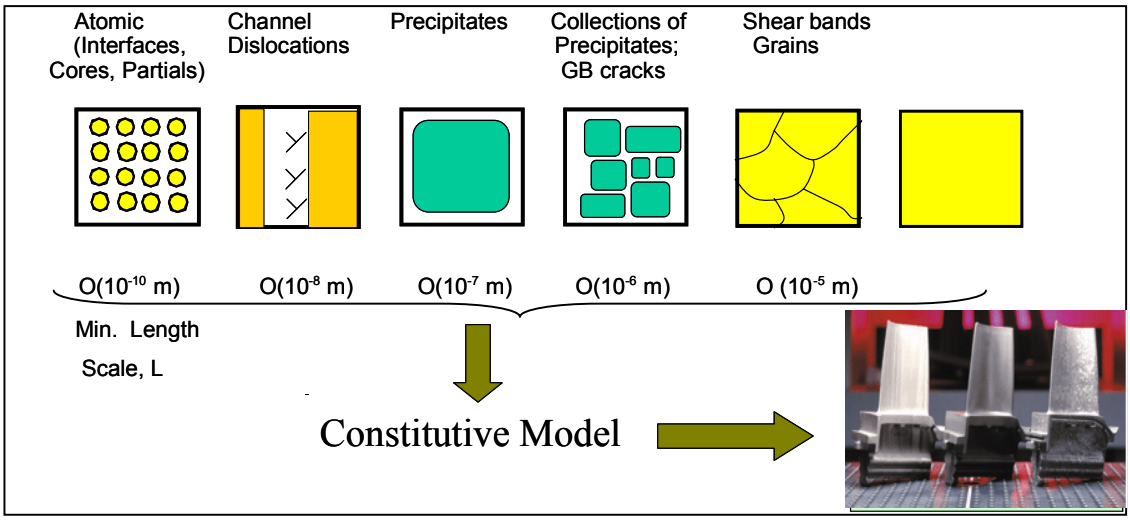

Figure 0.1 Relevant Length scales for constitutive modeling in Ni-base superalloys.

(4) Nanoscale Level Models: Atomistic simulations can be used to model the individual atoms. However, atomistic simulations are limited by the computational costs as well as the assumptions that must be made to develop and calibrate the atomistic potentials, especially for materials with complex microstructures like Ni-base superalloys.

The final objective is to use these models in analyzing actual components for specific applications, e.g. forming processes, life and assessment using fracture concepts. In this thesis the constitutive models are restricted to the 'meso' and 'macro' scale to capture the stress-strain response in Ni-base superalloys. These models are then used to analyze the variability in fatigue crack initiation life based on intrinsic and extrinsic microstructural features.

This research investigates the microstructure dependence of the fatigue life of two Ni-base superalloys; DS GTD111, which has been developed by GE Energy for use in gas turbine blades, and IN100, developed by Pratt and Whitney, which is used in turbine discs. The choice of the two materials is dictated by material availability so that experimental data can be obtained if desired; however, the focus is on developing multiscale constitutive models and computational frameworks for life prediction. The frameworks developed in this thesis are intended to be generic and should serve as a guide for studying other alloy systems.

Constitutive models will be developed for the two materials using a crystal plasticity framework since it explicitly treats crystallographic orientation effects at the scale of grains. The overall cyclic stress-strain response and the cyclic plastic shear strain distribution for the local material heterogeneities is studied and an attempt is made to correlate these parameters with microstructural descriptors that permit assessment of

relative fatigue resistance. This should facilitate the estimation of variability in fatigue life with respect to the microstructural parameters and help to achieve improved fatigue life estimates, reducing the number of experiments required; in addition, such a study is potentially useful in designing the material microstructure, so as to maximize the fatigue resistance. It is noted that crystal plasticity models are often too computationally intensive if the objective is to model the macroscopic behavior of a textured or randomly oriented 3-D polycrystal in an engineering component, which involves analyses at much larger length scales; a macroscopic elastoviscoplastic model is usually used in most industry analyses. The main objectives of this research are as follows:

- Develop a physically-based crystal plasticity constitutive model that can account for creep, isothermal fatigue, and thermomechanical fatigue in DS GTD111.
- Develop a transversely isotropic model to capture the fatigue and creep responses in DS GTD111
- Develop a physically-based crystal plasticity constitutive model that includes the microstructural dependence in the form of grain and γ' precipitate size distributions and volume fractions in IN100.
- Study the role of material microstructure in the form of MC carbide inclusions in crack initiation in fatigue-dominated loading conditions in DS GTD111 using experiments and to assist in developing a computational micromechanics framework to study the variability of fatigue crack initiation life.
- Incorporate the microstructure dependence in a macroscopic isotropic model to capture the stress-strain response for IN100.

- Study the role of the grain and γ' precipitate size distribution and the γ' precipitate volume fraction in IN100 on crack initiation in fatigue-dominated loading conditions using a computational micromechanics framework.

More emphasis is placed on using computational tools and frameworks to facilitate parametric study of effects of microstructure features to estimate variability in fatigue due to randomness of microstructure and to provide tools to support microstructure-sensitive design.

1.3 Thesis Layout

The following chapters describe the strategies and methods that are used to achieve the objectives listed above.

- Chapter II focuses on the formulation and implementation of a crystal plasticity based constitutive model, which can be used to capture the deformation behavior (stress-strain response) in fatigue, creep, and thermomechanical fatigue (TMF) loading in DS GTD111, at temperatures ranging from room temperature to 1038°C. This model can be used to predict the stress-strain response for use in life prediction models and to study the effect of microstructural variability on fatigue life.
- Chapter III discusses the formulation of a macroscopic transversely isotropic continuum viscoplasticity model for DS GTD111 that can capture the fatigue and creep responses. This model is implemented as an ABAQUS User MATerial (UMAT) subroutine using a semi-implicit integration scheme, which is shown to

reduce the associated computational costs when compared to the crystal viscoplasticity model.

- Chapter IV explains a framework to study the role of carbides or other hard ceramic particles in fatigue crack formation in DS GTD111. The effects of loading parameters (strain amplitude) and microstructural parameters (nonmetallic inclusion shape, spacing, etc.) on local cyclic plasticity at microstructure-scale notches are evaluated. The effect of neighboring grain orientation on intensification of plastic strain around inclusions is analyzed, and functions are determined for relating applied strain to the cyclic plastic shear strain near the inclusion-matrix interface that contributes to LCF and HCF crack formation. Use of such a framework for predicting microstructure-dependence of fatigue crack initiation life and its variability are discussed, as are additional mechanisms of micro-fracture associated with cumulative plastic deformation.
- In Chapter V a rate dependent crystallographic constitutive theory is formulated to predict the mechanical behavior in IN100, which is a polycrystalline superalloy as opposed to the directionally solidified DS GTD111. Even though a crystal plasticity model is used similar to Chapter II, the main objective here is to explicitly embed the microstructural dependence of the stress-strain response. The model has the capability to capture the first order effects such as (a) grain size, (b) the γ' precipitate size distribution, and (c) the γ' precipitate volume fraction dependence of the stress-strain response.
- Chapter VI explains a framework which is used to embed the microstructural dependence of the stress-strain response in IN100 into an initially isotropic

macroscale model for a polycrystal with random orientation distribution. A hierarchical scheme is used in which the calibrated microscale crystal plasticity model developed in Chapter V is used to guide the determination of the functional forms for the material parameters in the macroscale constitutive model.

- Chapter VII lays out a scheme to assess the intrinsic fatigue resistance in IN100 as a function of the microstructure (grain size, precipitate size, spacing and distribution) using the model developed in Chapter V. The effect of varying microstructure on the inelastic strain distribution is studied for fatigue loading histories using statistical volume elements subject to periodic boundary conditions to build up statistically significant measures of distributions of cyclic microplasticity.

The relevant details with respect to the literature, motivation, underlying assumptions involved, and results are listed in the individual chapters. A conscious effort has been made to keep these chapters independent and complete; however, for brevity details which have been explained in earlier Chapters are only explained briefly.

In this thesis, bold face letters indicate tensors, with the Cartesian components of first and second orders tensors denoted by u_i and A_{ij}, respectively. The summation convention over repeated indices is implied, i.e. $\sigma_{kk} = \sigma_{11} + \sigma_{22} + \sigma_{33}$. The inner product of two second-rank tensors is defined as $\mathbf{A} \cdot \mathbf{B} = \mathbf{C}$ where $C_{ik} = A_{ij}B_{jk}$. The scalar product of two second-rank tensors is defined as $\mathbf{A} : \mathbf{B} = A_{ij}B_{ij}$ and the Euclidean norm of a second rank tensor is given by $(\mathbf{A} : \mathbf{A})^{1/2} = \left(A_{ij}A_{ij}\right)^{1/2}$. The dyadic product of two vectors, $\mathbf{a} \otimes \mathbf{b}$, has components $a_i b_j$.

CHAPTER II

Crystal Plasticity Based Model for a Directionally Solidified Ni-Base Superalloy

Abstract

A 3D continuum crystal plasticity model is used to simulate the material behavior of a directionally solidified Ni-base superalloy, DS GTD111, with application to uniaxial loading in the longitudinal and transverse orientations. Isothermal uniaxial fatigue tests with hold times and creep tests are conducted at temperatures ranging from room temperature (RT) to 1038 °C to characterize the deformation response. The constitutive model is implemented as a User MATerial subroutine (UMAT) in ABAQUS and a parameter estimation scheme is developed to obtain the material constants. Both in-phase and out-of-phase thermo-mechanical fatigue tests are conducted and modeled. An anisotropic damage model is used to model the tertiary creep response in both the longitudinal and transverse orientation, which is calibrated using the experimental creep data.

2.1. Introduction

Directionally solidified (DS) Ni-base superalloys are extensively used in applications such as turbine blades that require a material with high strength, good creep, and fatigue

and corrosion resistance, even at elevated temperatures. The operating temperatures of these components can range from room temperature (RT) to very high temperatures (>1000 °C) and they are exposed to complex mechanical loading superimposed with thermal transients; for example, creep deformation interacts with thermal and/or mechanical fatigue. In DS superalloys, the grain boundaries are eliminated along the turbine blade axis by directional solidification. However, this introduces new challenges in constitutive modeling of the deformation behavior and life prediction due to the anisotropic deformation response of the material.

In this chapter, a constitutive model is developed for a DS Ni-base superalloy, DS GTD111, which is typically used in second stage turbine blades. The deformation mechanisms in Ni-base superalloys change with varying loads, orientations, strain rates, and temperatures. The constitutive model is formulated using the crystal plasticity approach since it naturally captures the orientation dependent deformation response in single crystals and the deformation mechanisms can be embedded more easily (Meric et al., 1991). A physically-based constitutive model is outlined to capture the homogenized deformation response without explicitly considering the precipitate and matrix phases. The material parameters are determined based on experimental low cycle fatigue (LCF) and creep data in both the longitudinal (L) and transverse (T) orientations. Fatigue tests with short hold times are also used to calibrate the short-term primary creep behavior.

2.2. Material Microstructure and Composition

DS GTD111 Ni-base superalloy has the chemical composition as shown in Table 2.1. The as-cast structure contains coherent, ordered γ' intermetallic precipitates dispersed uniformly in the austenitic γ - phase, as shown in Figure 2.1. There is a bi-modal distribution of γ' - precipitates, with cuboidal primary precipitates (0.5-1 μm) and spheroidal secondary precipitates (0.05-0.2 μm), with an overall volume fraction of

approximately 40-50%. These precipitates are interspersed in the relatively soft matrix and are separated by the thin matrix channels. The grains are columnar and are roughly 125 mm long and 0.5-2 mm wide and the primary dendrite stems grow parallel to the solidification direction. These stems are accompanied by secondary and tertiary dendrite arms, which grow outward along [100] and [010] directions, as shown in Figure 2.2.

Table 0.1 Nominal composition of DS GTD111.

	Cr	Co	Al	Ti	W	Mo	Ta	C	Zr	B	Fe	Si	Mn	Cu	P	S	Ni
Min	13.7	9.0	2.8	4.7	3.5	1.4	2.5	.08	.005	.005	-	-	-	-	-	-	Bal.
Max	14.3	10.0	3.2	5.1	4.1	1.7	3.1	.12	.040	.020	.35	.30	.10	.10	.015	.005	Bal.

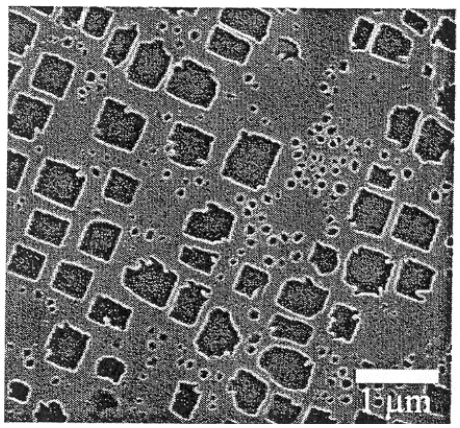

Figure 0.1 Two-phase microstructure of DS GTD111 superalloy (Trexler, 2004).

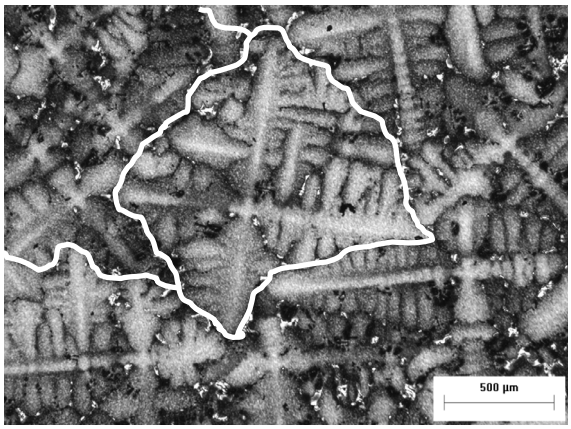

Figure 0.2 Optical micrograph of heat-treated section transverse to the direction of columnar growth (Trexler, 2005).

2.3 Deformation Response

The observed deformation response in DS GTD111 is consistent with that of other Ni-base superalloys and can be summarized as follows (Westbrook, 1996):

1) The yield strength increases with increasing temperature in the intermediate temperature regime up to a peak temperature of 750°C, beyond which it decreases as shown in Figure 2.3.

2) Slip is generally dictated by the resolved shear stresses along the favorable crystallographic slip planes. However, Ni-base superalloys do not obey Schmid's law in all orientations and slip on any given plane can also depend on the resolved stresses on other planes (e.g. dislocation cross slip planes) due to dislocation core spreading effects in the γ' precipitates.

3) There is tension (T)-compression (C) asymmetry of the flow stress. The nature of this asymmetry is orientation and temperature dependent (Lall et al., 1979 ; Paidar et al., 1984;

Umakoshi et al., 1984; Jiao et al., 1996; Osterle et al., 2000). For example, the flow stress for the stabilized cycles in tension is higher than that in compression in the longitudinal orientation at 650°C, while this trend is reversed in the transverse orientation as shown in Figures 2.4 and 2.5.

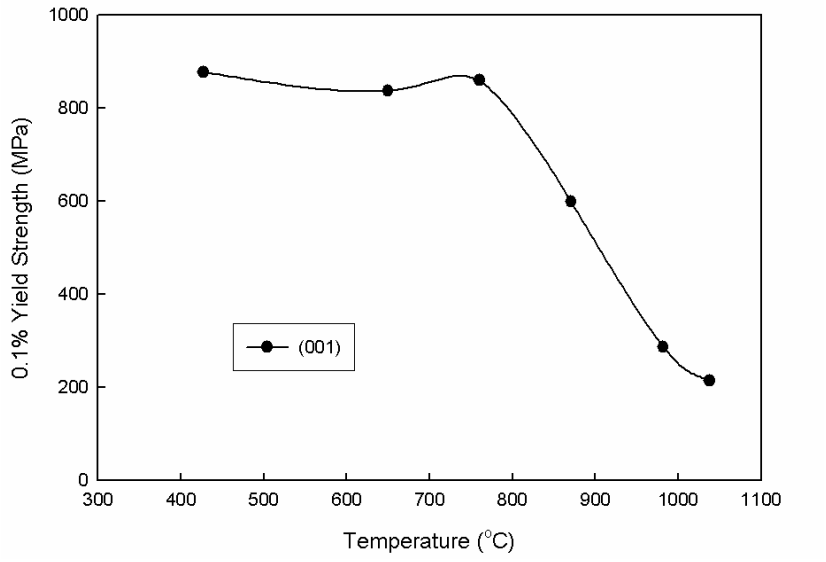

Figure 0.3 Variation of the yield strength in DS GTD111 as a function of temperature in the longitudinal (001) orientation.

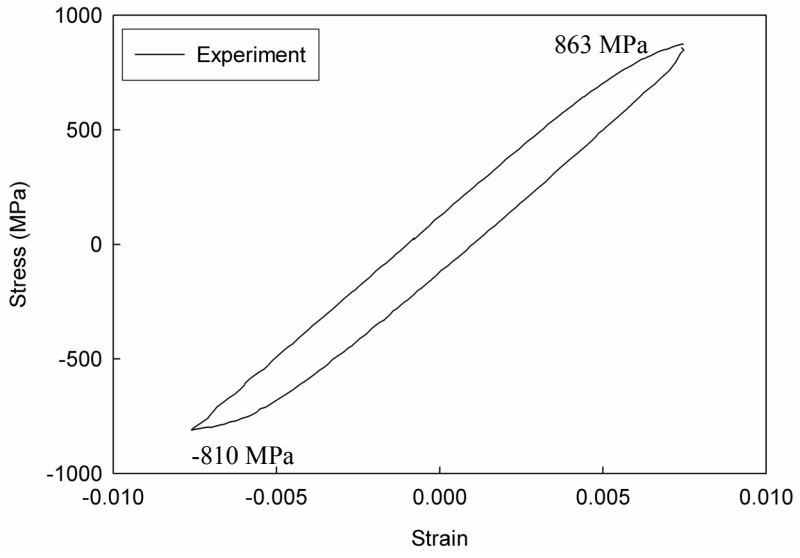

Figure 0.4 Stabilized cycle for completely reversed loading in the longitudinal orientation at 650°C ($R_\varepsilon = -1$).

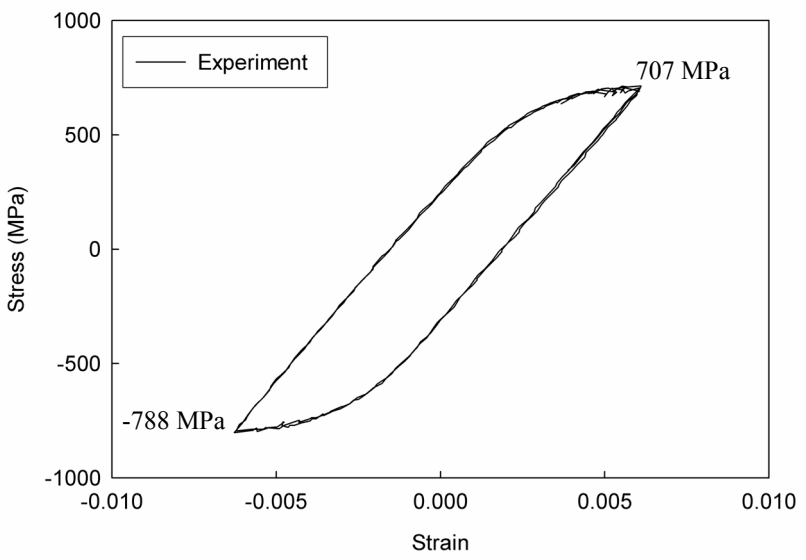

Figure 0.5 Stabilized cycles for completely reversed loading in the transverse orientation at 650°C ($R_\varepsilon = -1$, $\dot{\varepsilon}$=0.005 s^{-1}).

4) The initial yield behavior is nearly temperature path history independent, i.e., if a sample is first deformed at a high temperature at which the yield strength is high and then deformed at a low temperature, the material response is similar to a virgin material deformed at the lower temperature (Vitek et al., 1996).

Any physically-based constitutive model should take all these mechanisms into consideration.

2.4. Crystal Plasticity Formulation

A homogeneous constitutive model is developed in this chapter in which no explicit distinction is made between the matrix and precipitate phases. A crystal plasticity framework is employed to capture the orientation dependent material response. As the temperature increases, strain rate effects are increasingly important and a rate dependent method is employed.

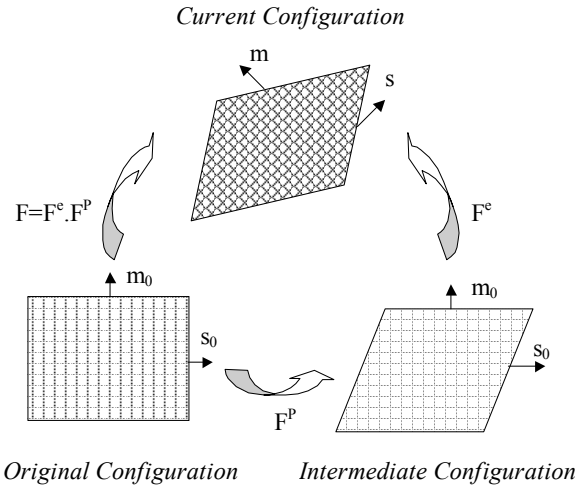

Figure 0.6 Elastoplastic decomposition of the deformation gradient (Bilby et al., 1955; Lee, 1969).

The foundations for the constitutive model for single crystal elasto-plasticity considered here may be traced to the papers by (Bilby et al., 1955; Teodosiu, 1970; Rice, 1971; Hill and Rice, 1972; Mandel, 1974; Asaro, 1983a; 1983b) from a continuum mechanics viewpoint, and Conrad, Kocks, and Argon (1964; 1975; 1995) from a material science viewpoint. The deformation of a crystal is taken as the sum of contributions from two independent atomic mechanisms: (i) an overall "elastic" distortion of the lattice, $\mathbf{F^e}$ and (ii) a "plastic" deformation that does not disturb the lattice geometry, $\mathbf{F^p}$. In a large range of temperatures and at sufficiently high stress levels, the major mechanism of plastic deformation in ductile single crystals is dislocation glide on well-defined crystallographic slip systems in the crystal. The governing variables in the constitutive model are: (i) the 2nd Piola Kirchhoff stress, $\boldsymbol{\sigma}^{pk2}$, (ii) the deformation gradient, $\mathbf{F}$, (iii) the absolute temperature, T, (iv) the crystal slip systems labeled by integers α, (v) slip system unit normal, $\mathbf{s}^{\alpha}$, to the slip plane, (vi) and a unit vector, $\mathbf{m}^{\alpha}$, denoting the slip direction,

(vii) the plastic deformation gradient, $\mathbf{F}^{\mathrm{p}}$, with $\det\left(\mathbf{F}^{\mathrm{p}}\right)=1$, (viii) the slip system threshold stress or the slip resistance, κ^{α}, with units of stress, and (ix) the slip system kinematic stress or backstress, χ^{α}.

A multiplicative rule is used for the deformation gradient, **F**, given as (Bilby et al., 1955; Lee, 1969), i.e.,

$$\mathbf{F}=\mathbf{F}^{\mathbf{e}}\cdot\mathbf{F}^{\mathbf{p}} \tag{2.1}$$

As shown in Figure 2.6, the deformation gradient is separated into two parts: (i) the plastic deformation gradient ($\mathbf{F}^{\mathbf{p}}$) formed due to dislocation motion, associated with a change in the shape of the grain but not its crystal lattice and (ii) the elastic deformation gradient ($\mathbf{F}^{\mathbf{e}}$), which essentially models the reversible elastic stretch and the rigid body rotation of the lattice. It should be noted that the intermediate, relaxed configuration in Figure 2.6 is not unique since any superimposed rigid body rotation on the deformation gradient will also satisfy Eq. (2.1). Uniqueness of the intermediate configuration is obtained by assuming that the substructure spin is co-rotational with the lattice, such that the lattice orientation is fixed during $\mathbf{F}^{\mathbf{p}}$.

Next, with $\boldsymbol{\sigma}^{\mathrm{pk1}}=\det\left(\mathbf{F}\right)\boldsymbol{\sigma}\cdot\mathbf{F}^{-\mathrm{T}}$ denoting the first Piola–Kirchhoff stress, the stress power per unit reference volume is obtained as $\dot{\omega}=\boldsymbol{\sigma}^{\mathrm{pk1}}:\dot{\mathbf{F}}$, which is also equal to the stress power per unit volume of the isoclinic relaxed configuration determined by $\mathbf{F}^{\mathbf{p}}$, since dislocation glide is incompressible ($\det\left(\mathbf{F}^{\mathrm{p}}\right)=1$). This stress power may be additively decomposed as $\dot{\omega}=\dot{\omega}^{\mathrm{e}}+\dot{\omega}^{\mathrm{p}}$, with $\dot{\omega}^{\mathrm{e}}=\boldsymbol{\sigma}^{\mathrm{pk2}}:\dot{\boldsymbol{\varepsilon}}^{\mathrm{e}}$ as the elastic stress power per unit volume of the intermediate configuration, where

$$\boldsymbol{\varepsilon}^{e} = \frac{1}{2}\left(\mathbf{F}^{eT}\cdot\mathbf{F}^{e} - \mathbf{1}\right) \text{ and } \boldsymbol{\sigma}^{pk2} = \det\left(\mathbf{F}^{e}\right)\mathbf{F}^{e-1}\cdot\boldsymbol{\sigma}\cdot\mathbf{F}^{e-T} \tag{2.2}$$

are the Green elastic strain measure and the symmetric second Piola–Kirchhoff stress tensor relative to the relaxed intermediate configuration, respectively, and

$$\dot{\omega}^{p} = \left(\mathbf{F}^{eT}\cdot\mathbf{F}^{e}\cdot\boldsymbol{\sigma}^{pk2}\right):\left(\dot{\mathbf{F}}^{p}\cdot\mathbf{F}^{p-1}\right) \tag{2.3}$$

is the plastic stress power per unit volume in the intermediate configuration.

Elastic stretches in metallic single crystals including those in Ni-base superalloys are typically small. Temperature changes need not be small, but for simplicity, only the isothermal case is considered. The extension of this framework for thermomechanical (TMF) fatigue is discussed later. The constitutive equation for the linear elastic behavior in a metallic single crystal for the isothermal case is taken as

$$\boldsymbol{\sigma}^{pk2} = \mathbf{C}:\left(\boldsymbol{\varepsilon}^{e}\right) \tag{2.4}$$

where **C** is the forth order anisotropic elasticity tensor.

For any given lattice, the close packed planes act as the slip planes with unit normal vector $\mathbf{m}_{o}^{\alpha}$ in the reference configuration for each of the α slip systems, along which the dislocations move in the slip direction in the reference configuration with unit vector $\mathbf{s}_{o}^{\alpha}$.The shearing rates $\dot{\gamma}^{\alpha}$ along each of the active slip systems (α) depend on the resolved shear stress on the slip systems. The macroscopic plastic velocity gradient ($\hat{\mathbf{L}}^{p}$) is obtained by summing over all slip systems in the intermediate relaxed configuration according to

$$\hat{\mathbf{L}}^{\mathbf{p}} = \dot{\mathbf{F}}^{\mathrm{p}} \cdot \mathbf{F}^{\mathrm{p}-1} = \hat{\mathbf{D}}^{\mathbf{p}} + \hat{\mathbf{W}}^{\mathbf{p}} = \sum_{\alpha=1}^{N_{slip}} \dot{\gamma}^{\alpha} \left(\mathbf{s}_{o}^{\alpha} \otimes \mathbf{m}_{o}^{\alpha} \right) \tag{2.5}$$

where the intermediate configuration plastic rate of deformation ($\hat{\mathbf{D}}^{\mathbf{p}}$) and plastic spin ($\hat{\mathbf{W}}^{\mathbf{p}}$) are given by the symmetric and anti-symmetric parts of the associated plastic velocity gradient, i.e.,

$$\hat{D}_{ij}^{p} = \frac{1}{2}\left(\hat{L}_{ij}^{p} + \hat{L}_{ji}^{p} \right), \ \hat{W}_{ij}^{p} = \frac{1}{2}\left(\hat{L}_{ij}^{p} - \hat{L}_{ji}^{p} \right) \tag{2.6}$$

2.5. Flow Rule

The evolution of the plastic velocity gradient is given by Eq. (2.5). The plastic shearing rate, $\dot{\gamma}^{\alpha}$, on the α^{th} slip system, is given by the Orowan equation (Orowan, 1940)

$$\dot{\gamma}^{\alpha} = \rho_{m}^{\alpha} b \bar{v}^{\alpha} \tag{2.7}$$

and represents the physical picture that the strain rate $\dot{\gamma}^{\alpha}$ is produced by a density ρ_{m}^{α} of mobile dislocations with Burgers vector magnitude b moving with an average velocity $\bar{v}^{\alpha}$ (in the slip direction $\mathbf{m}_{o}^{\alpha}$), through a field of obstacles.

Using Eqs. (2.3) and (2.5), the resolved shear stress, τ^{α}, for the slip system, α, is defined through the relation, $\dot{\omega}^{p} = \sum_{\alpha} \tau^{\alpha} \dot{\gamma}^{\alpha}$, which gives

$$\tau^{\alpha} = \left(\mathbf{F}^{eT} \cdot \mathbf{F}^{e} \cdot \boldsymbol{\sigma}^{pk2} \right) : \left(\mathbf{s}_{o}^{\alpha} \otimes \mathbf{m}_{o}^{\alpha} \right) \tag{2.8}$$

It should be noted that $\mathbf{F}^{eT} \cdot \mathbf{F}^{e} \approx \mathbf{1}$ for metals in which the elastic strains are typically very small, therefore giving the relation

$$\tau^{\alpha} = \boldsymbol{\sigma}^{pk2} : \left(\mathbf{s}_{o}^{\alpha} \otimes \mathbf{m}_{o}^{\alpha} \right) \tag{2.9}$$

With the resolved shear stress as defined in Eq. (2.9), the average dislocation velocity on the slip system, α, is taken to be governed by a constitutive function, i.e.,

$$\overline{v}^{\alpha} = \overline{v}^{\alpha} \left(\tau^{\alpha}, T, \kappa^{\alpha}, \chi^{\alpha} \right) = M \overline{F}^{\alpha} \tag{2.10}$$

where M is the mobility coefficient and $\overline{F}^{\alpha}$ is a statistical measure of the driving force on dislocations through the obstacle field. Here, κ^{α} is a temperature-dependent critical slip resistance and χ^{α} is the backstress for the slip system, α. In a pure single crystal, the backstresses may be neglected but they form a very important component in two-phase materials like Ni-base superalloys and cannot be neglected (Ferney et al., 1991). The average dislocation velocity $\overline{v}^{\alpha}$ at applied shear stress τ^{α} at any temperature, T, depends on the waiting time of mobile dislocations at the obstacles; κ^{α} and χ^{α} re1ect the strength, density and arrangement of these obstacles.

The constitutive equation for the average dislocation velocity is formulated as follows (Balasubramanian and Anand, 2002). At a temperature of absolute zero, let $\hat{\kappa}^{\alpha}(0)$ denote the critical slip resistance; then the sign of $\overline{v}^{\alpha}$ is the same as that of the effective resolved shear stress $\left(\tau^{\alpha} - \chi^{\alpha} \right)$, and its magnitude is given by

$$\begin{aligned} &\overline{v}^{\alpha} = 0 && \text{if } \left| \tau^{\alpha} - \chi^{\alpha} \right| < \hat{\kappa}^{\alpha}(0) \\ &\overline{v}^{\alpha} > 0 && \text{if } \left| \tau^{\alpha} - \chi^{\alpha} \right| = \hat{\kappa}^{\alpha}(0) \end{aligned} \tag{2.11}$$

Note that the backstress, χ^{α}, must be subtracted from the applied stress to reflect the net driving force on dislocations. The slip resistance $\hat{\kappa}^{\alpha}(0)$ at absolute zero is called the mechanical threshold (Kocks et al., 1975). Because of the usual variability of the microstructural state of real materials, the transition from zero dislocation velocity to a high velocity will not be as sharp as idealized in Eq.(2.11), but it should still exhibit a "threshold" behavior. At a finite temperature, T > 0K, this response is modified; since the underlying mechanism which governs the magnitude of κ^{α} is an elastic interaction on the atomic scale of a mobile dislocation segment with the microstructural barriers, an increase in temperature should result in a decrease in the magnitude of κ^{α}, primarily due to the attendant decrease in the elastic modulus. Let

$$\tau_{v}^{\alpha} = \left|\tau^{\alpha} - \chi^{\alpha}\right| - \frac{\mu}{\mu_{o}}\kappa^{\alpha} \qquad (2.12)$$

denote an effective stress, also called the viscous overstress, where μ and μ_{o} refer to the elastic shear modulus at the temperature (T) and at absolute zero, respectively. It is noted that $\frac{\mu}{\mu_{o}}\kappa^{\alpha}$ is regarded as an athermal component of resistance to dislocation motion at all temperatures, corresponding to very probability of barrier bypass due to thermal fluctuation. Intrinsic lattice resistance is included. Eq. (2.11) is then given as

$$\overline{v}^{\alpha} = \overline{v}^{\alpha}\left(\tau_{v}^{\alpha}, T\right)$$

At temperatures, T>0 K, the motion of the mobile dislocation segments is thermally activated. Using the framework of transition-state theory (Krausz and Eyring, 1975), with

ΔG^{α} denoting the difference in the free enthalpy between the saddle point and the ground point for a shear increment, the quantity $\left(\exp\left\{-\Delta G / k_B T\right\}\right)$ is the probability that a thermal fluctuation of the required energy (or larger) for a shear increment can occur at a temperature, T. Here, ΔG^{α} is the activation free enthalpy or the Gibbs' free energy for activation, and k_B is the Boltzmann's constant. The rate at which dislocations overcome the obstacles is given by $\left(\nu \exp\left\{-\Delta G / k_B T\right\}\right)$, where ν is a characteristic attempt frequency factor on the order of 10^{12} s^{-1}. Then, with $\bar{l}^{\alpha}$ denoting the mean distance of advance of a mobile dislocation segment, the magnitude of the average dislocation velocity may be written as

$$\begin{aligned} \bar{v}^{\alpha} &= 0 && \text{if } \tau_v^{\alpha} \le 0 \\ \bar{v}^{\alpha} &= \bar{l}^{\alpha} \nu \exp\left(-\frac{\Delta G^{\alpha}\left(\tau_v^{\alpha}\right)}{k_B T}\right) && \text{if } \tau_v^{\alpha} > 0 \end{aligned} \qquad (2.13)$$

Based on Eq.(2.13) the shearing rates may be written as

$$\begin{aligned} \dot{\gamma}^{\alpha} &= 0 && \text{if } \tau_v^{\alpha} \le 0 \\ \dot{\gamma}^{\alpha} &= \dot{\gamma}_0^{\alpha} \exp\left(-\frac{\Delta G_*^{\alpha}\left(\tau_v^{\alpha}\right)}{k_B T}\right) \operatorname{sgn}\left(\tau^{\alpha} - \chi^{\alpha}\right) && \text{if } \tau_v^{\alpha} > 0 \end{aligned} \qquad (2.14)$$

$$\text{with } \dot{\gamma}_0^{\alpha} = \rho_m^{\alpha} b \bar{l}^{\alpha} \nu \qquad (2.15)$$

The mobile dislocation density, which contributes to $\dot{\gamma}_0^{\alpha}$ could be a function of the applied stress and the temperature (Kocks et al., 1975), but any such dependence is

neglected here. The considerations of Kocks et al. (1975)concerning the nature of the activation free enthalpy suggest that ΔG_*^α may be expressed as

$$\Delta G_*^\alpha = F_o\left[1-\left(\frac{\tau_v^\alpha}{D^\alpha}\right)^p\right]^q \tag{2.16}$$

where F_o is the activation free energy required to overcome the obstacles to slip without the aid of an external work. In this model, $D^\alpha+\kappa^\alpha$ is the maximum glide resistance at which dislocations can be mobilized without the aid of thermal activation, i.e. at 0 K. It is noted that this theory differs from the original Kocks model effectively by assigning zero probabilility of bypassing certain barriers by thermal fluctuations.

Based on Eqs. (2.14) and (2.16), the shearing rate for the α^{th} system is related to its associated viscous overstress by (McDowell, 1992)

$$\dot\gamma^\alpha = \dot\gamma_o\Theta(T)\left\langle\frac{\tau_v^\alpha}{D^\alpha}\right\rangle^n \exp\left\{B_o\left\langle\frac{\tau_v^\alpha}{D^\alpha}\right\rangle^{n+1}\right\}\mathrm{sgn}\left(\tau^\alpha-\chi^\alpha\right) \tag{2.17}$$

where the slip system viscous overstress τ_v^α is given in terms of the resolved shear stress τ^α by

$$\tau_v^\alpha = \left|\tau^\alpha-\chi^\alpha\right|-\kappa^\alpha\frac{\mu}{\mu_o} \quad \text{and} \quad D^\alpha = D_o\frac{\mu}{\mu_o} \tag{2.18}$$

Here, χ^α is the backstress and κ^α is the threshold stress (or slip resistance) on each slip system. Increase in the threshold stress effectively leads to an increase in size of the viscoplastic flow potential, while the backstress results in a shift of the potential surface.

In Ni-base superalloys, the threshold stress may be viewed as the resistance to plastic flow arising from athermal statistical strengthening mechanisms associated with an increase in the dislocation density, solid solution strengthening, etc., while D^{α} reflects the component of flow resistance that can be overcome by thermal fluctuation, e.g. climb assisted glide. The backstress displays a directional dependence and is manifested by slip heterogeneity at the microscale, including internal stresses that develop with deformation due to net dislocation pile-up at obstacles such as precipitate particles, grain or phase boundaries, differential yielding among grains or within hard (dislocation walls) and soft regions of the microstructure, and to incorporate statistical aspects of dislocations bypassing barriers. Both backstress, χ^{α}, and the threshold stress, κ^{α}, depend on the history of temperature and viscoplastic deformation.

Equations (2.17) and (2.18) contain several other additional parameters defined as follows: $\dot{\gamma}_o$ is a reference shearing rate, n governs the power law creep regime, B_o and (n+1) collectively govern the power law breakdown behavior at higher strain rates where the response becomes nearly rate independent, The drag stress, D^{α} is weakly dependent on the history of temperature and viscoplastic deformation when the behavior of the γ and γ' phases are homogenized, μ is the shear modulus, with μ_o being the value of the shear modulus at absolute zero. $\Theta(T)$ is the diffusivity parameter given by

$$\Theta(T) = \exp\left(-\frac{Q_o}{RT}\right) \quad \text{for } T \geq \frac{T_m}{2}$$
$$\Theta(T) = \exp\left\{-\frac{2Q_o}{RT_m}\left[\ln\left(\frac{T_m}{2T}\right)+1\right]\right\} \quad \text{for } T \leq \frac{T_m}{2} \tag{2.19}$$

where Q_o is the activation energy for thermally-activated dislocation bypass of obstacles. Here, R is the universal gas constant and T_m is the absolute melting point temperature.

The effective strain rate sensitivity exponent on the stress (inverse strain rate sensitivity) is given by

$$m = \frac{\partial \ln \dot{\gamma}^{\alpha}}{\partial \ln \tau^{\alpha}} = \frac{\partial \ln \dot{\gamma}^{\alpha}}{\partial \ln \tau_{v}^{\alpha}} = n + \frac{B_{o}(n+1)}{D^{\alpha}} \left\langle \frac{\tau_{v}^{\alpha}}{D^{\alpha}} \right\rangle^{n} \tag{2.20}$$

It is assumed that the flow rule given in Eq. (2.17) is suitable for modeling the homogenized $\gamma - \gamma'$ phases, but with a much higher intrinsic lattice friction necessary to model the higher activation energy for slip compared to modeling only a single phase, such as the γ matrix. It is commonly observed that the creep exponent of Ni-base superalloys is more or less invariant with respect to the γ' precipitate volume fraction and morphology, suggesting that slip is indeed restricted in the precipitates, which provide primary elevated temperature strength.

2.6 Slip Systems

Eighteen slip systems are used; 12 octahedral slip systems and 6 cube slip systems as shown in Figure 2.7. The slip systems are listed in Table 2.2. All slip systems are assumed active above the threshold stress.

Table 0.2 Slip systems in DS GTD111.

Slip System (α)	Octahedral Slip		Cube Slip	
	Slip Plane	Slip Direction	Slip Plane	Slip Direction
1	$\{111\}$	$\langle 01\bar{1}\rangle$	$\{100\}$	$\langle 011\rangle$
2	$\{111\}$	$\langle \bar{1}01\rangle$	$\{100\}$	$\langle 01\bar{1}\rangle$
3	$\{111\}$	$\langle 1\bar{1}0\rangle$	$\{010\}$	$\langle 101\rangle$
4	$\{1\bar{1}\bar{1}\}$	$\langle 0\bar{1}1\rangle$	$\{010\}$	$\langle 10\bar{1}\rangle$
5	$\{1\bar{1}\bar{1}\}$	$\langle \bar{1}0\bar{1}\rangle$	$\{001\}$	$\langle 110\rangle$
6	$\{1\bar{1}\bar{1}\}$	$\langle 110\rangle$	$\{001\}$	$\langle \bar{1}10\rangle$
7	$\{\bar{1}1\bar{1}\}$	$\langle 011\rangle$		
8	$\{\bar{1}1\bar{1}\}$	$\langle 10\bar{1}\rangle$		
9	$\{\bar{1}1\bar{1}\}$	$\langle \bar{1}\bar{1}0\rangle$		
10	$\{\bar{1}\bar{1}1\}$	$\langle 0\bar{1}\bar{1}\rangle$		
11	$\{\bar{1}\bar{1}1\}$	$\langle 101\rangle$		
12	$\{\bar{1}\bar{1}1\}$	$\langle \bar{1}10\rangle$		

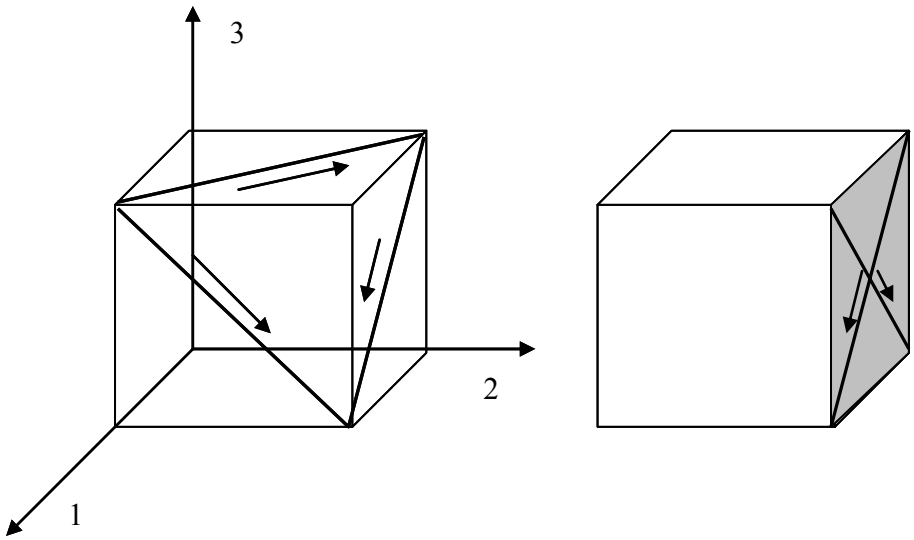

Figure 0.7 (a) Octahedral slip systems and (b) cube slip systems Note: Only 1 plane is shown for each type of slip system for clarity.

The twelve octahedral <110> slip systems are appropriate for FCC single crystals and are active for the entire temperature range. The 6 cube slip systems {100}<110> type (3 planes with 2 directions in each = 6 systems) may be active at high homologous temperatures and high resolved shear stress (in γ' phase), but their role is less well understood and characterized. A precise mechanism is still largely conjectural, since the identification of the role of cube slip is challenging. It is often inferred by fitting experimental stress strain data for loading in <111> direction of single crystals for which the resolved shear stress is very low on the octahedral planes.

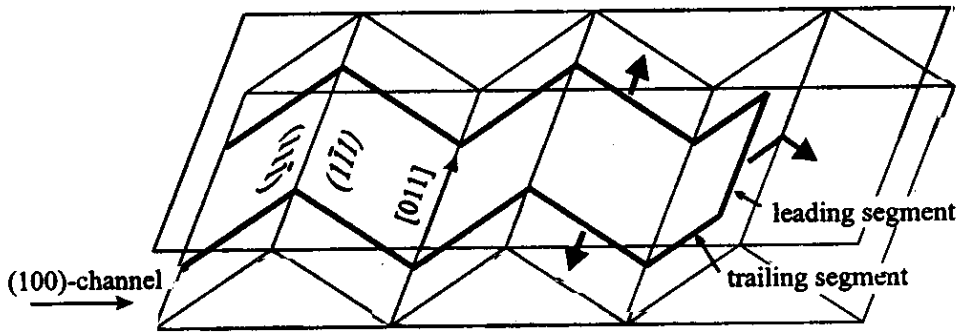

Figure 0.8 Zig-zag motion of screw dislocations at the precipitate interface (Osterle et al., 2000).

For homogenized $\gamma-\gamma'$ single crystals, the role of cube slip is usually assessed by considering the breakdown of the capability of octahedral slip to model the stress-strain-time behavior as a function of temperature, which of course depends on other elements of the constitutive framework. There are two sources of cube slip: (i) manifestation of zig-zag octahedral slip at the $\gamma-\gamma'$ interface in the γ - matrix and (ii) actual cube slip in the γ'- precipitates at the higher temperatures, along orientations close to [111] (Sun and Hazzledine, 1996). The work of Bettge and Osterle (1999) on SC16 have revealed that macroscopic cube slip is a manifestation of octahedral slip in the γ matrix at the $\gamma-\gamma'$ interface and takes place by multiple cross slip events on octahedral planes, producing zig-zag dislocation lines as shown in Figure 2.8. The screw segment of a dislocation loop with Burger's vector along 1/2(011) and gliding on the $(1\bar{1}1)$ plane is blocked by an (100) $\gamma-\gamma'$ interface and cross slips onto $(11\bar{1})$. After gliding on this plane, it encounters the $\gamma-\gamma'$ interface at the precipitate on the opposite side and cross slips back onto $(1\bar{1}1)$. The leading screw segment generates two trailing zig-zag shaped dislocation lines marking its way. This goes on resulting in the formation of the zig-zag dislocation

pattern. The trailing dislocation segments can glide along (011), thus shearing material parallel to the (100) plane. This enables the dislocations to travel large distances along matrix channels, thus effectively shearing material along the cube planes. This leads to formation of the macroscopic (100) slip traces.

From experimental observations, softening occurs as the orientation is rotated from the [100] orientation at intermediate and high temperatures (Mielek et al., 1997). When only octahedral slip is active, hardening is predicted as the loading axis is rotated from the [100] direction, which is inconsistent with experimental observation. Both sources of cube slip, zig-zag cross slip in the γ phase and motion of dislocation segments on cube planes in the γ' phase, are lumped together in the present model, treated via the activation of the cube slip systems. Both the octahedral and cube slip systems are assumed to be active in this model at all times.

2.7 Thermodynamics

The thermodynamic state of the material can be defined by a number of independent state variables in addition to the elastic strain and temperature. The state variables are classified into two groups; one contains the observable variables and the other contains internal variables that must be inferred. Both groups relate to microstructure change and energy dissipation.

The Helmholtz free energy ψ can be written in a decomposed form of the elastic term ψ^e and nonelastic term ψ^p (Shin et al., 1997; Ortiz and Stainier, 1999)

$$\psi = \psi^e\left(\mathbf{C}^e, T\right) + \psi^p\left(\xi_i^\alpha, T\right) \tag{2.21}$$

where ξ^{α}_{i} is a set of i=1,2,…N state variables of kinematic type, and

$$\psi^{e}\left(\mathbf{C}^{e}\right)=\frac{1}{2}\boldsymbol{\sigma}:\mathbf{C}^{-1}:\boldsymbol{\sigma}=\frac{1}{2}\boldsymbol{\varepsilon}:\mathbf{C}^{-1}:\boldsymbol{\varepsilon} \tag{2.22}$$

Due to the restrictions of the principle of material frame indifference, the elastic part of the Helmholtz free energy, ψ^{e}, is formulated most generally in terms of the elastic right Cauchy–Green tensor, $\mathbf{C}^{e}=\mathbf{F}^{eT}\cdot\mathbf{F}^{e}$ (Miehe and Stein, 1992). The nonelastic part of the Helmholtz free energy, ψ^{p}, depends on the thermodynamic displacements, ξ^{α}_{i}, corresponding to the internal state variables, threshold slip resistance (κ^{α}) and backstresses (χ^{α}) respectively, i.e.

$$\rho\frac{\partial\psi^{p}}{\partial\xi^{\alpha}_{1}}=\kappa^{\alpha}\ \text{and}\ \rho\frac{\partial\psi^{p}}{\partial\xi^{\alpha}_{2}}=\chi^{\alpha} \tag{2.23}$$

For an isothermal deformation, the Clausius–Duhem inequality is expressed in terms of the effective 2nd Piola–Kirchhoff stress tensor as (Miehe et al., 1999)

$$\frac{1}{2}\boldsymbol{\sigma}^{pk2}:\left[\dot{\mathbf{C}}^{e}+2\left(\mathbf{C}^{e}\cdot\hat{\mathbf{L}}^{p}\right)^{sym}\right]-\dot{\psi}\geq 0 \tag{2.24}$$

From Clausius–Duhem inequality Eq. (2.24) and using Eqs. (2.21) and (2.22)

$$\frac{1}{2}\boldsymbol{\sigma}^{pk2}:\dot{\mathbf{C}}^{e}+\left(\mathbf{C}^{e}\cdot\boldsymbol{\sigma}^{pk2}\right):\hat{\mathbf{L}}^{p}-\rho\frac{\partial\psi^{e}}{\partial\mathbf{C}^{e}}:\dot{\mathbf{C}}^{e}-\sum_{\alpha}\rho\frac{\partial\psi^{p}}{\partial\xi^{\alpha}_{1}}\dot{\xi}^{\alpha}_{1}-\sum_{\alpha}\rho\frac{\partial\psi^{p}}{\partial\xi^{\alpha}_{2}}:\dot{\xi}^{\alpha}_{2}\geq 0 \tag{2.25}$$

Using Eq. (2.23) this leads to

$$\frac{1}{2}\boldsymbol{\sigma}^{pk2}:\dot{\mathbf{C}}^{e}+\left(\mathbf{C}^{e}\cdot\boldsymbol{\sigma}^{pk2}\right):\hat{\mathbf{L}}^{p}-\rho\frac{\partial\psi^{e}}{\partial\mathbf{C}^{e}}:\dot{\mathbf{C}}^{e}-\sum_{\alpha}\kappa^{\alpha}:\dot{\xi}_{1}^{\alpha}-\sum_{\alpha}\chi^{\alpha}:\dot{\xi}_{2}^{\alpha}\geq 0 \tag{2.26}$$

In order to ensure that Eq. (2.26) is satisfied for every admissible process

$$\begin{aligned}&\boldsymbol{\sigma}^{pk2}=2\rho\frac{\partial\psi^{e}}{\partial\mathbf{C}^{e}}=\mathbf{C}^{e}:\boldsymbol{\varepsilon}^{e}\\&\left(\mathbf{C}^{e}\cdot\boldsymbol{\sigma}^{pk2}\right):\hat{\mathbf{L}}^{p}-\sum_{\alpha}\kappa^{\alpha}\dot{\xi}_{1}^{\alpha}-\sum_{\alpha}\chi^{\alpha}\dot{\xi}_{2}^{\alpha}\geq 0\end{aligned} \tag{2.27}$$

From Eqs. (2.3) and (2.8),

$$\left(\mathbf{C}^{e}\cdot\boldsymbol{\sigma}^{pk2}\right):\hat{\mathbf{L}}^{p}=\sum_{\alpha}\tau^{\alpha}\dot{\gamma}^{\alpha} \tag{2.28}$$

which leads to

$$\sum_{\alpha}\tau^{\alpha}\dot{\gamma}^{\alpha}-\sum_{\alpha}\kappa^{\alpha}\dot{\xi}_{1}^{\alpha}-\sum_{\alpha}\chi^{\alpha}\dot{\xi}_{2}^{\alpha}=\sum_{\alpha}\tau^{\alpha}\dot{\gamma}^{\alpha}-\kappa^{\alpha}\dot{\xi}_{1}^{\alpha}-\chi^{\alpha}\dot{\xi}_{2}^{\alpha}\geq 0 \tag{2.29}$$

Note that a given crystal plasticity formulation should automatically yield a non-negative value in Eq.(2.29) even for materials exhibiting strain hardening (Busso and Cailletaud, 2005).

2.8 Evolution Equations for the Internal State Variables (ISVs)

The anomalous yield behavior of γ-γ' Nickel base superalloys, i.e., the yield stress increases with temperature in the intermediate temperature regime, is incorporated in the

threshold stress. The anomalous behavior has been attributed to mechanisms involving $\{111\}\langle 110\rangle$ octahedral slip within the γ' precipitates. Several models attempt to explain this mechanism, including the Takeuchi and Karamoto model (1971; 1973), the Paidar-Pope-Vitek (PPV) model (Paidar et al., 1984) and the model proposed by Hirsch (1992). Though recent experimental evidence (Sun and Hazzledine, 1996) seems to support the Hirsch theory, the PPV model has perhaps been the most widely used model (Sheh and Stouffer, 1990), at least in the anomalous temperature regime (room temperature-750ºC). It should also be noted that the orientation dependent tension compression asymmetry is controlled by the probability of cross slip in the Hirsch model, which is still explained by the PPV theory, therefore the PPV theory is considered adequate in the current formulation.

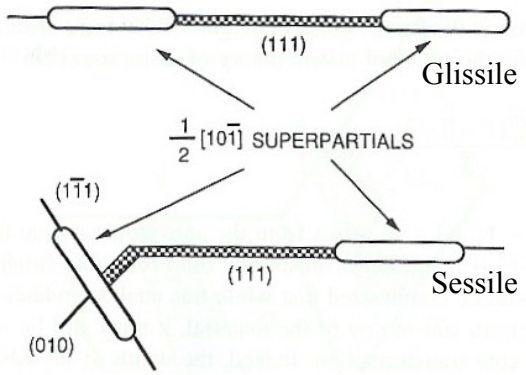

Figure 0.9 Glissile and sessile dislocation configuration based on the PPV model (Vitek et al., 1996).

According to the PPV model (Paidar et al., 1984), in the anomalous behavior temperature regime (room temperature-750°C) $\langle 10\bar{1}\rangle$ screw dislocations on (111) planes split into two super-Shockley partials separated by an anti-phase boundary (APB). There are two configurations of the $a/2\langle 10\bar{1}\rangle$ screw dislocation: a glissile configuration with its core spread in the (111) plane and a sessile configuration with a non-planar core

spread in the $(1\,\bar{1}\,1)$ plane as shown in Figure 2.9. The sessile dislocation core acts as pinning points for subsequent dislocations, thus, increasing the slip resistance. The transformation from the glissile to sessile configuration is a thermally activated process and increases with temperature in the intermediate temperature regime. At higher temperatures, thermally activated diffusion process allow the pinned screw dislocations to move on the {001} planes.

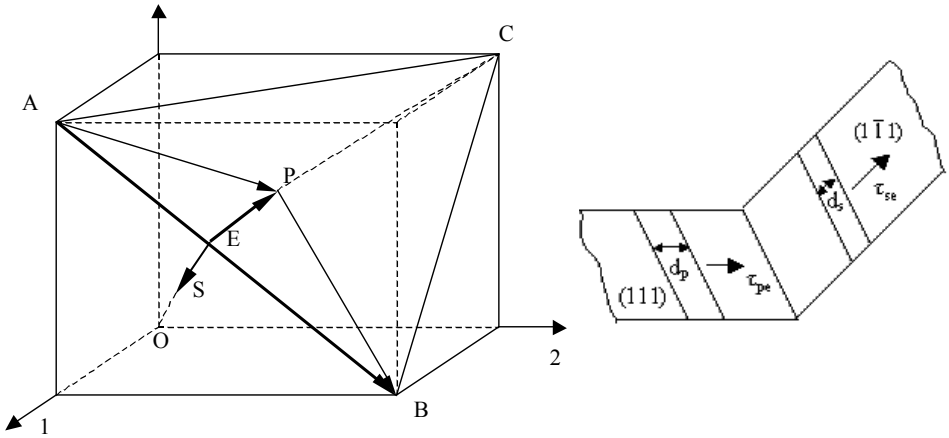

(a) (b)

Figure 0.10 (a) Directions of the non-Schmid stresses (Qin and Bassani, 1992) and (b) schematic picture showing screw dislocations split in (111) and $(1\,\bar{1}\,1)$ planes with the shear stress components playing a role in the cross slip process. τ_{pe} is in the direction perpendicular to the burgers vector in the primary (111) plane and τ_{se} is in the direction perpendicular to the burgers vector in the cross slip $(1\,\bar{1}\,1)$ plane.

The glissile to sessile core transformation is explained in three steps: (i) constriction of the glissile core on the (111) plane, (ii) movement of the constricted dislocation along the (010) plane, and (iii) spreading of the dislocation on the $(1\,\bar{1}\,1)$ plane. The glissile core has to constrict first for this to happen; hence, any shear stress that aids in the constriction of the partial dislocations will assist cross-slip, leading to formation of sessile locks which act as obstacles to the glissile dislocations. Slip on the octahedral planes will be

influenced by the shear stresses on the primary cross slip planes (τ_{pe}) (step (i)) the shear stresses acting on the cube plane (step (ii)) and shear stresses on the secondary cross slip planes (τ_{se}) (step (iii)). A slip system on the (111) plane in $\langle 1\bar{1}1 \rangle$ direction is illustrated geometrically in Figure 2.10(a). The primary slip plane is ABC and the secondary slip plane is ABO. The primary slip direction (Burgers vector) is AB; AP and PB are the Shockley partials and EP is their edge direction which defines the sense of τ_{pe} for the slip system. Similarly, ES defines the direction of τ_{se}. The cross-slip plane is the cube face that contains the slip direction AB, i.e. the (100) plane, which defines the sense for τ_{cb}. The additional dependence of the activation enthalpy for the glissile to sessile transformation on the shear stress components (τ_{pe}, τ_{se} and τ_{cb}) leads to a non-Schmid effect. Since the enthalpy is also dependent on the sign of the stress components for steps (i) and (iii), it will differ in tension and compression. This leads to a tension-compression asymmetry that is orientation dependent. It should be noted that step (iii) is independent of the sense of loading. The activation enthalpy for this glissile-sessile transformation is given as (Vitek et al., 1996)

$$H_p = \frac{\mu b^3}{2\pi}\left\{ h + \frac{\lambda}{\mu}\left(\tau_{pe} - \kappa\tau_{se}\right) + \frac{c}{2} - \left[\frac{\left(\frac{\Delta E}{b^2} + \frac{|\tau_{cb}|}{2}\right)\pi}{\mu}\right]^{\frac{1}{2}}\right\} \qquad (2.30)$$

where b is the burgers vector, c is the normalized self energy of the kink in Step (ii), and h is a dimensionless parameter which depends on the width of the splitting of the partials in the cross slip plane in an unstressed solid. ΔE is the energy difference per unit length

of the dislocation, between the sessile and Glissile core configuration. The planes and normals that define τ_{pe}, τ_{se}, and τ_{cb} are listed in Table 2.3.

Table 0.3 Slip Systems of the shear stresses (Qin and Bassani, 1992).

	τ^{α}	τ^{α}_{pe}	τ^{α}_{se}	τ^{α}_{cb}
1	$\{111\}\langle 01\bar{1}\rangle$	$\{111\}\langle \bar{2}11\rangle$	$\{1\bar{1}\bar{1}\}\langle \bar{2}\bar{1}\bar{1}\rangle$	$\{100\}\langle 01\bar{1}\rangle$
2	$\{111\}\langle \bar{1}01\rangle$	$\{111\}\langle 1\bar{2}1\rangle$	$\{\bar{1}1\bar{1}\}\langle \bar{1}2\bar{1}\rangle$	$\{010\}\langle \bar{1}01\rangle$
3	$\{111\}\langle 1\bar{1}0\rangle$	$\{111\}\langle 11\bar{2}\rangle$	$\{\bar{1}\bar{1}1\}\langle \bar{1}\bar{1}2\rangle$	$\{001\}\langle 1\bar{1}0\rangle$
4	$\{1\bar{1}\bar{1}\}\langle 0\bar{1}1\rangle$	$\{1\bar{1}\bar{1}\}\langle \bar{2}\bar{1}\bar{1}\rangle$	$\{111\}\langle \bar{2}11\rangle$	$\{100\}\langle 0\bar{1}1\rangle$
5	$\{1\bar{1}\bar{1}\}\langle \bar{1}0\bar{1}\rangle$	$\{1\bar{1}\bar{1}\}\langle 12\bar{1}\rangle$	$\{\bar{1}\bar{1}1\}\langle \bar{1}21\rangle$	$\{0\bar{1}0\}\langle \bar{1}0\bar{1}\rangle$
6	$\{1\bar{1}\bar{1}\}\langle 110\rangle$	$\{1\bar{1}\bar{1}\}\langle 1\bar{1}2\rangle$	$\{\bar{1}1\bar{1}\}\langle \bar{1}12\rangle$	$\{00\bar{1}\}\langle 110\rangle$
7	$\{\bar{1}1\bar{1}\}\langle 011\rangle$	$\{\bar{1}1\bar{1}\}\langle 21\bar{1}\rangle$	$\{\bar{1}\bar{1}1\}\langle 2\bar{1}1\rangle$	$\{\bar{1}00\}\langle 011\rangle$
8	$\{\bar{1}1\bar{1}\}\langle 10\bar{1}\rangle$	$\{\bar{1}1\bar{1}\}\langle \bar{1}2\bar{1}\rangle$	$\{111\}\langle 1\bar{2}1\rangle$	$\{010\}\langle 10\bar{1}\rangle$
9	$\{\bar{1}1\bar{1}\}\langle \bar{1}\bar{1}0\rangle$	$\{\bar{1}1\bar{1}\}\langle \bar{1}12\rangle$	$\{1\bar{1}\bar{1}\}\langle 1\bar{1}2\rangle$	$\{00\bar{1}\}\langle \bar{1}\bar{1}0\rangle$
10	$\{\bar{1}\bar{1}1\}\langle 0\bar{1}\bar{1}\rangle$	$\{\bar{1}\bar{1}1\}\langle 2\bar{1}1\rangle$	$\{\bar{1}1\bar{1}\}\langle 21\bar{1}\rangle$	$\{\bar{1}00\}\langle 0\bar{1}\bar{1}\rangle$
11	$\{\bar{1}\bar{1}1\}\langle 101\rangle$	$\{\bar{1}\bar{1}1\}\langle \bar{1}21\rangle$	$\{1\bar{1}\bar{1}\}\langle 12\bar{1}\rangle$	$\{0\bar{1}0\}\langle 101\rangle$
12	$\{\bar{1}\bar{1}1\}\langle \bar{1}10\rangle$	$\{\bar{1}\bar{1}1\}\langle \bar{1}\bar{1}2\rangle$	$\{111\}\langle 11\bar{2}\rangle$	$\{001\}\langle \bar{1}10\rangle$

The activation enthalpy in Eq. (2.30) depends on τ_{pe}, τ_{se}, and τ_{cb}. The contribution from τ_{pe} and τ_{se} are sensitive to the sense of loading (positive or negative) and leads to the tension-compression asymmetry of the stress response while τ_{cb} is not dependent on the sign. To include the non-Schmid effect, Sheh and Stouffer (1988) included an additional contribution to the threshold stress, i.e.

$$\kappa_c^\alpha = \kappa_o^\alpha(T) + h_{pe}(T)\tau_{pe}^\alpha + h_{se}(T)\tau_{se}^\alpha + h_{cb}(T)\left|\tau_{cb}^\alpha\right| \tag{2.31}$$

Therefore the critical threshold stress (κ^α) is

$$\kappa^\alpha = \kappa_c^\alpha + \kappa_e^\alpha \tag{2.32}$$

where

$$\dot{\kappa}_e^\alpha = h_o \sum_{\beta=1}^{N_{slip}} q^{\alpha\beta}\left|\dot{\gamma}^\beta\right| - h_{\kappa s}\kappa^\alpha \sum_{\beta=1}^{N_{slip}}\left|\dot{\gamma}^\beta\right| - h_s\left\langle \kappa^\alpha - \kappa_{th}\right\rangle^{r_s} \tag{2.33}$$

where h_{pe}, h_{se}, h_{cb}, are temperature dependent material parameters. It is noted that the critical stress, τ_{cr}, changes as a function of temperature and is embedded in $\kappa_o^\alpha(T)$. These terms (h_{pe}, h_{se}, h_{cb}) are turned off at high temperatures (>750°C) at which the PPV model is no longer applicable. However, $\kappa_o^\alpha(T)$ is temperature dependent even at the higher temperatures to account for the unpinning mechanism of the sessile dislocation cores, which leads to a decrease in the threshold slip resistance. κ_e^α is a measure of the work hardening.

The backstress evolution for homogenized $\gamma - \gamma'$ models can be written in the hardening-dynamic recovery plus static thermal recovery format as

$$\dot{\chi}^{\alpha} = h_{\chi} \left| \dot{\gamma}^{\alpha} \right| \operatorname{sgn}\left(\tau^{\alpha} - \chi^{\alpha}\right) - h_{\chi d} \chi^{\alpha} \left| \dot{\gamma}^{\alpha} \right| + \left(\frac{1}{R_{\chi}} \frac{\partial R_{\chi}}{\partial T} + \frac{1}{h_{\chi d}} \frac{\partial h_{\chi d}}{\partial T} \right) \chi^{\alpha} \dot{T} - \Omega_{\chi}^{\alpha} \qquad (2.34)$$

where $\Omega_{\chi}^{\alpha} = h_{\chi s}(T) \left| \chi^{\alpha} \right|^{r_{\chi s}} \chi^{\alpha}$ is the static thermal recovery term, (h_{χ} , $h_{\chi d}$, $h_{\chi s}$, $r_{\chi s}$) are material parameters, and $R_{\chi} = h_{\chi} / h_{\chi d}$. The temperature rate dependent term is necessary to properly model the hysteresis behavior under thermomechanical fatigue (TMF) (McDowell, 1992), since the model parameters that govern the backstress evolution rates are themselves functions of temperature. Note that for single phase models, the backstress evolution equation can likely be neglected, but it is essential to describe the overall average behavior of the crystallographic grains in homogenized $\gamma - \gamma'$ models. Backstress is a very significant fraction of the flow stress (typically > 30%) for Ni-base superalloys (Castelli and Ellis, 1993). The constitutive equations are summarized in Table 2.4.

Table 0.4 Summary of constitutive model for DS GTD111.

Flow Rule:

$$\dot{\gamma}^{\alpha} = \dot{\gamma}_{o}\Theta(T)\left\langle \frac{\tau_{v}^{\alpha}}{D^{\alpha}} \right\rangle^{n} \exp\left\{ B_{o}\left\langle \frac{\tau_{v}^{\alpha}}{D^{\alpha}} \right\rangle^{n+1} \right\} \mathrm{sgn}\left(\tau^{\alpha} - \chi^{\alpha}\right)$$

where

$$\tau_{v}^{\alpha} = \left|\tau^{\alpha} - \chi^{\alpha}\right| - \kappa^{\alpha}\frac{\mu}{\mu_{o}} \qquad \text{and} \qquad D^{\alpha} = D_{o}\frac{\mu}{\mu_{o}}$$

$$\Theta(T) = \exp\left(-\frac{Q_{o}}{RT}\right) \qquad T \geq \frac{T_{m}}{2}$$

$$\Theta(T) = \exp\left\{-\frac{2Q_{o}}{RT_{m}}\left[\ln\left(\frac{T_{m}}{2T}\right) + 1\right]\right\} \qquad T \leq \frac{T_{m}}{2}$$

Evolution Equations for Hardening Variables:

Back stress

$$\dot{\chi}^{\alpha} = h_{\chi}\left|\dot{\gamma}^{\alpha}\right|\mathrm{sgn}\left(\tau^{\alpha} - \chi^{\alpha}\right) - h_{\chi d}\chi^{\alpha}\left|\dot{\gamma}^{\alpha}\right| + \left(\frac{1}{R_{\chi}}\frac{\partial R_{\chi}}{\partial T} + \frac{1}{h_{\chi d}}\frac{\partial h_{\chi d}}{\partial T}\right)\chi^{\alpha}\dot{T} - \Omega_{\chi}^{\alpha}, \qquad R_{\chi} = h_{\chi}/h_{\chi d}$$

where $\Omega_{\chi}^{\alpha} = h_{\chi s}\left|\chi^{\alpha}\right|^{r_{\chi s}}\chi^{\alpha}$

Threshold Stress

$$\kappa^{\alpha} = \kappa_{c}^{\alpha} + \kappa_{e}^{\alpha}, \qquad \kappa_{c}^{\alpha} = \kappa_{o}^{\alpha}(T) + h_{pe}\tau_{pe}^{\alpha} + h_{se}\tau_{se}^{\alpha} + h_{cb}\left|\tau_{cb}^{\alpha}\right|$$

$$\dot{\kappa}_{e}^{\alpha} = h_{o}\sum_{\beta=1}^{N_{slip}} q^{\alpha\beta}\left|\dot{\gamma}^{\beta}\right| - h_{\kappa s}\kappa^{\alpha}\sum_{\beta=1}^{N_{slip}}\left|\dot{\gamma}^{\beta}\right| - h_{s}\left\langle \kappa^{\alpha} - \kappa_{th}\right\rangle^{r_{s}}$$

Initial conditions: $\chi^{\alpha}(0) = 0$, $\kappa_{e}^{\alpha}(0) = 0$

2.9. Experimental Data

Test sections were sectioned from three batches of cast plates of DS GTD111. Solid specimens with a uniform gage length of 12.7 mm (0.5 in) and a diameter of 6.35 mm (0.25 in) were machined from sections oriented in the longitudinal (L) and transverse (T) directions. The tests were conducted under mechanical strain control using an extensometer with ceramic tips in direct contact with the specimen to measure the total strain. The mechanical strain ratio $R_\varepsilon = \varepsilon_{min}/\varepsilon_{max}$ was held constant at $R_\varepsilon = -1$. For both LCF and TMF tests, the temperature was maintained using a PID temperature controller. In TMF tests, the temperature reading was transmitted to the TestStar controller and used to calculate the components of thermal and mechanical strain. All TMF tests were conducted using closed-loop, temperature-based thermal strain control. A total of 36 strain-controlled isothermal LCF tests and 5 TMF tests were conducted. Three types of cycles were used: continuous cycling with (a) no hold time (CC), (b) with 2 minute hold time in tension (HT), and (c) with 2 minute hold time in compression (HC). A constant total strain rate of 0.005 s^{-1} was used during the loading and unloading ramps. These tests were conducted by Gordon and the details of the testing procedure can be obtained in Gordon's thesis (2006)

2.10. Implementation

The constitutive model was implemented as User MATerial (UMAT) subroutine in ABAQUS (ABAQUS, 2003). A hyperelastic formulation was used, valid for arbitrary finite strain. The purpose of the user material subroutine is to update the values of the stress and Jacobian matrix for any given deformation gradient increment.

The essence of the method is to evaluate the slip system shearing rates in the flow rule based upon quantities at the end of the time step in a fully implicit (backward Euler) scheme, i.e.,

$$\dot{\gamma}^{\alpha} = \dot{\gamma}_{o}\Theta(T)\left\langle \frac{\tau_{v}^{\alpha}}{D^{\alpha}} \right\rangle_{t+\Delta t}^{n} \exp\left\{ B_{o}\left\langle \frac{\tau_{v}^{\alpha}}{D^{\alpha}} \right\rangle_{t+\Delta t}^{n+1} \right\} \mathrm{sgn}\left(\tau^{\alpha}-\chi^{\alpha}\right)_{t+\Delta t} \tag{2.35}$$

However, the resolved shear stress and backstress at the end of the time step depend on the values of $\left(\dot{\gamma}^{\alpha}\right)$; thus, a Newton-Raphson (N-R) technique is used to find the roots for these sets of equations. A time step sub-incrementation scheme and a linear search algorithm were employed in the constitutive subroutine to ensure convergence based on McGinty and McDowell (1999). A detailed description of the implementation procedure can be obtained in McGinty (2001).

2.11 Determination of material parameters for DS GTD11

2.11.1 Octahedral Slip Systems

The material parameters for the octahedral slip systems are determined from data obtained from uniaxial cyclic loading of longitudinal specimens along the [100] orientation, for which the loading axis is oriented along the grain growth direction in DS GTD111. Cube slip is not activated in this orientation for small deformations. The stress-strain response in the longitudinal orientation is obtained using a single element simulation for one grain with loading in the (001) orientation.

2.11.2 Cube Slip Systems

The material parameters for the cube slip systems are determined using data from the transverse specimens (loading perpendicular to the grain growth direction) due to lack of data in other orientations. It should be noted that the response of directionally solidified material in the transverse orientation is an average response comprising several grains, shown schematically in Figure 2.11.

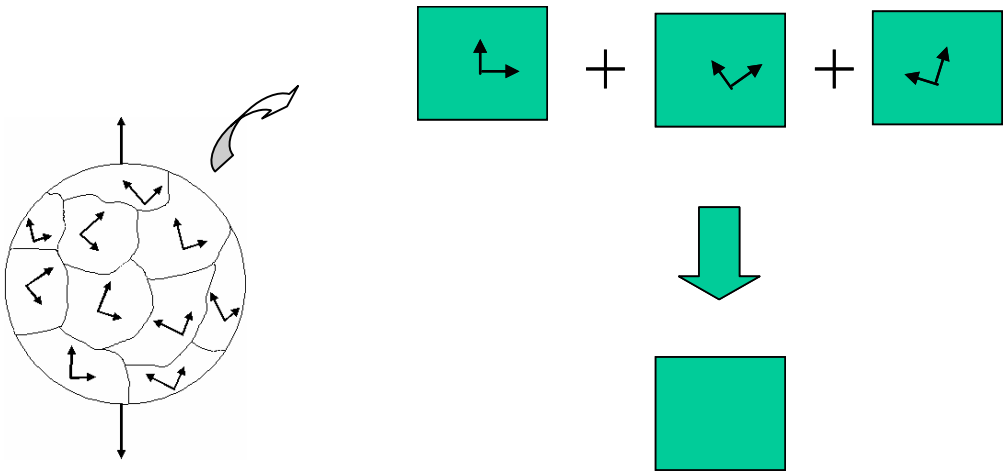

Figure 0.11 Schematic of the stress strain response in the transverse orientation.

Even though the stress response can be modeled reasonably accurately with as few as 10 grains, a total of 30 grains with random transverse orientations are used to obtain the average stress behavior along the loading axis. The Taylor constraint for intergranular interactions is assumed in this averaging process, such that each grain (with different orientations along the transverse direction) is subjected to the same deformation gradient; this approach is convenient in that a single element can be used to obtain the initial estimate of the material parameters, and is sufficiently accurate for slip of polycrystals with high symmetry cubic structures. In this case, with $\sigma^{(k)}$ denoting the uniform Cauchy

stress in each grain, the volume averaged Cauchy stress is given by (Asaro and Needleman, 1985)

$$\bar{\boldsymbol{\sigma}} = \sum_{k=1}^{N} \nu^{(k)} \boldsymbol{\sigma}^{(k)} \tag{2.36}$$

where $\nu^{(k)}$ is the volume fraction of each grain. When all the grains have equal volume, the averaged stress, $\bar{\boldsymbol{\sigma}}$, is given as

$$\bar{\boldsymbol{\sigma}} = \frac{1}{N} \sum_{k=1}^{N} \boldsymbol{\sigma}^{(k)} \tag{2.37}$$

A more rigorous finite element analysis is subsequently run with 30 hexagonal grains, each containing 96 elements, to optimize the fit of material parameters.

Under cyclic loading, lattice rotation may be insignificant, but in the presence of creep or cyclic ratcheting, lattice rotation may build up at sites of stress concentration or near interfaces such as grain boundaries. However, the creep and ratcheting strains are small in the cyclic loading experiments conducted to determine the material parameters. So these lattice rotations are neglected for the purpose of estimating the preliminary material parameters using the Taylor constraint. Several other simplifications can be made regarding the deformation behavior of this material at this temperature. In the temperature range under consideration, the precipitate structures (size, shape, morphology) are stable so higher-scale microstructural changes such as coarsening of precipitates can be neglected in the evolution equations. From the cyclic deformation data, it is observed that the initial yield strength does not change significantly with cyclic loading. This indicates that the threshold and drag stresses are nearly constant and that the backstress is the primary internal state variable that evolves with deformation.

Moreover, the cyclically stable response is of interest. The threshold stress is mainly limited to the critical value κ_c^{α} that incorporates non-Schmid terms as previously explained, and the drag stress (D^{α}) is constant at each temperature. The remaining material parameters must be physically admissible. This calls for a systematic procedure for determining the constants. First, certain physical parameters such as elastic properties and activation energies of thermally activated diffusional processes are obtained from the literature. The activation energy for self diffusion is set to Q = 309 kJ/mol, based on the data from Daleo and Wilson on GTD111 (Daleo and Wilson, 1998). Estimating the remaining material parameters by using graphical methods in the analysis of deformation data is often not possible with viscoplasticity models because there is a strong coupling between creep and cyclic plasticity. Approximate values of the material parameters can often be obtained, but a trial-and-error approach almost always must be employed to refine the parameters to accurately capture the experimental deformation response. A more robust and efficient approach is to integrate the constitutive model, simulating the actual loading histories, and to use an optimization scheme to iteratively evaluate the model parameters (Tanner et al., 1999).

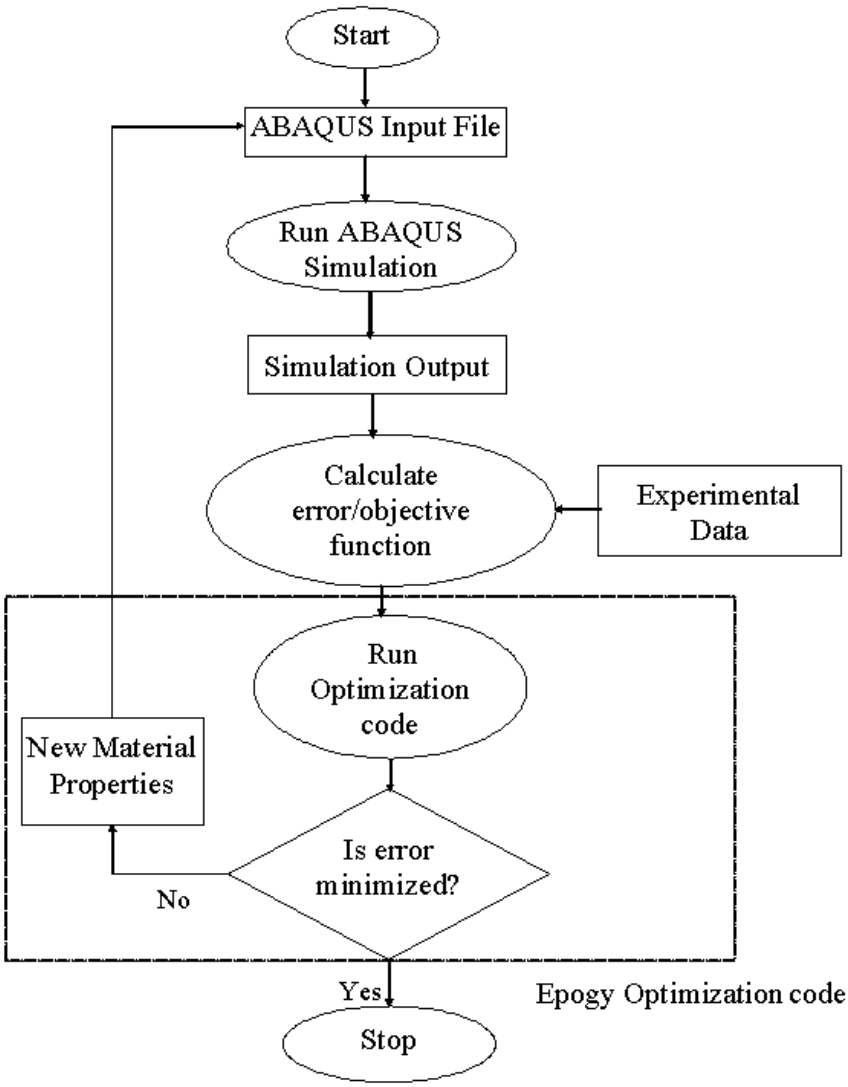

Figure 0.12 Flowchart for determination of the material parameters.

The general optimization scheme as shown in Figure 2.12 involves running several simulations involving different thermomechanical histories including cyclic deformation with and without hold periods, as well as creep deformation, using a set of parameters suggested by the optimization code. Then the model response is compared to the actual experimental response generating a value of an objective function defined on the basis of the norm of the error between the experimental and predicted deformation stress responses at a given strain and time. The Epogy code by Synaps (Epogy, 2004) is used to minimize the objective function by iteratively modifying the material parameters based on minimization of the objective function. Epogy employs four widely used search methods (linear simplex, downhill simplex, gradient, and genetic algorithms) to assure stability and enhance the probability that an optimum set of material parameters will be obtained among various local minima. The rate of convergence and effectiveness of the optimization is highly dependent on the objective function, which in turn depends on the type of loading history. For uniaxial cyclic loading, the error function is defined as

$$\text{Error} = \sum_i \left(\sigma^i_{exp} - \sigma^i_{pre} \right)^2 W_i \qquad (2.38)$$

where σ^i_{exp} is the experimentally measured stress along the loading direction, σ^i_{pre} is the stress predicted by the model at the same strain and time, and W_i is a weighting parameter for the i^{th} strain value. The weighting parameter is varied from 0.8 to 1.2, depending on which region of the stress-strain response is being simulated. Less weight is placed on the elastic portions of the deformation (W_i = 0.8) while W_i = 1.2 is used during inelastic flow. During strain hold periods in which inelastic deformation and stress relaxation occurs, W_i = 1.0.

Table 0.5 Material Parameters for DS GTD111.

(a) Octahedral Slip System Constants Initial Conditions: $\chi^{\alpha}(0)=0$, $\kappa_e^{\alpha}(0)=0$

Temperature (°C)	h_χ (MPa)	R_χ (MPa)	$h_{\chi s}$	$r_{\chi s}$	κ_o^{α} (MPa)	h_o (MPa)	$h_{\kappa s}$	h_s	r_s	$q^{\alpha\beta}$
427.0	55160	110.0	-	-	93.0	6895	135	-	-	1
650.0	110320	134.45	-	-	138.0	0	0	-	-	-
760.0	186165	148.0	2.37E-7	1	148.0	0	0	-	-	-
871.1	137900	92.0	7.77E-8	1	70.0	0	0	-	-	-
982.2	41370	69.0	-	-	14.0	0	0	-	-	-
1037.8	17238	64.3	-	-	14.0	0	0	-	-	-

(b) Cube slip system constants Initial Conditions: $\chi^{\alpha}(0)=0$, $\kappa_e^{\alpha}(0)=0$

Temperature (°C)	h_χ (MPa)	R_χ (MPa)	$h_{\chi s}$	$r_{\chi s}$	$\kappa_o^{\alpha}(T)$ (MPa)	h_o (MPa	$h_{\kappa s}$	h_s	r_s	$q^{\alpha\beta}$
427.0	-	-	-	-	-	-	-	-	-	-
650.0	110320	134.45	-	-	110.3	0	0	-	-	-
760.0	-	-	-	-	-	-	-	-	-	-
871.1	172400	81.2	7.77E-8	1	64.2	0	0	-	-	-
982.2	55160	54.5	-	-	11.0	0	0	-	-	-
1037.8	17238	44.8	-	-	11.0	0	0	-	-	-

(c) Common constants

Temperature (°C)	C_{11} (MPa)	C_{12} (MPa)	C_{44} (MPa)	n	B_o	μ (MPa)	h_{pe}	h_{cb}	h_{se}
427.0	169617	70675	132000	5	0.05	132000	0.15	-	-0.03
650.0	169000	70501	128000	5	0.05	128000	0.15	-0.25	-0.03
760.0	151690	70329	125750	5	0.05	125750	0.15	-	-0.03
871.1	138830	69980	120360	4	0.05	120360	0.0	0.0	0.0
982.2	134450	67770	113880	4	0.05	113880	0.0	0.0	0.0
1037.8	131000	65700	108180	4	0.05	108180	0.0	0.0	0.0

Q_o (KJ/mol)	R (J/mol K)	μ_o (MPa)	$\dot{\gamma}_o$ (s^{-1})	κ_{th} (MPa)	D_o (MPa)
309	8.314	166000	1.15×10^9	0.0	102.0

Since the static thermal recovery terms are influential only for long hold periods and into the steady state creep regime, these terms can be neglected in the preliminary parameter estimation exercise that uses only continuous cycling data without hold times. The results of this preliminary exercise provides tighter bounds on those parameters that are less sensitive to rate for purposes of later optimization exercises that include cyclic data with strain holds and creep data intended to refine the estimates of material parameters. The error norm used for estimating parameters associated with creep behavior is

$$\text{Error}_{\text{creep}} = \sum_{i} \left(\varepsilon^{i}_{\text{exp}} - \varepsilon^{i}_{\text{pre}} \right)^2 E^2_{\text{av}} \tag{2.39}$$

where $\varepsilon^{i}_{\text{exp}} - \varepsilon^{i}_{\text{pre}}$ is the difference between experimentally measured strain and predicted strain at given time and stress. This error norm employs the average value of the Young's modulus, E_{av}, in the specified orientation to scale the errors in terms of pseudo-stresses. For this final optimization step, the total error is the sum of the errors for the cyclic and creep deformation data, i.e.,

$$\text{Error} = \text{Error}_{\text{cyclic}} + \text{Error}_{\text{creep}} \tag{2.40}$$

The material parameters obtained are listed in Table 2.5. Some of the material parameters are not listed due to unavailability of experimental data for fitting parameters. Static thermal recovery effects in evolution of κ^{α} are omitted at 427ºC, for example. The cube slip constants cannot be determined at 427ºC and 760ºC due to unavailability of experimental data in the transverse orientation at those temperatures and the static thermal recovery parameters are not determined at temperatures greater than 871ºC due

to insufficient experimental creep data. Accordingly, dashed entries in Table 2.5 signify non availability of experimental data to calibrate the parameters.

The most sensitive material parameters for this data set as determined by the optimization scheme are $h_{\chi s}$ and $h_{\chi d}$, which control the backstress evolution. It should be noted that backstress plays an important role in Ni-base superalloys. Based on the tests by Ferney et al. (1991)and Latif et al. (1994), the backstress magnitude can be to the order of 50-60% of the flow stress. Experimental data used to fit parameters and correlated simulations based on the constitutive model are compared in Figures 2.13-2.22. From these figures it is noted that the fits are reasonable in the entire temperature range for all three strain-time loading histories: CC - continuous cycling, HT – Cycling with a 2 min strain hold at peak strain amplitude in tension and HC – cycling with a 2 in strain hold at minimum strain amplitude in compression. From Figures 2.13-2.15, the tension-compression asymmetry is captured adequately by the PPV model. The short term stress relaxation response during the strain holds is also captured by the viscoplastic flow rule. Both the primary and secondary creep responses are captured in the longitudinal orientation as shown in Figure 2.21. As seen in Figure 2.22, there is a significant difference in the creep response in the transverse orientation. This could be due to the activation of the $[111]\langle 121\rangle$ slip systems at the lower strain rates (Sheh and Stouffer, 1988) and have not been taken into account in the current formulation. The limited experiment creep data did not generate enough confidence to warrant the inclusion of these slip systems.

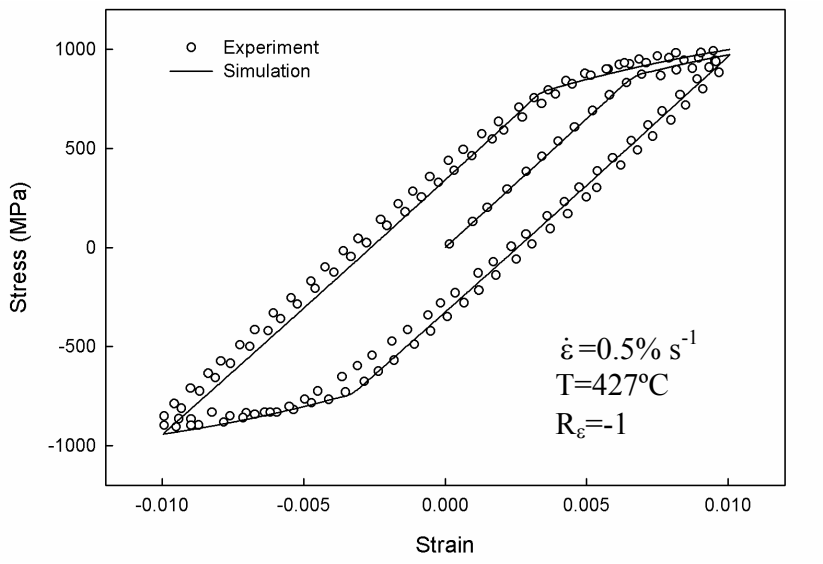

Figure 0.13 Stress-strain response: experimental data and correlated simulations at 427°C (longitudinal, CC, 1st cycle).

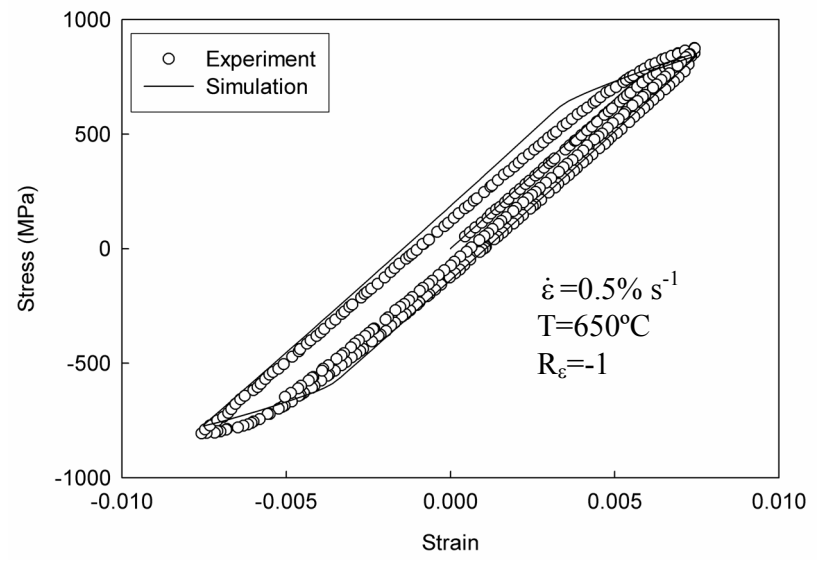

Figure 0.14 Stress-strain response: experimental data and correlated simulations at 650°C (longitudinal, CC, 1st cycle).

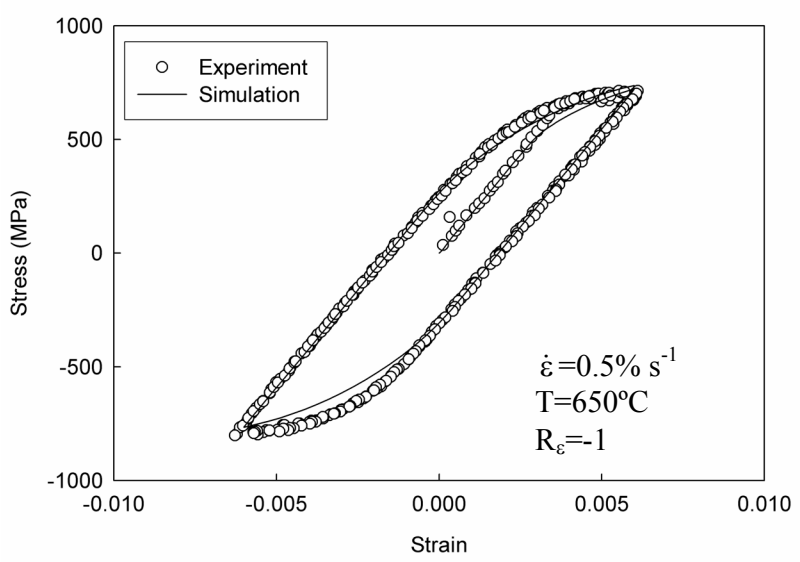

Figure 0.15 Stress-strain response: experimental data and correlated simulations at 650°C (transverse, CC, 1st cycle).

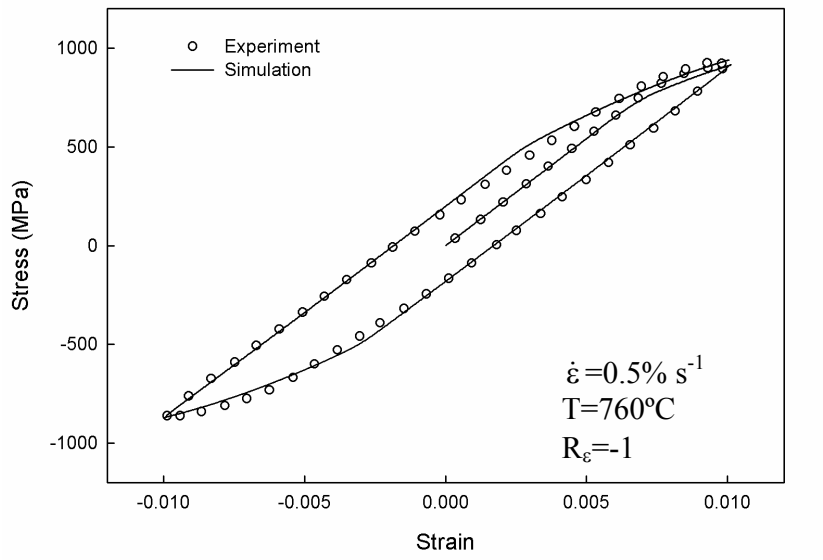

Figure 0.16 Stress-strain response: experimental data and correlated simulations at 760°C (longitudinal, CC, 1st cycle).

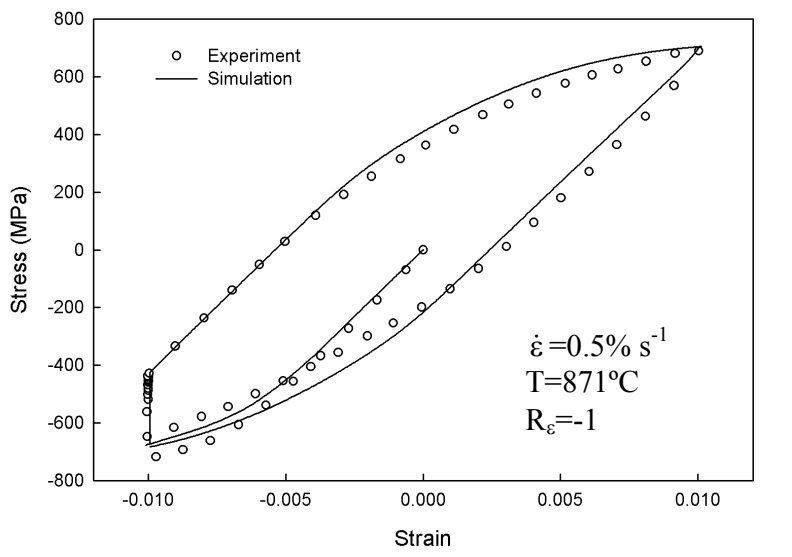

Figure 0.17 Stress-strain response: experimental data and correlated simulations at 871°C (longitudinal, HC, 1st cycle).

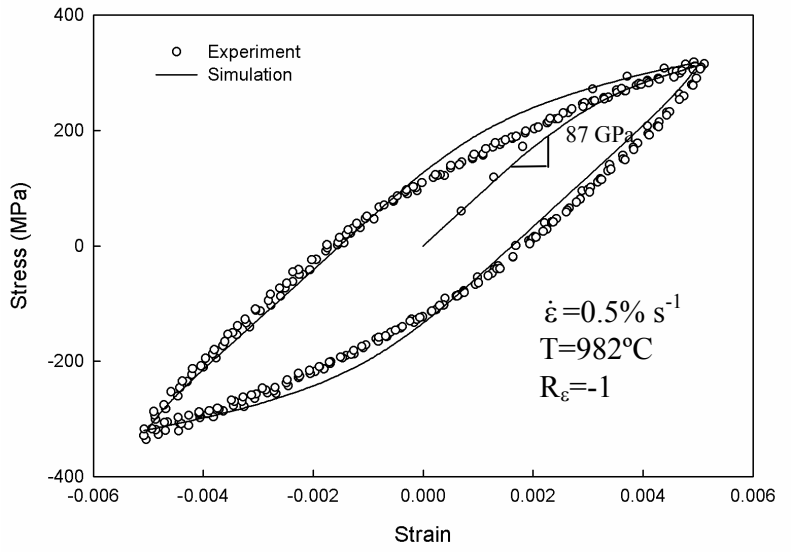

Figure 0.18 Stress-strain response: experimental data and correlated simulations at 982°C (longitudinal, CC, 1st cycle).

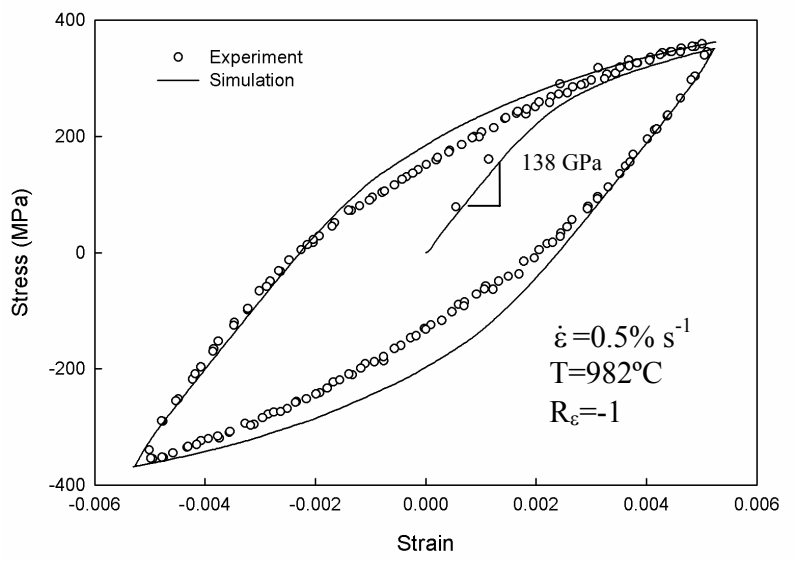

Figure 0.19 Stress-strain response: experimental data and correlated simulations at 982°C (Transverse, CC, 1st cycle).

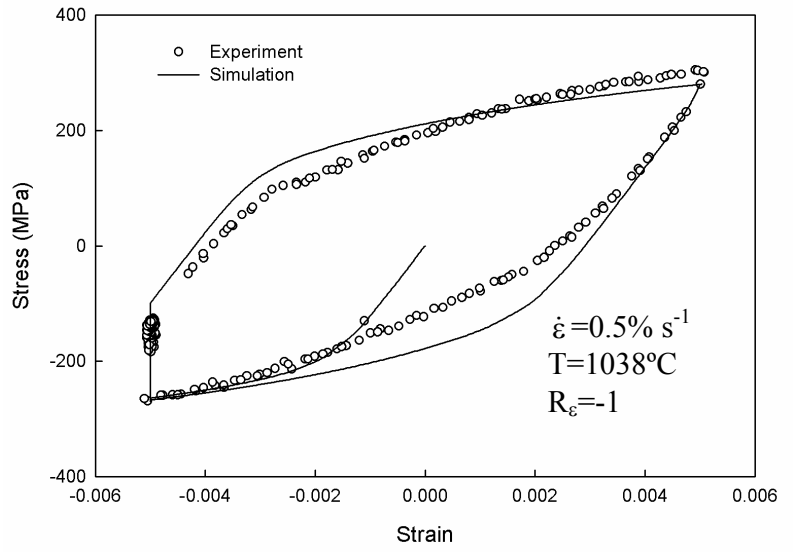

Figure 0.20 Stress-strain response: experimental data and correlated simulations at 1038°C (transverse, CC, 1st cycle).

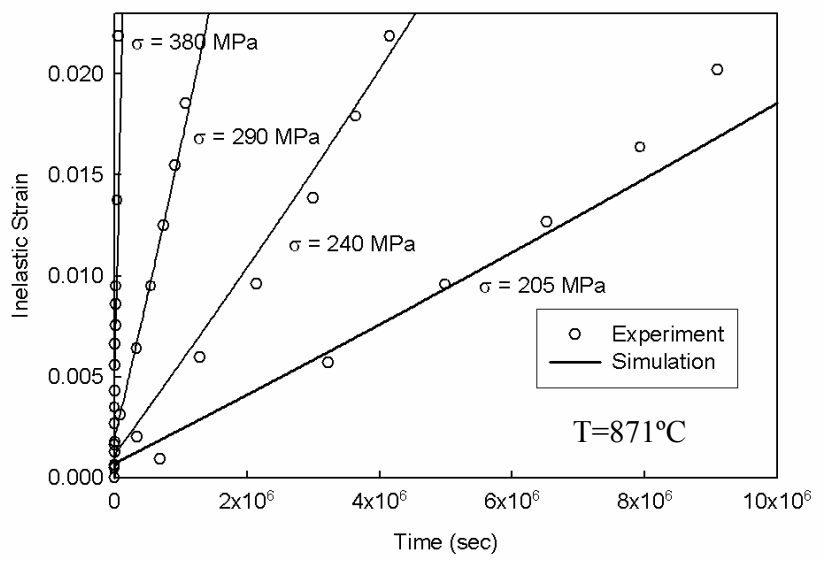

Figure 0.21 Primary and secondary creep responses: experimental data and correlated simulations at 871°C (longitudinal). Note: σ is the engineering stress.

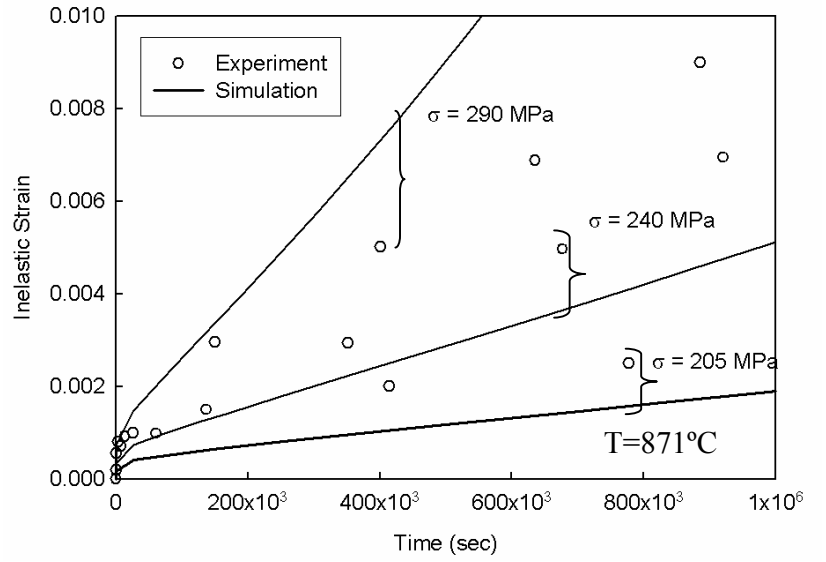

Figure 0.22 Primary and secondary creep responses: experimental data and correlated simulations at 871°C (transverse). Note: σ is the engineering stress.

2.12. Constitutive Model Predictions

2.12.1 Thermomechanical Fatigue (TMF)

For TMF, a deformation gradient $\mathbf{F}^{\theta}$ corresponding to the thermal expansion is included in the multiplicative decomposition of the deformation gradient. An intermediate, thermally expanded, hot unstressed configuration and a hot plastically deformed relaxed configuration are introduced, as shown in Figure 2.23 (Shrikanth and Zabaras, 1999). Thus, the total deformation gradient is given by $\mathbf{F} = \mathbf{F}^{e} \cdot \mathbf{F}^{p} \cdot \mathbf{F}^{\theta}$, where the linearized elastic deformation and rigid body lattice rotation is described by $\mathbf{F}^{e}$, the plastic deformation by $\mathbf{F}^{p}$, and the thermal expansion/contraction by $\mathbf{F}^{\theta}$.

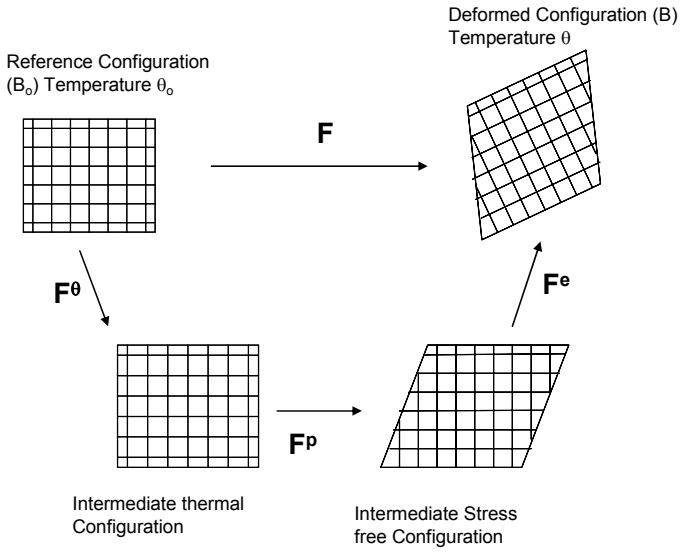

Figure 0.23 Multiplicative decomposition of the deformation gradient for TMF.

Assuming isotropic thermal expansion, the velocity gradient associated with thermal expansion effects is given as

$$\mathbf{L}_o^\theta = \dot{\mathbf{F}}^\theta \cdot \left(\mathbf{F}^\theta\right)^{-1} = \alpha\,\dot{\theta}\,\mathbf{I} \tag{2.41}$$

where α is the thermal expansion coefficient (assumed constant) and $\mathbf{I}$ is the 2nd rank identity tensor. Solving the differential equation over a time step gives

$$\mathbf{F}_{t+\Delta t}^\theta = \exp\left(\mathbf{L}_o^\theta \Delta t\right)\mathbf{F}_t^\theta \tag{2.42}$$

Material parameters are assigned temperature dependence using third order interpolative polynomial fits of values determined for isothermal cyclic loading cases. The temperature is updated and held constant for each Newton-Raphson step and the material parameters relevant to that temperature are used. These TMF simulations can be considered as true predictions which correlate reasonably well with the experimental results for loading in both the longitudinal and transverse orientations, as shown in Figures 2.24-2.26.

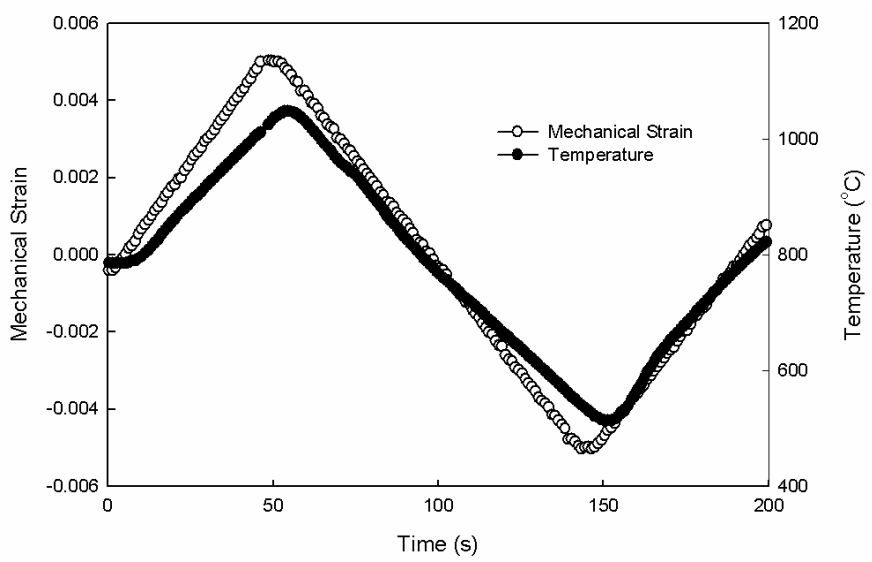

(a)

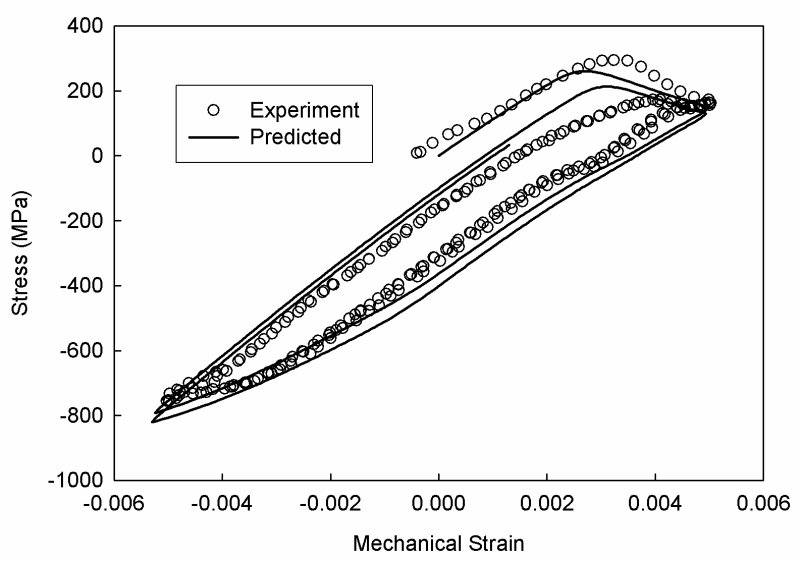

(b)

Figure 0.24 (a) Plot of Mechanical strain and temperature versus time for in-phase (IP) TMF 538°C–1038°C in the longitudinal orientation and (b) stress-strain response: comparison of experimental data with model predictions (1st cycle).

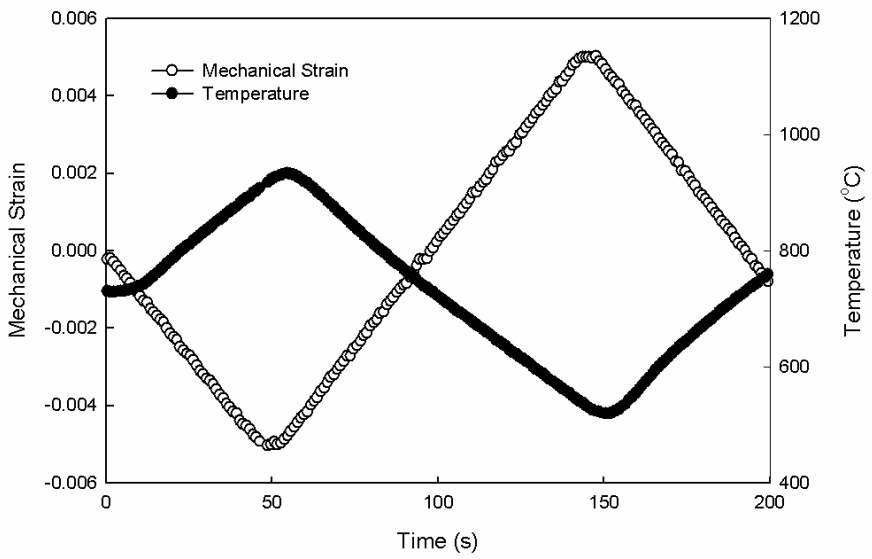

(a)

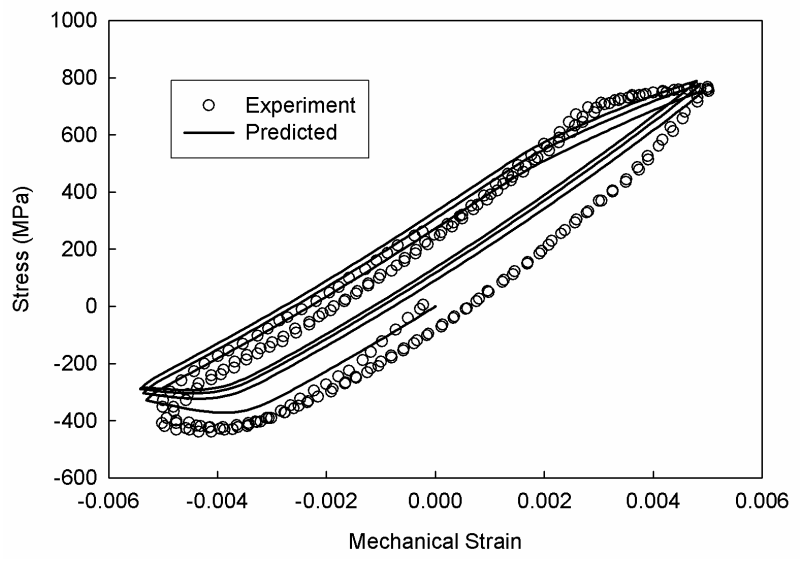

(b)

Figure 0.25 (a) Plot of Mechanical strain and temperature versus time for out-of-phase (OP) TMF 538°C–927 °C in the longitudinal orientation and (b) stress-strain response: comparison of experimental data with model predictions.

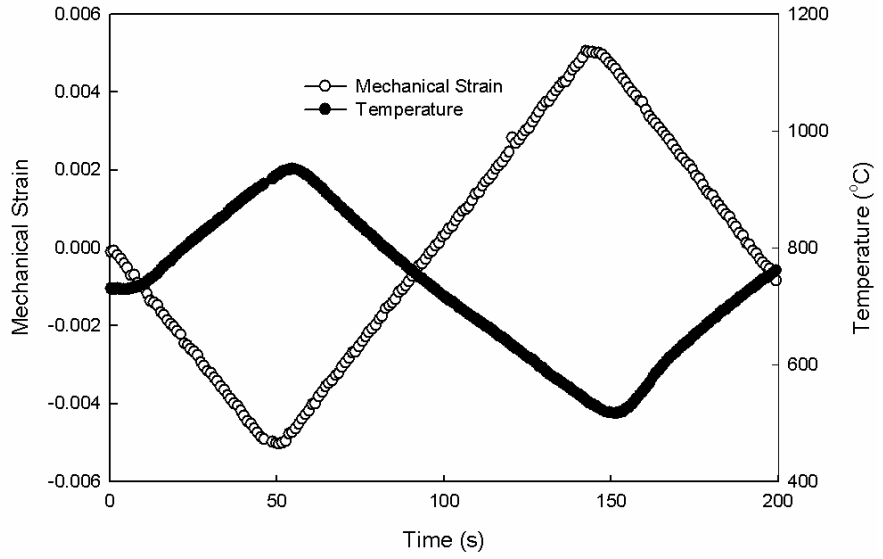

(a)

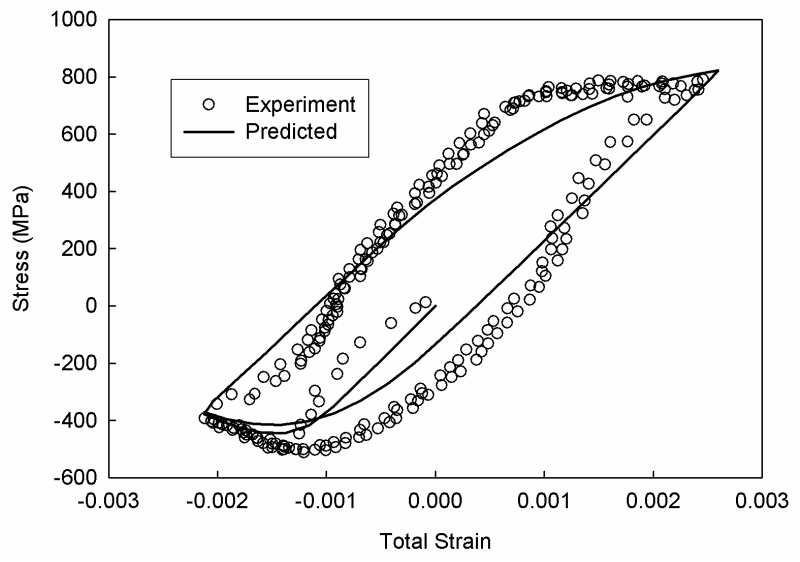

(b)

Figure 0.26 (a) Plot of Mechanical strain and temperature versus time for in-phase (IP) TMF 538°C–927°C in the transverse orientation and (b) stress-strain response: comparison of experimental data with model predictions.

2.12.2 Strain Rate Effects

The strain rate dependence of the stress-strain response is demonstrated in Figures 2.27 and 2.28 for strain controlled isothermal uniaxial cycling at 982°C in both the longitudinal and the transverse orientations at strain rates of 0.01 % s^{-1} and 0.5% s^{-1}. From Figures 2.27 and 2.28, the constitutive model stress-strain predictions agree with the experimentally observed strain rate dependence adequately, thus further validating the model parameters. In Figure 2.29, the predicted stress strain response is shown for 3 strain rates at 650°C and 871°C. The strain rate sensitivity is much more pronounced at 871°C than at 650°C, which is consistent with literature on other Ni-base superalloys(Sheh and Stouffer, 1988).

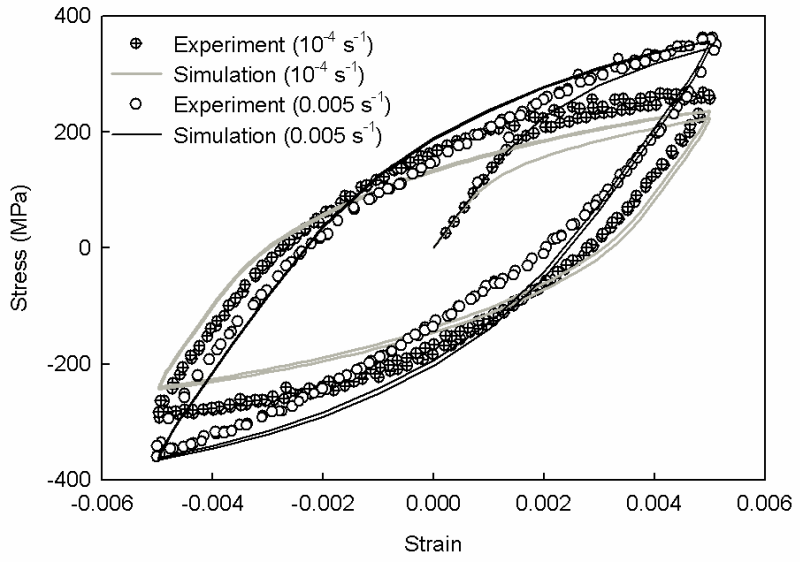

Figure 0.27 Stress-strain response: experimental data and simulations at 982°C for 2 strain rates (R_ε=-1, longitudinal, CC, 1st cycle).

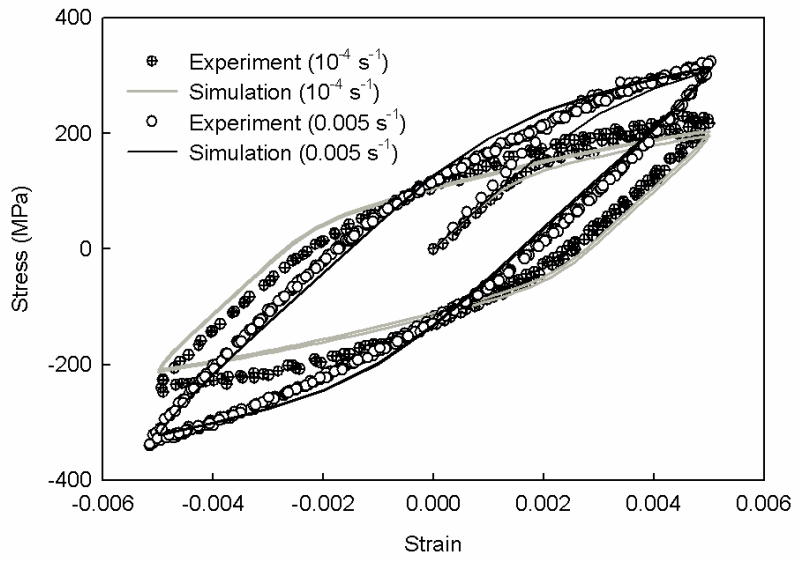

Figure 0.28 Stress-strain response: experimental data and predicted simulations at 982°C for 2 strain rates (R_ε=-1, transverse, CC, 1st cycle).

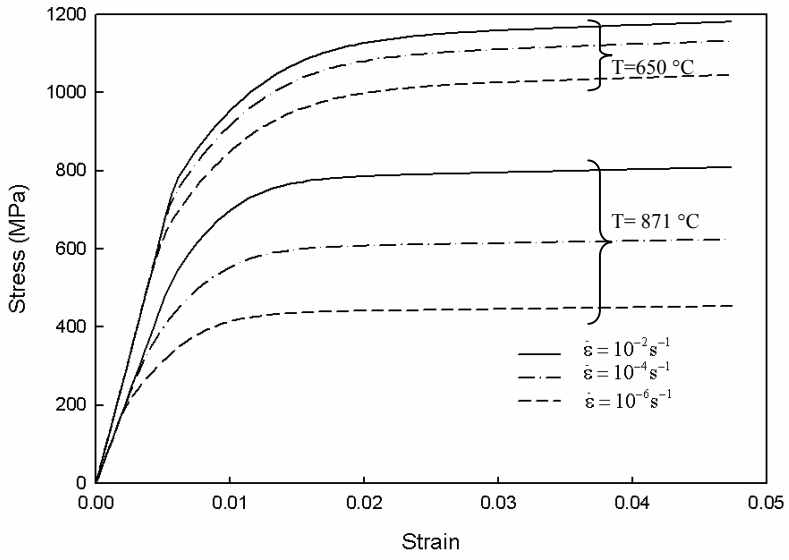

Figure 0.29 Monotonic stress-strain response: Predicted simulations at 650°C and 871°C as a function of strain rate (longitudinal).

2.12.3 Orientation Dependence

The orientation dependence of the monotonic uniaxial stress strain response of DS GTD111 is shown using three orientations ($\vartheta = 0, 45$ and 90°) in Figure 2.30 and 2.31. Temperatures of 650 and 982°C are used to illustrate the dependence of the stress-strain response on temperature. In both Figures 2.30 and 2.31, the elastic modulus is higher at $\vartheta = 45^\circ$ as compared to that at $\vartheta = 0$ and 90°. The model reflects the dependence of the elastic modulus on orientation reasonably well. This will be discussed in greater detail in Chapter III.

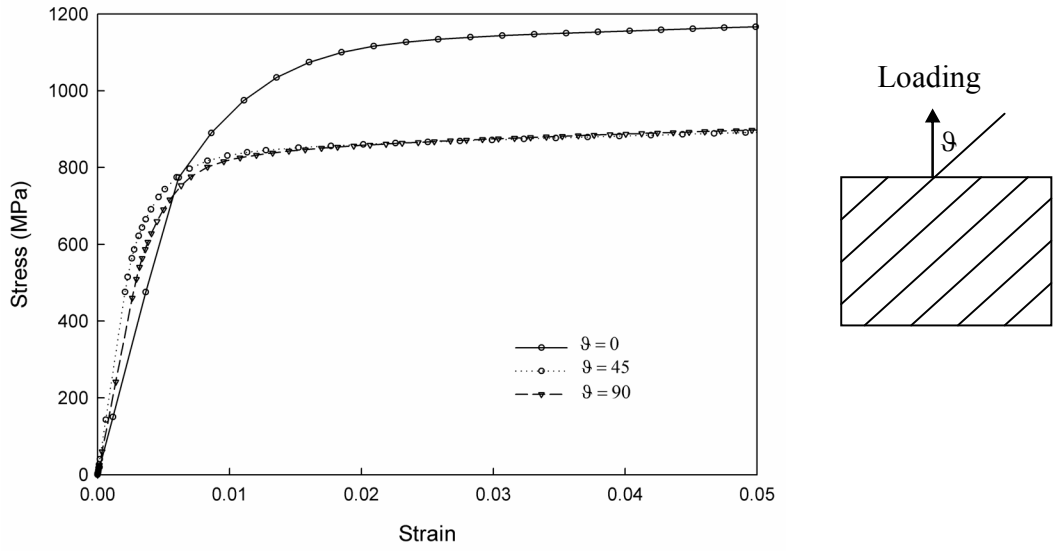

Figure 0.30 Simulated effect of orientation on the monotonic stress-strain response at 650°C (Strain rate=0.5% s^{-1}).

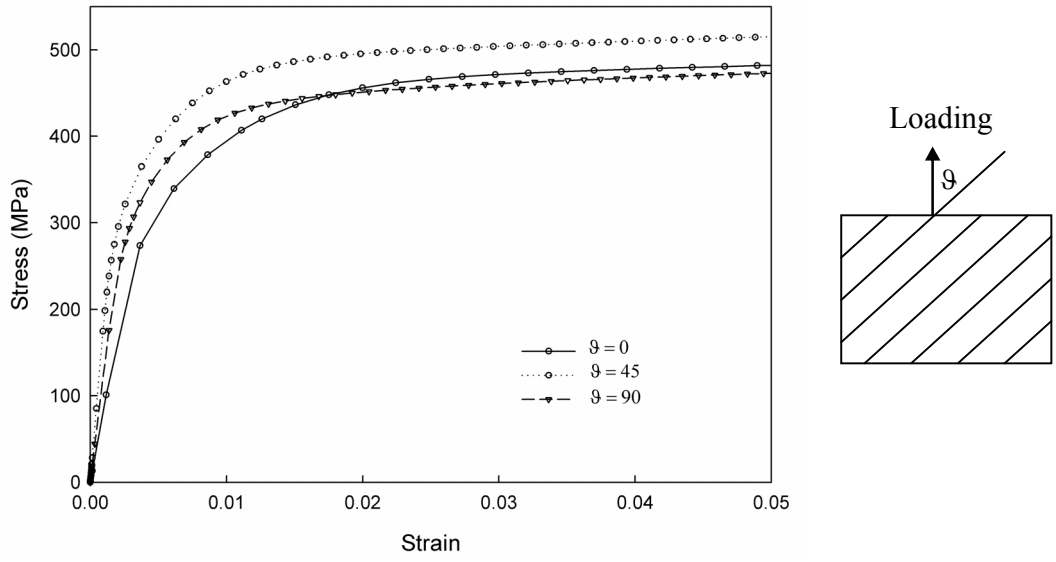

Figure 0.31 Effect of orientation on the monotonic stress strain response at 982°C (Strain Rate = 0.005 s^{-1}).

At 650°C, the saturated stress is highest in the longitudinal orientation. This justifies orienting the directionally solidified direction (longitudinal orientation) along the axis of the blade at which the stresses will be highest due to the centrifugal forces. At 982°C, the orientation dependence of the saturated stress differs from 650°C and is higher at $\vartheta = 45^{\circ}$. However it is noted that the inelastic response is less anisotropic at 982°C as compared to that at 650°C, since the dislocations are assumed to be more homogeneously distributed at higher temperatures. This is consistent with experimental observations in other directionally solidified superalloys (Hasebe et al., 1992).

2.12.4 Internal State Variable Evolution

The evolution of the backstress on an octahedral slip system is shown in Figure 2.32 as a function of temperature for DS GTD111 loaded in the longitudinal orientation to a monotonic strain of 10%. The backstress magnitude is 30-40% of the resolved shear stress ay 872°C and 982°C. The backstresses have a high hardening rate and saturate at low strains (<2%). This may be due to the rapid increase in the dislocation density at the primary γ' precipitate interfaces(Pollock and Argon, 1992).

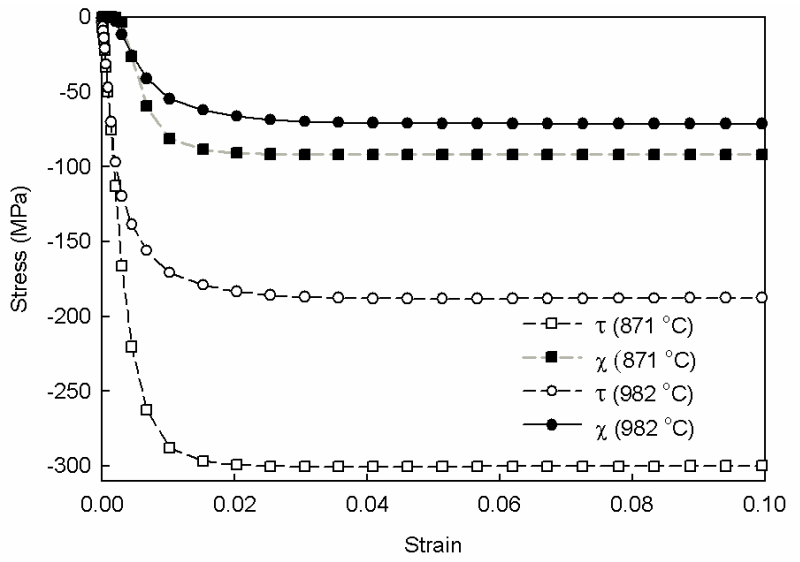

Figure 0.32 Variation of the backstress (χ^{α}) and the resolved shear stress (τ^{α}) as a function of the applied strain for monotonic loading in the longitudinal orientation at 871°C and 982°C (Strain Rate = 0.005 s^{-1}).

2.13 Creep

Primary creep is captured by the strain rate sensitivity in the flow rule coupled with backstress evolution while secondary creep is modeled using the static thermal recovery of the internal state variables (ISVs), as shown in Figures 2.21 and 2.22. Tertiary creep in Nickel-base superalloys has been attributed to many deformation mechanisms in the literature, although not necessarily in a very consistent manner. Based on their study on single crystal CMSX4 and SRR99, MacLachlan et al. (2001) attribute it to the decrease in strength due to shearing of the γ' precipitates and use a damage parameter to model this decrease in strength. According to Yaguchi et al. (2002a; 2002b), there is an increase in the dislocation spacing at the γ' precipitate interface, which leads to a decrease in the backstress. An additional ISV is used that evolves as a function of the backstress variables to capture this effect. Mukherji and Wahi (1996) have observed formation of the precipitates into plate-like structures (known as rafts) at high homologous temperatures, which leads to an increase in the average spacing between the precipitates. The Orowan stress is inversely proportional to the spacing and the increase in inelastic strain rate is linked explicitly to the increase in average precipitate spacing. However, their study was based at high temperatures (>980°C) at which significant rafting is observed. It should be noted that significant rafting of the precipitates might not take place at the lower temperatures at which precipitates are stable.

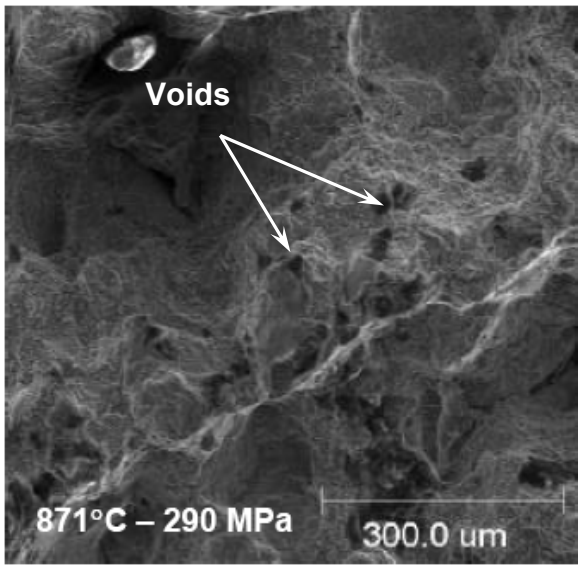

Figure 0.33 SEM micrograph of the fracture surface of the creep deformation specimen.

Examination of the creep specimens in DS GTD111 at 871°C has revealed formation of voids and cracks perpendicular to the loading orientation in the interdentritic regions in both the longitudinal and transverse orientations (Ibanez, 2003; Gordon, 2006). The cracks are primarily arranged in parallel planes perpendicular to the loading orientation with a separation distance on the order of the secondary dendrite arm spacing. A SEM micrograph of the fracture surface of the creep deformation specimen is shown in Figure 2.33. In Figure 2.33, voids are observed on the fracture specimen which vary from 10-30 μm in size. Precipitate rafting is not observed in DS GTD111, except at very high temperatures ($\geq$ 982°C). Therefore, damage by void formation is assumed to be the primary contributing mechanism responsible for the softening of the material in the tertiary creep regime. The number of voids is observed to be lesser in the transverse specimen as compared to that in the longitudinal specimen, suggesting the need for an anisotropic damage model.

A comprehensive damage model is outside the scope of this study since insufficient experimental data are available. The main objective in this section is to demonstrate the

implementation of a continuum damage model in a crystal plasticity framework. Damage is characterized kinematically through a second order damage tensor which is based on the growth of microcracks. The damage here is viewed in the context of irreversible thermodynamics and the internal state variable theory. An existing low order anisotropic damage evolution law is used to model the observed damage mechanism in tertiary creep based on Altenbach et al. (2002). This is based on the assumption that the net area reduction due to cavity formation proceeds mainly on planes perpendicular to the maximum tensile principal stress direction in the interdendritic regions (Murakami et al., 1988). This is also consistent with the voiding mechanism in other single crystal and directionally solidified superalloys (Feng et al., 2002).

2.13.1 Damage Model

Since the pioneering work of Kachanov (1958) and Rabotnov (1968), continuum damage mechanics (CDM) has been developed into a major research area and finds widespread application. According to the effective stress concept of CDM, the deformation behavior of the damaged material damage can be described by any deformation constitutive equation when the stress tensor in it is replaced by an adequately defined effective stress tensor (McDowell et al., 1990). Equivalence of the undamaged and damaged configuration can be established based on strain or energy (Lemaitre and Chaboche, 1990). The present work addresses creep damage in single crystals of cast DS GTD111 using an anisotropic damage model.

Anisotropic damage models are formulated using the concept of the effective stress tensor (Lemaitre and Chaboche, 1990). In the uniaxial case, the damage state of a material loaded by the stress σ can be characterized by a scalar state variable, ω which may be viewed as the ratio of the original specimen cross section area (A) to the damaged

area (A_ω), which reduces due to cavity formation. This leads to an increase in the effective stress defined as

$$\tilde{\sigma} = \sigma \frac{A}{A_\omega} = \frac{F}{A(1-\omega)} = \frac{\sigma}{(1-\omega)} \tag{2.43}$$

where F is the uniaxial force and ω is the damage variable. In the case of multiaxial stress states, a relationship between the stress tensor, $\boldsymbol{\sigma}$, and the net stress tensor, $\tilde{\boldsymbol{\sigma}}$, similar to Eq. (2.43) can be assumed for anisotropic behavior , i.e.,

$$\tilde{\boldsymbol{\sigma}} = \frac{1}{2}\left(\boldsymbol{\sigma}\cdot\boldsymbol{\phi} - \boldsymbol{\phi}\cdot\boldsymbol{\sigma}\right) \tag{2.44}$$

with $\boldsymbol{\phi} = \dfrac{\mathbf{I}}{\mathbf{I} - \mathbf{D}_d}$ where $\mathbf{D}_d$ is a second-rank symmetric damage tensor (Murakami and Ohno, 1981) which gives the current damage state and **I** is the 2nd rank identity tensor. The damage tensor, **D**, is related to the three dimensional cavity area density and is based on the formulation by Murakami and Ohno (1981) which postulates that the principal effect of creep damage results in the net area reduction caused by cavity formation. It should be noted that higher order damage terms have been used in other formulations (Betten, 1983; McDowell et al., 1990). However, material parameter estimation gets exceedingly difficult with an increase in the complexity of the function.

By assuming a decoupling of the intrinsic and thermal dissipation and, for practical purposes, by postulating that the dissipation due to the damage processes and the dissipation associated with the other mechanisms such as the plastic strain and the hardening process are independent (Qi and Bertram, 1998), the dual dissipation potential associated with damage, ϕ_D, takes the form

$$\phi_D = \mathbf{Y}_D : \overset{\langle 4 \rangle}{\mathbf{S}} : \mathbf{Y}_D \tag{2.45}$$

where $\overset{\langle 4 \rangle}{\mathbf{S}}$ is a fourth rank tensor (the structure tensor) and $\mathbf{Y}_D$ is the thermodynamic driving force associated with damage. The damage evolution law is then given by

$$\dot{\mathbf{D}}_d = \frac{\partial \phi_D}{\partial \mathbf{D}_d} = \mathbf{S} : \mathbf{Y}_D \tag{2.46}$$

where

$$\overset{\langle 4 \rangle}{\mathbf{S}} = \left(\gamma_D \mathbf{I} \otimes \mathbf{I} + \left(1 - \gamma_D\right) \overset{\langle 4 \rangle}{\mathbf{I}} \right) \tag{2.47}$$

$$\mathbf{Y}_D = B \left\langle \tilde{\sigma}_I \right\rangle^u \left[\mathrm{tr}\left(\boldsymbol{\phi} \cdot \mathbf{n}_I \otimes \mathbf{n}_I \right) \right]^{k-1} \left(\mathbf{n}_I \otimes \mathbf{n}_I \right) \tag{2.48}$$

If the fourth rank tensor, $\overset{\langle 4 \rangle}{\mathbf{S}}$, is symmetric and positive definite, the thermodynamic restrictions are automatically satisfied (Feng et al., 2002).

Based on the metallographic observations of the creep tested specimens in DS GTD111, cavities are formed mainly at the inclusions in the interdendritic regions perpendicular to the maximum tensile stress (Ibanez, 2003; Trexler, 2005; Gordon, 2006). Under the assumption that the net area reduction due to cavity formation proceeds mainly on the planes perpendicular to the direction of the maximum tensile effective stress, $\tilde{\sigma}_I$ (Altenbach et al., 2002) we write

$$\dot{\mathbf{D}}_{\mathrm{d}} = \overset{\langle 4 \rangle}{\mathbf{S}} : \mathbf{Y}_{\mathrm{D}} = \left(\gamma_{\mathrm{D}} \mathbf{I} \otimes \mathbf{I} + \left(1 - \gamma_{\mathrm{D}}\right) \overset{\langle 4 \rangle}{\mathbf{I}} \right) : \mathrm{B} \left\langle \tilde{\sigma}_{\mathrm{I}} \right\rangle^{\mathrm{u}} \left[\mathrm{tr}\left(\boldsymbol{\phi} \cdot \mathbf{n}_{\mathrm{I}} \otimes \mathbf{n}_{\mathrm{I}} \right) \right]^{\mathrm{k}-1} \left(\mathbf{n}_{\mathrm{I}} \otimes \mathbf{n}_{\mathrm{I}} \right) \quad (2.49)$$

where γ_{D} gives a measure of the anisotropy in the damage response. The damage is completely isotropic when $\gamma_{\mathrm{D}} = 1$ and is completely anisotropic when $\gamma_{\mathrm{D}} = 0$. The anisotropy of damage growth depends on the principal directions, $\mathbf{n}_{\mathrm{I}}$, of the maximum tensile principal stress tensor ($\tilde{\sigma}_{\mathrm{I}}$). Also, $\overset{\langle 4 \rangle}{\mathbf{I}}$ is the 4th rank identity tensor and B, u and k are scalar parameters that are determined experimentally.

2.13.2 Calibration Results

The parameters ($\gamma_{\mathrm{D}}, \mathrm{B}, \mathrm{u}, \mathrm{k}$) are determined using the uniaxial tertiary creep data in the longitudinal and transverse direction. The representative temperature of 871ºC is used to demonstrate the applicability of the model since more uniaxial creep data are available at this temperature. The anisotropy parameter (γ_{D}) is fixed to be γ_{D}=1, i.e. completely anisotropic, due to lack of multiaxial data. The other parameters, B, u and k are determined by varying these parameters manually and minimizing the least square error norm based on the experimental uniaxial creep data in the longitudinal and one datapoint in the transverse orientation. The other responses in the transverse orientation may be viewed as a prediction. The fits/predictions in longitudinal and the transverse orientation are shown in Figures 2.34 and 2.35.

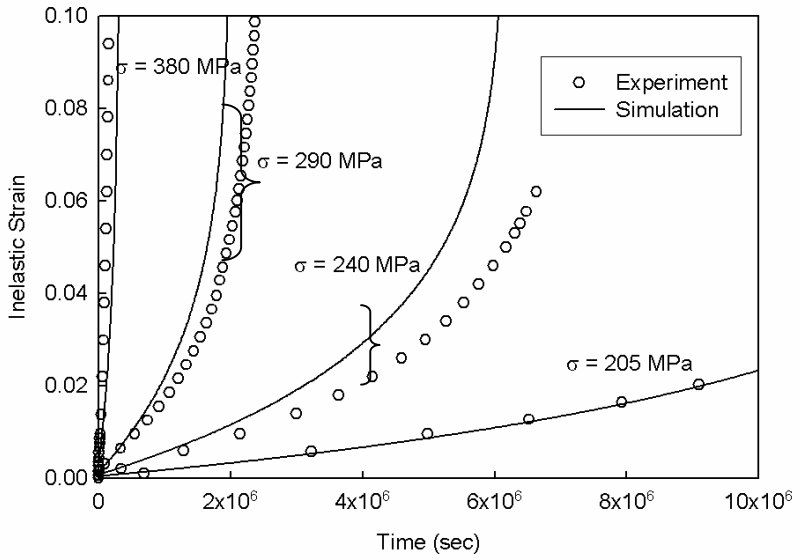

Figure 0.34 Tertiary creep fit for the longitudinal uniaxial creep data at 871°C. Note: σ is the engineering stress.

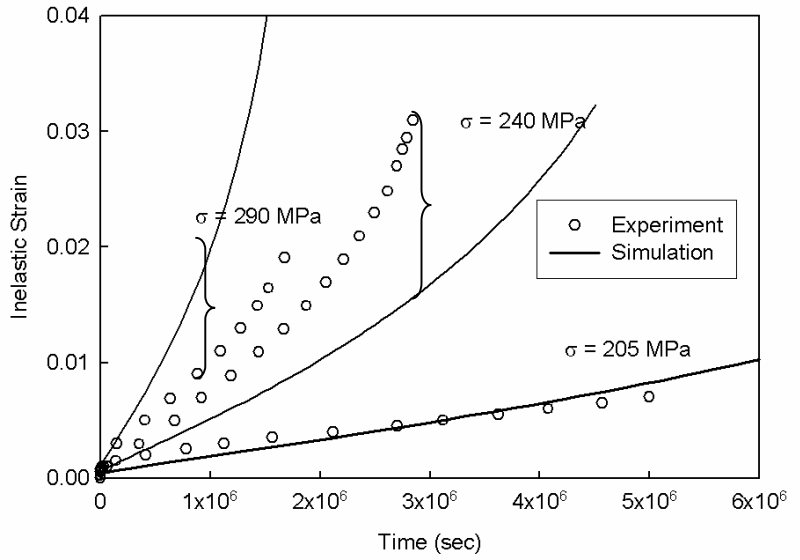

Figure 0.35 Tertiary creep predictions for the transverse uniaxial creep data at 871°C. Note: σ is the engineering stress.

Table 0.6 Material properties for tertiary creep at 871°C.

γ_D	B (MPa^{-1})	u	k
1	9.4e-23	6	1

2.14 Limitations

Limitations of the model are discussed in this section

- The crystal plasticity model does an adequate job of capturing the uniaxial stress-strain response in the longitudinal and transverse orientation. However, the validity of the model needs to be tested for other orientations.
- Only uniaxial data has been used to test the model. The validity of the model should be tested for multiaxial loading histories.
- The cube slip system parameters are calibrated using an averaged response from the grains in the transverse orientation. The material response is not very sensitive to the cube slip parameters in the transverse orientation and therefore they cannot be determined accurately. Ideally, the cube slip system parameters should be calibrated using single crystal data in the (111) orientation but the current approach does give an average measure for these parameters.
- The effect of rafting is neglected in the current formulation based on the relatively low temperature considered (871°C) but it cannot be neglected at higher temperatures, especially for creep loading.
- It should be noted that more creep data are required to calibrate the model with some degree of confidence.

2.15 Summary

The deformation in a directionally solidified Ni-base superalloy, DS GTD111, has been characterized as a function of temperature and loading history. A continuum crystal plasticity model is developed to characterize the material behavior in the longitudinal and transverse orientations. Isothermal and thermomechanical uniaxial fatigue tests with hold times and creep tests are conducted at temperatures ranging from room temperature (RT) to 1038°C to characterize the deformation response. Using isothermal test data to fit constants, IP and OP TMF responses are adequately predicted, therefore validating the model for uniaxial fatigue loading. A continuum damage model is implemented to capture the tertiary creep response, assuming dominance of cavity nucleation and growth, in conjunction with the crystal plasticity framework.

CHAPTER III

Transversely Isotropic Viscoplasticity Model for a Directionally Solidified Ni-Base Superalloy

Abstract

A transversely isotropic continuum viscoplasticity model has been formulated to capture the fatigue and creep responses of a directionally solidified (DS) polycrystalline Ni-base superalloy (DS GTD111) used mainly in turbine blades. This model has been implemented as an ABAQUS User MATerial (UMAT) subroutine using a semi-implicit integration scheme. Isothermal uniaxial fatigue data from tests conducted with and without hold times and creep data are used to characterize the stress-strain response at temperatures ranging from 427°C to 1038°C. The scheme leads to reduction of the associated computational costs when compared to a crystal viscoplasticity model that explicitly considers the 3-D grain structure. The macroscopic elastoviscoplastic model is shown to simulate the homogenized deformation response of the polycrystalline DS alloy for various isothermal histories. The predictive capability of this model is verified using both in-phase and out-of-phase TMF data, and is compared to the results of analysis of a single crystal in terms of stress concentration and stress distribution for a model problem of a plate with a central hole.

3.1 Introduction

For directionally solidified (DS) polycrystal and single crystal superalloys, the macroscopic material stress-strain behavior is anisotropic. In Chapter II, a polycrystal plasticity based constitutive model was formulated to capture this anisotropic behavior. While the physically based crystal plasticity model adequately captures the material stress-strain response, it is computationally expensive. In this work, a transversely isotropic model is formulated to capture the fatigue and creep responses of DS Ni-base superalloy, DS GTD-111. This model has been implemented as an ABAQUS (ABAQUS, 2004) User MATerial (UMAT) subroutine using a semi-implicit integration scheme. Thermomechanical fatigue experiments are used to validate the capabilities of the model, after calibration to isothermal cyclic loading and creep data.

3.2 Motivation for Transversely Isotropic Equivalent Continuum Model

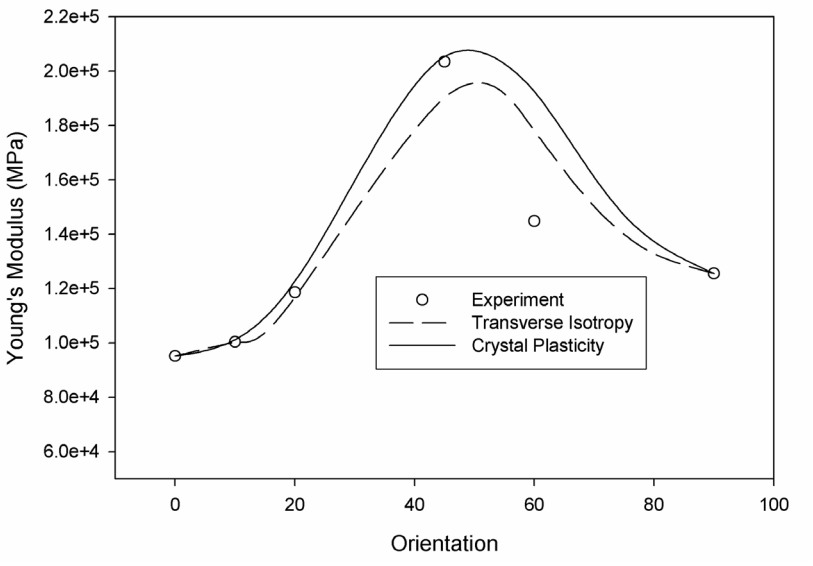

Figure 0.1 Young's modulus as a function of loading orientation with respect to the solidification direction at 871°C.

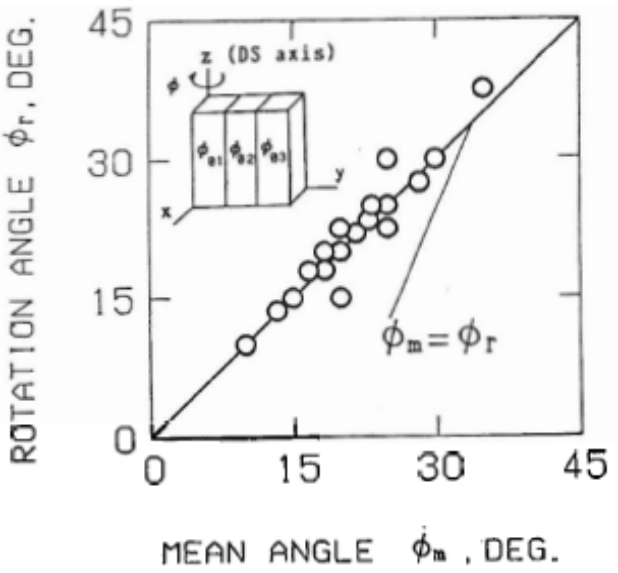

Figure 0.2 Comparison of the axis of anisotropy and the mean orientation angle in DS MAR-M247 at 900°C (Hasebe et al., 1992b).

Crystal plasticity models have been used to simulate the stress-strain behavior of single crystal and DS materials (Franciosi, 1985; Sheh and Stouffer, 1988; Nouailhas and Cailletaud, 1996; Busso et al., 2000; Shenoy et al., 2005), but are often too computationally intensive if the objective is to model the macroscopic behavior of a textured 3-D polycrystal in an engineering component. The Young's modulus of DS GTD111, as a function of the loading orientation at 871°C, is plotted in Figure 3.1. The Young's modulus reported for the crystal plasticity model is obtained from the uniaxial stress-strain response in the elastic regime using a 3-D model with 30 grains in the transverse section (perpendicular to the solidification direction). These grains are assigned a random orientation distribution with respect to rotation about the [001] solidification (longitudinal) axis. This assumption is realistic since the rotation about the [001] axis cannot be controlled during directional solidification of the DS plates. The

elastic response of the equivalent homogeneous transversely isotropic model, to be described later, is also shown in Figure 3.1. The elastic response of the homogeneous transverse isotropy model reasonably represents the experimental data as well as the results of the polycrystal model simulation. A study of the elastic compliance matrix (and the Young's modulus) of a DS MAR-M247 Ni-base superalloy by Hasebe and co-workers (Hasebe et al., 1992a; Shirafuji et al., 1998) showed that the elastic stiffness of the matrix was well-described by the symmetry class of transverse isotropy when a sufficiently large number of grains was considered (i.e., statistically Representative Volume Element (RVE)). The error in assuming a transversely isotropic stiffness matrix was less than 10% even when only 5 columnar grains were used with random rotation angles about the [001] axis, as shown in Figure 3.2 (Hasebe et al., 1992a; Shirafuji et al., 1998). In Figure 3.2, the rotation angle for orthotropy ϕ_r is compared to the mean angle of initial rotation angles, ϕ_m, which indicates that the average of the initial rotation angles approximately estimates the exact value for orthotropy. The DS material becomes increasingly closer to a transversely isotropic material with an increasing number of grains. It is therefore assumed that transverse isotropy should provide a suitable representation of the elastic behavior of DS GTD-111 even if there are only 6-10 grains across the test specimen gage section in the transverse direction to the long axis of the grains.

3.3 Kinematics and Thermodynamics

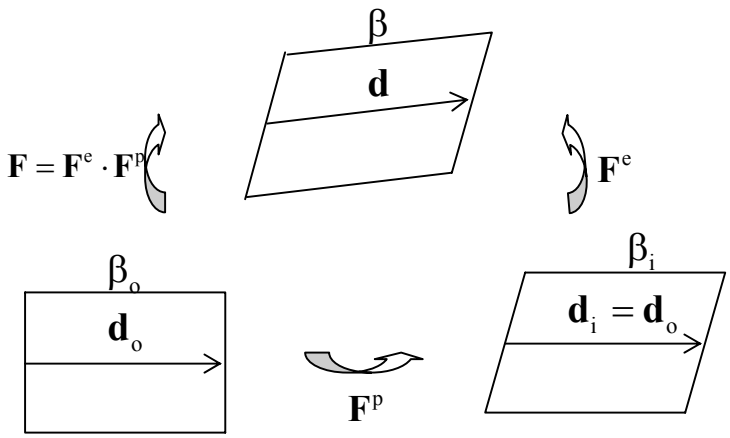

Figure 0.3 Multiplicative decomposition of the displacement gradient.

The kinematics of isothermal finite elastoplastic deformation are prescribed by the multiplicative decomposition of the deformation gradient, $\mathbf{F} = \mathbf{F}^e \cdot \mathbf{F}^p$ (Lee, 1969). The material point is mapped from the undeformed configuration, β_o, to the intermediate unstressed configuration, β_i, by the plastic part $\mathbf{F}^p$ and then carried to the current, deformed configuration by the elastic part, $\mathbf{F}^e = \mathbf{R}^e \cdot \mathbf{U}^e$, as shown in Figure 3.3. Here $\mathbf{R}^e$ and $\mathbf{U}^e$ refer to the elastic rotation and the right elastic stretch tensor respectively. The intermediate configuration is defined in such a way that the [001] longitudinal axis of symmetry in the case of the DS grains (lattice director vector), $\mathbf{d}_i$, at β_i is the same as the corresponding orientation with respect to the global system in the reference configuration, β_o. The intermediate configuration is therefore an 'isoclinic configuration,' as defined by Mandel (1971). In the case of a homogenized, transversely isotropic ensemble of grains, this configuration is unique to within a rigid rotation about

the [001] symmetry axis. The constitutive equations are updated in the intermediate configuration. A hyperelastic formulation is used in which the second Piola-Kirchhoff stress, $\boldsymbol{\sigma}^{pk2}$, the lattice stress in the intermediate configuration, is linearly related to the Green elastic strain $\mathbf{E}^{e} = \frac{1}{2}\left(\mathbf{F}^{eT}\mathbf{F}^{e} - \mathbf{I}\right)$ associated with elastic lattice distortion relative to the intermediate configuration, i.e.,

$$\boldsymbol{\sigma}^{pk2} = \mathbf{C}_{o} : \mathbf{E}^{e} \tag{3.1}$$

where $\mathbf{C}_{o}$ is the invariant 4th rank elasticity tensor in the undeformed configuration, and $\mathbf{I}$ is the 2nd rank identity tensor. The assumption of infinitesimal elastic strain is sufficient for our applications, i.e., $\mathbf{U}^{e} = \mathbf{I} + \mathbf{O}(\varepsilon)$ with $\varepsilon << 1, \mathbf{R}^{e} \approx \mathbf{R}$ as the rigid body rotation of the lattice. In this case, $\mathbf{E}^{e} \approx \boldsymbol{\varepsilon}^{e}$ is the infinitesimal elastic strain tensor with respect to the intermediate configuration.

The velocity gradient in the current configuration is given by

$$\mathbf{L} = \dot{\mathbf{F}} \cdot \mathbf{F}^{-1} = \mathbf{D} + \mathbf{W} = \mathbf{D}^{e} + \dot{\mathbf{R}}^{e} \cdot \mathbf{R}^{eT} + \mathbf{F}^{e} \cdot \hat{\mathbf{L}}^{p} \cdot \mathbf{F}^{e-1} = \mathbf{D}^{e} + \dot{\mathbf{R}} \cdot \mathbf{R}^{T} + \mathbf{R} \cdot \hat{\mathbf{L}}^{p} \cdot \mathbf{R}^{T} \tag{3.2}$$

where $\mathbf{D}$ and $\mathbf{W}$ are the symmetric and skew symmetric parts, respectively. Here, $\mathbf{D}^{e} \approx \mathbf{R} \cdot \dot{\boldsymbol{\varepsilon}}^{e} \cdot \mathbf{R}^{T}$. The plastic velocity gradient in the intermediate configuration, $\hat{\mathbf{L}}^{p}$, is given by

$$\hat{\mathbf{L}}^{p} = \dot{\mathbf{F}}^{p} \cdot \mathbf{F}^{p-1} = \frac{1}{2}\left(\hat{\mathbf{L}}^{p} + \hat{\mathbf{L}}^{pT}\right) + \frac{1}{2}\left(\hat{\mathbf{L}}^{p} - \hat{\mathbf{L}}^{pT}\right) = \hat{\mathbf{D}}^{p} + \hat{\mathbf{W}}^{p} \tag{3.3}$$

where $\hat{\mathbf{D}}^p$ and $\hat{\mathbf{W}}^p$ are the plastic rate of deformation tensor and the plastic spin tensor, respectively, in the intermediate configuration.

Virtually any attribute of microstructure that undergoes irreversible rearrangement associated with change of free energy is a candidate for description by an internal state variable (ISV) (McDowell, 1991; 1992). ISV constitutive theory is based on the assumption that a non-equilibrium, irreversible process can be treated as a sequence of constrained equilibrium states. The path history dependence of the irreversible process is embedded in the evolution of the ISVs, thereby extending the equilibrium state space to describe non-equilibrium processes. In so doing, it is presumed that the processes involved are not too far from equilibrium at each stage.

For any irreversible quasistatic process, the non-negative intrinsic energy production rate per unit volume is given by

$$\rho\gamma_{loc} = \rho\dot{\eta} - \frac{1}{T}\left(\rho\gamma - \nabla\cdot\mathbf{q}\right) \geq 0 \tag{3.4}$$

where ρ is the mass density, η is the entropy per unit mass, γ is the internal rate of heat supply per unit mass (exclusive of dissipation associated with microstructural rearrangement), T is absolute temperature, and $\mathbf{q}$ is the heat flux vector, all expressed in the intermediate configuration, β_i. The inequality $\rho\gamma_{loc} \geq 0$ is the strong form of the Clausius-Duhem inequality. The existence of both the state function entropy and temperature is assumed to continue into the domain of irreversible processes. The local form of the first law of thermodynamics is written in the intermediate configuration for infinitesimal elastic strain as

$$\rho\gamma - \nabla\cdot\mathbf{q} = \rho\dot{u} - \boldsymbol{\sigma}^{pk2} : \hat{\mathbf{D}} \tag{3.5}$$

where u is the internal energy per unit mass.

Next consider the Helmholtz free energy $\psi\left(\boldsymbol{\varepsilon}^{e}, T, \xi_i\right) = u - T\eta$, a thermodynamic state function defined on the intermediate configuration, where ξ_i is the set of n ISVs and u is the internal energy per unit mass. Non-equilibrium path history dependence is embedded in the evolution of the ISVs, which may be of scalar, vector or higher order tensor character. From the definition of Helmholtz free energy, its total differential is expressed as

$$\dot{\psi} = \frac{\partial \psi}{\partial \boldsymbol{\varepsilon}^{\varepsilon}} : \dot{\boldsymbol{\varepsilon}}^{e} + \frac{\partial \psi}{\partial T}\dot{T} + \sum_{j=1}^{n} \frac{\partial \psi}{\partial \xi_j} * \dot{\xi}_j \tag{3.6}$$

where * is a scalar product operator appropriate to the space of each ξ_j. Combining $\hat{\mathbf{D}} = \dot{\boldsymbol{\varepsilon}}^{\mathbf{e}} + \hat{\mathbf{D}}^{\mathbf{p}}$ and $\dot{\psi} = \dot{u} - \dot{T}\eta - T\dot{\eta}$ with Eqs. (3.5) and (3.6) gives

$$\left(\rho \frac{\partial \psi}{\partial \boldsymbol{\varepsilon}^{\varepsilon}} - \boldsymbol{\sigma}^{pk2}\right) : \dot{\boldsymbol{\varepsilon}}^{e} - \boldsymbol{\sigma}^{PK2} : \hat{\mathbf{D}}^{\mathbf{p}} + \left(\rho \frac{\partial \psi}{\partial T} + \rho\eta\right)\dot{T} + \rho T\dot{\eta} - \rho\gamma + \boldsymbol{\nabla} \cdot \mathbf{q} + \rho \sum_{i=1}^{n} \frac{\partial \psi}{\partial \xi_i} * \dot{\xi}_i = 0 \tag{3.7}$$

Since $\boldsymbol{\varepsilon}^{\varepsilon}$ and T are independent variables, each term in parentheses should vanish independently, giving the relations $\boldsymbol{\sigma}^{pk2} = \rho \frac{\partial \psi}{\partial \boldsymbol{\varepsilon}^{\varepsilon}}$, $\eta = -\frac{\partial \psi}{\partial T}$. Substituting Eq. (3.7) into Eq. (3.4) gives the 2nd Law of thermodynamics as

$$\boldsymbol{\sigma}^{pk2} : \hat{\mathbf{D}}^{\mathbf{p}} - \rho \sum_{i=1}^{n} \frac{\partial \psi}{\partial \xi_i} * \dot{\xi}_i \geq 0 \tag{3.8}$$

The intrinsic dissipation inequality in Eq. (3.8) should be satisfied for any irreversible process. The evolution equations for the plastic strain measure and the ISVs are expressed as $\hat{\mathbf{D}}^{\mathbf{p}} = \mathbf{G}\left(\boldsymbol{\sigma}^{\mathrm{pk2}}, \boldsymbol{\alpha}_{\mathrm{j}}, \mathrm{T}\right)$ and $\dot{\boldsymbol{\xi}}_{\mathrm{i}} = \mathbf{g}_{\mathrm{i}}\left(\boldsymbol{\varepsilon}^{e}, \boldsymbol{\xi}_{\mathrm{j}}, \mathrm{T}\right) = \mathbf{h}_{\mathrm{i}}\left(\boldsymbol{\sigma}^{\mathrm{pk2}}, \boldsymbol{\alpha}_{\mathrm{k}}, \mathrm{T}\right)$, where $\boldsymbol{\alpha}_i$ are the thermodynamic forces conjugate to the thermodynamic displacement $\boldsymbol{\xi}_i$ (Rice, 1971), i.e., $\boldsymbol{\alpha}_{\mathrm{i}} = \rho \dfrac{\partial \psi}{\partial \boldsymbol{\xi}_{\mathrm{i}}}$. We often proceed to assert the existence of a dissipation potential with the postulate of generalized normality to unconditionally satisfy the 2nd Law (Lemaitre and Chaboche, 2000); this will be assumed in what follows.

It is noted that the Cauchy stress and plastic rate of deformation tensors in the current configuration are respectively pushed forward from associated quantities in the intermediate configuration, i.e., $\boldsymbol{\sigma} = \left(1/\det \mathbf{F}^{\mathrm{e}}\right) \mathbf{F}^{\mathrm{e}} \cdot \boldsymbol{\sigma}^{\mathrm{pk2}} \cdot \mathbf{F}^{\mathrm{e}^{\mathrm{T}}} \approx \mathbf{R} \cdot \boldsymbol{\sigma}^{\mathrm{pk2}} \cdot \mathbf{R}^{\mathrm{T}}$ and $\mathbf{D}^{\mathbf{p}} = \mathbf{F}^{\mathrm{e}} \cdot \hat{\mathbf{D}}^{\mathbf{p}} \cdot \mathbf{F}^{\mathrm{e}^{-1}} \approx \mathbf{R} \cdot \hat{\mathbf{D}}^{\mathbf{p}} \cdot \mathbf{R}^{\mathrm{T}}$. Owing to the infinitesimal elastic strain assumption, these are simply rigid rotational transformations. The Cauchy stress must be updated at each time step in the displacement-based FE code (ABAQUS, 2004).

3.4 Constitutive Formulation

Since the intermediate configuration is assumed to be isoclinic, the rate of change of the fixed unit director vector $\mathbf{d}_{\mathrm{i}}$ in the communal [001] direction in the intermediate configuration must vanish (Aravas, 1992), i.e.,

$$\dot{\mathbf{d}}_{\mathrm{i}} = \boldsymbol{\omega} \times \mathbf{d}_{\mathrm{o}} = \left(\hat{\mathbf{W}}^{\mathrm{p}} + \hat{\mathbf{D}}^{\mathrm{p}} \cdot (\mathbf{d}_{\mathrm{o}} \otimes \mathbf{d}_{\mathrm{o}}) - (\mathbf{d}_{\mathrm{o}} \otimes \mathbf{d}_{\mathrm{o}}) \cdot \hat{\mathbf{D}}^{\mathrm{p}}\right) \cdot \mathbf{d}_{\mathrm{o}} = \mathbf{0} \tag{3.9}$$

where $\mathbf{d}_o\,(=\mathbf{d}_i)$ is the director vector in the [001] direction in the reference configuration and $\boldsymbol{\omega}$ is the angular velocity. From Eq. (3.9), the plastic spin can be determined in the intermediate configuration as

$$\hat{\mathbf{W}}^p = (\mathbf{d}_o \otimes \mathbf{d}_o)\cdot\hat{\mathbf{D}}^p - \hat{\mathbf{D}}^p\cdot(\mathbf{d}_o \otimes \mathbf{d}_o) \tag{3.10}$$

It should be noted that all the equations are formulated in the intermediate configuration using the second Piola-Kirchhoff stress as the stress measure (Dafalius, 1998). The plastic spin expression in Eq. (3.10) is necessary to update lattice orientation in the current configuration (texture development) by isolating the skew symmetric spin terms in Eq. (3.2), giving the differential equation for the lattice spin as $\dot{\mathbf{R}}\cdot\mathbf{R}^T = \mathbf{W} - \mathbf{R}\cdot\hat{\mathbf{W}}^p\cdot\mathbf{R}^T = \mathbf{W} - \mathbf{W}^p$.

3.4.1 Flow Rule: Viscoplastic Kinetic Relation

In this section, forms will be developed for the evolution equations for ISVs that satisfy the restrictions on the constitutive equations that were laid out in Eq. (3.8). The material being considered comprises a statistically representative set of grains that are randomly oriented in the transverse orientation, giving rise to an average stress-strain response in the transverse orientation as explained in Section 2. The material is considered to be an elastoviscoplastic solid characterized by persistent transverse isotropy. At each material point we specify the axis of transverse isotropy by unit vector $\mathbf{d}_o$; the mechanical behavior at each point depends not only on the stress and deformation history but also on this local preferential direction.

Unified creep-plasticity models do not separately postulate constitutive laws for creep and plasticity, considering all deformation as rate dependent to varying degree (Nan and

Krempl, 1991). The transition from low to high temperature is characterized by changes of strength and rate dependence that can be reflected by temperature dependent parameters in the constitutive equations. The viscoplastic rate of deformation tensor (symmetric part of the viscoplastic velocity gradient) in the intermediate configuration is related to the effective stress via the simple power law relation

$$\hat{\mathbf{D}}^{\,p} = \dot{p}\mathbf{N} = A\exp\left(-\frac{Q}{RT}\right)\left\langle\frac{\bar{\sigma}-K}{D_o}\right\rangle^{n}\mathbf{N} \tag{3.11}$$

where $\bar{\sigma}$ is the effective stress, K is the threshold stress, D_o is the drag stress, Q is the activation energy, R is the universal gas constant, T is the temperature, $\mathbf{N}$ is the unit vector in the direction of inelastic strain rate, and A is a constant. Also, K and n are temperature dependent. The effective stress depends on the symmetric viscous overstress, $\boldsymbol{\Sigma}$ ($\boldsymbol{\Sigma} = \boldsymbol{\sigma}'^{PK2} - \boldsymbol{\alpha}$), where $\boldsymbol{\sigma}'^{pk2} = \boldsymbol{\sigma}^{pk2} - 1/3\,\mathrm{tr}\left(\boldsymbol{\sigma}'^{pk2}\right)\mathbf{I}$ is the deviatoric second Piola-Kirchhoff stress, and $\boldsymbol{\alpha}$ is the deviatoric backstress tensor in the intermediate configuration. The dyad $\mathbf{M} = \mathbf{d}_o \otimes \mathbf{d}_o$ is an element of the irreducible integrity basis for the scalar-valued isotropic tensor function $\bar{\sigma}\left(\boldsymbol{\Sigma}, \mathbf{M}\right)$. In order to maintain invariance under arbitrary rigid body rotations, the effective stress $\bar{\sigma}\left(\boldsymbol{\Sigma}, \mathbf{M}\right)$ must be expressed in terms of the invariants and joint invariants of its tensorial arguments (Spencer and Rivlin, 1962; Spencer, 1971). The admissible invariants are given as

$\mathrm{tr}\left(\mathbf{M}\right), \mathrm{tr}\left(\mathbf{M}^2\right), \mathrm{tr}\left(\mathbf{M}^3\right)$, $\mathrm{tr}\left(\boldsymbol{\Sigma}\right), \mathrm{tr}\left(\boldsymbol{\Sigma}^2\right), \mathrm{tr}\left(\boldsymbol{\Sigma}^3\right)$ where $tr\left(\boldsymbol{\Sigma}\right) = 0$

and

$$\mathrm{tr}\left(\mathbf{M}\cdot\boldsymbol{\Sigma}\right), \mathrm{tr}\left(\mathbf{M}^2\cdot\boldsymbol{\Sigma}\right), \mathrm{tr}\left(\mathbf{M}\cdot\boldsymbol{\Sigma}^2\right), \mathrm{tr}\left(\mathbf{M}^2\cdot\boldsymbol{\Sigma}^2\right) \tag{3.12}$$

The set of invariants is compact in the present case of transverse isotropy since $\mathrm{tr}\left(\mathbf{M}\right)=\mathrm{tr}\left(\mathbf{M}^2\right)=\mathrm{tr}\left(\mathbf{M}^3\right)=1$, $\mathrm{tr}\left(\mathbf{M}\cdot\boldsymbol{\Sigma}\right)=\mathrm{tr}\left(\mathbf{M}^2\cdot\boldsymbol{\Sigma}\right)$, and $\mathrm{tr}\left(\mathbf{M}\cdot\boldsymbol{\Sigma}^2\right)=\mathrm{tr}\left(\mathbf{M}^2\cdot\boldsymbol{\Sigma}^2\right)$. Restricting the invariants to only the quadratic arguments in $\boldsymbol{\Sigma}$ and neglecting the trivial terms, the effective stress can be represented, following Robinson and colleagues (Robinson, 1983; Robinson and Binienda, 2001), as

$$\bar{\sigma}=\sqrt{3\left(\mathrm{J}_2-\xi\left(\mathrm{J}-\mathrm{J}_\mathrm{o}^2\right)-\frac{3}{4}\varsigma\mathrm{J}_\mathrm{o}^2\right)} \tag{3.13}$$

where $\mathrm{J}_2=\frac{1}{2}\Sigma_{ij}\Sigma_{ij}$, $\mathrm{J}_\mathrm{o}=\mathrm{M}_{ij}\Sigma_{ij}$ and $\mathrm{J}=\mathrm{M}_{ij}\Sigma_{jk}\Sigma_{ki}$. Here, ξ and ς are temperature dependent material parameters that are determined from experimental data that describe initial yield behavior.

In Eq. (3.11), $\mathbf{N}$ is a unit vector in the inelastic strain rate direction, given by normality as

$$\mathbf{N}=\frac{\nabla_{\boldsymbol{\sigma}^{\mathrm{pk}2}}\bar{\sigma}}{\left\|\nabla_{\boldsymbol{\sigma}^{\mathrm{pk}2}}\bar{\sigma}\right\|}=\frac{\boldsymbol{\Gamma}}{\left\|\boldsymbol{\Gamma}\right\|} \tag{3.14}$$

where the components of $\boldsymbol{\Gamma}$ are given as (Arnold et al., 1992)

$$\Gamma_{ij}=\Sigma_{ij}-\xi\left(\mathrm{M}_{ki}\Sigma_{jk}+\mathrm{M}_{jk}\Sigma_{ki}-2\mathrm{J}_\mathrm{o}\mathrm{M}_{ij}\right)-\frac{3}{2}\varsigma\mathrm{J}_\mathrm{o}\left(\mathrm{M}_{ij}-\frac{1}{3}\delta_{ij}\right)$$

and

$$\left\|\boldsymbol{\Gamma}\right\|=\sqrt{\Gamma_{ij}\Gamma_{ij}} \tag{3.15}$$

It is understood that the gradient operator in Eq. (3.14) is defined in the space of 2nd Piola-Kirchhoff stress components in the intermediate configuration. Incompressibility of the inelastic strain rate is ensured since $\mathrm{tr}(\boldsymbol{\Gamma}) = \Gamma_{ii} = 0$.

3.4.2 Internal State Variables

Although threshold stress (K) could evolve with plastic strain as an isotropic hardening variable, it is not employed as an ISV in this application. DS GTD111 exhibits a cyclically stable stress-strain response at each temperature of interest; accordingly, a constant value of the threshold stress at each temperature is appropriate to capture the initial yield strength. The back stress ($\boldsymbol{\alpha}$) is used as an internal state variable (ISV) to capture the directional effects of work-hardening on the stress-strain behavior (i.e., Bauschinger effect), associated with elastic energy storage due to heterogeneity of the microstructure. Intergranular interactions are a primary source of backstress in polycrystalline materials; however, there are several other sources of backstresses, which become more prominent in single crystal and DS Ni-base superalloys. Based on the experiments by Ferney et al. (1991)and Latif et al. (1994), the magnitude of backstress can be on the order of 50% of the flow stress in the regime of dominant particle-shearing at low to moderate temperatures. In their study of deformation behavior in single crystal Ni-base superalloy PWA1480, Milligan and Antolovich (1989) showed that when dislocations emerge from precipitates, constrictions of the dislocations occur because of high anti-phase energy (APBE). This shows that portions of the dislocation that exit the precipitate are split because of elastic repulsion and suggests a source of backstress for γ' strengthened alloys. Backstress is also generated due to pile-ups of dislocations at γ' precipitate boundaries. The evolution equation for the components of the 2nd rank backstress tensor are given in the intermediate configuration by

$$\dot{\boldsymbol{\alpha}} = H\left(L\hat{\mathbf{D}}^{\,p} - \boldsymbol{\pi}\dot{p}\right) - R_\alpha \bar{\alpha}^m \boldsymbol{\pi} \tag{3.16}$$

where $\dot{p} = \sqrt{\mathbf{D}_i^{\,p} : \mathbf{D}_i^{\,p}}$, and the components of $\boldsymbol{\pi}$ are given by

$$\pi_{ij} = \alpha_{ij} - \xi\left(M_{ki}\alpha_{jk} + M_{jk}\alpha_{ki} - 2\hat{J}_o M_{ij}\right) - \frac{3}{2}\varsigma\hat{J}_o\left(M_{ij} - \frac{1}{3}\delta_{ij}\right). \tag{3.17}$$

Other variables in Eq. (3.16) are given by

$$\bar{\alpha} = \sqrt{3\left(\hat{J}_2 - \xi\left(\hat{J} - \hat{J}_o^2\right) - \frac{3}{4}\varsigma\hat{J}_o^2\right)} \tag{3.18}$$

$$\hat{J}_2 = \frac{1}{2}\alpha_{ij}\alpha_{ij},\ \hat{J}_o = M_{ij}\alpha_{ij},\ \hat{J} = M_{ij}\alpha_{jk}\alpha_{ki} \tag{3.19}$$

In Eq. (3.16), H, L R_α and m are constants for a given temperature. The backstress evolution equation in Eq. (3.16) presumes that hardening is characterized by the first term and dynamic recovery by the second term. A static thermal recovery term is also included (third term involving $R_\alpha \bar{\alpha}^m \boldsymbol{\pi}$) to engender a Bailey-Orowan format for a balance of hardening and thermal recovery at steady state, which is pertinent for moderate to low strain rates, especially at high temperatures. It should be noted that even though constants ξ and ς in Eq. (3.13) are determined experimentally, there are certain restrictions placed on their values so that Eq. (3.8) is satisfied. The backstress ($\boldsymbol{\alpha}$) is assumed to be proportional to its thermodynamic conjugate displacement ($\mathbf{A}$), which is a strain-like quantity, i.e.,

$$\boldsymbol{\alpha} = \mathrm{HL}\,\mathbf{A} \tag{3.20}$$

where

$$\dot{\mathbf{A}} = \hat{\mathbf{D}}^{\mathrm{p}} - \frac{\boldsymbol{\pi}}{\mathrm{L}}\dot{\mathrm{p}} - \frac{\mathrm{R}_{\alpha}}{\mathrm{HL}}\bar{\alpha}^{\mathrm{m}}\boldsymbol{\pi} \tag{3.21}$$

Substituting the backstress in the intrinsic dissipation inequality gives

$$\boldsymbol{\sigma}^{\mathrm{pk2}} : \hat{\mathbf{D}}^{\mathrm{p}} - \boldsymbol{\alpha} : \dot{\mathbf{A}} = \boldsymbol{\sigma}'^{\mathrm{pk2}} : \hat{\mathbf{D}}^{\mathrm{p}} - \boldsymbol{\alpha} : \dot{\mathbf{A}} \geq 0 \tag{3.22}$$

Eq. (3.22) places certain restrictions on the values for ξ and ζ. Using the constraint Eq. (3.22) and substituting the Eq. (3.20)

$$\boldsymbol{\sigma}'^{\mathrm{pk2}} : \hat{\mathbf{D}}^{\mathbf{p}} - \boldsymbol{\alpha}' : \left(\hat{\mathbf{D}}^{\mathbf{p}} - \frac{\boldsymbol{\pi}}{\mathrm{L}}\dot{\mathrm{p}} - \frac{\mathrm{R}}{\mathrm{HL}}\bar{\alpha}^{\mathrm{m}}\boldsymbol{\pi} \right) \geq 0 \tag{3.23}$$

Using Eq. (3.11) and dividing by $\dot{p}$

$$\left(\boldsymbol{\sigma}'^{\mathrm{pk2}} - \boldsymbol{\alpha}'\right) : \frac{\boldsymbol{\Gamma}}{\|\boldsymbol{\Gamma}\|} + \boldsymbol{\alpha}' : \frac{\boldsymbol{\pi}}{\mathrm{L}}\left(1 + \frac{\mathrm{R}}{\mathrm{H}\dot{\mathrm{p}}}\bar{\alpha}^{\mathrm{m}}\right) = \boldsymbol{\Sigma} : \frac{\boldsymbol{\Gamma}}{\|\boldsymbol{\Gamma}\|} + \boldsymbol{\alpha}' : \frac{\boldsymbol{\pi}}{\mathrm{L}}\left(1 + \frac{\mathrm{R}}{\mathrm{H}\dot{\mathrm{p}}}\bar{\alpha}^{\mathrm{m}}\right) \geq 0 \tag{3.24}$$

Since backstress could have any value, the inequality condition in Eq. (3.24) should be satisfied for each of the terms. Hence

$$\boldsymbol{\Sigma} : \boldsymbol{\Gamma} \geq 0 \quad \text{and} \quad \boldsymbol{\alpha}' : \boldsymbol{\pi} \geq 0 \tag{3.25}$$

Using the 1st inequality constraint in Eq. (3.25) gives

$$\begin{aligned} \boldsymbol{\Sigma} : \boldsymbol{\Gamma} &= \Sigma_{ij}\Gamma_{ij} = \Sigma_{ij}\left[\Sigma_{ij} - \xi\left(M_{ki}\Sigma_{jk} + M_{jk}\Sigma_{ki} - 2J_o M_{ij}\right) - \frac{3}{2}\varsigma J_o\left(M_{ij} - \frac{1}{3}\delta_{ij}\right)\right] \\ &= 2J_2 - 2\xi J + 2\xi J_o{}^2 - \frac{3}{2}\varsigma J_o{}^2 \geq 0 \end{aligned} \tag{3.26}$$

Note that $2J_2 \geq J$ which gives

$$1 - 2\xi \geq 0 \text{ and } 2\xi - \frac{3}{2}\varsigma \geq 0 \quad \Rightarrow \quad \xi \leq \frac{1}{2} \text{ and } \xi \geq \frac{3}{4}\varsigma \tag{3.27}$$

It should be noted that these conditions will also satisfy $\boldsymbol{\alpha}' : \boldsymbol{\pi} \geq 0$. Within these constraints, ξ and ς can be adjusted to fit stress-strain data and dissipation. The set of constitutive equations are summarized in Table 3.1.

Table 0.1 Summary of constitutive equations for the transverse isotropy model.

Flow Rule

$$\hat{\mathbf{D}}^{p} = \dot{p}\mathbf{N} = A\exp\left(-\frac{Q}{RT}\right)\left\langle\frac{\bar{\sigma}-K}{D_o}\right\rangle^{n}\mathbf{N}$$

where

$$\mathbf{N} = \frac{\nabla_{\boldsymbol{\sigma}^{pk2}}\bar{\sigma}}{\left\|\nabla_{\boldsymbol{\sigma}^{pk2}}\bar{\sigma}\right\|} = \frac{\boldsymbol{\Gamma}}{\|\boldsymbol{\Gamma}\|} \text{ and } \bar{\sigma} = \sqrt{3\left(J_2 - \xi\left(J - J_o^2\right) - \frac{3}{4}\varsigma J_o^2\right)}$$

$$\Gamma_{ij} = \Sigma_{ij} - \xi\left(M_{ki}\Sigma_{jk} + M_{jk}\Sigma_{ki} - 2J_o M_{ij}\right) - \frac{3}{2}\varsigma J_o\left(M_{ij} - \frac{1}{3}\delta_{ij}\right)$$

$$J_2 = \frac{1}{2}\Sigma_{ij}\Sigma_{ij},\ J_o = M_{ij}\Sigma_{ij},\ J = M_{ij}\Sigma_{jk}\Sigma_{ki},\ \mathbf{M} = \mathbf{d}_o \otimes \mathbf{d}_o,\ \boldsymbol{\Sigma} = \boldsymbol{\sigma}'^{PK2} - \boldsymbol{\alpha},\ \|\boldsymbol{\Gamma}\| = \sqrt{\Gamma_{ij}\Gamma_{ij}}$$

Backstress Evolution Equation $(\boldsymbol{\alpha})$

$$\dot{\boldsymbol{\alpha}} = H\left(L\hat{\mathbf{D}}^{p} - \boldsymbol{\pi}\dot{p}\right) - R_\alpha\bar{\alpha}^{m}\boldsymbol{\pi}$$

where

$$\dot{p} = \sqrt{\hat{\mathbf{D}}^{p} : \hat{\mathbf{D}}^{p}} \text{ and } \bar{\alpha} = \sqrt{3\left(\hat{J}_2 - \xi\left(\hat{J} - \hat{J}_o^2\right) - \frac{3}{4}\varsigma\hat{J}_o^2\right)}$$

$$\pi_{ij} = \alpha_{ij} - \xi\left(M_{ki}\alpha_{jk} + M_{jk}\alpha_{ki} - 2\hat{J}_o M_{ij}\right) - \frac{3}{2}\varsigma\hat{J}_o\left(M_{ij} - \frac{1}{3}\delta_{ij}\right)$$

$$\hat{J}_2 = \frac{1}{2}\alpha_{ij}\alpha_{ij},\ \hat{J}_o = M_{ij}\alpha_{ij},\ \hat{J} = M_{ij}\alpha_{jk}\alpha_{ki}$$

3.5 Implementation

The constitutive model is implemented as an User Material subroutine (UMAT) in ABAQUS (ABAQUS, 2004) using a semi-implicit integration scheme. This subroutine is called at each integration point and at each increment. The subroutine must perform two functions: (a) update the stresses and the internal state variables to their values at the end of each increment of strain and temperature, and (b) update the material Jacobian matrix. The coefficient of thermal expansion, α_T, depends only on temperature, and thermal expansion is isotropic for cubic crystal lattices. Thermal expansion or contraction can be taken into account by introducing a deformation gradient $\mathbf{F}^{\theta}$ in the multiplicative decomposition of the deformation gradient. An intermediate, thermally expanded, hot unstressed configuration and a hot plastically deformed relaxed configuration are introduced (Shenoy et al., 2005). The total deformation gradient is given by $\mathbf{F} = \mathbf{F}^{e} \cdot \mathbf{F}^{p} \cdot \mathbf{F}^{\theta}$, where the linearized elastic deformation is described by $\mathbf{F}^{e}$, the plastic deformation by $\mathbf{F}^{p}$, and the thermal expansion/contraction by $\mathbf{F}^{\theta}$. The velocity gradient associated with thermal expansion effects is prescribed as

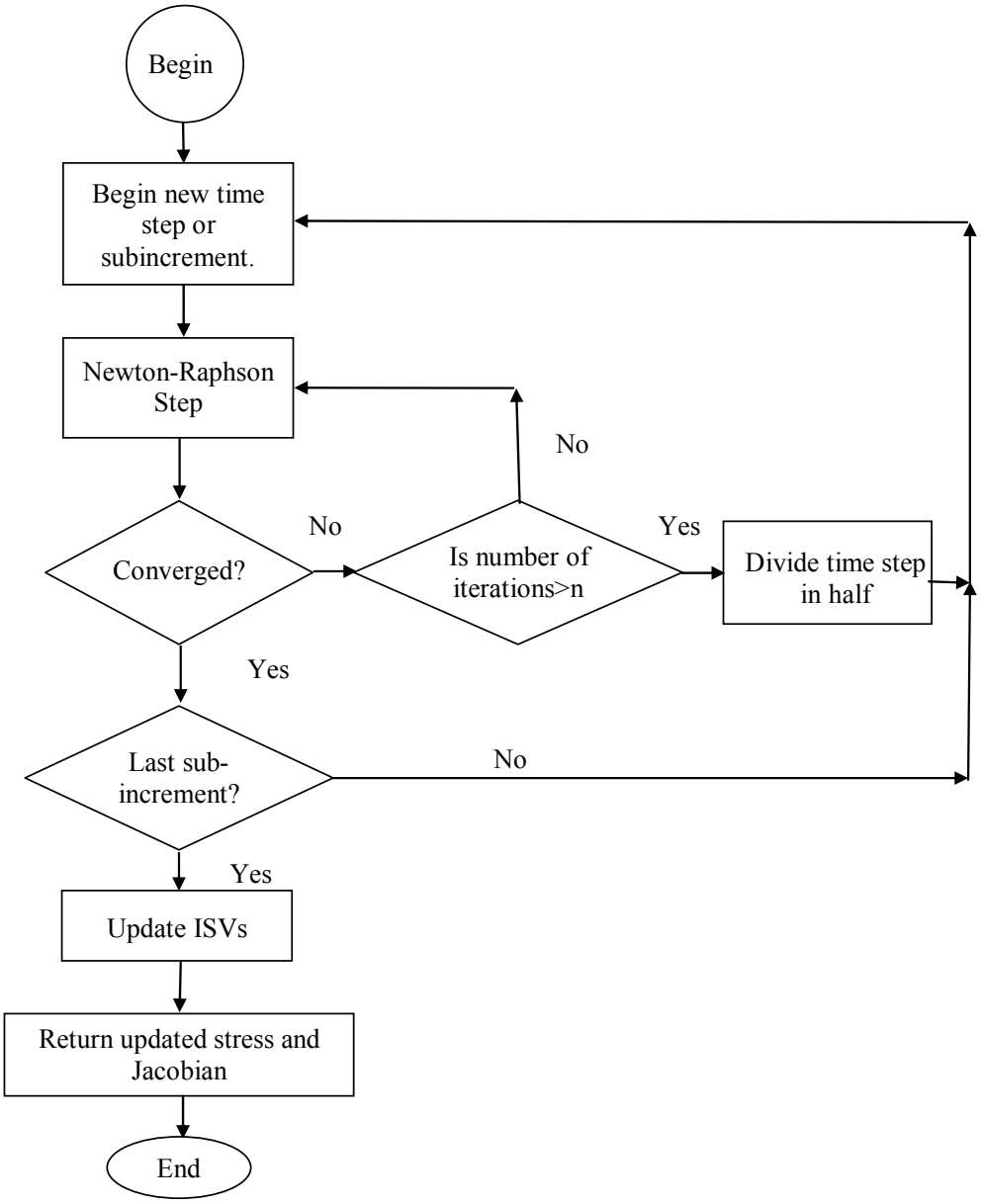

Figure 0.4 Flowchart of the algorithm for the user material subroutine.

$$\hat{\mathbf{L}}^{\theta} = \dot{\mathbf{F}}^{\theta} \cdot \mathbf{F}^{\theta^{-1}} = \alpha_T \dot{T}\, \mathbf{I} \tag{3.28}$$

The parameters in the constitutive equations are functions of temperature and are determined from isothermal experimental fatigue and creep data.

A flowchart of the algorithm is shown in Figure 3.4. For each time step, the constitutive equations are integrated from an initial state at $t = t_n$ to a final state at $t = t_n + \Delta t = t_{n+1}$. The inputs of the integration scheme are the prescribed total strain increment and the temperature increment for that time step and the stress ($\boldsymbol{\sigma}_n$) and the internal state variables (K_n and $\boldsymbol{\alpha}_n$) from the previous time step. The thermoelastic properties and the model parameters are maintained constant at their values at the beginning through the time step, which is reasonable for small time steps. The semi-implicit scheme described in detail in Marin and McDowell (1997) is employed in this work. The direction of the inelastic strain rate is held fixed during each time step (or sub-increment thereof). It is noted that parameter K depends only on temperature, and not on deformation history. The flow rule in Eq. (3.11) should be satisfied at the end of the time step. A Newton-Raphson scheme is used to solve the plastic strain increment, i.e.,

$$\Delta p^{i+1} = \Delta p^{i} - \frac{f^{i}}{f'^{i}} \tag{3.29}$$

where

$$f^{i} = \dot{p}\Delta t - A\exp\left(-\frac{Q}{RT^{i}}\right)\left\langle \frac{\bar{\sigma}^{i} - K^{i}}{D_o} \right\rangle^{n} \Delta t \text{ and } f'^{i} = \frac{\partial f^{i}}{\partial \Delta p^{i}}. \tag{3.30}$$

A time step subincrementation scheme is used along with the Newton-Raphson scheme to assist convergence (McGinty, 2001) as shown in Figure 3.4. The convergence criterion for the Newton-Raphson iterations is set as

$$\left|f^{i}\right| \leq \text{tolerance} \tag{3.31}$$

The direction of plastic flow ($\mathbf{N}$) is kept constant for the Newton-Raphson iterations in each subincrement (Marin and McDowell, 1997). The Jacobian matrix is defined as

$$J_{ijkl} = \frac{\partial \dot{\sigma}_{ij}}{\partial \dot{\varepsilon}_{kl}} = \frac{\partial}{\partial \dot{\varepsilon}_{kl}}\left[C_{ijop}\left(\dot{\varepsilon}_{op} - \dot{\varepsilon}^{p}_{op} - \dot{\varepsilon}^{thermal}_{op}\right)\right] \approx \left[C_{ijop}\left(I_{opkl} - \frac{\partial \dot{\varepsilon}^{p}_{op}}{\partial \dot{\varepsilon}_{kl}}\right)\right] \tag{3.32}$$

where I_{opkl} is the 4^{th} order symmetric identity tensor i.e.

$$I_{opkl} = \frac{\delta_{op}\delta_{kl} + \delta_{ok}\delta_{pl}}{2}$$

and

$$\frac{\partial \dot{\varepsilon}^{p}_{op}}{\partial \dot{\varepsilon}_{kl}} = \frac{\partial \dot{\varepsilon}^{p}_{op}}{\partial \sigma_{mn}} \frac{\partial \sigma_{mn}}{\partial \dot{\sigma}_{st}} \frac{\partial \dot{\sigma}_{st}}{\partial \dot{\varepsilon}_{kl}} \tag{3.33}$$

It is noted that the thermal strain increment is not included in the determination of this approproximate Jacobian, since the Jacobian is only necessary to assist in the convergence of iteration towards global equilibrium. Since $\boldsymbol{\sigma}_{n+1} = \boldsymbol{\sigma}_{n} + \dot{\boldsymbol{\sigma}}\Delta t$ and $\frac{\partial \sigma_{mn}}{\partial \dot{\sigma}_{st}} = I_{mnst}\,\Delta t$, we may substitute into Eq. (3.33) and then into Eq. (3.32). Upon rearranging, the Jacobian is given by

$$J_{ijkl} \simeq \left(C^{-1}_{ijkl} + \frac{\partial \dot{\varepsilon}^{p}_{ij}}{\partial \sigma_{kl}} \Delta t \right)^{-1} \tag{3.34}$$

3.6 Initial Axis for Transverse Isotropy

The initial axis of transverse isotropy ($\mathbf{d}_o$) in global co-ordinates is specified using the Roe convention. In the Roe convention the crystal orientation is specified by three Euler angles (ψ, θ, ϕ), which represent rotations about (1) the global Z-axis, (2) the new local Y'-axis, and (3) the new local Z''-axis, respectively, as shown in Figure 3.5 (McGinty, 2001). Note that ψ and θ together define an axis of rotation, and ϕ gives the rotation angle about that axis. In the case of transverse isotropy, the initial axis of transverse isotropy in global co-ordinates (i.e. $\mathbf{d}_o$ - directed along $\mathbf{x}_3$ in Figure 3.5), can be specified using only ψ and θ. The material response does not change with ϕ since this is the plane of isotropy. The rotation matrix is given by Λ,

$$[\Lambda] = \begin{bmatrix} \cos\psi\cos\theta\cos\phi - \sin\psi\sin\phi & -\cos\psi\cos\theta\sin\phi - \sin\psi\cos\phi & \cos\psi\sin\theta \\ \sin\psi\cos\theta\cos\phi + \cos\psi\sin\phi & -\sin\psi\cos\theta\sin\phi + \cos\psi\cos\phi & \sin\psi\sin\theta \\ -\sin\theta\cos\phi & \sin\theta\sin\phi & \cos\theta \end{bmatrix} \tag{3.35}$$

The rotation matrix is used to initialize the axis of transverse isotropy, and the elasticity tensor. The initial axis for transverse isotropy in the global co-ordinate system is prescribed as follows

$$\mathbf{d}_o = \mathbf{\Lambda} \cdot \mathbf{d}_{mat} \tag{3.36}$$

where $\mathbf{d}_{mat} = \begin{bmatrix} 0 & 0 & 1 \end{bmatrix}$ is the initial axis of isotropy in the material co-ordinate system. The elasticity tensor in the intermediate coordinate system, $\mathbf{C}_o$, is initialized in global coordinates as follows

$$\mathbf{C}_o = \mathbf{\Lambda} \cdot \mathbf{\Lambda} \cdot \mathbf{C}_{mat} \cdot \mathbf{\Lambda}^T \cdot \mathbf{\Lambda}^T \tag{3.37}$$

where $\mathbf{C}_{mat}$ is the elasticity tensor along the principal axes of transverse isotropy. It should be noted that $\mathbf{d}_i = \mathbf{d}_o$ and $\mathbf{C}_i = \mathbf{C}_o$ in the intermediate configuration.

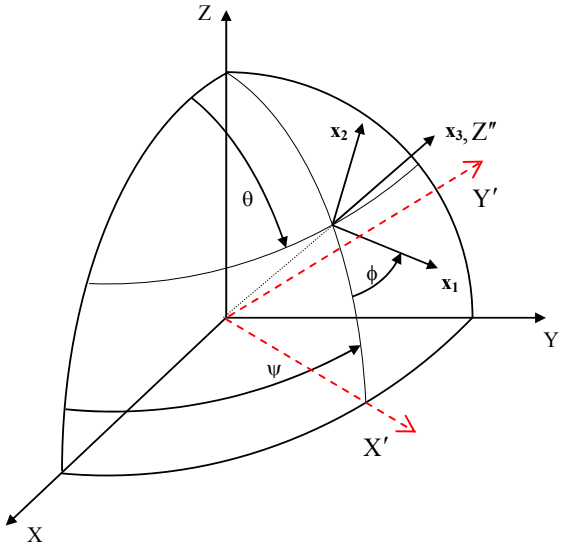

Figure 0.5 Roe convention of quantifying crystal orientation by rotations about (1) the global Z-axis, (2) the new local Y'-axis, and (3) the new local Z''-axis (McGinty, 2001).

3.7 Parameter Identification

For the transversely isotropic elastic stiffness matrix, there are five independent material parameters: the elastic modulus along the solidification axis E_L, the elastic modulus transverse to the solidification direction E_T, the Poisson's ratios ν_L and ν_T, and the shear modulus, G_L. These parameters are determined experimentally through the entire temperature range of interest. The material parameters in the inelastic strain evolution equation are determined from the experimental isothermal fatigue and creep tests. The Epogy code by Synaps (Epogy, 2004) is used to obtain a best fit by iteratively modifying the material parameters based on minimization of an objective function based on the L_2 norm of the error between simulation results and experimental data. Epogy employs four widely used search methods (linear simplex, downhill simplex, gradient, and genetic algorithms) to assure stability and enhance the probability that an optimum set of material parameters will be obtained among various local minima. More details on the error minimization procedure can be obtained in Shenoy et al. (2005). Material parameters are listed in Table 3.2. At 427°C, static thermal recovery effects are negligible and are therefore omitted ($R_\alpha = 0$). At 1038°C, secondary creep data are not available and hence values for R_α and m are not assigned; accordingly, only higher strain rate histories are modeled for which static thermal recovery effects are negligible as a good approximation.

It should be noted that parameter ξ does not influence the stress-strain response in the longitudinal and transverse orientation for uniaxial tension-compression loading. It is assumed that $\xi = \frac{3}{4}\varsigma$ in order to satisfy Eq.(3.27). It is noted that with additional torsion

data, for example, the choice of these parameters can be refined. The present choice is based on convenience and should be clarified with more combined stress state experiments and/or more orientations of loading.

Table 0.2 Material Parameters for DS GTD111.

Initial conditions: at time t = 0, $\boldsymbol{\sigma} = \mathbf{0}$, $\boldsymbol{\alpha} = \mathbf{0}$

Temperature (°C)	E_L (MPa)	E_T (MPa)	ν_L	ν_T	G_L (MPa)
427	126340	159048	0.195	0.4	104000
650	120930	156190	0.195	0.4	97900
760	103425	146667	0.195	0.4	95200
871	95200	126000	0.195	0.4	89650
982	89650	121505	0.195	0.4	82740
1038	82740	121505	0.195	0.4	75850

Temperature (°C)	K (MPa)	n	ξ	ς	H	L (MPa)	R_α (MPa^{-3})	m
427	100	30	0.33	0.44	130	180	0	-
650	175	22	0.33	0.44	150	310	6.00E-15	3
760	150	8	0.165	0.22	500	275	1.00E-13	3
871	100	4	0.056	0.075	200	250	5.75E-13	3
982	20	4	0.056	0.075	225	190	4.00E-12	3
1038	20	4	0.056	0.075	125	190	-	-

Q (KJ/mol)	R (J/mol °K)	A (1/s)	D_o (MPa)
319	8.314	3.3174E+7	270

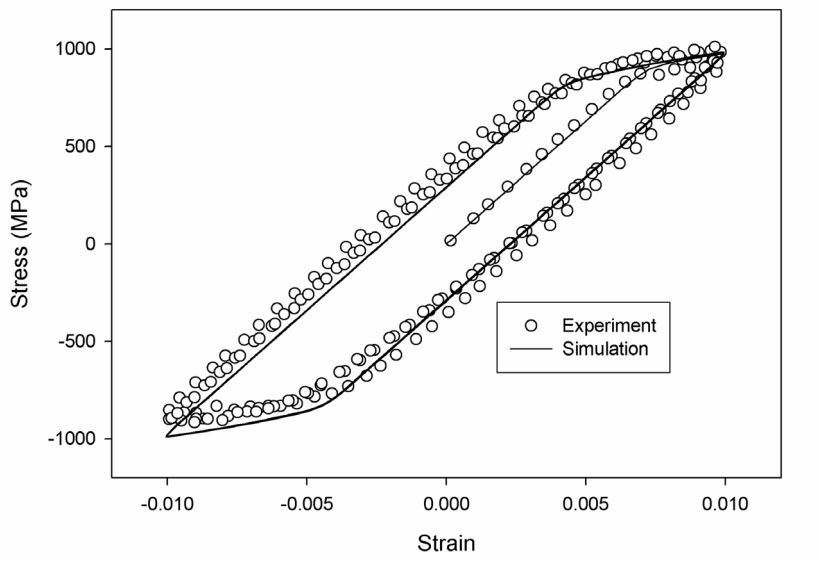

Figure 0.6 Stress-strain response at 426°C (1st cycle) in the longitudinal orientation.

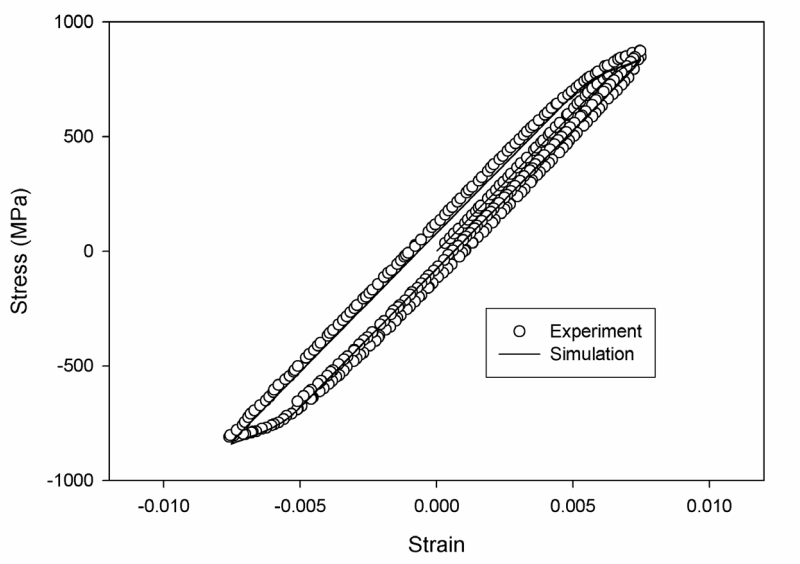

Figure 0.7 Stress-strain response at 650°C (1st cycle) in the longitudinal orientation.

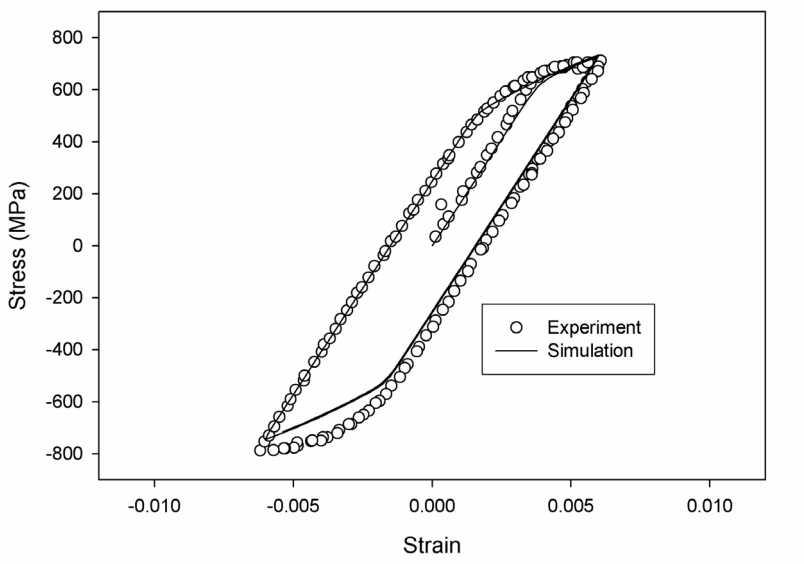

Figure 0.8 Stress strain response at 650°C (1st cycle) in the transverse orientation.

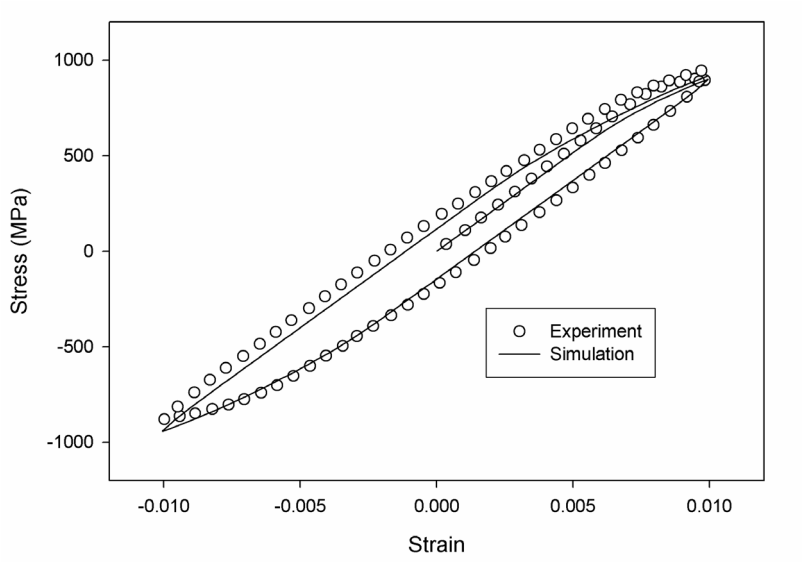

Figure 0.9 Stress-strain response at 760°C (1st cycle) in the longitudinal orientation.

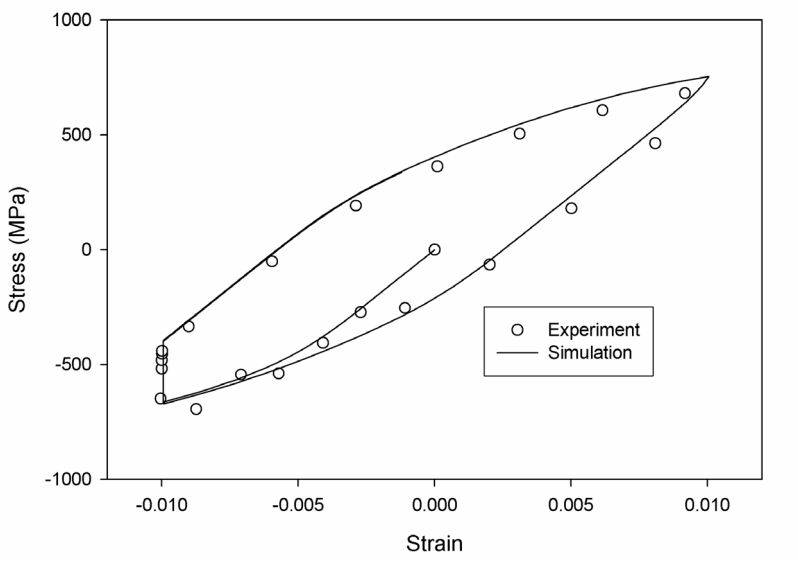

Figure 0.10 Stress-strain response at 871°C (1st cycle) in the longitudinal orientation with a 120 s hold time at the peak strain in compression.

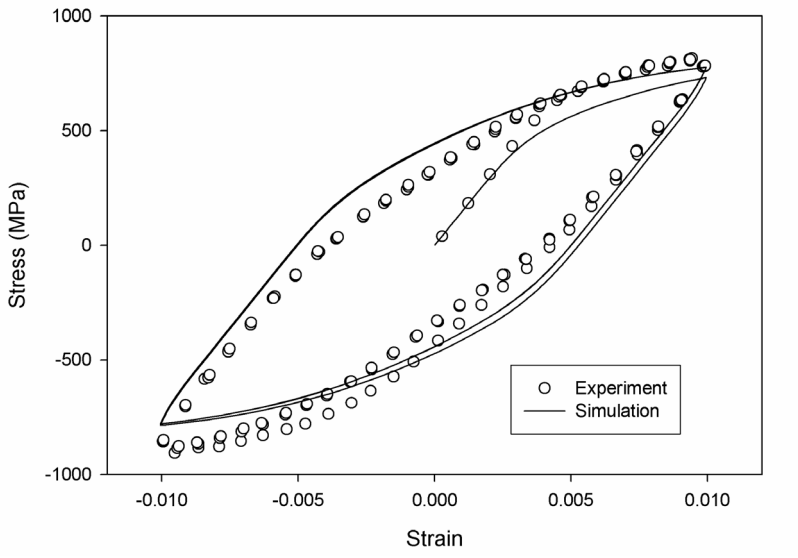

Figure 0.11 Stress-strain response at 871°C (1st cycle) in the transverse orientation.

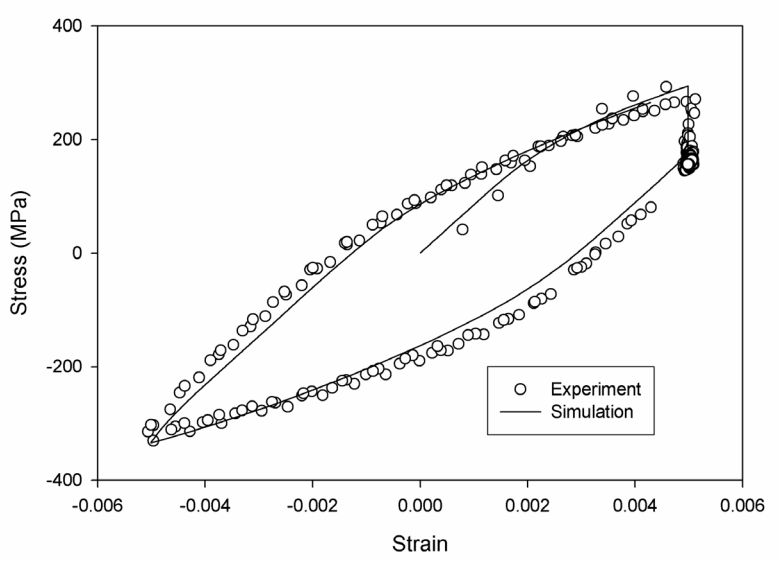

Figure 0.12 Stress-strain response at 982°C (1st cycle) in the longitudinal orientation with a 120 s hold time at the peak strain in tension.

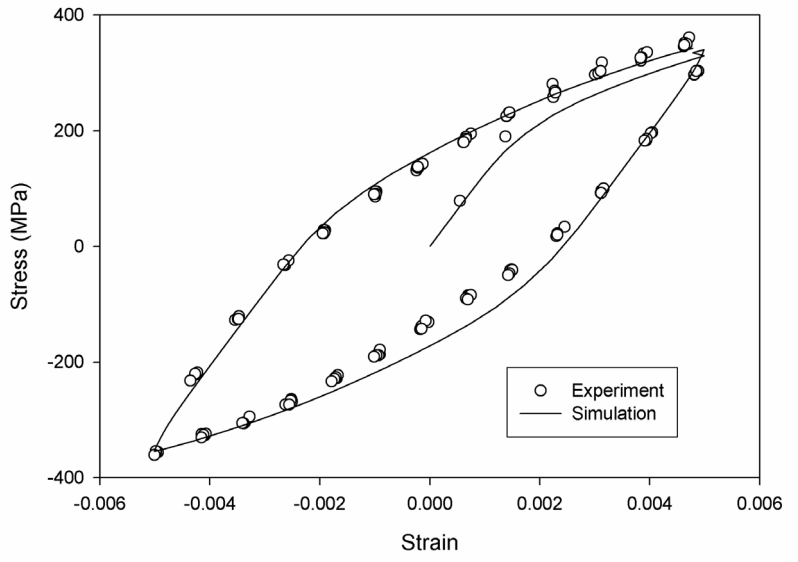

Figure 0.13 Stress-strain response at 982°C (1st cycle) in the transverse orientation.

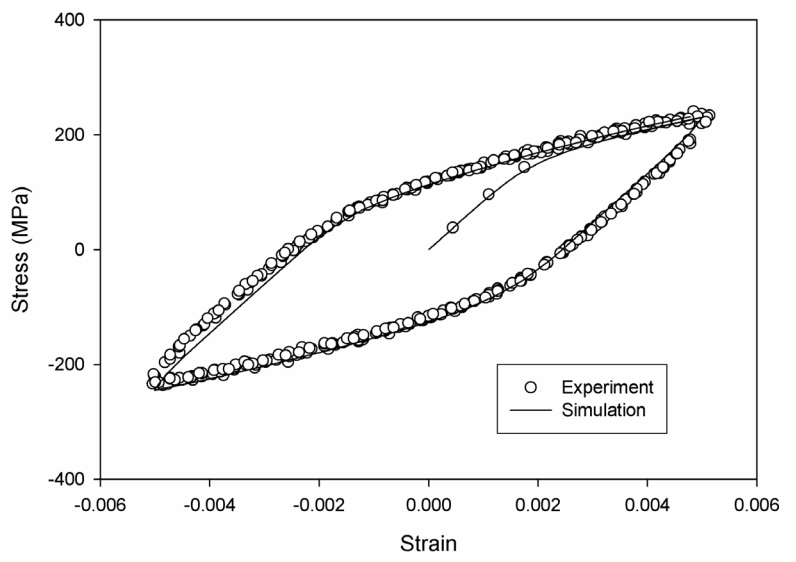

Figure 0.14 Stress-strain response at 1038°C (1st cycle) in the longitudinal orientation.

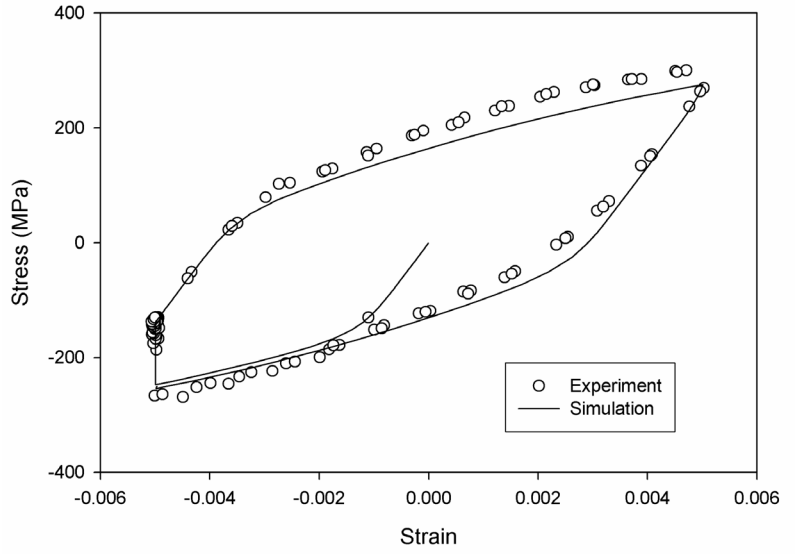

Figure 0.15 Stress-strain response at 1038°C (1st cycle) in the transverse orientation with a 120 s hold time at the peak strain in compression.

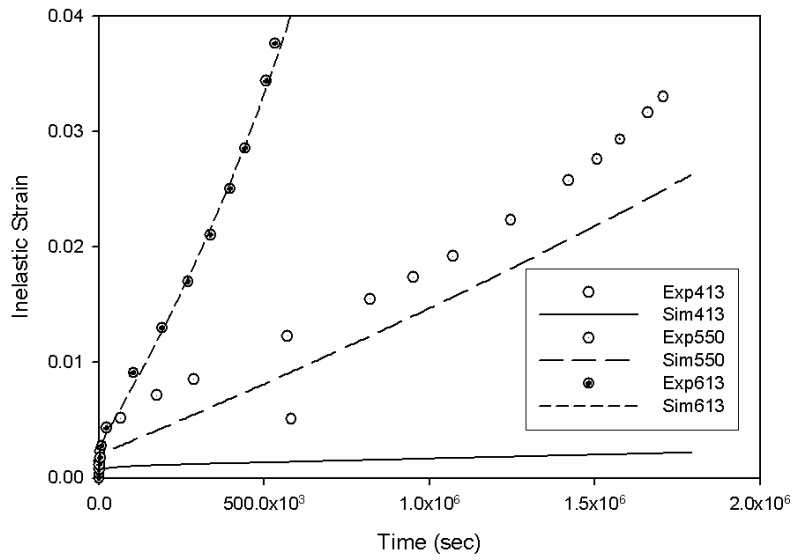

Figure 0.16 Creep response at 760°C in the longitudinal orientation for three experiments with engineering stress held constant at 413, 550 and 613 MPa.

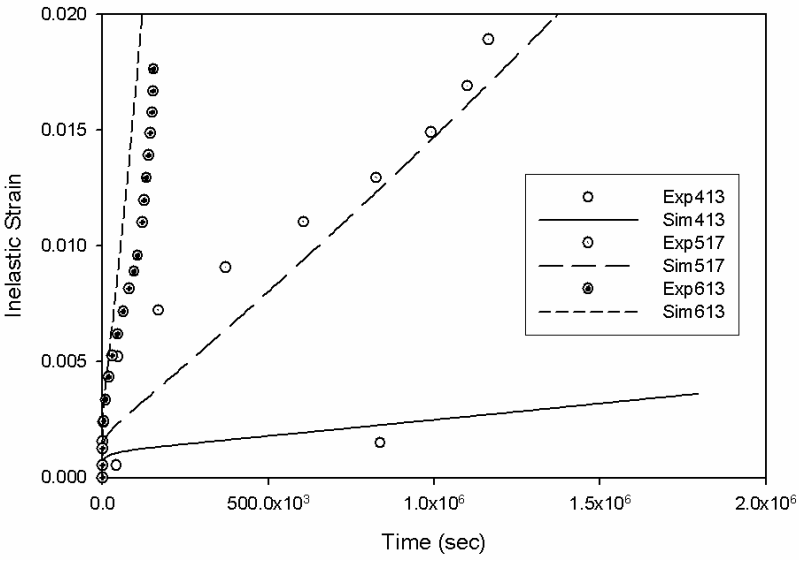

Figure 0.17 Creep response at 760°C in the transverse orientation for three experiments with engineering stress held constant at 413, 517 and 613 MPa.

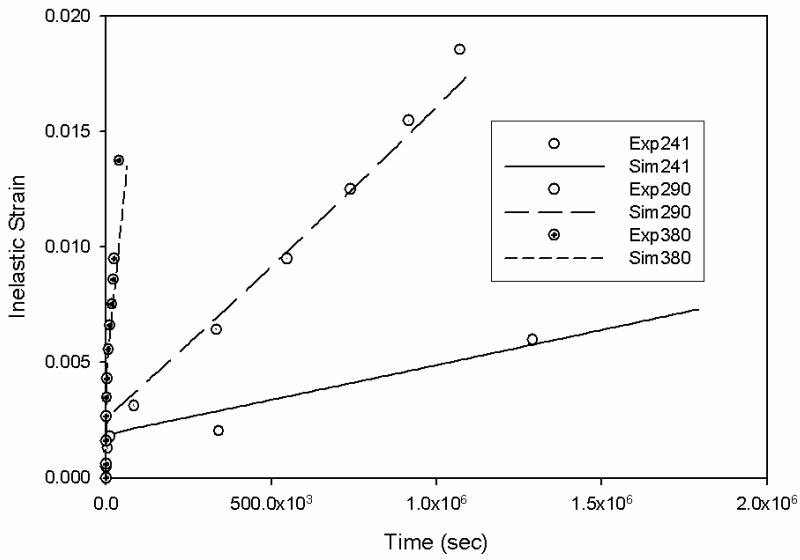

Figure 0.18 Creep response at 871°C in the longitudinal orientation for three experiments with engineering stress held constant at 241, 290 and 380 MPa.

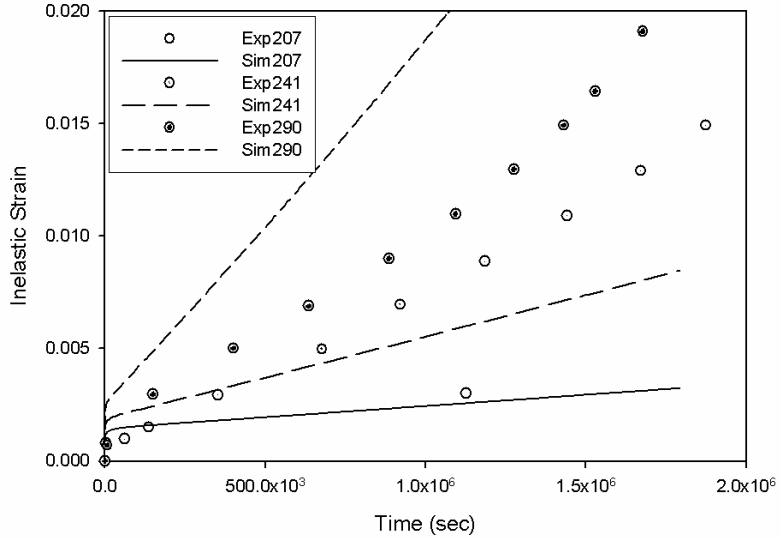

Figure 0.19 Creep response at 871°C in the transverse orientation for three experiments with engineering stress held constant at 207, 241 and 290 MPa.

Experimental data used to estimate model parameters and resulting model correlations are presented in Figs. 3.6-3.19. The fits are observed to be reasonable in both the longitudinal and transverse orientations over the entire temperature range. As seen in Figures 3.6 and 3.7, tension-compression (TC) asymmetry is observed at 426°C and 650°C, the yield strength in tension is higher than that in compression in the longitudinal orientation. The nature of the tension-compression asymmetry is reversed in the transverse orientation, the yield strength in compression is higher than that in tensile loading as observed in Figure 3.8. Although, the current model does not have the capability to capture the TC asymmetry, it still reasonably captures the stress-strain response. The model captures the primary and secondary creep response in both the longitudinal and transverse orientation as shown in Figures 3.17-3.19. The static thermal recovery term is used to capture the secondary creep response.

3.8 Validation and Relative Comparisons

3.8.1 Prediction of Thermomechanical Fatigue

The parameters determined from the isothermal tests are assigned temperature dependence by using linear interpolation between their values determined at temperatures at which isothermal tests were conducted. The model is used to predict the stress-strain response for both in-phase (IP) and out-of-phase (OP) thermomechanical fatigue (TMF) tests. These TMF simulations can be considered as true predictions since they were not used to determine model parameters.

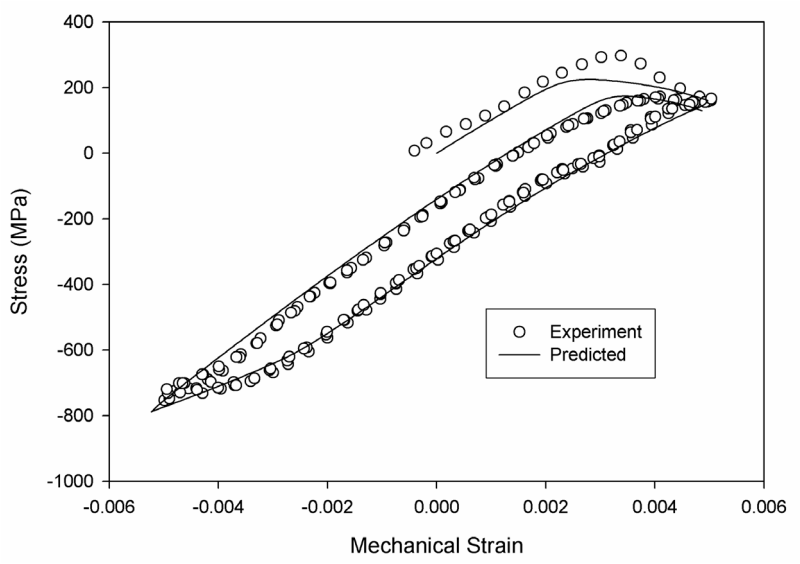

Figure 0.20 Stress-strain response for in-phase (IP) TMF from 538°C – 1038°C with loading in the longitudinal orientation (1st cycle).

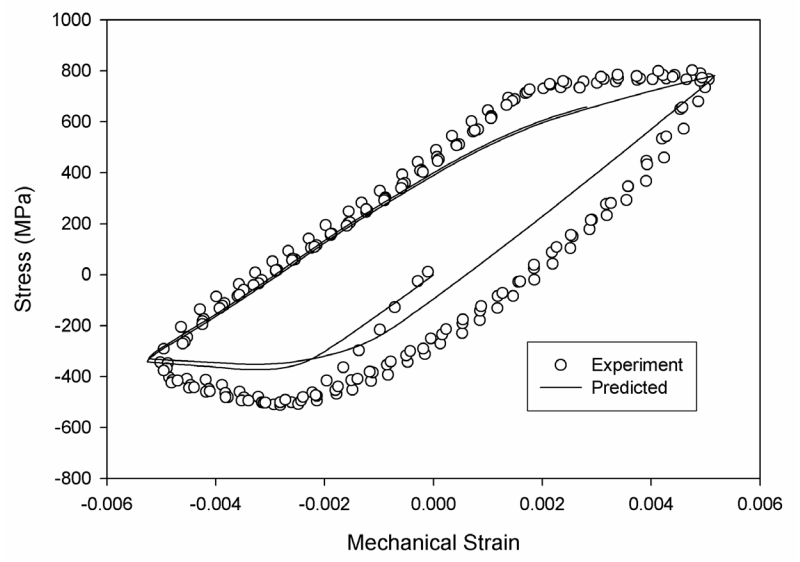

Figure 0.21 Stress-strain response for out-of-phase (OP) TMF from 538°C – 927°C with loading in the transverse orientation (1st cycle).

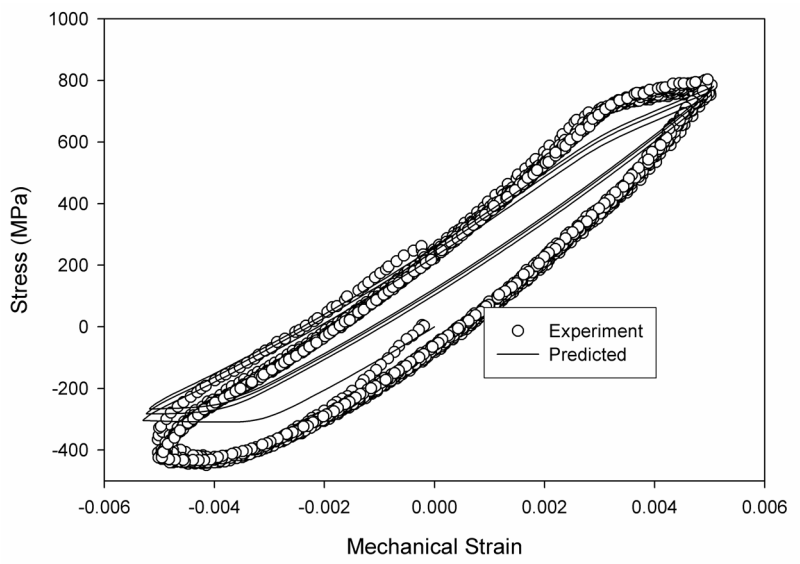

Figure 0.22 Stress-strain response for out-of-phase (OP) TMF from 538°C – 927°C with loading in the longitudinal orientation (1st cycle).

The model appears to capture the overall trends of experimental results for loading in both the longitudinal and transverse orientations, as shown in Figures 3.20-3.22. The corresponding mechanical strain and temperature loading histories are given in Figures 2.24-2.26. Some discrepancies between the experimental data and simulation are observed for the transverse loading orientation in Fig. 3.21. Possible sources include experimental error as well as the error introduced from linear interpolation of the material parameters between the values at temperatures at which isothermal tests were conducted. Also, fewer tests were conducted in the transverse orientation than in the longitudinal orientation.

3.8.2 Intrinsic Dissipation and Stored Energy

The intrinsic dissipation rate (ϕ_1) is the working rate of the stress on the plastic rate of deformation less the rate of energy storage associated with the evolution of the backstress, i.e.,

$$\phi_1 = \boldsymbol{\sigma}^{\mathrm{PK2}} : \hat{\mathbf{D}}^{\mathrm{p}} - \boldsymbol{\alpha} : \dot{\mathbf{A}} = \boldsymbol{\sigma}'^{\mathrm{pk2}} : \hat{\mathbf{D}}^{\mathrm{p}} - \boldsymbol{\alpha} : \dot{\mathbf{A}} \geq 0 \tag{3.38}$$

The non-recoverable (ϕ_2) energy stored in the material due to residual micro-stresses arising from dislocation interactions, pile-ups etc., is given by

$$\phi_2 = \boldsymbol{\alpha} : \dot{\mathbf{A}} \tag{3.39}$$

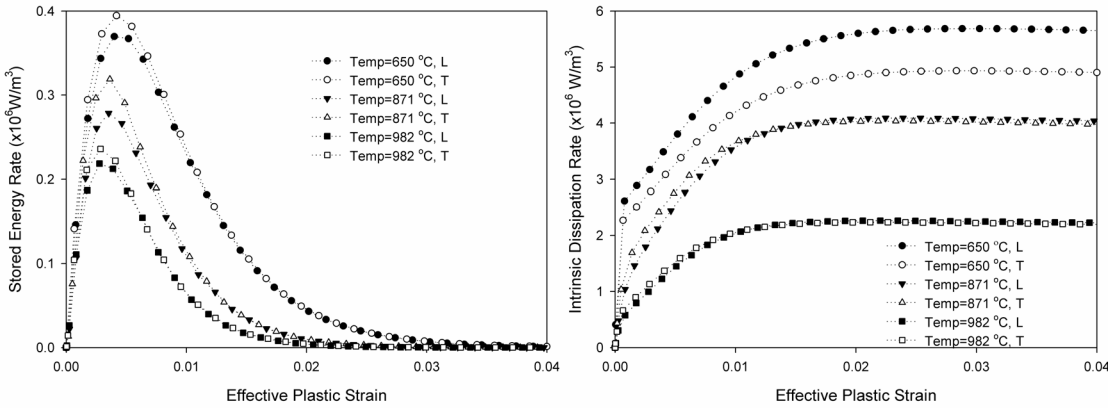

(a) (b)

Figure 0.23 (a) Rate of non-recoverable stored energy and (b) intrinsic dissipation rate for loading in the longitudinal (L) and transverse (T) directions as a function of effective plastic strain and temperature.

The rate of energy storage and the rate of intrinsic dissipation are plotted as a function of inelastic strain for loading in the longitudinal and transverse orientations in Figure 3.23.

Both the rate of energy storage and the rate of intrinsic dissipation decrease with increasing temperatures. The stored energy is typically significantly less that 20% of the intrinsic dissipation, which is consistent with other metals (Lemaitre and Chaboche, 2000). It is noted that the ratio of rate of energy storage to the rate of dissipation is maximum at strains around 0.5%; the maximum ratio is about 20%, occurring at the upper end of the temperature range considered, i.e., 982°C.

3.8.3 Computational Comparison with Crystal Plasticity

Analyses conducted using the transversely isotropic model are compared to the full 3D crystal plasticity theory by Shenoy et al. (2005), based on ABAQUS UMAT implementations. Analyses are conducted for a thin square plate with a cylindrical hole, subjected to uniaxial tension. Single crystal analyses for various crystallographic orientations relative to the direction of applied loading are compared to the predicted response of the equivalent homogeneous transversely isotropic plasticity model. Three dimensional 8-noded brick elements are used and the analyses are conducted using different mesh sizes. Loading is considered in both the longitudinal orientation and the transverse orientation for the transversely isotropic model.

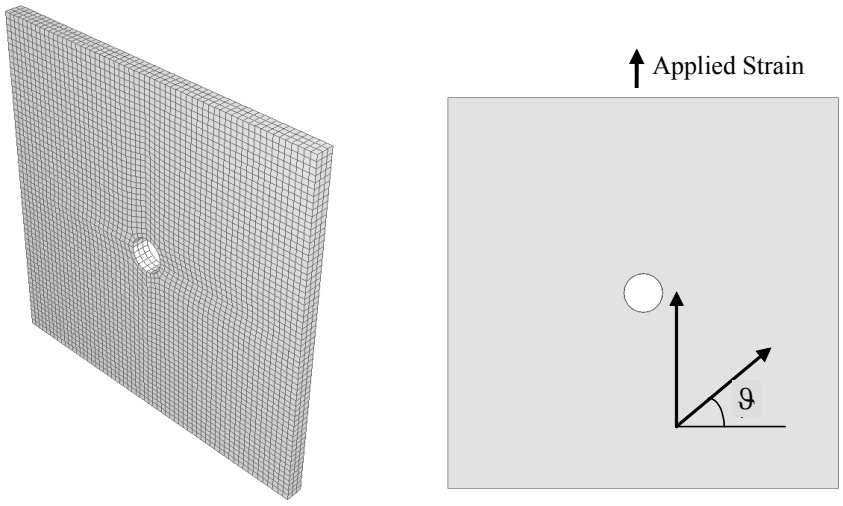

(a) (b)

Figure 0.24 (a) Three dimensional mesh with 60x60x3 elements for the square plate with hole and (b) the orientation angle, ϑ, for the [001] crystallographic direction in the single crystal plasticity simulations; the [010] direction is normal to the plane.

As shown in Figure 3.24, the orientation angle, ϑ, which denotes the [001] crystallographic direction in the single crystal plasticity simulations (the [010] direction is normal to the plane), is varied from 0-45º for the single crystal analyses. It should be noted that this covers the entire range of possible orientation angles for the grains in the transverse orientation due to cubic symmetry in FCC crystals for the applied loading condition. In reality, the macroscopic stress-strain response for a DS material in the transverse orientation will be the average response from multiple grains with random transverse orientations. The square plate has equal height and width dimensions, with a plate thickness and hole diameter 1/10 of these dimensions, as shown in Figure 3.24. Actual dimensions are irrelevant since the constitutive equations are of local character with no intrinsic length scale. Full integration is used to ensure convergence of the analyses and symmetry conditions are employed about the [010] plane. The simulations are carried out at 650ºC under strain control with 1.5% strain amplitude; the strain is completely reversed.

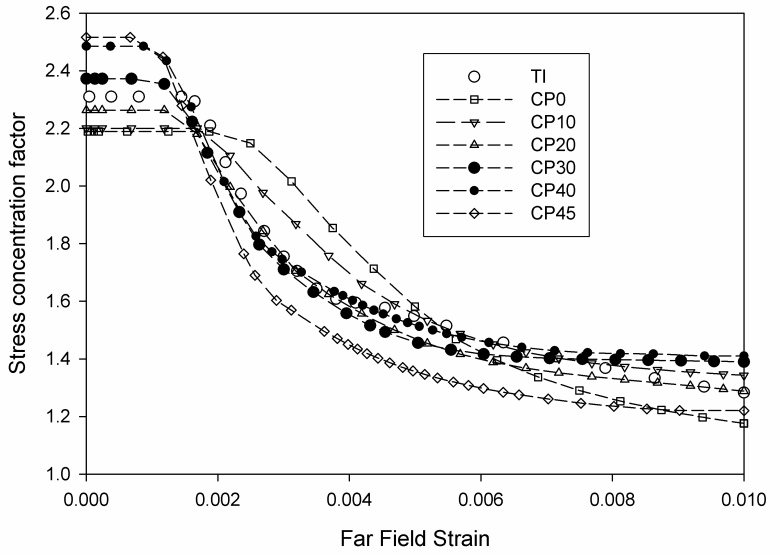

Figure 0.25 Stress concentration factor for the single crystal plasticity (CP) model where ϑ varies from 0-45º and the transverse isotropy (TI) model loaded in the transverse orientation at 650°C.

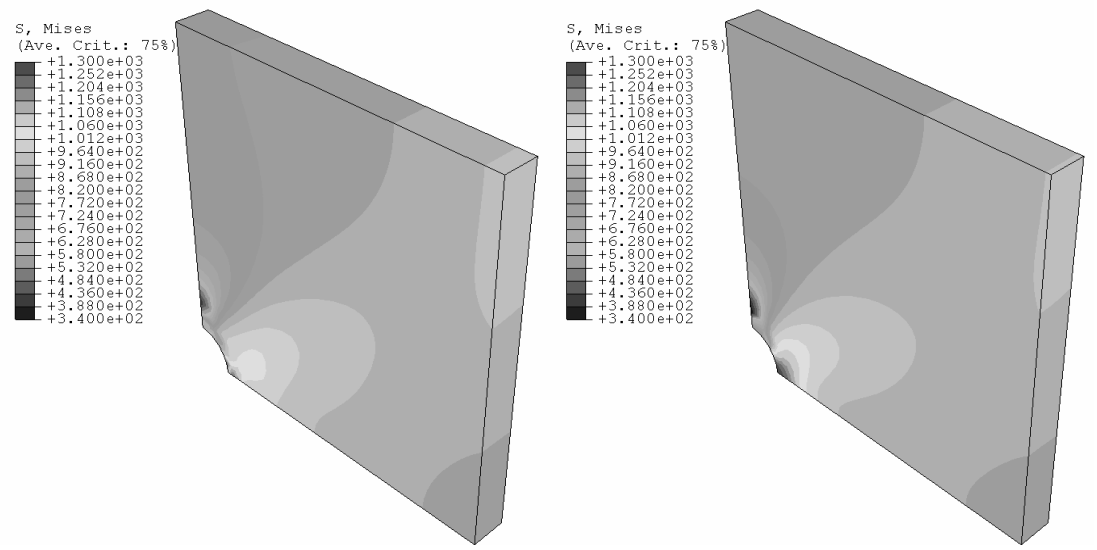

(a) (b)

Figure 0.26 von Mises stress contour using the (a) single crystal plasticity (CP) in the [001] orientation and (b) transverse isotropy (TI) model loaded in the longitudinal orientation at 650°C, 0.75% applied strain (Note: $1/8^{th}$ of the model is shown due to symmetric response along all three axes in this case).

The notch stress concentration factor is compared for the two models as a function of the number of elements and both the analyses converge for a mesh with 60x60x3 elements. The average analysis time is observed to be a factor of two lower for the transversely isotropic model simulations when compared to the crystal plasticity model. It should be noted that the computational time saved for the transversely isotropic model would be more substantial in cases where multiple grains are modeled explicitly in the crystal plasticity simulations to capture the macroscopic stress-strain response in the transverse orientation. The stress concentration factor is defined as the ratio of the maximum von Mises equivalent stress at an element at the notch root to the Mises equivalent far field stress. A uniaxial monotonic strain is applied from 0 to 1% and the stress concentration factor is determined as a function of the applied strain, as shown in Figure 3.25. The stress concentration factor in the transverse isotropy model correlates well with the crystal plasticity simulations and the stress concentration values in the transverse orientation generally fall in between the values predicted from the single crystal simulations. In Figure 3.26, the von Mises equivalent stress contours in the longitudinal orientation ([001] orientation for the crystal plasticity model) are compared for the two models for an applied strain of 0.75%. It is observed that although the stress contours are qualitatively similar, the stress concentration is somewhat more localized in the crystal plasticity simulation.

3.9 Limitations

Limitations of the model are discussed next.

a) Most of the experimental data are generated for isothermal uniaxial fatigue in the longitudinal and transverse orientations. The validity of the model should be tested for other loading orientations and also for multiaxial fatigue. Multiaxial fatigue testing is a non-trivial task since there are no set standards for conducting

these tests on DS materials. For example, axial-torsion testing of thin-walled tubes requires a specimen with a minimum number of grains in the thickness direction, which cannot be achieved with DS GTD-111.

b) Even though an effort has been made to encapsulate the physics of the deformation behavior in the formulation, the macroscopic transversely isotropic formulation smears the influence of individual grains and gives an averaged response.

c) While the model addresses the first three points in section 2, it does not have the capability to capture the tension-compression (T-C) asymmetry, which could be significant in the anomalous temperature regime. However, it should be noted that DS GTD-111 is mainly used in second stage turbine blades and the temperature range of interest is mainly above the peak anomalous temperature (750°C), where T-C asymmetry may be less significant. The addition of T-C asymmetry can be undertaken, if necessary, but its neglect does not appear to compromise model capabilities over a wide range of temperature in the present study for a specific DS polycrystal.

3.10 Summary

The viscoplastic deformation behavior of a directionally solidified GTD-111 Ni-base superalloy has been characterized as a function of temperature and loading history for both longitudinal and transverse loading histories. A homogeneous, transversely isotropic model is developed to capture the stress-strain response in the longitudinal and transverse orientations for component level analyses. The model is implemented in ABAQUS as an user material subroutine. Isothermal and thermomechanical uniaxial fatigue tests with hold times and creep tests are conducted at temperatures ranging from room temperature

427°C to 1038°C. Using isothermal test data to fit constants, IP and OP TMF responses are adequately predicted. The transversely isotropic viscoelastoplastic model is shown to reduce the analysis time compared to that of a continuum polycrystal plasticity model.

CHAPTER IV

Modeling Effects of Inclusions on Crack Initiation Life in DS Nickel-Base Superalloys

Abstract

Inclusions often play a dominant role in limiting fatigue life in both cast and wrought alloys under nominally elastic cyclic loading conditions. The hierarchical scales of fatigue crack formation and their correspondence to strain-life relations were considered for cast A356-T6 Al in recent work by McDowell and co-workers (2003) using a microstructure-property framework that related cyclic plasticity near debonded silicon particle and large casting pores to formation and early growth of microstructurally and physically small fatigue cracks. In this chapter, the analogous role of carbides or other hard ceramic particles in fatigue crack formation in directionally solidified (DS) Ni-base superalloys are analyzed. Cyclic plasticity of a DS Ni-base superalloy is evaluated for loading in the longitudinal and the transverse orientations. The effects of loading parameters (strain amplitude, *R*-ratio) and microstructural parameters (nonmetallic inclusion shape, spacing, etc.) on local cyclic plasticity at microstructure-scale notches are evaluated. The effect of grain orientation on intensification of plastic strain around inclusions is analyzed, and functions are determined for relating applied strain to cyclic plastic shear strain near the inclusion/matrix debond (micronotch) that contributes to LCF crack formation. Use of such a framework for predicting microstructure-dependence of fatigue crack initiation life and its variability is discussed, as are additional mechanisms

of micro-fracture associated with cumulative plastic deformation. DS GTD111 is used as the representative material; however, it is stressed that the primary objective is to develop and demonstrate a framework to include microstructural dependence in crack initiation life prediction models using computational tools.

4.1 Introduction

Numerous life prediction models have been proposed for Ni-base superalloys and can be broadly separated into two classes; parametric approaches (Coffin, 1974; Ostergren, 1976) and physics-based approaches (Leckie and Hayhurst, 1977; Neu and Sehitoglu, 1989; Lemaitre and Chaboche, 1990; Miller et al., 1992; Gallerneau and Chaboche, 1999; Koster et al., 2002). Physics-based approaches have been preferred in the recent past due because they have direct relations with the material microstructural features and deformation mechanisms. Good understanding of the microstructural features and their implications on fatigue crack initiation and propagation are essential to accurate life prediction. Finite element analysis (FEA) provides a convenient tool to assess the microstructural influence on fatigue life and has been increasingly used in life prediction schemes (Horstemeyer and Ramaswamy, 2000; Gall et al., 2001; McDowell et al., 2003).

Inclusions play an important role in fatigue crack formation in multiphase alloys such as Ni-base superalloys. These inclusions, which are found near the grain boundaries in wrought alloys or in the interdendritic regions of cast alloys, are typically somewhat stiffer than the surrounding material. In some cases, however, these are relatively soft and ductile. The incompatibility of deformation between the inclusions and the surrounding material leads to local plasticity even when the applied loading is well below the macroscopic yield point. Under cyclic loading conditions, fatigue cracks may form within

these localized plastic zones. If these cracks have sufficient driving force they may propagate and lead to overall component failure.

In this work, the role of inclusions in crack initiation life of a characteristic DS Ni-base superalloy is systematically studied and a scheme is introduced to estimate "potency" of inclusions with regard to fatigue crack formation. In contrast to classical fatigue crack *initiation* correlations, which are typically based on correlation of macroscopic stress and strain with cracks of length from 0.5 mm-1 mm, the approach taken here considers driving forces for the formation and early propagation (just beyond the domain of influence of the inclusion or micronotch root field) of microstructural-scale cracks at inclusions or other relevant heterogeneities in the material. Microstructurally small fatigue cracks that arrest due to loss of driving force within the domain of influence of the micronotch root field in which they are formed do not represent a threat to component longevity. Hence, there are important scale effects to consider.

Once a small crack grows beyond the influence of the micronotch root field, it behaves more like a microstructurally or physically small crack, depending on length relative to heterogeneous microstructural features, and is subject to threshold conditions of a different sort than the conventional long crack threshold (Miller, 1993a; Miller, 1993b). In fatigue-critical applications under remote elastic loading conditions, LCF at micronotches may be essentially characterized as a "go - no go" condition on formation of small cracks at the largest inclusions or grains that are subject to further propagation. The determination of whether a propagating crack will form is based on the scale of the cyclic microplasticity relative to the size of the inclusion or micronotch as well as the absolute scale of the cyclic plastic zone. If the scale of the cyclic plastic shear localization is small compared to micronotch size, this case is termed "constrained microplasticity." Otherwise, it is termed "unconstrained." This kind of approach, which can be pursued using computational micromechanics, has been advanced recently for cast Al alloys (Gall et al., 2001; McDowell et al., 2003). It has also been applied to study

driving forces for fatigue crack formation in Ti alloys (Goh, 2002; Morrissey et al., 2003). The approach requires mappings on "influence functions" to be developed between applied stress states and local cyclic plastic shear strain and strain ratios for materials with microstructure (Bennett, 1999a; Gall et al., 2001; Goh, 2002; McDowell et al., 2003; Morrissey et al., 2003; Bennett and McDowell, 2003a), similar in principle to notch root stress/strain concentration factors. The key difference lies in the additional complexity of microstructure-scale modeling that must consider elastic anisotropy and slip anisotropy, microstructure heterogeneity, and details of inclusion cracking or debonding from the matrix.

One of the principal objectives that motivates explicit consideration of microstructure in estimating fatigue resistance is to facilitate comparison of fatigue driving forces among microstructures. In this way, understanding is sought regarding the most significant microstructure features and how the processing steps might be altered to enhance fatigue resistance. A second principal objective of modeling cyclic plasticity in explicit microstructures is to obtain quantitative estimates of the effect of variability of microstructure features on scatter in fatigue lives or fatigue strength for a given life by considering variation of driving forces for crack formation and early propagation (cf.(Roven and Nes, 1991; McDowell, 1996a; Sauzay and Gilormini, 2000; McDowell et al., 2003; Bennett and McDowell, 2003b). Moreover, the current objective is to model the coupling of microstructure with fatigue response for simple loading histories such as completely reversed, constant amplitude loading. This distinguishes the present effort from many phenomenological fatigue modeling studies in the prior literature that are motivated by component design or component failure mitigation goals that seek to address, for example, complex history effects or mean stress effects with the assistance of experiments. This approach is rather more directed towards the goal of design or specification of material microstructure than design of components.

Another important distinction between the approach taken here and perhaps the majority of previous models in the literature that have addressed the effects of microstructure-scale "notches" (pores, inclusions, and so forth) is that the validity of the Linear Elastic Fracture Mechanics (LEFM) ΔK parameter as a driving force for microstructurally or even physically small cracks in heterogeneous microstructures is not assumed, especially considering anisotropic crystallographic slip over extended distances relative to crack length and crack paths that pass through arrangements of second phase particles (McDowell, 1996a). Some works have addressed crack-initiating inclusion populations in detail in terms of establishing initial crack size distribution (Murakami, 1994; DeBartolo and Hillberry, 1998; Laz and Hillberry, 1998), with the fatigue methodology based on crack propagation using LEFM concepts, including threshold effects for nonpropagating cracks and effects of crack growth and load history on plasticity-induced closure (Tanaka, 1987; Newman, 1994). Use of a LEFM-based threshold for small cracks growing from micro-inclusions is indeed problematic from a fundamental perspective of validity of such models/fields. Moreover, it is quite difficult, from a practical perspective, to separate the effects of development of plasticity-induced crack closure on reduction of crack growth rate, with interpretation predicated upon the use of simplified, idealized theoretical treatments such as LEFM, from transients associated with crack growth away from strain-concentrating, microstructure-scale crack formation sites, considering the complexity of slip mode, strain intensification associated with cracked or debonded nonmetallic inclusions or clusters of inclusions, interactions with grain boundaries, and so on. A number of studies have demonstrated the significant role of microstructure in influencing small crack growth, and with slip distances on the order of crack length it is essential to consider models other than LEFM to correlate microstructurally and physically small fatigue crack growth rates measured in practical alloy systems (Nisitani, 1987; Tanaka and Akinawa, 1989; Wang and Miller, 1992). Recent microstructure-level modeling efforts have provided a basis for understanding

limitations of conventional fracture mechanics such as LEFM (Navarro and de los Rios, 1987; Hoshide and Socie, 1988; Gall et al., 1997; Zhang et al., 1997) and advocate appropriate elastoplastic solutions for the cyclic crack tip displacement as a means of correlating small crack growth behavior in real materials for cracks below typically 500 μms in length, depending on alloy system and applied stress amplitude (Donahue et al., 1972; Li, 1990; McDowell and Bennett, 1997; McClintock, 1999). The crack tip displacement has proven quite successful in correlating mixed mode elastic-plastic fracture of long cracks as well (Ma et al., 1999).

These various complex considerations regarding the fatigue behavior of real microstructures suggest favorability of a simple, robust methodology for assessing fatigue resistance of microstructures subjected to constant amplitude fatigue loading. Such a methodology was introduced in McDowell et al. (2003) for a hierarchy of microstructure features that may act as micronotches to form cracks and will be extended here to address LCF in generic directionally solidified (DS) Ni-base superalloys. Coarse grain DS alloys require single crystal constitutive description of matrix plasticity. The primary application focus for illustrative purposes is on modeling fatigue crack formation in DS GTD111 with hard inclusions, loaded uniaxially along the longitudinal orientation. The transverse orientation is briefly analyzed to illustrate the effect of the loading orientation on the intensification of plastic strain around inclusions.

4.2 Background Literature

Microstructural features at different length scales play an important role in dictating the fatigue life in Ni-base superalloys. This section presents a brief review of the crack initiation mechanisms observed in DS Ni-base superalloys.

Unlike their polycrystalline counterparts, the grain boundaries typically do not play a very important role in crack initiation in DS and SC Ni-base superalloys (Antolovich, 1996). Instead, microstructural features such as inclusions and secondary phases tend to act as sites for crack formation. High cycle fatigue (HCF) and low cycle fatigue (LCF) tests by Leverant and Gell (1969) on DS MAR-M200 indicated that pre-cracked carbides and micropores act as crack initiation sites at the lower homologous temperatures ($\leq 870°C$). At higher temperatures, oxidation plays a more important role and surface cracking is observed. In DS MAR-M200, the carbides were similar in shape to those in DS GTD111 and varied from 50 to 140 μm, with large variation of the aspect ratio. Pre-cracked carbides oriented normal to the stress axis primarily acted as crack formation sites. The cracks were parallel to the long dimension of the carbide and could be observed only using electropolishing i.e. they could not be observed using conventional mechanical polishing. The cracks incubated along slip bands in the matrix with Stage I crack propagation is shown in Figure 4.1 (Gell and Leverant, 1968). The fatigue life decreased with an increase in the MC carbide size as seen in Figure 4.2. Stage 1 cracking was observed to be dominant at lower temperatures and higher frequencies at which the deformation is expected to be more heterogeneously distributed in planar slip bands.

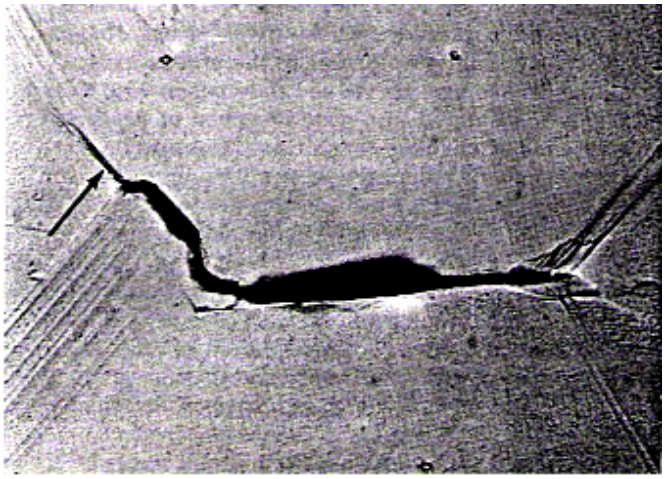

Figure 0.1 A cracked carbide acting as crack incubation site in DS MAR-M200.

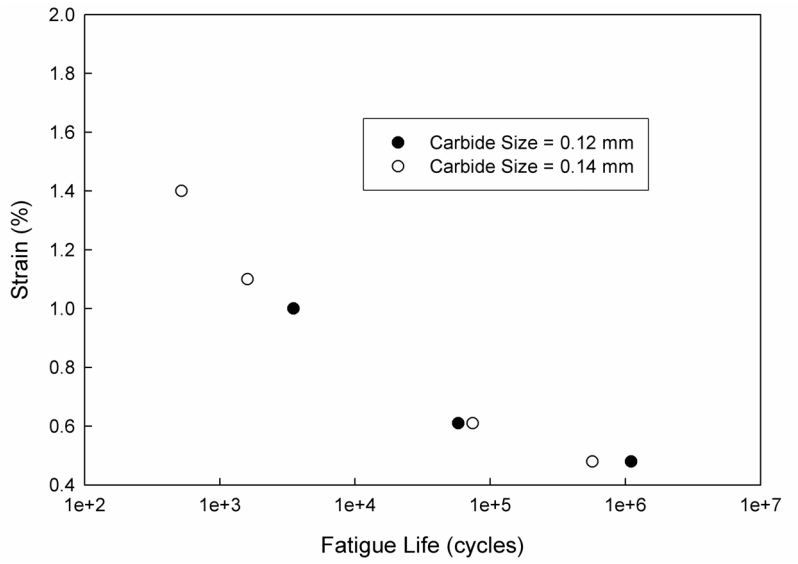

Figure 0.2 Variability in fatigue life of cast DS MAR-M200 as a function of the MC carbide size at 760°C (Leverant and Gell, 1969).

Crack initiation tests conducted by Okazaki et al. (1990)on DS Rene′80 at 650°C, which has a similar material composition to DS GTD111, also confirmed the dominant role of the MC carbides as crack initiators. However, in addition to the inclusions, cracks also emanated from micropores and by the classical intrusion-extrusion slip mechanism. A similar role of MC carbides was observed by Liu et al. (Liu et al., 2003) in a commercial single crystal superalloy, where the MC carbides provided sites for crack formation by debonding from the matrix. As opposed to MAR-M200 and DS Rene′80, these carbides were blocky and were relatively smaller (5-10 μm). From the available literature, it is fairly clear that the carbides and voids are potential sites of crack formation in SC and DS Ni-base superalloys.

4.3 Experimental Observations - DS GTD111

DS GTD111 is a two-phase material similar to DS Rene′80, with cuboidal primary precipitates (0.5-1 μm) and spheroidal secondary precipitates (0.05-0.2 μm), with an overall volume fraction of approximately 40-50% as shown in Figure 2.1. The grains are columnar and are roughly 125 mm long and 0.5-2 mm wide. Figure 4.3 shows an optical microscopic image for the untested material and Figure 4.4 shows scanning electron microscope (SEM) images of this material after a uniaxial LCF test with loading in the [100] orientation. The images clearly reveal the two-phase microstructure of the material and the presence of many plate-like carbide inclusions. The inclusions are $M_{23}C_6$ and M_6C type carbides, 1-2 % in volume fraction and are mainly found in the interdendritic regions. The carbides do not show any preferred orientation and are present in all shapes and sizes ranging from 2-150 μm.

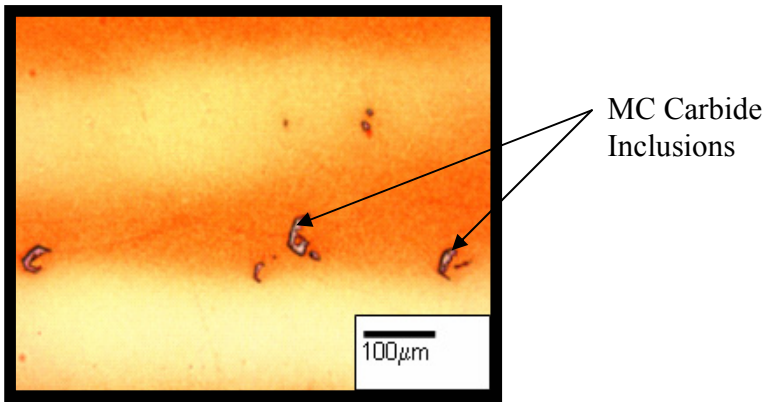

Figure 0.3 Optical microscopic image of MC carbide in the untested material (Trexler, 2004).

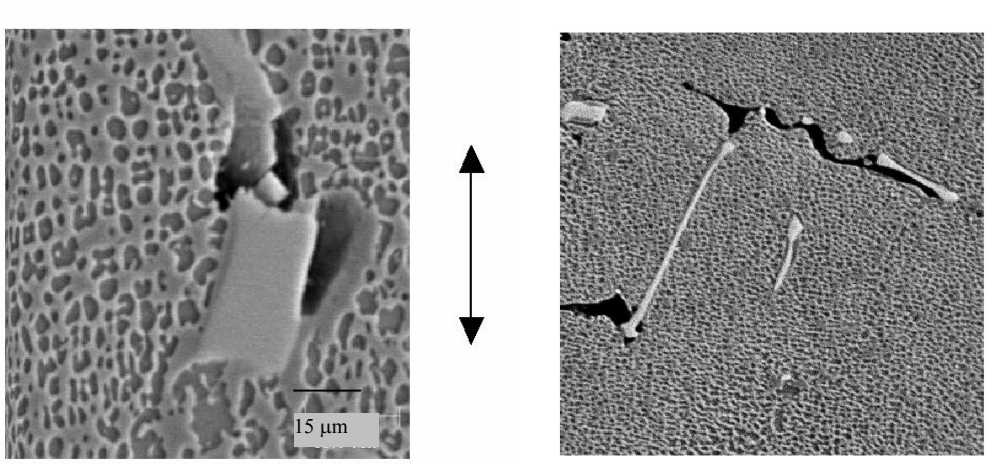

(a) (b)

Figure 0.4 (a) A cracked carbide inclusion in a specimen with loading along longitudinal orientation, and (b) carbide inclusions debonded from the surrounding matrix material (T=871ºC, ε_a =0.5%, $\dot{\varepsilon}$ =0.5% s^{-1}, R_ε =-1).

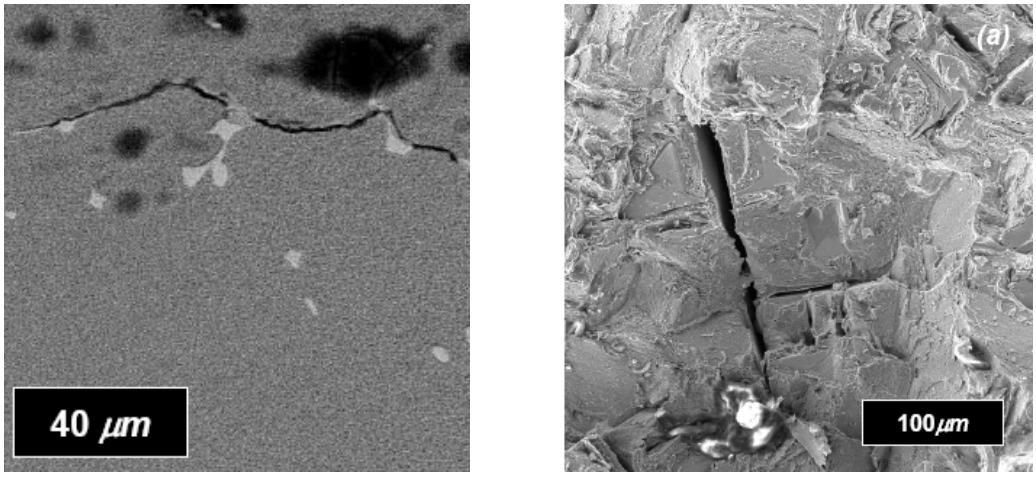

(a) (b)

Figure 0.5 Role of MC carbide inclusions as crack formation sites at 871°C, loaded along the transverse orientation (ε_a =0.25%, $\dot{\varepsilon}$ =0.5% s^{-1}, R_ε =-1).

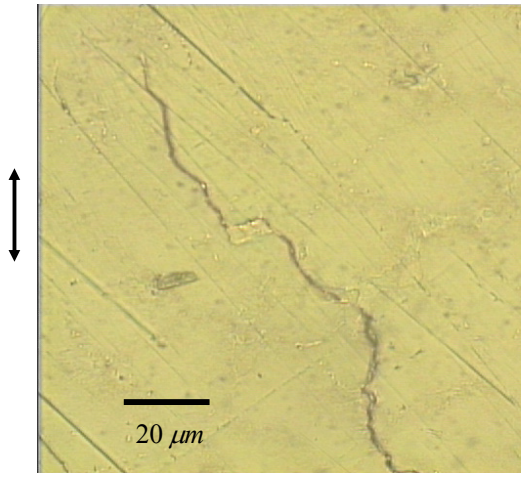

Figure 0.6 A crack formed at a carbide inclusion for the fatigue tested material at 650°C, loaded along the longitudinal orientation (ε_a =1.5%, $\dot{\varepsilon}$ =0.5% s^{-1}, R_ε =-1).

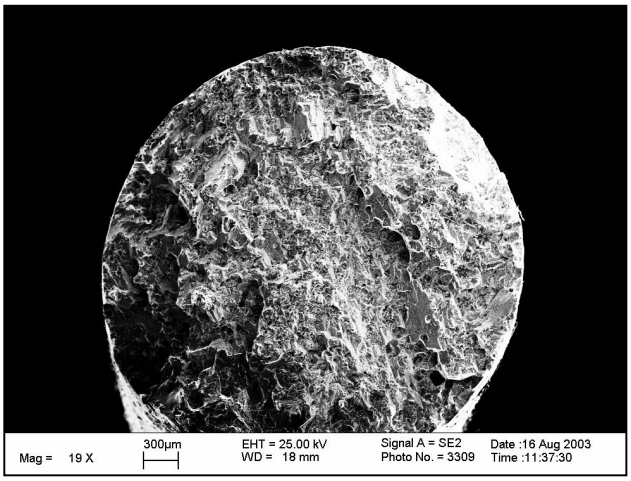

Figure 0.7 Typical fracture surface of the fatigue tested specimen (Trexler, 2004) (T=871ºC, ε_a =1%, $\dot{\varepsilon}$ =0.5% s^{-1}, R_ε =-1).

Experimental fatigue tests on DS GTD111 have been conducted by Gordon (Gordon, 2006) on uncoated smooth and Compact Tension (CT)-type specimens, with the specimen cycled to failure in uniaxial fatigue in both the longitudinal and transverse orientations. The details on the testing procedures, experimental observations and crack initiation life data can be obtained in Gordon's thesis (2006) and the work of Trexler (2004). The significant observations that can be made from these tests are summarized below:

- Microstructural observations of the fatigue specimens cycled in both the longitudinal and transverse orientations at the lower strain ranges show that the carbide inclusions play an important role in crack formation as shown in Figures 4.5-4.7. In the early stages of fatigue crack growth, subsurface carbides influence the direction of propagation. This is evidenced by the presence of carbides along the fracture surfaces and crack planes. Even though the volume fraction of

carbides is relatively low ($\leq$1-2%), a large volume fraction of carbides ($\approx$8%) have been observed along the fracture surface, suggesting their contributing role in crack initiation and propagation (Trexler, 2004).

- Sub-surface inclusion particles that were not in the vicinity of the external specimen surface were shown to be involved in the damage process by way of two separate mechanisms: (a) cracking of carbides and (b) debonding at the carbide-matrix interfaces. Figure 4.4a shows a MC type carbide inclusion that cracked internally and Figure 4.4b and 4.6 show debonded carbides. Aside from the damage that is localized at these inclusions, the microstructure of the specimen was virtually undisturbed.
- Experimental observations show that surfaces of longer cracks are surrounded by a thin layer of oxide ($\approx$4 μm) and a γ′ precipitate-free zone ($\approx$8 μm), suggesting that oxidation might also play a role in crack incubation and propagation at higher homologous temperatures. Of the fatigue tested specimens at 871°C, those conducted at the low mechanical strain ranges and low strain rates represent the most favorable opportunity for extensive oxide penetration to occur. However, limited oxide-assisted surface cracking occurred even in these cases (Gordon, 2006). Therefore, oxidation assisted crack surface cracking should be a major factor only at higher temperatures for surface cracks with oxygen ingress or for inclusions near uncoated surfaces, and hence will not be considered in this initial analysis of the early stages of LCF crack formation at inclusions.
- Casting pores and voids, which could be sites for fatigue crack formation, are observed but to a much lesser extent.
- The large variation in size, orientation, distribution and aspect ratios of inclusions suggests a high probability that a critically oriented inclusion with a high aspect ratio is responsible for LCF crack formation.

The macroscopic fracture surface of a fatigued specimen normal to the loading axis is as shown in Figure 4.7. The rupture surface consists of many cleavage-like facets inclined to the loading axis, similar to the observations by Okazaki et al. (1990) on DS Rene′80 , which are inclined at an angle of 30-40° to the loading axis. This agrees well with the angle between the <100> loading orientation and the [111] planes, which shows that crystallographic slip plays an important role in fatigue crack growth in DS GTD111. A surface replication test was conducted at relatively high strain amplitude of 1.5% in the longitudinal orientation. Based on the surface replication tests, cracks were observed to form at the carbide inclusions, as shown in Figure 4.6. A relatively large number of cracks are observed at this high applied strain amplitude. The total crack initiation life is defined as a 20% drop in the peak stress, at which the cracks are expected to be 0.5-2 mm in length (Gordon, 2006). Beyond this point they are expected to coalesce, resulting in specimen failure.

4.4 Constitutive Model

The crystal plasticity based model formulated in Chapter II is adopted for the constitutive modeling of the homogenized matrix and precipitate phases. This framework naturally captures the orientation dependent anisotropic response of the grains and therefore can be used to evaluate the variability in crack initiation life due to grain orientation. Since the inclusions considered are substantially larger than the γ' sizes, the homogenized description is appropriate. The details of the model are described in Chapter II. The MC carbide inclusions are modeled as a linearly elastic material with a Young's modulus of 405 GPa and a Poisson's ratio of 0.14 (Kozaczek et al., 1995; Kral et al., 1998).

4.5 Driving Forces

Fatigue life in Ni-base superalloys is composed of crack initiation and propagation. Fatigue crack initiation life can comprise a significant proportion of the fatigue life, in high cycle fatigue (Fleury and Remy, 1993; Fleury and Remy, 1994; Chen et al., 1997). Crack initiation can be broadly separated into phases of crack formation, microstructurally small crack growth and physically small crack growth. While the growth of long cracks can be adequately described by essentially the Paris equation perhaps modified for R-ratio effects and crack growth history effects, small crack behavior is not characterized well by LEFM (Suresh, 1998). Microstructurally small crack growth may be associated with some limiting situation that violates continuum approximations or similitude. Local microscopic heterogeneities such as grain boundaries, γ' precipitates and inclusions can affect the crack path and their rate of crack advance. Deformation of small flaws submerged within individual grains is dictated by crystal plasticity and the crystallographic growth of these flaws promotes mixed mode conditions at the crack tip.

4.5.1 Crack Incubation

Fatigue crack incubation life refers to the number of cycles required for a microstructurally small crack to form. In the case of precracked and/or debonded inclusions, this refers to the number of cycles for the crack to form and grow outside the influence of the notch root plastic zone. Various stress/strain-based damage parameters have been suggested for predicting crack incubation life. Multiaxial fatigue criteria with critical plane approaches such as Smith-Watson-Topper (SWT) (Smith et al., 1970) and

Fatemi-Socie (FS) (1988) have demonstrated superior predictive capabilities in modeling fatigue crack formation (McDowell, 1996a). The FS parameter is given as

$$P_{FS} = \frac{\Delta\gamma^{p}_{max}}{2}\left(1 + K^{*}\frac{\sigma_{n}^{max}}{\sigma_{y}}\right) \tag{4.1}$$

where $\Delta\gamma^{p}_{max}/2$ is the maximum plastic shear strain amplitude, and σ_{n}^{max} is the maximum normal stress on the plane of maximum shear strain amplitude, normalized by the cyclic yield strength σ_{y}. The SWT parameter is given as

$$P_{SWT} = \frac{\Delta\varepsilon_{max}}{2}\sigma_{max} \tag{4.2}$$

where $\Delta\varepsilon_{max}/2$ is the maximum normal strain amplitude and σ_{max} is the maximum normal stress acting on this plane during a cycle. The FS and SWT parameters can be related to the crack incubation life using modified Coffin-Manson laws. The FS and SWT parameters display mean stress dependence, which primarily reflects the dependence of small crack propagation on crack opening stress (Goh, 2002).

Fatigue crack formation at inclusions and notches is often associated with the development of persistent slip bands (PSBs) and is mainly dominated by slip irreversibility. A crack incubation criterion based on the critical notch depth by random slip in PSBs was proposed by Cheng and Laird (1978) in which the crack incubation life

is controlled by the maximum cyclic plastic shear strain amplitude, $\Delta\gamma_p^{max}/2$. This can be related to the crack incubation life using a modified Coffin-Manson relation, i.e,

$$\frac{\Delta\gamma_p^{max*}}{2} = \gamma_f' \left(2N_{inc}\right)^{c'} \tag{4.3}$$

where $\Delta\gamma_p^{max*}/2$ is averaged over a relevant notch root domain, N_{inc} is the crack incubation life and γ_f' and c' are constants. It should be noted that the crack incubation life is small at elevated temperatures (>900°C) and high strain amplitudes ($>\varepsilon_y$) in Ni-base superalloys (Reger and Remy, 1988; Fleury and Remy, 1993).

4.5.2 Small Crack Growth

When the crack forms it is said to be a microstructurally small crack (MSC), if the crack length or cyclic plastic zone size is on the order of key microstructural features. Fatigue crack growth in the MSC regime cannot be characterized based on the conventional linear elastic fracture mechanics (LEFM) driving forces such as the cyclic stress intensity parameter (ΔK) or the elastoplastic fracture mechanics (EPFM) driving force (ΔJ) due to lack of similitude (Suresh, 1998). On the other hand, the cyclic crack tip displacement (ΔCTD) is a good measure of the driving force for MSC propagation rate (Lankford et al., 1984). The advantage of using this as the driving force is that it naturally reflects the influence of the microstructure and accurately captures the crack tip plasticity conditions. It also merges naturally with ΔK mechanics as the crack lengthens. The disadvantage is that ΔCTD can depend on the microstructure in a complicated way.

The ΔCTD parameter can be related to the fatigue crack propagation rate as follows (Donahue et al., 1972; Fan et al., 1999; McClintock, 1999).

$$\left.\frac{da}{dN}\right|_{msc} = C\left(\Delta CTD - \Delta CTD_{Th}\right) \tag{4.4}$$

where ΔCTD_{Th} refers to the threshold for crack propagation and C is the slip irreversibility factor. It should be noted that creep and environmental effects play an important role in determining the fatigue life at elevated temperatures but will not be considered in this particular phase of the study.

4.6 Computational Micromechanics Approach

The formation of cracks in low cycle fatigue (LCF) is dominantly related to the cyclic plastic shear strain range, as well as the local stress state. A range of microstructural parameters, applied loading conditions and material properties affect the local cyclic plastic strain localization in the neighborhood of an inclusion that is stiffer than the matrix. Relevant microstructural parameters include:

1. Elastic stiffness and strength of inclusions.
2. Elastic and inelastic properties of the matrix.
3. Geometric attributes of inclusions – size, shape (aspect ratio).
4. Spatial distribution of the inclusions – nearest neighbor distance of large inclusions, including correlation of position with respect to grain boundaries and free surfaces.
5. Crystallographic orientation of the grain in which the inclusion lies as well as that of the neighboring grain(s) (i.e., misorientation).

6. Integrity of inclusion and matrix-inclusion interface (i.e., perfectly bonded, partially debonded, fully debonded, or cracked inclusion).

In addition to these microstructural parameters, loading parameters such as the amplitude of the applied strain and (strain) ratio, R_ε , can significantly affect the fatigue crack formation life. Due to the large number of parameters involved, it is computationally prohibitive to simulate all the permutations and combinations of different parameters. Furthermore such a study is not warranted because fatigue cracks form at the most severe inclusions. Hence, only the extreme characteristics of microstructure features such as inclusions are considered. In this work a range of critical microstructural and loading parameters are identified to focus the parametric studies.

Three different conditions for inclusions are considered: completely intact with the matrix, cracked, and partially debonded from the matrix. Even though voids have been observed to play a role in fatigue, they typically offer less intensification of local cyclic plasticity than partially debonded inclusions that have higher elastic stiffness than the matrix (McDowell et al., 2003). Computational analyses have shown that the maximum range of cyclic plastic shear strain for the partially debonded inclusion is much higher than that of either the cracked or intact inclusion cases. The maximum range of cyclic plastic shear strain computed for the intact inclusions is an order of magnitude lower than those of the other two cases, while those computed for the debonded inclusions are about three to four times those for the cracked inclusions. From this analysis, it is concluded that the partially debonded inclusion offers the most conservative scenario for assessment of LCF potency. This is consistent with the results obtained by McDowell et al. (McDowell et al., 2003)and Gall et al. (2001). The inclusion is assumed to be elliptical in shape with a representative aspect ratio, $A_r = c/b = 4$, unless otherwise specified, where c and b are the semi-major and semi-minor dimensions of the ellipse, respectively (Figure

4.8). The crystal orientation [100] coincides with the loading direction, which is normal to the major axis of the inclusion for the initial runs for displaying the framework.

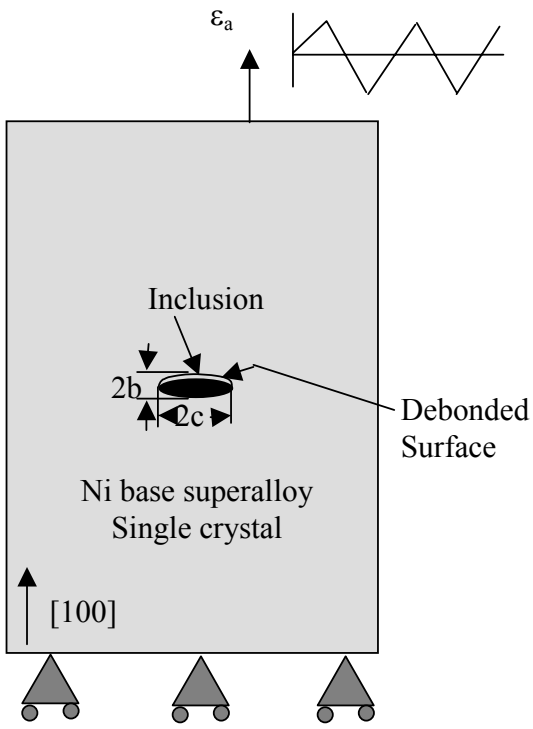

Figure 0.8 A schematic showing a partially debonded elliptical inclusion in a single crystal loaded in the [100] direction.

4.7 Relevant Length Scales and Driving Forces

4.7.1 Cyclic Plastic Shear Strain Range

The cyclic plastic shear strain range is essential to the evaluation of LCF potency of inclusions. The lower bound on the length scale over which the nonlocal maximum plastic shear strain range should be averaged can be associated with the minimum slip length over which fatigue cracks might nucleate due to the classical PSB formation (Venkataraman et al., 1990; Venkataraman et al., 1991). The lower bound may range from about 300 nm to 1000 nm and effectively establishes the minimum FE mesh size for the calculation of slip within the matrix to be associated with fatigue crack formation. It is noted that the micronotch root *maximum* plastic shear strain range is mesh-sensitive (increases with a decrease in element size), and it is also necessary to introduce a nonlocal volume averaging procedure over integration points in the mesh to effectively remove mesh dependence. Moreover, because the process zone for crack formation is finite, such a procedure is physically justified. Accordingly, local (pointwise) measures of cyclic plastic strains are not used in this fatigue life estimation scheme.

4.7.2 Non Local Averaging Area

An arbitrary averaging area could be used for a non-local averaging area relative to the inclusion or micronotch size; however, crack growth analyses are conducted to get a better estimate. The non-local averaging area is conveniently chosen as the area beyond which the cyclic crack tip displacement range (ΔCTD) is not influenced by inclusion

micronotch root field. Cracks growing from the partially debonded inclusions are conducted and the ΔCTD values are calculated as a function of the crack length.

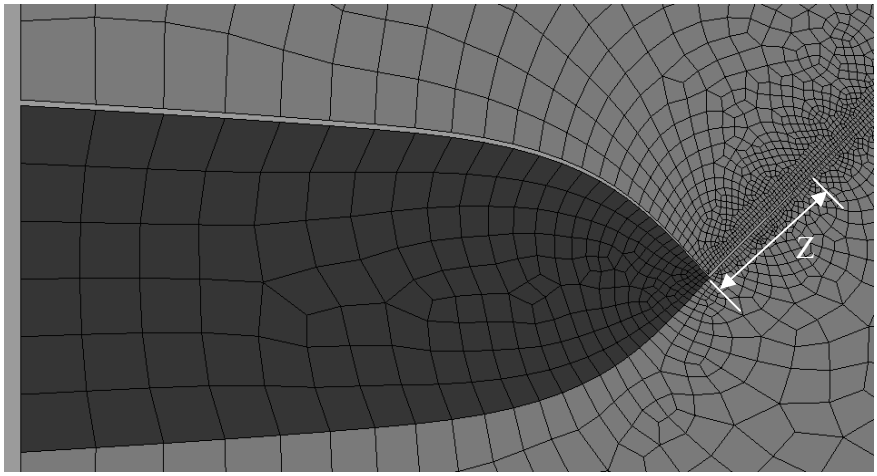

Figure 0.9 Finite element mesh for the crack growth analysis with crack at 45°.

A 2-D finite element model is constructed with a prescribed crack path at 45° from the partially debonded inclusion, as shown in Figure 4.9. Four-noded bilinear generalized plane strain elements (CPEG4) are primarily used for modeling; three-noded generalized plane strain elements (CPEG3) are also used to enable a smooth mesh transition. A frictionless surface-to-surface contact is used to model all contact interfaces. Stationary cracks are used (i.e., cracks do not contain effects of prior growth history) because propagating a crack would require a critical condition for releasing the node along the crack front, in addition to the enormous computational costs involved. Stationary cracks can provide a certain level of understanding of the dependence of crack tip driving forces on microstructure (Bennett, 1999a).

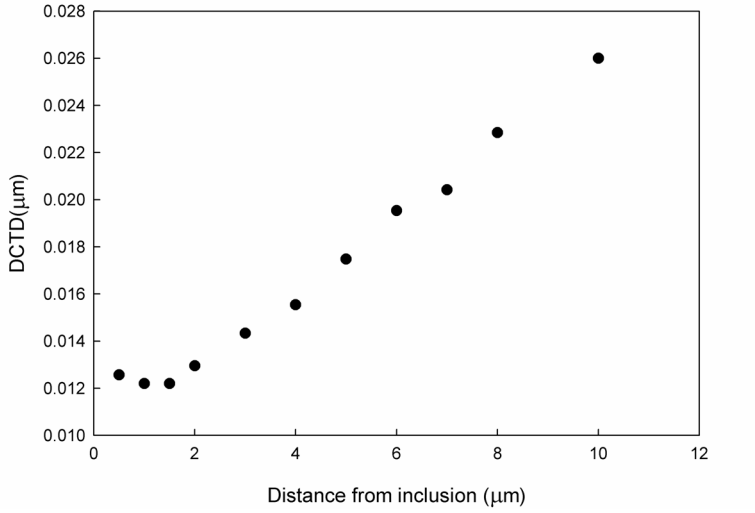

Figure 0.10 Plot of the cyclic crack tip displacement as a function of the crack length from the inclusion.

An ellipsoidal inclusion (major axis=20 μm, A_r=4, i.e., D=10 μm as defined by Eq.(4.8)) is used and the crack length is varied from $\frac{z}{D}=0.025$ to $\frac{z}{D}=1$, where z is the crack length measured from the inclusion notch as shown in Figure 4.10. The cyclic crack tip displacement (ΔCTD) is calculated 0.1 μm behind the crack tip for each crack length; details on this calculation can be obtained in the thesis by Bennett (1999a). The cyclic crack tip displacement varies as a function of the crack length as shown in Figure 4.10. From this figure, the cyclic crack tip displacement increases almost linearly with the crack length except when the crack length is very small. Therefore, the crack is affected by the stress field at the notch only for a crack length approximately equal to 2 μm, which corresponds to around 5% of the inclusion area. This is in agreement with the values suggested by McClintock (1999). It is acknowledged that the area of the influence due to the notch stress gradient will be affected by the inclusion shape and the notch radius. However, the objective is to get an approximate estimate of this averaging area

which is consistent, and is therefore kept constant (= 5% of the equivalent inclusion area) for all the subsequent analyses.

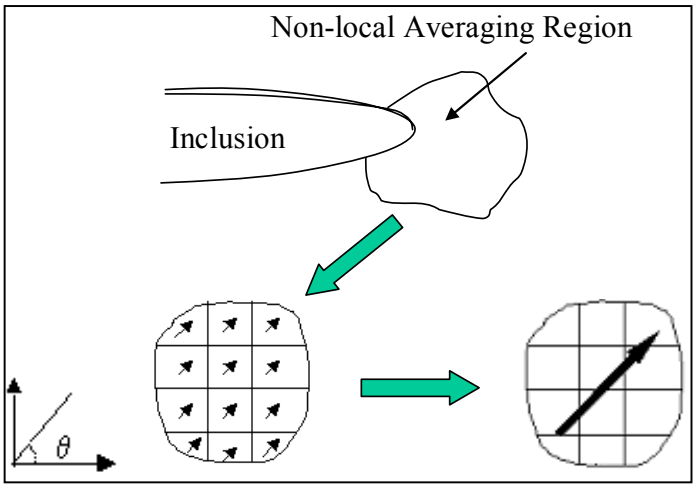

Figure 0.11 Non-local averaging area used for calculating $\Delta\gamma^{p*}_{max}$.

The average maximum plastic shear strain is calculated over 5% of the inclusion area. At each integration point lying within the nonlocal averaging region, a set of planes (directions) 10-degrees apart are considered. The plastic shear strain γ^p_θ on plane-θ is calculated by projecting onto it the plastic strain tensor ε^p_{ij} at each integration point, i.e.,

$$\frac{\gamma^p_\theta}{2} = n_i \varepsilon^p_{ij} t_j \qquad \theta = 1 \ldots N \tag{4.5}$$

where n_i is the unit normal vector on plane-θ, t_i is a unit tangent vector in the considered direction along this plane, and N is the number of discrete planes. The nonlocal average plastic shear strain associated with the θ-plane is calculated by

averaging the plastic shear strain on the θ-plane over the area A of the nonlocal region as shown schematically in Figure 4.11, i.e,

$$\gamma_\theta^{p*} = \frac{1}{A}\int_A \gamma_\theta^p dA \tag{4.6}$$

The nonlocal cyclic plastic shear strain range for each plane (averaged over area A) is then calculated using this expression in the third cycle of the simulation. The maximum of the range of γ_θ^{p*} amongst all planes is taken to be the nonlocal maximum cyclic plastic shear strain range, i.e.,

$$\Delta\gamma_{max}^{p*} = \max_\theta\left(\Delta\gamma_\theta^{p*}\right) \tag{4.7}$$

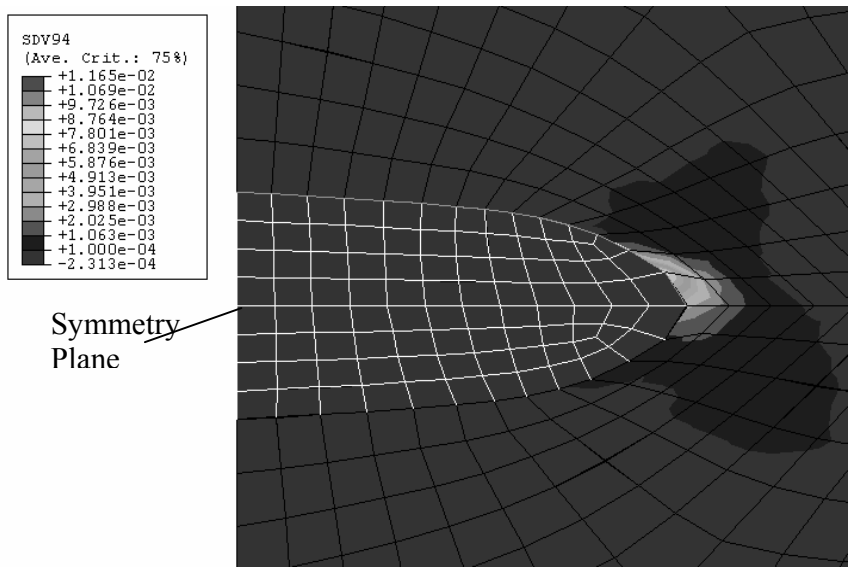

Figure 0.12 Contours of effective plastic strain (3rd cycle) at an applied strain amplitude of 0.3% (R_ε = -1 at 871°C, longitudinal orientation).

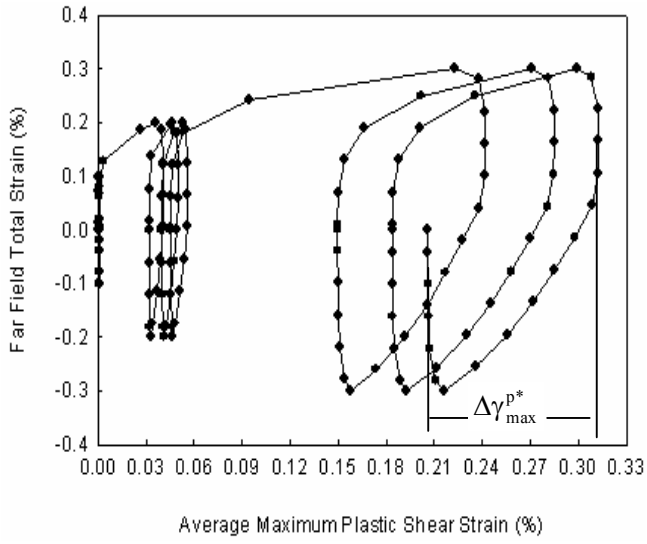

Figure 0.13 Applied strain versus nonlocal (average) maximum plastic shear strain at notch root of partially debonded inclusion (R_ε = -1 at 871°C, longitudinal orientation).

To study the variation of $\Delta\gamma^{p*}_{max}$ with the mesh size, a single partially debonded inclusion ($A_r = 4$) is analyzed at three different applied uniaxial strain amplitudes, $\varepsilon_a = 0.5(\varepsilon_{max} - \varepsilon_{min})$: 0.1%, 0.2% and 0.3% in the longitudinal orientation at R_ε = –1. Different meshes with element size (length) varying from D/8 to D/16 are considered, where D is the equivalent inclusion diameter, to be defined later. A typical mesh is shown in Figure 4.12. The plot in Figure 4.12 shows the contours of effective plastic strain $\left(\varepsilon^p_{eff} = \sqrt{(2/3)\varepsilon^p_{ij}\varepsilon^p_{ij}}\right)$. Note that due to symmetry, only half of the domain shown in Figure 4.7 is analyzed.

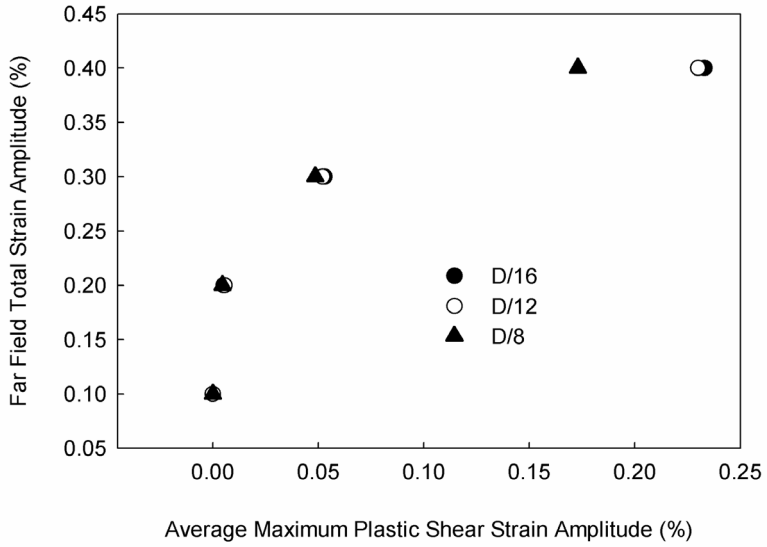

Figure 0.14 Effect of minimum element size on nonlocal (average) maximum plastic shear strain amplitude $\Delta\gamma^{p*}_{max}/2$ (R_ε = -1) at the notch root of a partially debonded inclusion of diameter D (T=871°C, longitudinal orientation).

The nonlocal maximum plastic shear strain amplitude $\Delta\gamma^{p*}_{max}/2$ is calculated over the stabilized third cycle, as shown in Figure 4.13. The contiguous area (=5% of the inclusion area) is chosen in the notch-root region to enclose the highest $\Delta\gamma^{p*}_{max}/2$. Results for effect of three different mesh sizes on average maximum plastic shear strain amplitude are shown in Figure 4.14; the nonlocal measure of maximum plastic shear strain shows good convergence characteristics and insensitivity to mesh size so long as the minimum element size is roughly an order of magnitude smaller than D.

The size of an incubated crack at the root of an inclusion will be assumed to be proportional to inclusion diameter, following the concept of transition crack length from fracture mechanics (Smith and Miller, 1977; Chan and Enright, 2005). The $\Delta\gamma^{p*}_{max}/2$ averaged over the notch root area provides a measure of driving force to form cracks on the order of transition length, beyond which the effective crack length exceeds the inclusion diameter.

4.7.3 ℓ / d *parameter*

In addition to the length-scale discussed above for physically based averaging of $\Delta\gamma^{p*}_{max}/2$, it is necessary to introduce another length scale parameter, ℓ/D, that reflects the spatial extent, ℓ, of cyclic plasticity at the inclusion. This non-dimensional parameter is introduced for purposes of estimating whether or not a crack will form that can grow beyond the influence of the notch, effectively establishing whether cyclic plasticity is constrained to the notch root (ℓ/D <<1) or if the inclusion is embedded within far-field cyclic plasticity (ℓ/D >1). It is arbitrarily (but consistently) defined as the ratio of the area to the perimeter of a region in which the cyclic plastic shear strain amplitude is greater than some prescribed value (Gall et al., 2001; McDowell et al., 2003), i.e.,

$$\ell = \frac{A}{P} \quad \text{and} \quad D = \sqrt{\frac{4A_{inc}}{\pi}} \tag{4.8}$$

Note that D is defined as the equivalent diameter of an inclusion with area A_{inc}; A is the area of a contiguous matrix region around the inclusion from which the maximum plastic shear strain is $\geq 0.01\%$, and P is the perimeter of this area. It is noted that D is defined in a manner similar that adopted in the approach of Murakami and colleagues (Murakami, 1994; McEvily et al., 2003), which has proven quite robust and useful in applications.

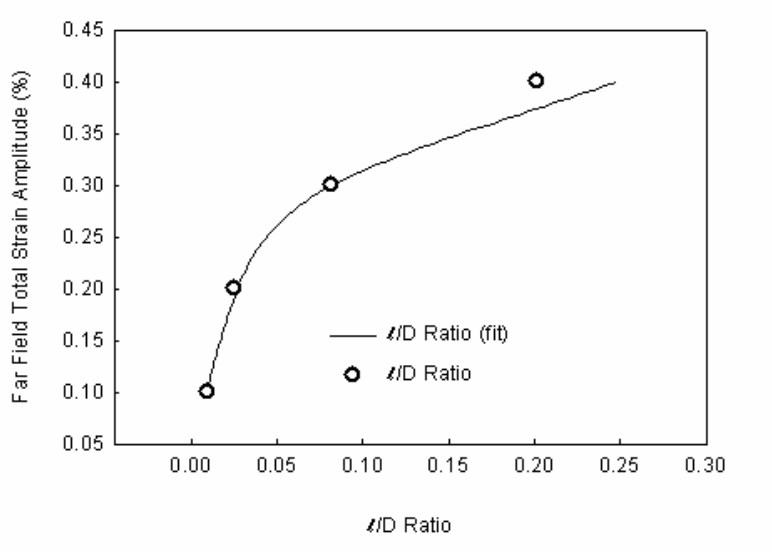

Figure 0.15 Computational results for ℓ/D as a function of applied strain amplitude for cyclic loading with R_ε = -1 for a debonded center inclusion with an aspect ratio of 4:1, T=871ºC, longitudinal orientation.

Figure 4.15 presents ℓ/D as a function of the applied far field strain amplitude; ℓ/D values are calculated based on the third cycle value of the cyclic plastic shear strain amplitude for different simulations of a debonded center inclusion shown in Figure 4.8. Open circles represent the finite element results and the curve-fit is given by

$$\frac{\ell}{D} = 0.0029 \exp\left(\frac{22.25\varepsilon_a}{1 - R_\varepsilon}\right) \tag{4.9}$$

Based on the non-dimensional scale parameter, ℓ/D, three regions are identified by McDowell et al. (1999): constrained microplasticity ($\ell \ll D$), unconstrained microplasticity ($\ell \approx D$), and limit plasticity (($\ell \gg D$), extensive far field plasticity). The condition of macroscopic yielding and plastic flow is essentially a manifestation of percolation of microplasticity throughout the entire microstructure, i.e., reaching the limit

plasticity regime. The practical regime of constrained microplasticity for which $\ell/D < 1$, as shown in Figure 4.14, is of most interest in the case of HCF.

4.8 Algorithm for Crack Incubation Life

The nonlocal maximum cyclic plastic shear strain amplitude $\Delta\gamma^{p*}_{max}/2$ is used to estimate the number of cycles, N_{inc}, required to form and propagate (i.e., "incubate") a crack of dimension on the order of the domain of influence of the micronotch root, which is proportional to the inclusion size. A notch root Coffin-Manson law is applied for this purpose, i.e.,

$$\beta \equiv \frac{\Delta\gamma^{p*}_{max}}{2} = C_{inc}\, N^{\alpha}_{inc} \qquad (4.10)$$

where α and C_{inc} are material dependent parameters. The formulation of a nonlocal Coffin-Manson law at the microstructure-scale is consistent with rigorous energetic arguments based on slip irreversibility (Venkataraman et al., 1990; Venkataraman et al., 1991) and energy release associated with creation of the crack. The exponent α in Eq. (4.10) is estimated using a regression fit of experimentally determined macroscopic plastic shear strain versus fatigue crack initiation life data for uniaxial fatigue (R_ε=-1), as shown in Figure 4.16. Definitions of fatigue crack initiation life based on different final crack lengths that are all relatively small (<1 mm), typically manifest little variation in slope α, but rather shift the curve horizontally. Coefficient C_{inc} is estimated by fitting the total fatigue crack initiation life data for the case of a center inclusion with a severe aspect ratio ($A_r = 150$, $\varepsilon_a = 0.5\%$, R_ε=-1, T=871ºC). Incubation life N_{inc} in this case is assumed to be 2% of the total fatigue crack initiation life $N_i = N_{inc} + N_{small,prop}$, at the

strain amplitude $\varepsilon_a = 0.5\%$, since N_i is dominated by small crack propagation life $N_{small,prop}$ at high strain amplitudes; this is consistent with literature on other Ni-base superalloys (Smith and Miller, 1977). Strain ratio dependence is explicitly embedded in C_{inc} (McDowell et al., 2003). These parameters are estimated as $C_{inc} = 19.0\left(1 - \langle R_\varepsilon \rangle\right)$ and α = -0.663. In these relations, the strain measures β and ε_a are expressed in percent.

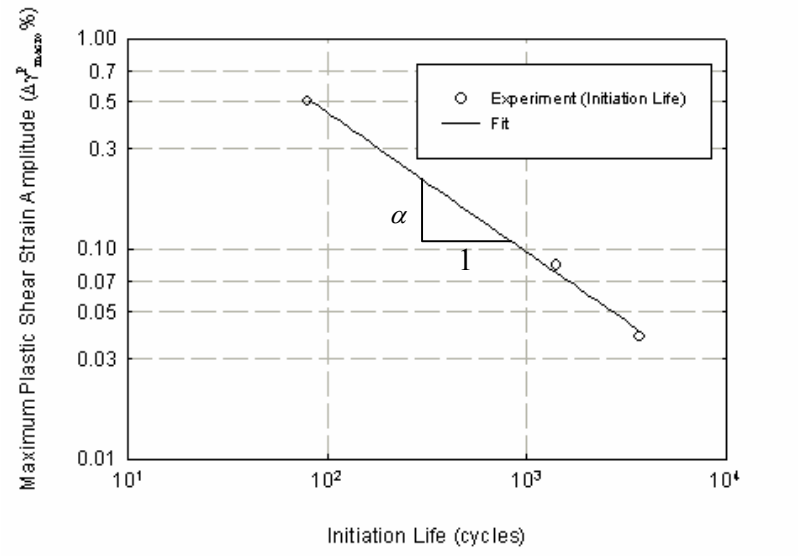

Figure 0.16 Slope α from macroscopic fatigue crack initiation data for use in notch root Coffin-Manson law ($R_\varepsilon = -1$, $\dot{\varepsilon} = 0.5\%\ s^{-1}$,T=871ºC) in Eq. (4.10).

4.9 Parametric Simulations to Determine β

In order to use Eq. (4.10) to determine the incubation life, the nonlocal maximum plastic shear strain amplitude (β) for a given microstructure must be determined (or range of such β values subject to stochastic analysis). In an actual microstructure, inclusions of various sizes and aspect ratios are present. Furthermore, some of the inclusions might be clustered and hence their interaction may affect the nonlocal maximum plastic shear

strain. Inclusions are also found near the free surface, which promotes shear localization and can lead to premature fatigue crack formation. In addition, the applied R_ε ratio affects the intensity of cyclic plastic shear strain at the notch root, especially when the inclusions are partially debonded. This is due to the contact interaction between the inclusion and the surrounding material. We do not know a priori which of these scenarios would be most critical. Hence, parametric studies are conducted to determine the maximum plastic shear strain amplitude (β) as a function of these parameters. Then, information regarding inclusion populations in actual materials can be evaluated using these relations to assess probabilities of failure based on distribution functions for defect number densities, sizes, shape, clustering, surface proximities, etc.

Parametric simulations are specifically conducted with respect to inclusion aspect ratio, spacing and the proximity to the free surface. Only partially debonded inclusions are considered in the parametric analyses since they produce the highest degree of notch root strain intensification. Based on the results of the parametric simulations, correlations are developed to relate the applied strain amplitude and applied R_ε ratio to the nonlocal maximum plastic shear strain amplitude as a function of microstructural parameters such as distance to free surface, nearest neighbor distance, etc. With these correlations, the potency of various kinds of representative inclusions to form HCF cracks can be assessed. Of course, microstructurally small crack propagation relations must also be introduced in order to obtain estimates of crack initiation life (incubation plus small crack propagation to a pre-defined length of 0.5 mm to 1 mm). The aim of these functions is to quantify the range of fatigue crack initiation lives based on the distribution of microstructural defects, thus serving as an aid in designing the material to achieve enhanced fatigue resistance (i.e., shifting the mean) or to achieve less sensitivity of fatigue crack initiation life to defects (decreasing the variability).

Finite element analyses are conducted using a generalized plane strain approximation with fully 3D constitutive relations. Periodic boundary conditions are not used, but the

window size used for analysis is sufficiently large to avoid effects of surfaces on the deformation behavior near the inclusion (except when quantifying the effects of proximity to the free surface). Four-noded bilinear generalized plane strain elements (CPEG4) are primarily used for modeling; three-noded generalized plane strain elements (CPEG3) are also used to enable a smooth mesh transition. Symmetry considerations are employed to reduce analysis time. A frictionless surface-to-surface contact is used to model all debonded inclusion-matrix interfaces.

4.9.1 Effects of R_ε - Ratio

A partially debonded center inclusion is considered (Figure 4.8), with an aspect ratio of $A_r = 4$. Finite element simulations are conducted for three applied strain amplitudes of 0.1%, 0.2% and 0.3%. For each of these strain amplitudes, three different strain ratios are considered: $R_\varepsilon = 0$, 0.5 and -1. Results for β are presented in Figure 4.17 as a function of the applied strain amplitude; β exhibits a dependence on the applied strain ratio, R_ε, due to contact interaction between the inclusion and the surrounding matrix. A fit to the computational results for the debonded center inclusion is obtained as

$$\beta_{center} = \left(\frac{\Delta\gamma^{p*}_{max}}{2} \right)_{center} = \left(70 - 37\left|R_\varepsilon\right|\right)\left(\varepsilon_a - 0.0375\left(1 - R_\varepsilon\right)\right)^{4.35} \qquad (4.11)$$

In Figure 4.17, β increases with an increase in the remote tensile mean strain for the debonded inclusions. The yield strain for this material is nearly 0.35%; thus, appreciable cyclic microplasticity is evident even for applied strains well below the macroscopic yield point.

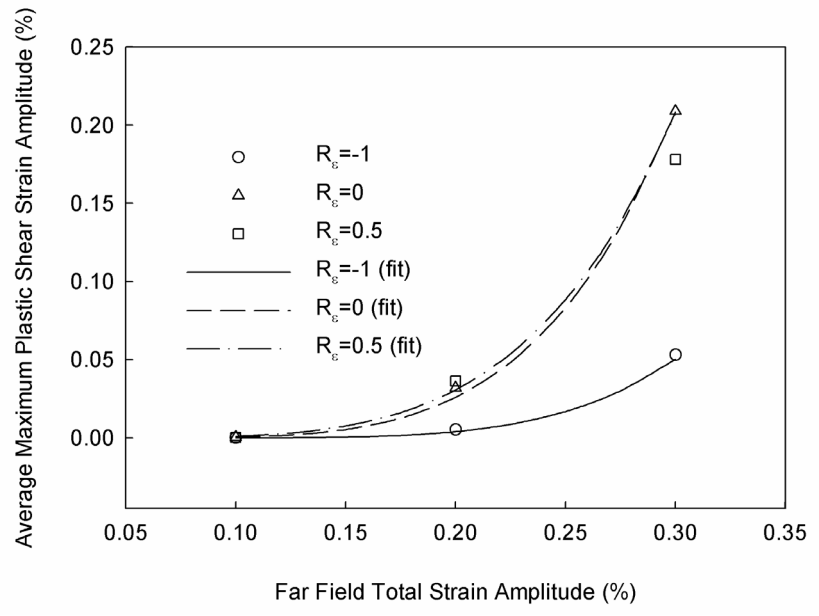

Figure 0.17 Nonlocal average maximum plastic shear strain amplitude β for various applied strain amplitudes and R_ε ratios of a debonded center inclusion (T=871ºC, $\dot{\varepsilon} = 0.5\%\ s^{-1}$, longitudinal orientation).

4.9.2 Effects of Aspect Ratio (A_r*)*

It is seen from optical and SEM images such as those in Figures 4.3 and 4.4 that the inclusion size varies from 2-150 μm and inclusion aspect ratios can be as high as 150:1. In order to quantify the effects of the aspect ratio on crack incubation, the inclusion aspect ratio (A_r) is varied from 1:1 (circle) to 8:1 (ellipse) and the average micronotch maximum plastic shear strain amplitude is obtained using finite element simulations (T=871ºC, $\dot{\varepsilon} = 0.5\%\ s^{-1}$). Debonded inclusions with major axis perpendicular to the loading direction display the highest value of $\Delta\gamma^{p*}_{max}$ of all orientations. Hence, only partially debonded inclusions with major axis perpendicular to loading direction are considered. The notch root maximum plastic shear strain amplitude increases with an increase in the aspect ratio. Based on the computational results, a fit is obtained as

$$\beta = \frac{\Delta\gamma^{p*}_{max}}{2} = \left(\frac{\Delta\gamma^{p*}_{max}}{2}\right)_{center} \left(0.479\ln\left(A_r\right) + 0.336\right) \tag{4.12}$$

where $\left(\frac{\Delta\gamma^{p*}_{max}}{2}\right)_{center}$ is the nonlocal maximum plastic shear strain amplitude associated with the center inclusion with an aspect ratio $A_r = 4$, given in Eq. (4.11).

4.9.3 Effects of Proximity to Free Surface and Inclusion Spacing

The proximity of the inclusion to a free boundary (χ) and distance between two inclusions (δ) are studied to quantify their effects on nonlocal maximum plastic shear strain amplitude. The configuration used for the analysis is shown in Figure 4.18.

The contours of the effective plastic strain $\varepsilon^p_{eff} = \sqrt{(2/3)\varepsilon^p_{ij}\varepsilon^p_{ij}}$ at the end of the third cycle are shown in Figure 4.19a for the case in which $\chi = 0.5D$, whereas Figure 4.19b shows the contours for the neighboring inclusion case, $\delta = 0.5D$. In assessing the effects of nearest neighbor inclusions, a plane of symmetry exists midway between the two inclusions. Significant intensification of plasticity is observed for both cases, suggesting a large decrease in the LCF crack incubation life.

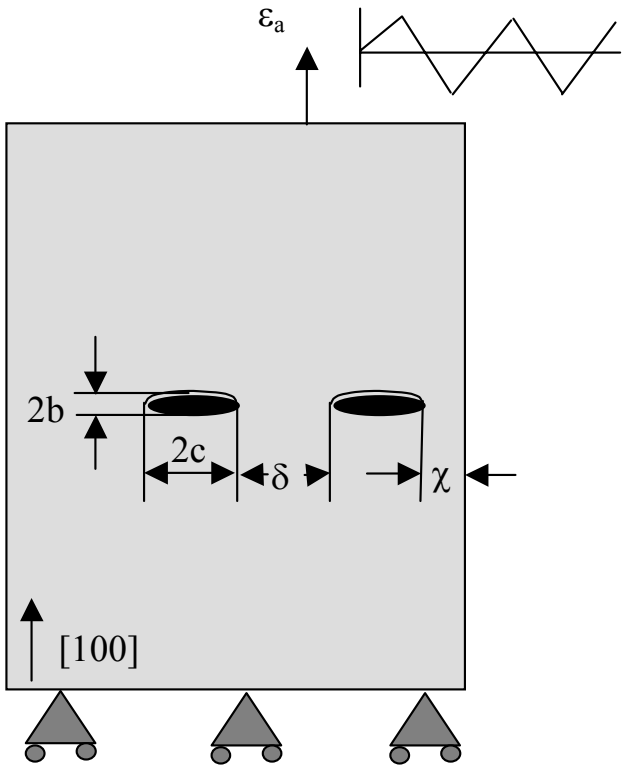

Figure 0.18 Configuration for studying inclusions near a free surface and effects of nearest neighbor inclusions.

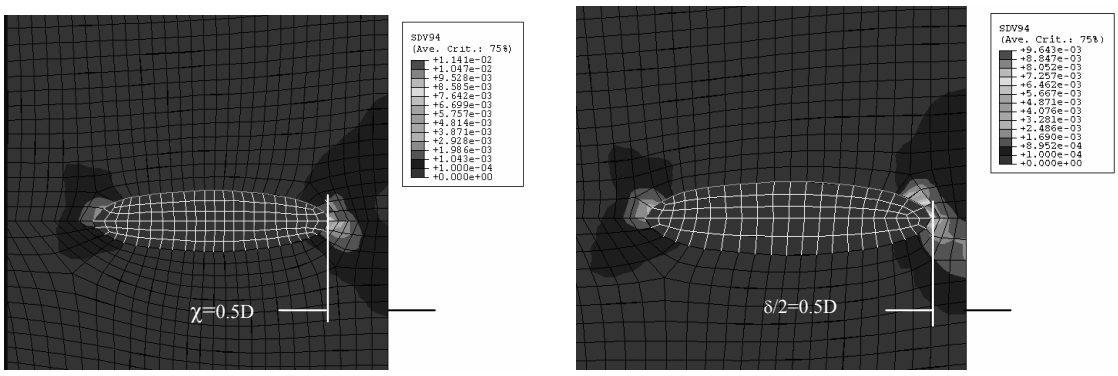

(a) **(b)**

Figure 0.19 (a) Contours of effective plastic strain (3rd cycle) to study free surface proximity effects, $\varepsilon_a = 0.3\%$, $R_\varepsilon = -1$; (b) Contours of effective plastic strain (3rd cycle) to study inclusion spacing effects ($\varepsilon_a = 0.3\%$, $R_\varepsilon = -1$, T=871ºC, $\dot{\boldsymbol{\varepsilon}} = 0.5\%\ s^{-1}$, longitudinal orientation).

The average maximum plastic shear strain amplitude β is plotted against the applied strain amplitude for various values of χ and δ in Figure 4.20. All the simulations are conducted at R_ε = -1 for inclusions with $A_r = 4$; "center" inclusion refers to a single inclusion at the center of the matrix, which is not subjected to finite boundary effects. Both increased proximity to the free surface and the decrease in distance between the two inclusions increase β. There is a significant increase of β when the inclusion spacing δ is less than D. Therefore, the crack incubation life is expected to significantly decrease with increasing proximity to the surface or other debonded inclusions.

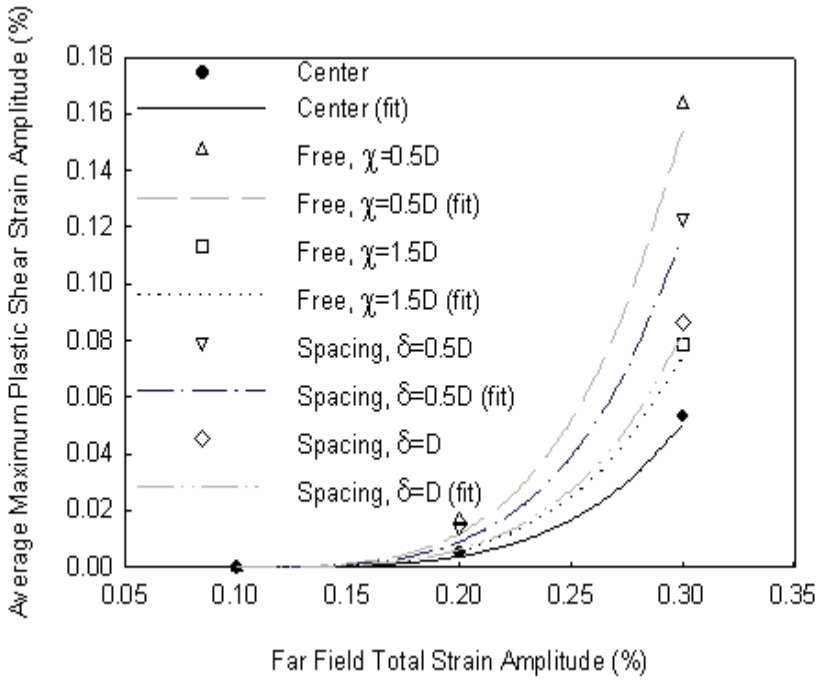

Figure 0.20. Nonlocal average maximum plastic shear strain amplitude for various spacings and free surface proximities (R_ε = -1, $A_r = 4$, T=871ºC, $\dot{\varepsilon} = 0.5\%\ s^{-1}$, longitudinal orientation).

The micronotch plastic shear strain intensification due to the free surface proximity and spacing effects are captured by fitting to computational results, respectively, i.e.,

$$\beta_{\chi} = \frac{\Delta\gamma^{p*}_{max}}{2} = \left(\frac{\Delta\gamma^{p*}_{max}}{2}\right)_{center}\left(1+4.30\exp\left(-1.4576\frac{\chi}{D}\right)\right) \quad (4.13)$$

$$\beta_{\delta} = \frac{\Delta\gamma^{p*}_{max}}{2} = \left(\frac{\Delta\gamma^{p*}_{max}}{2}\right)_{center}\left(1+2.78\exp\left(-1.4865\frac{\delta}{D}\right)\right) \quad (4.14)$$

where $\left(\frac{\Delta\gamma^{p*}_{max}}{2}\right)_{center}$ is given by Eq. (4.11), χ is the distance of the inclusion from the free surface and δ is the inclusion spacing distance (Figure 4.18).

4.10 Prediction of Crack Initiation Life

In this Section, Eq. (4.10) is used to predict the number of cycles necessary to incubate a fatigue crack with length on the order of inclusion size and then estimate the total initiation life by combining with a microstructurally small crack propagation relation. Compounding influences of oxidation effects are not considered here, but could be included if desired.

As previously mentioned, the fatigue crack incubation life is defined as the number of cycles required to form a crack at an inclusion and then grow to a point where it can be treated as a microstructurally or physically small propagating crack sufficiently long to include the inclusion diameter as part of the crack length i.e., the transition crack length (Smith and Miller, 1977; McDowell et al., 2003). The total crack initiation life is defined as the sum of the incubation life and the number of cycles required by the small crack to grow until it can be considered as a long crack (in the LEFM sense) under remote elastic loading, typically to a length of 0.5mm to 1 mm. An effective inclusion diameter D = 10 μm is used for all the analyses in this section. An aspect ratio of $A_r = 150$ is considered

to study the effect of this parameter on the incubation life. A specific distance from the free surface, $\chi / D = 0.5$, spacing of $\delta / D = 0.5$, and aspect ratio $A_r = 4$ are assumed for an inclusion to study the effect of extreme values of these parameters on the crack incubation life.

The predicted fatigue crack incubation life is shown in Figure 4.21 as a function of extreme values of several microstructural parameters and is compared to the experimentally measured fatigue crack initiation life (defined as the life for a 20% load drop or an equivalent crack length of 1mm (Gordon, 2006)). The initiation life includes small crack propagation as well as incubation, accounting for its location well to the right of the incubation curves in Figure 4.21. At longer lives, incubation consumes an increasing fraction of initiation life and the curves eventually converge. Increased proximity of the inclusion to the free surface is seen to be most critical, although it is apparent that inclusion spacing and aspect ratio effects are nearly equally deleterious.

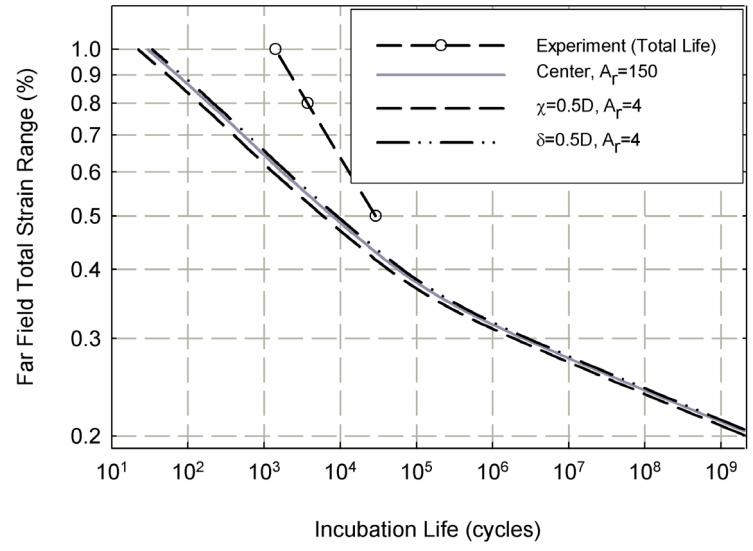

Figure 0.21 Effects of inclusion aspect ratio, spacing, and proximity to free surface on crack incubation life (R_ε=-1, T=871ºC, $\dot{\varepsilon} = 0.5\%\ s^{-1}$, longitudinal orientation); experimental data pertain to total initiation life (incubation plus propagation).

It should be noted that effects of spacing and aspect ratio compound, although not according to linear superposition. For example, a large debonded inclusion with a very high aspect ratio that is located close to a free surface, with its major axis oriented perpendicular to the loading direction and with a large inclusion nearby is always more likely to act as a crack formation site, thus lowering the life substantially. However, the general framework for analysis would remain the same. Furthermore the interactions would be of a secondary nature and crack incubation life would still likely be dominated by the most critical microstructural parameter.

The total fatigue crack initiation life of a specimen is the sum of the crack incubation life and the propagation life to a predefined crack length, in this case assumed to be 1 mm. The initial crack length is taken to correspond to a crack that is given by, a = c+0.25D, where c is the major axis radius of the inclusion and D is the equivalent diameter of the inclusion given by Eq. (4.8). Although the crack incubation life constitutes a major part of the total life in the high cycle fatigue (HCF) regime, small crack propagation plays the dominant role in conventional LCF. Once the microstructurally small crack is formed, the propagation life is estimated by assuming that the crack growth rate is proportional to the range of the crack tip displacement ΔCTD (Donahue et al., 1972), i.e.,

$$\frac{da}{dN} = \frac{1}{3}\left(\Delta CTD - \Delta CTD_{th}\right) \tag{4.15}$$

where an irreversibility factor of 1/3 is assumed. In reality it depends on slip irreversibility in secondary and tertiary γ'. For small fatigue crack growth through a particle system (2003),

$$\Delta CTD = C_{II}\left(\frac{\Delta\sigma}{(1-R)S_u}\right)^{4.43} a \qquad R < 0 \tag{4.16}$$

$$\Delta CTD = C_{II}\left(\frac{\Delta\sigma}{S_u}\right)^{4.43} a \qquad R \geq 0 \qquad (4.17)$$

The exponent 4.43 is chosen for consistency with long crack propagation relations (Ibanez, 2003). Also, C_{II} = 0.027 is estimated by fitting Eq. (4.16) to the experimental data for fatigue crack initiation life in Figure 4.21 (number of cycles to incubate a crack and then grow to a length of a = 1 mm) at $\varepsilon_a = 0.5\%$ for a center inclusion with A_r =150. The small crack propagation life is assumed to be 98% of the experimentally obtained initiation life, N_i, at this strain amplitude (Reger and Remy, 1988), as mentioned previously. The ultimate strength $S_u \approx 710$ MPa at 871°C. A threshold value for microstructurally small fatigue crack growth is assumed on the order of the Burgers vector, i.e., ΔCTD_{th} = 0.25 nm. Finally, $N_i = N_{inc} + N_{small,prop}$, where N_{inc} is obtained from Eq. (4.10) and $N_{small,prop}$ from integration of Eq. (4.16).

Several aspects of the results presented in Figures 4.22-4.24 are worth mentioning. First, the sensitivity to inclusion aspect ratio is much more pronounced in the LCF regime than inclusion spacing or surface proximity. Recall that the severe aspect ratio case of A_r = 150 was used to fit the experimental data in the high strain amplitude regime; much lower aspect ratios of A_r = 4 lead to a significant increase in total LCF initiation life due to decreasing initial crack size with decreasing aspect ratio. In the HCF regime, the total life is affected by both the surface proximity and inclusion spacing. Second, note that the applied total strain versus life curve has rather classical form, in spite of the use of only a microstructure-level Coffin-Manson relation for incubation, by virtue of both nonlinearity in the $\beta = \Delta\gamma^{p*}_{max}/2$ versus applied strain relation and small crack propagation near threshold conditions, $\Delta CTD \approx \Delta CTD_{th}$. This is also apparent for cast Al alloys (McDowell et al., 2003). It is noted that at an elevated temperature of 871°C, the ultimate strength is low enough that threshold conditions are not met even at long lives

under R_ε = -1 loading; oxidation effects, not explicitly addressed here, are known to further mitigate against thresholds.

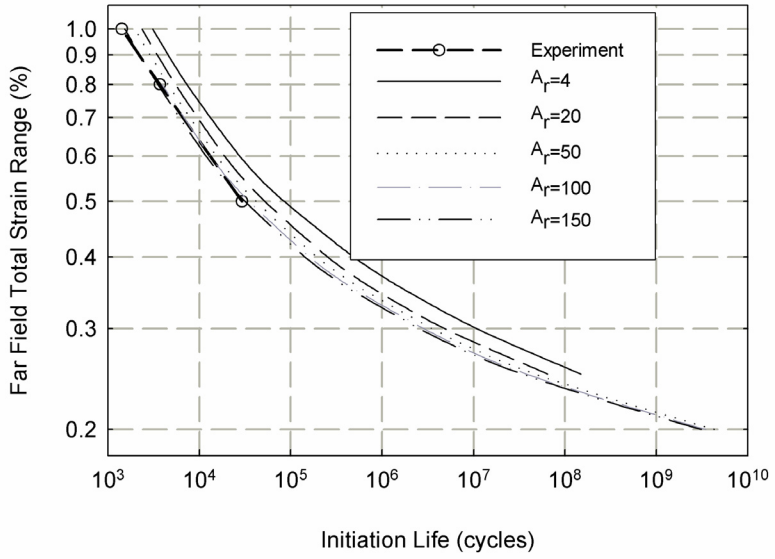

Figure 0.22 Effect of inclusion aspect ratio on total crack initiation life N_i (R_ε = -1, T=871ºC, $\dot{\boldsymbol{\varepsilon}} = 0.5\%\ s^{-1}$, center inclusion, longitudinal orientation).

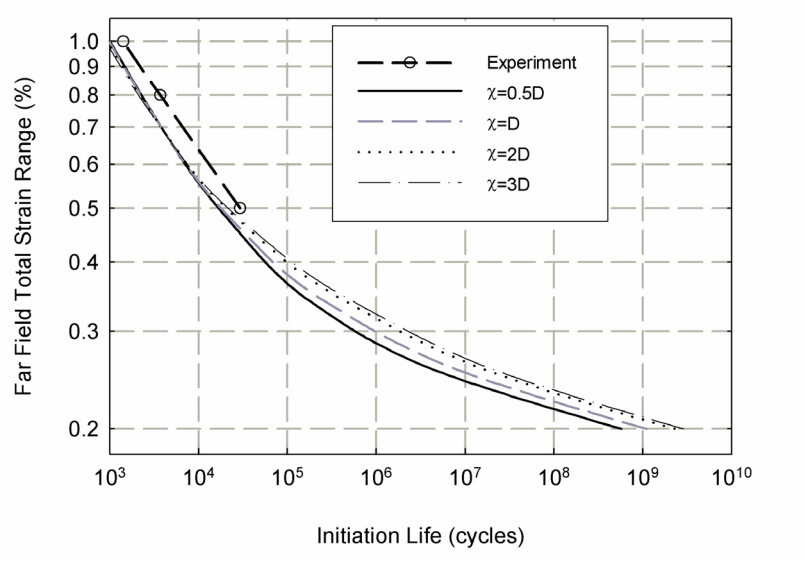

Figure 0.23 Effect of inclusion proximity to free surface (χ) on total crack initiation life N_i (R_ε = -1, A_r = 150, T=871ºC, $\dot{\boldsymbol{\varepsilon}} = 0.5\%\ s^{-1}$, longitudinal orientation).

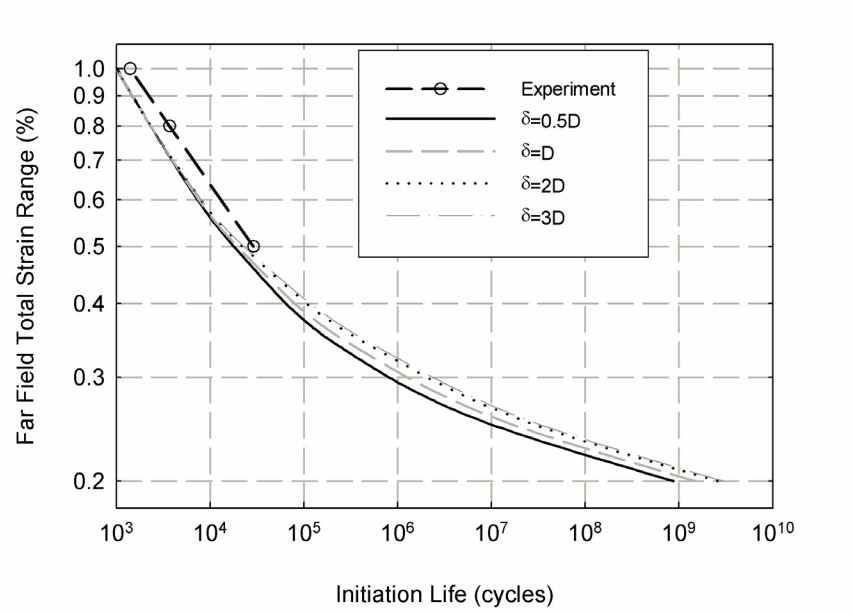

Figure 0.24 Effect of inclusion spacing distance (δ) on total crack initation life N_i (R_ε = -1, A_r = 150, T=871ºC, $\dot{\varepsilon} = 0.5\%\ s^{-1}$, longitudinal orientation).

4.11 Transverse Orientation

Experimental observations based on fatigue test in DS GTD111 in the transverse orientation (Trexler, 2004) show that the cracks mainly initiate at carbides located in the interdendritic regions inside the grains and near grain boundaries. The localized plastic zone at the inclusion notch in the transverse orientation is analyzed is this section.

4.11.1 Effect of Primary Grain Orientation

In the transverse orientation, the macroscopic stress-strain response is an average response from a number of grains; therefore any inclusion lying inside a grain would be subjected to the average far-field stresses. A partially debonded center inclusion (located

inside the grain) with an aspect ratio, $A_r = 4$, is analyzed in the transverse orientation, as shown in Figure 4.25. It is noted that the grains in DS GTD111 are relatively large (0.5-2 mm) and the neighboring grain orientations are not expected to play an important role in dictating the crack incubation life for partially debonded center inclusions, at least in the constrained microplasticity regime, unless they are in the vicinity of a grain boundary. The solidification direction is perpendicular to the plane of the diagram. The effect of the primary grain orientation on the plastic zone at the debonded inclusion notch is studied by varying the orientation angle (ω) from 0-45°as shown in Figure 4.25. Sixty five hexagonal grains are used with random orientations perpendicular to the solidification direction (other than the grain containing the inclusion), since the grain orientation cannot be controlled in the transverse orientation during directional solidification. Furthermore, the purpose of these grains is to provide the appropriate far-field stresses for the primary grain.

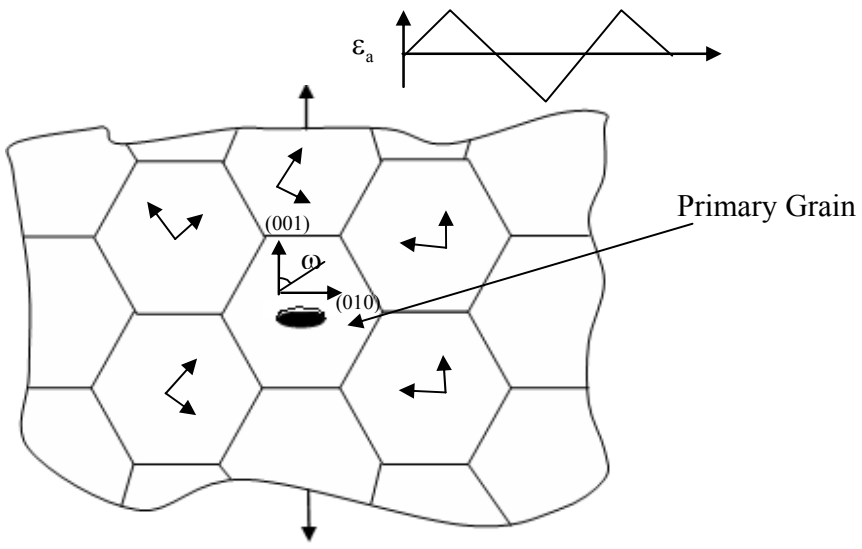

Figure 0.25 Configuration for studying the primary grain orientation effect in the transverse orientation. (Note: figure is not drawn to scale; the inclusion is larger in the schematic for clarity).

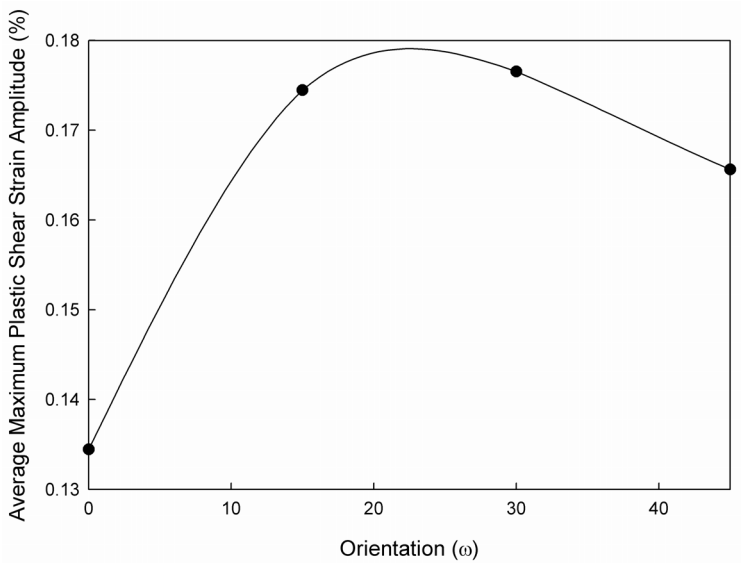

Figure 0.26 Variation of the average maximum plastic shear strain amplitude as a function of the primary grain orientation (ω) (A_r=4:1, R_ε=-1, $\varepsilon_a = 0.3\%$, T=871ºC, $\dot{\varepsilon} = 0.5\%\ s^{-1}$).

The variation of the average maximum cyclic plastic shear strain amplitude, $\Delta\gamma^{p*}_{max}/2$, as a function of the orientation (ω) at a strain amplitude of 0.3% ($R_\varepsilon = -1$) is shown in Figure 4.26. The crack is most likely to incubate in a grain with an orientation of ω = 20-30°, at which $\Delta\gamma^{p*}_{max}$ is maximum. However, $\Delta\gamma^{p*}_{max}/2$ shows relatively low sensitivity to the primary grain orientation in the transverse orientation, thus raising doubts regarding the necessity for modeling the explicit grains which increases the computation time, at least for those inclusions that are not in the vicinity of grain boundaries. The value of $\Delta\gamma^{p*}_{max}$ is higher in the transverse orientation as compared to the longitudinal orientation at the same applied strain amplitude implying a lower incubation life, which is consistent with experimental observations.

4.11.2 Effect of neighboring grain orientation

Effects of neighboring crystal orientation could be important when the inclusion is in the vicinity of a grain boundary. The configuration analyzed is shown in Figure 4.27. A partially debonded elliptical inclusion with aspect ratio $A_r = 4$ is considered in the 'primary' crystal. The inclusion is located at a distance, d_{gbd}, from the grain boundary interface. The primary grain orientation is kept constant at ω_1=25°. The neighboring grain orientation (ω_2) is varied from 0-45°. The distance of the inclusion, d_{gbd}, from the grain boundary is changed from 0.5D to D, where D=10 μm. A strain amplitude of 0.3% and $R_\varepsilon = -1$ is applied for all the simulations.

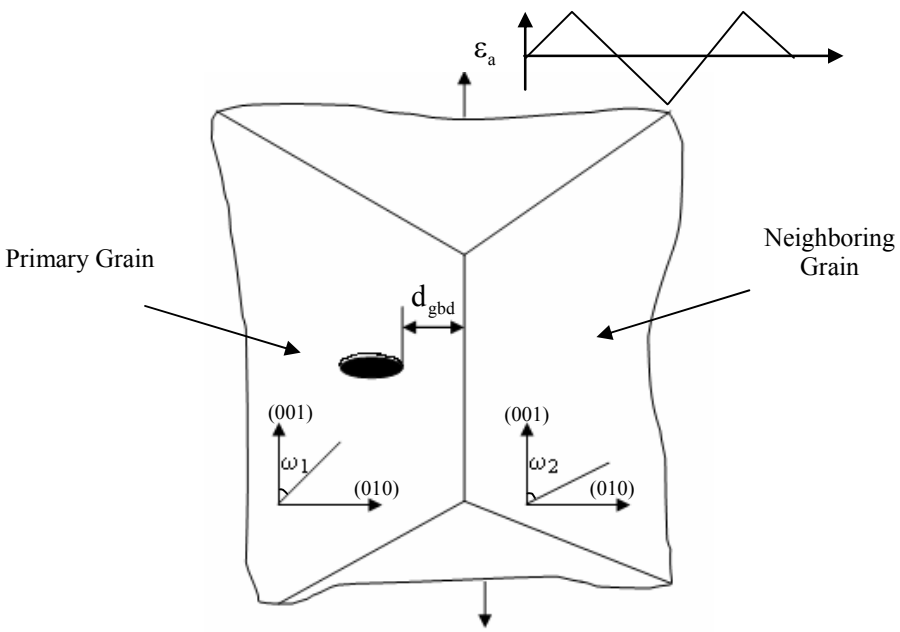

Figure 0.27 Configuration for studying the neighboring grain orientation effect for loading in the transverse orientation (Note: figure is not drawn to scale).

Table 0.1 Variation of the average maximum plastic shear strain amplitude based on neighboring grain orientations ($\varepsilon_a = 0.3\%,\ R = -1$).

$d_{gbd} = D$			$d_{gbd} = 0.5D$		
ω_1	ω_2	$\Delta\gamma^{p*}_{max}/2$	ω_1	ω_2	$\Delta\gamma^{p*}_{max}/2$
25	0	0.31	25	0	0.342
25	25	0.20	25	25	0.227
25	45	0.15	25	45	0.17

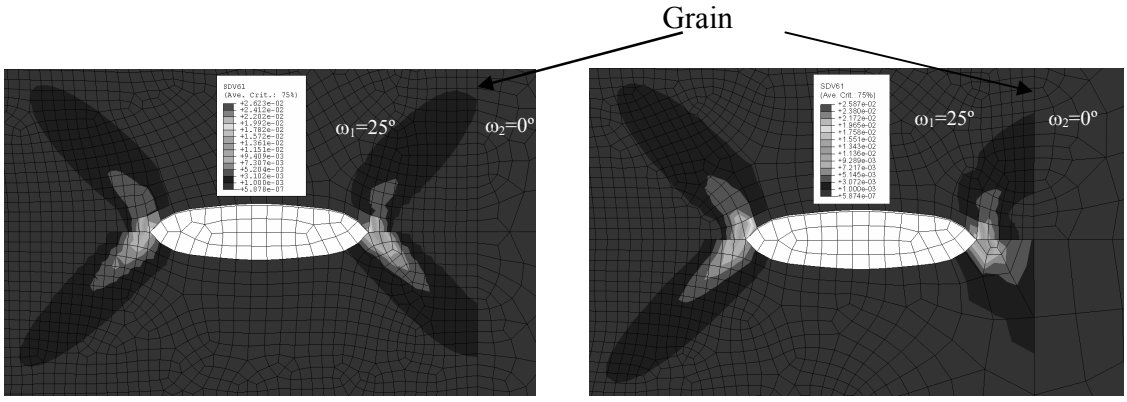

(a) (b)

Figure 0.28 (a) Contours of effective plastic strain (3rd cycle) to study neighboring grain orientation effects, $\varepsilon_a = 0.3\%$, $R_\varepsilon = -1$, $\omega_1=25°$, $\omega_2=0°$, $d_{gbd} = D$; (b) Contours of effective plastic strain (3rd cycle) to study inclusion spacing effects ($\varepsilon_a = 0.3\%$, $R_\varepsilon = -1$, $\omega_1=25°$, $\omega_2=0°$, $d_{gbd} = 0.5D$).

The inelastic strain contours for $d_{gbd} = D$ and $0.5D$ near the inclusion notch are shown in Figure 4.28. As shown in the figure, plastic strain intensification takes place at the inclusion notch due to the grain boundary interface. The variation of the average maximum plastic shear strain range with respect to d_{gbd} and ω_2 is shown in Table 4.1. The average maximum plastic shear strain at the inclusion notch is significantly affected by the neighboring grain orientation, even when it is at a distance of D from the grain boundary. There is a complex interaction with the elastic and inelastic behavior of the neighboring grain; $\Delta\gamma^{p*}_{max}/2$ is maximum when ω_2=0°. Even though the values increase slightly, the dependence of the plastic zone intensification on neighboring grain orientation does not change significantly with proximity to the grain boundary. The higher value of $\Delta\gamma^{p*}_{max}/2$ with proximity to the grain boundary is due to the intensification of plasticity by virtue of interaction with the grain boundary interface. Note that grain boundaries in this work are treated as finite element boundaries; the influence of their structure on deformation mechanism is not addressed.

The effects of crystallographic misorientation angle on fatigue crack initiation in the transverse orientation are expected to be especially important for inclusions at or near grain boundaries. Similarly, effects of orientation (misorientation) distribution of grains on $\Delta\gamma^{P*}_{max}/2$ should be characterized for polycrystals with and without inclusions.

4.12 Limitations

Limitations of the model are discussed next

- Inclusion shape – An idealized elliptical inclusion is used to illustrate the microstructural framework in this chapter. It should be noted that the inclusions have complex shapes in DS GTD111 (Trexler, 2004), and the finite element mesh

can be created for the realistic shapes by mapping the microstructural images into the finite element model. However, the procedure would remain the same and the framework should still be applicable.

- Crack propagation – In this chapter more emphasis is given to crack incubation or the early stages of crack formation. It is acknowledged that crack propagation life could vary as a function of the microstructural features but this aspect has not been investigated.
- Generalized plane strain (GPS) assumption – The finite element analyses are conducted using generalized plane strain assumptions for computational efficiency. Three dimensional analyses are desired for more accurate results to validate the GPS calculations.
- Validation – It is not possible to isolate the carbide size and shape in DS GTD111 at this time without affecting the other microstructural features (γ' precipitate size and shape (Trexler, 2005). The predicted variability in life therefore cannot be validated experimentally.
- Driving force - The cumulative plastic strain per cycle, Δp, has been proposed at various times as a pointwise driving force for LCF fatigue crack formation within the microstructure where cumulative plastic strain is defined as the Euclidean norm given by

$$p = \int_{cyc} \sqrt{2/3 d\varepsilon_{ij}^{p} d\varepsilon_{ij}^{p}} \tag{4.18}$$

However, Δp is a somewhat indirect measure of driving force. Though more computationally involved, the intent of $\Delta\gamma_{max}^{P*}/2$ is to provide a measure of slip range *resolved* onto specific planes, consistent with slip band and critical plane

concepts. It is further maintained that nonlocal averaging is desirable for any microstructure-scale driving force parameter for purposes of use in microstructure-scale crack formation relations, as per length scale arguments elucidated in McDowell et al. (2003). However, it is important to recognize that classical to-and-fro slip is not responsible for all crack formation/propagation mechanisms at the microstructure scale. Progressive pileup of dislocations within slip bands that impinge on grain or phase boundaries (Zener mechanism), or at oxidized inclusion interfaces, can lead to formation of cracks and progressive early extension. More experiments might be needed to determine the exact mechanisms responsible for crack incubation.

4.13 Conclusions

In this work, the role of inclusions in fatigue crack initiation is studied for a generic DS nickel-base superalloy. A simple framework is introduced for estimating crack initiation (formation and small crack propagation) life in a manner that is sensitive to shape, surface proximity and distribution of hard inclusions, and accounts for crystallographic orientation. The [100] orientation is primarily studied. Effects of primary and neighboring grain orientations are also analyzed in the transverse orientation; the grain misorientation angle is shown to influence the plastic strain intensification at the inclusion notch when the inclusion lies at the proximity of a grain boundary. This framework can be useful in assessing relative fatigue resistance of various microstructures and statistical variability of fatigue life as a function of microstructure variability. Furthermore, it can be supplemented with oxidation effects if the role of environment in interacting with microstructure or producing variability of fatigue response is to be considered (Fleury and Remy, 1993; Fleury and Remy, 1994; Chateau and Remy, 1998). Finally, if warranted, more intensive studies can be devoted to

quantifying the crack incubation process, including small crack formation and initial propagation within the domain of influence of the micronotch root field, as well as microstructurally small crack propagation through a field of microstructure heterogeneities. The construct employed here is a very simple one to address crystal orientation, viscoplasticity, and explicit microstructure features that can enhance fatigue crack formation with the two fold goals of:

- Estimation of variability in fatigue.
- Rank order microstructures and inclusions with regard to potency in fatigue.

CHAPTER V

Microstructure-Dependent Crystal Plasticity Based Model for a Polycrystalline Nickel-Base Superalloy

Abstract

A rate dependent crystallographic constitutive theory is formulated for predicting the mechanical behavior of a commercially used polycrystalline Ni-base superalloy; IN100. In contrast to Chapter II, where the primary focus was to develop a physically-based homogeneous model to capture the stress-strain behavior over a large temperature regime for creep and fatigue in a directionally solidified superalloy, attention is devoted here to embedding the microstructural dependence into the stress-strain constitutive model of a polycrystalline superalloy at 650°C. This model has the capability to capture first order effects on the stress-strain response due to (a) grain size, (b) the γ' precipitate size distribution, and (c) the γ' precipitate volume fraction. Experimental fatigue data with variable strain rates are used to calibrate the model for the polycrystalline superalloy with selected microstructural features. Physically-based hardening laws are employed to

evolve the dislocation densities for each slip system, taking into consideration the dislocation interaction mechanisms.

5.1 Introduction

Polycrystalline Ni-base superalloys are commonly used for hot section applications like turbine discs, because of their enhanced creep and fatigue properties at the intermediate temperatures (<750°C). Constitutive modeling is employed by engine designers to predict stresses and strains in turbine engine components, to support life prediction. Current models used in industry are mainly empirical and are essentially developed from simple curve fits of test data and macroscopic continuum mechanical models (Milligan, 2004). From design and life prediction perspectives, it would be highly desirable to have a physically-based microstructure dependent constitutive model with good predictive capability.

Nickel-base superalloys contain two phases: γ matrix, with a face centered cubic (FCC) lattice structure and coherent γ' precipitates with Ll_2 lattice structure. The anomalous temperature dependence of the flow stress in Ni-base superalloys, characterized by a yield strength increase with an increase in temperature, has been researched extensively and the mechanisms responsible are fairly well understood (Reppich, 1982; Paidar et al., 1984; Nitz and Nembach, 1998; Fedelich, 2002; Milligan, 2004) and have been partly explained in Chapter II. However, it is worth noting that the grain size and the precipitate size, spacing and distribution can greatly affect the behavior of nickel-base superalloys. The deformation mechanisms depend on these microstructural

features; for example dislocation mechanisms change from precipitate shearing to bypassing by Orowan looping, depending on the precipitate size and volume fraction.

An extensive database from experimental tests is warranted to get an accurate description of the influence of these microstructural features on the stress-strain response and the intrinsic fatigue resistance. Computational resources can be very useful tools in this regard since they are relatively inexpensive and do not contain the inherent variability associated with experiments both with regard to processing and testing conditions. Constitutive models that convey microstructural dependence of the stress-strain response are rarely observed in literature. This is mainly due to complexities such as (a) lack of systematic experimental data to isolate the effects (b) lack of applicability of a simple mixture theory to model the particle-matrix interactions, (c) Ni-base superalloys typically have a bi-modal/tri-modal distribution of the precipitate, which are sheared or bypassed depending on their size and (d) the change of deformation mechanisms with temperature. The smaller particles, which are sheared at lower temperatures, may be bypassed by dislocation climb at higher temperatures. Polycrystalline Ni-base superalloys also display a grain size dependent stress-strain response.

In this work, a set of physically-based crystal viscoplastic constitutive models is developed to simulate the cyclic deformation behavior of a two-phase Ni-base superalloy IN100 at 650°C. Dependence on microstructural features at multiple length scales is addressed. This model is used to study the microstructural effects on low cycle fatigue (LCF) to provide support for quantifying microstructure-dependent material constants in

a macroscopic constitutive model suitable for structural analysis and also for crack incubation life assessment analyses as discussed in Chapters V1 and VII, respectively.

5.2 Background

A number of constitutive models have been proposed in the past to capture the stress-strain response of Ni-base superalloys at different length scales. These models can be classified into the following types:

- Rate independent elastoplastic models, which are used to capture the constitutive response at low homologous temperatures (Ding et al., 2004). Models have been developed both at the macroscopic level, at which no explicit distinction is made between the phases and grains, and at the slip system level using continuum crystal plasticity. These models are not suitable at higher homologous temperatures at which the rate dependent material response is significant.
- Macroscopic rate dependent viscoelastoplastic models, which are formulated at a much higher length scale and do not explicitly account for the grains and precipitates (Bodner and Partom, 1975; McDowell, 1992). These models can capture the rate dependence of the stress-strain response but cannot explicitly capture effects of heterogeneity in the inelastic strain distribution.
- Viscoelastoplastic anisotropic models with cubic symmetry which can be used to model the individual grains are physically attractive since they can account for the anisotropy of the polycrystalline material at the grain scale (Walker and Jordan, 1985; Sheh and Stouffer, 1990; Shenoy et al., 2005). However, most of these

cannot account for the heterogeneity in deformation behavior within the grains arising from the precipitate-matrix phase contrast.

- Explicit modeling of the two phases (γ matrix and the γ' precipitates) has been conducted by (Pollock and Argon, 1992; Nouailhas and Cailletaud, 1996; Ohashi et al., 1997; Busso et al., 2000) for single crystal Ni-base superalloys with a uni-modal precipitate size and a periodic distribution. These models assume different phenomenological viscoelastoplastic constitutive laws for both phases and can account for the internal stress distribution within the grains. It should be noted, however, that these models are mainly restricted to monotonic loading histories and are currently infeasible for application to structural analyses due to their high computational costs.
- Analytical models of the two-phase superalloy using simplifying assumptions for the dislocation distribution (Ohashi et al., 1997; Probst et al., 1999) can be used but are not appropriate for general multi-axial or non-monotonic loading histories.
- Dislocation dynamics based simulations are used to study the basic interactions between the dislocations and the γ' precipitates; however, these analyses are still in the primitive stages and cannot be realistically used in superalloys with complex microstructures (Yashiro et al., 2005). Moreover, discrete dislocation theory might not incorporate behavior of partial dislocations which are important in $\gamma - \gamma'$ systems.

Continuum crystal plasticity based models in literature assume a purely random distribution of precipitate phases, and the influence of the microstructural features (grain size, precipitate size and volume fraction) are implicit in the model; there are no explicit

terms to account for their individual contribution to the stress-strain response(Fedelich, 2002). A constitutive model which can predict the microstructure dependent stress-strain response should be very useful; therefore, an effort is made to build on these approaches to formulate a viscoelastoplastic constitutive model, with embedded microstructure dependence. This model is formulated at the slip system level using a continuum crystal plasticity framework, which does not explicitly differentiate between the phases and assumes homogeneous stress-strain response within a grain.

5.3 Material and Experimental Testing

The baseline material used for this study is a subsolvus-processed IN100, which is prepared using powder metallurgy techniques. The material contains large γ' precipitates that do not dissolve during the solutionizing step as well as secondary and tertiary precipitates, which form during cooling and subsequent aging. A typical microstructure is shown in Figure 5.1. As seen in Figure 5.1, the primary precipitates are large and are mainly located near the grain boundaries. The solution heat treatment temperature and cooling rate after the solutionizing step are varied to produce different microstructures.

Table 0.1 Microstructural details for IN100 (Milligan, 2004).

Material	Primary γ' f_{p1}	Secondary γ' d_2 (nm)	Secondary γ' f_{p2}	Tertiary γ' d_3 (nm)	Tertiary γ' f_{p3}	Grain d_{gr} (μm)
Matrix1	0	108	0.42	7	0.11	27
Matrix2	0	239	0.39	11	0.14	32
Matrix3	0.07	110	0.29	7	0.17	10
Super Weak	0	340	0.46	11	0.137	34
Sister Disk	0.25	109	0.32	21	0.024	4.2

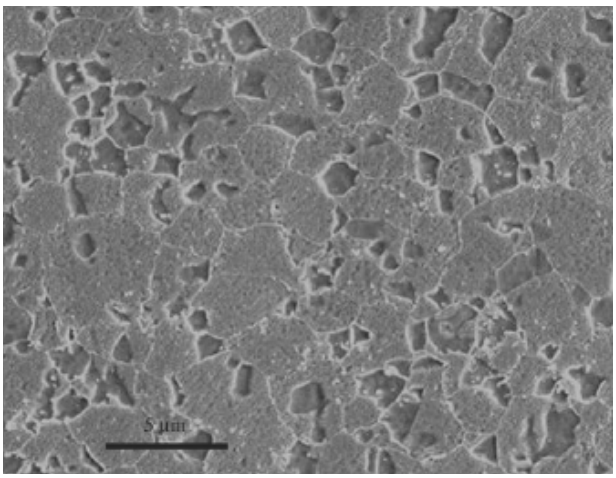

Figure 0.1 Microstructure for baseline IN100 (Milligan, 2004), with the large primary γ' precipitates.

A range of microstructures are obtained containing a different distribution of grain sizes as well as different sizes and distributions of the γ' precipitates as, shown in Table 5.1. The microstructural terms are listed in the first row in Table 5.1; f_{p1}, f_{p2}, f_{p3}, are the volume fractions of the primary, secondary and tertiary γ' precipitates respectively; d_1, d_2, and d_3 are the average diameters of the primary, secondary and tertiary γ' precipitates, respectively, and d_{gr} is the average grain size. In order to study the influence of the primary precipitates on the stress-strain deformation response, microstructures are also obtained that do not contain the primary precipitates. These 'matrix alloys' contain only secondary and tertiary γ' precipitates, without any primary γ' precipitates. Grain sizes are determined using standard stereological procedures. Primary and secondary γ' sizes and fractions are determined using field emission scanning electron microscopy and stereology, while tertiary γ' sizes are determined by energy-filtered transmission electron

microscopy. Details of the characterization techniques are presented in (Wusatowska-Sarnek et al., 2003). Tertiary γ' volume fractions are determined by subtracting the secondary and primary fractions from the known equilibrium volume fractions.

Uniaxial isothermal fatigue tests are conducted at 260°C and 650°C (Milligan, 2004) for each material with microstructure in Table 5.1. Two characteristic types of strain controlled histories are used for our purposes in fitting the models, one type with variable strain rate cycling and strain hold periods at maximum (or minimum) strain peaks before strain reversal, and the other type having no strain hold periods. A cyclic strain-time history with variable strain amplitudes and strain rates are used in each case. A strain rate of 10^{-3} s^{-1} is enforced for majority of the tests and the strain rate is varied by an order of magnitude in some parts of the strain history to capture the strain rate dependence of the flow stress response. It should be noted that the model and frameworks are developed for the material response at 650°C to focus on the LCF-critical regime; however, it should still be applicable at 260°C with appropriate assignment of the material parameters in the constitutive equations.

5.4 Motivation for the Crystal Plasticity Model

It could be argued that the microstructural dependence can be embedded directly into a macroscale model; however, the approach taken in this work is to use the crystal plasticity framework due to the following advantages:

- The physics of the problem can be embedded more accurately in a crystal plasticity framework.

- The grains can be modeled explicitly using different crystallographic orientations, which is especially important since grains play a very important role in determining the crack incubation life in polycrystalline Ni-base superalloys(Findley, 2005).
- Even though explicit modeling of precipitates has not been conducted in this thesis(Kumar et al., 2006), a crystal plasticity framework lays the foundation for a hierarchical scheme for linking length scales from precipitates in single crystals to polycrystalline grains to the homogenized stress-strain macroscopic response as shown in Figure 5.2.

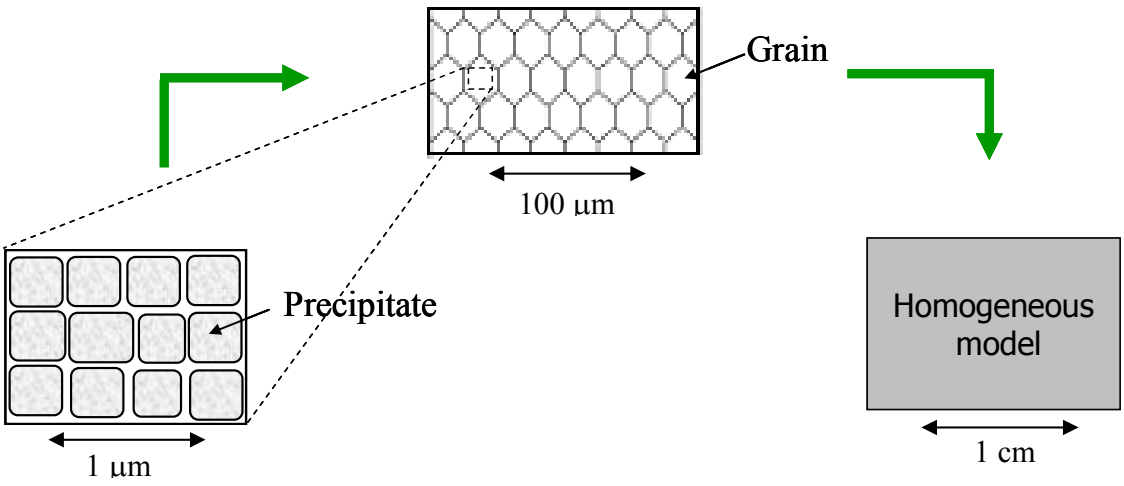

Figure 0.2 Hierarchical scheme for embedding the microstructural dependence in constitutive models.

5.5 'Micro' Constitutive Model

In this section, a microstructure-based crystal viscoplastic constitutive model is developed. The model accounts for important deformation mechanisms in the microstructure and is an extension of the models developed by McDowell and co-workers (McDowell, 1992; Shenoy et al., 2005; Wang et al., 2005). This model is formulated at the length scale of grains and the effects of the precipitates are included in the model in an averaged sense, i.e., the precipitates are not explicitly modeled. The objective is to develop an appropriate length scale-dependent constitutive model to study the role of microstructure on the stress-strain behavior. The following attributes are incorporated in the model:

- Influence of primary, secondary and tertiary γ' precipitates on the stress-strain response (both initial yield and work hardening)
- Averaged effect of the grain size on the constitutive response.
- Dependence of the flow stress on crystallographic orientation and the strain rate.

The physically-based constitutive model developed in this work is useful for modeling the effects of microstructural variability on LCF behavior, thus facilitating parametric studies regarding the influence of microstructure on cyclic deformation. The primary microstructure features and dislocation interactions are implemented in the model.

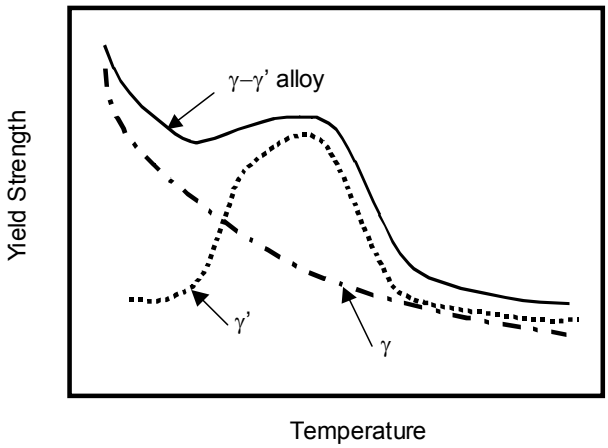

Figure 0.3 Schematic showing combined effects of γ and γ' phases on the yield strength as a function of temperature.

A single crystal Ni-base superalloy consists of two phases: fcc γ matrix and γ′ precipitate with Ll_2 lattice structure. The γ′ precipitates are responsible for the anomalous flow stress at high temperature. Dislocations interactions within the γ′ phase are assumed to result in the formation of Kear-Wilsdorf (KW) locks. These locks, which are formed by thermal activation, block further dislocation motion thereby increasing the critical resolved shear stress (CRSS) with increasing temperature and are also responsible for the tension-compression asymmetry (Paidar et al., 1984; Vitek et al., 1996).

The overall response of a two-phase Ni-base superalloy is essentially a superposition of the response of the constituent phases. As an example, the variation of flow stress of the superalloy as a function of temperature is schematically shown in Figure 5.3 as a superposition of the precipitate and matrix responses. However, it should be noted that a simple mixture rule in the conventional sense does not hold true since for example the yield strength of the superalloy could be higher than the yield strength of the precipitate and matrix phases, when tested individually. The γ matrix is a soft phase with solid

solution hardening. Dislocations nucleate within the matrix phase, typically at grain boundaries, multiply and form forest and cell-structures. The motion of dislocations within the matrix phase is affected by the volume fraction of the γ' precipitates: dislocation pairs can shear through them, loop around them or pile up at their interfaces. The precise mechanism depends on the size and spatial distribution of the γ' precipitates, stress/strain level, the anti-phase boundary energy (APBE), the stacking fault energy (SFE), and temperature. Therefore, the size and spacing of the precipitates are significant length scales in the two-phase microstructure. In addition, the grain size is important and should be considered in the formulation. It is a "grand challenge" to predict the influence of these microstructural features on the flow stress from "first principles". Self consistent methods have been extensively used in literature to determine the averaged properties in heterogeneous materials (Nemat-Nasser and Hori, 1999), however, this is not considered a valid approach for Ni-base superalloys. The nonlocal interaction between the matrix and precipitate phases plays the dominant role in dictating the stress-strain response in Ni-base superalloys, which would be extremely difficult to incorporate in a self consistent scheme. An alternate route is taken here in order to link the crystal viscoplasticity deformation model to the microstructural features. A model is formulated with the microstructure-dependent terms explicitly embedded in the model. The model is calibrated using stress-strain data for a selected range of microstructures.

5.5.1 Crystal Plasticity Framework

The kinematics of crystal plasticity theory have been explained comprehensively in Chapter II and will not be explained again for brevity.

5.5.2 Flow rule

The inelastic slip rate (flow rule) for each slip system could be based on the flow rule given by Eq. (2.17) (Shenoy et al., 2005; Wang et al., 2005), i.e.,

$$\dot{\gamma}^{(\alpha)} = \dot{\gamma}_o \Theta(T) \left\langle \frac{\left|\tau^{(\alpha)} - \chi^{(\alpha)}\right| - \kappa^{(\alpha)}}{D^{(\alpha)}} \right\rangle^n \exp\left\{ B_o \left\langle \frac{\left|\tau^{(\alpha)} - \chi^{(\alpha)}\right| - \kappa^{(\alpha)}}{D^{(\alpha)}} \right\rangle^{n+1} \right\} \mathrm{sgn}\left(\tau^{(\alpha)} - \chi^{(\alpha)}\right) \tag{5.1}$$

However, even though this flow rule can capture the power law breakdown of the strain rate dependence at higher stresses, determination of the constants can be difficult. An alternate approach is to use a slightly different form of the flow rule using a two term potential (Chaboche, 1989), i.e.,

$$\dot{\gamma}^{\alpha} = \left[\dot{\gamma}_o \left\langle \frac{\left|\tau^{\alpha} - \chi^{\alpha}\right| - \kappa^{\alpha}}{D^{\alpha}} \right\rangle^{n_1} + \dot{\gamma}_1 \left\langle \frac{\left|\tau^{\alpha} - \chi^{\alpha}\right|}{D^{\alpha}} \right\rangle^{n_2} \right] \mathrm{sgn}\left(\tau^{\alpha} - \chi^{\alpha}\right) \tag{5.2}$$

where $\dot{\gamma}_o$ and $\dot{\gamma}_1$ are constants; the temperature dependence of the constants is not embedded since they are only determined at 650°C, n_1 and n_2 are flow exponents, κ^{α} is the threshold stress, and D^{α} is an average drag resistance. The two term potential may in itself be regarded as an approximation of the power law breakdown regime at higher strain rates (Chaboche, 1989), thereby rendering the exponential terms nonessential. The rate sensitivity of material hardening arises from the dynamic equilibrium between

competing hardening and rate-dependent dynamic recovery processes. Klepaczko & Chiem (1986) have shown that the rate sensitivity of strain hardening is important and may play a dominant role in material rate sensitivity demonstrated in a given material response. The first term in the flow rule is of "quasi rate-independent" character, and is used to capture the dominant cyclic behavior; the threshold stress, κ^{α}, plays a role in this dominantly athermal term. The second term largely represents effects of thermally activated flow, and is used to capture stress relaxation behavior; it may also be regarded a reflecting mechanism for thermally activated flow at low to moderate stress levels, for example dislocation-dislocation interactions in the γ matrix. It is noted that this second thermal term effectively admits thermally activated motion below the threshold stress while the first term is more relevant to higher strain rate dislocation glide.

Note that the slip system backstress, χ^{α}, is required to capture the Bauschinger effect in cyclic loading due to the homogenized treatment of the two-phase superalloy. There are 12 octahedral slip systems <110>{111} and 6 cubic slip systems <110>{001}. Both the octahedral and cube slip systems are active at 650°C (Osterle et al., 2000). The microstructure-dependence of the stress-strain response is completely embedded in the evolution equations for the internal state variables (ISV's). Two ISV's are used: dislocation density, ρ^{α}, and backstress variable, χ^{α}.

5.5.3 Threshold Slip Resistance

The initial crystallographic yield/flow crystallographic flow behavior of two-phase Ni-base superalloys under a given temperature, microstructural state and critical resolved shear stress (CRSS) of a generic slip system (both octahedral and cubic) is modeled via overall threshold slip resistance, κ^{α}, as

$$\kappa_{\lambda}^{\alpha} = \kappa_{o,\lambda}^{\alpha} + \alpha\mu_{mix} b\sqrt{\rho_{\lambda}^{\alpha}} \tag{5.3}$$

where λ stands for either the octahedral or cube slip systems, ρ^{α} is the dislocation density and μ_{mix} is the volume fraction averaged shear modulus, given by

$$\mu_{mix} = \left(f_{p1} + f_{p2} + f_{p3}\right)\mu_{\gamma'} + f_m\,\mu_m \tag{5.4}$$

where $\mu_{\gamma'}$ and μ_m are the shear moduli for the precipitate and matrix phases, respectively and f_m is the volume fraction of the matrix phase. It is noted that volume fraction averaging is employed as first order approximation for all the elastic properties (i.e., C_{11}, C_{12} C_{44}). It is reasonable since the elastic mismatch of the two phases is not large. The slip resistance is expressed in terms of an initial reference critical resolved shear stress (CRSS) and the Taylor hardening term due to interactions of the statistically stored dislocations, ρ_{λ}^{α}. Here, α is a statistical coefficient that accounts for the deviation from the regular spatial arrangements of the dislocation population. The initial CRSS is analogous to the yield strength and is influenced by microstructure features such as the

average grain size, precipitate size distribution and volume fraction. The functional form for the microstructure-dependence of the CRSS is based on the work by Reppich and co-workers (Reppich, 1982; Heilmaier et al., 2001), who determined the increase in the CRSS based on precipitate size for a fixed volume fraction of precipitates in IN100. The deformation mechanism changes with the precipitate size and can be separated into mainly three distinct types: (a) for underaged precipitates (<100 nm), shearing takes place by weakly coupled dislocation pairs and the CRSS increases with precipitate size, (b) for slightly larger particles (100 $>d_p<$400 nm) shearing takes place by strongly coupled dislocation pairs and the CRSS decreases as a function of the precipitate size, and (c) for overaged particles (> 400 nm), the precipitates are not sheared and dislocation looping takes place. It is noted that dislocation looping has not been observed in this material (base IN100) even in the large primary γ' precipitates at 650ºC (Milligan, 2004), as opposed to the observations by Heilmaier et al. (2001). Accordingly, the CRSS contribution based on dislocation looping is not included. The influence of the mean grain size is introduced through the Hall-Petch relations.

The initial CRSS is given by

$$\kappa^{\alpha}_{o,oct} = \left[\left(\tau^{\alpha}_{o,\gamma} \right)^{n_\kappa} + \Psi_{oct} \left(f_{p1}, d_2, f_{p2}, d_3, f_{p3} \right)^{n_\kappa} \right]^{1/n_\kappa} + \frac{\left(f'_{p1} + f'_{p2} \right)}{f_{p\_ref}} \tau^{\alpha}_{ns}$$
$$\kappa^{\alpha}_{o,cub} = \left[\left(\tau^{\alpha}_{o,\gamma} \right)^{n_\kappa} + \psi_{cub} \left(f_{p1}, d_2, f_{p2}, d_3, f_{p3} \right)^{n_\kappa} \right]^{1/n_\kappa} \qquad (5.5)$$

and

$$\psi_{oct} = \psi_{cub} = c_{p1}\sqrt{0.81 w f'_{p1} \mu_{\gamma'} \frac{\Gamma_{APB}}{d_1}} + c_{p2}\sqrt{0.81 w f'_{p2} \mu_{\gamma'} \frac{\Gamma_{APB}}{d_2}} + c_{p3}\sqrt{\mu_{\gamma'} \frac{d_3}{d_{3ref}} f'_{p3} \frac{\Gamma_{APB}}{b}} + c_{gr} d_{gr}^{-0.5} \tag{5.6}$$

where the normalized precipitate volume fractions are defined as

$$f'_{p1} = \frac{f_{p1}}{f_{p1} + f_m}, f'_{p2} = \frac{f_{p2}}{f_{p2} + f_m}, f'_{p3} = \frac{f_{p3}}{f_{p3} + f_m} \tag{5.7}$$

where Γ_{APB} is the anti-phase boundary energy, w is a constant that accounts for the elastic repulsion within the precipitates, d_{3ref} is a reference parameter used for normalizing the tertiary γ' precipitate size, and c_{p1}, c_{p2}, c_{p3} and c_{gr} are determined by fitting the initial yield strength to the experimental data.

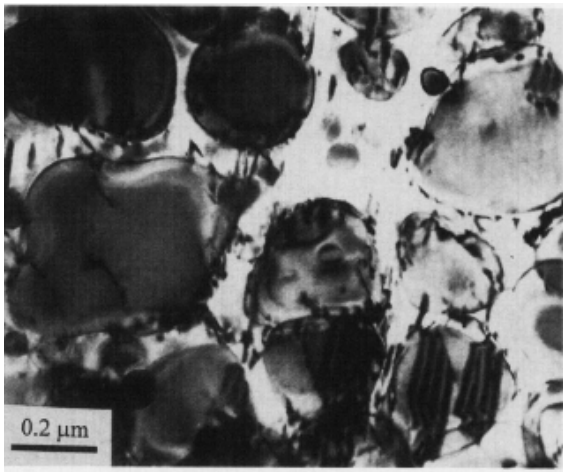

Figure 0.4 Bright-field TEM micrograph of γ′ secondary precipitates after compressive deformation at 650°C showing dislocation pairs at the interface, indicative of strong pair shearing (Sinharoy et al., 2001).

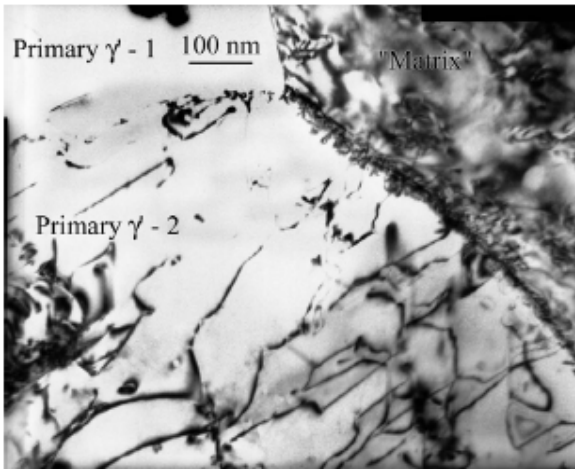

Figure 0.5 Bright-field TEM micrograph of 2.5% deformation at room temperature showing dislocation debris in the γ′ primary precipitates (Milligan, 2004) .

In Eq.(5.6), the first two terms correspond to an increase in the CRSS based on shearing of the primary and secondary precipitates by strongly coupled dislocation pairs while the third term corresponds to shearing of the tertiary precipitates by weakly coupled dislocation pairs. The fourth term corresponds to the increase in the CRSS with a decrease in grain size based on the Hall-Petch relation. TEM observations on a commercial Ni-base superalloy, similar to IN100, tested at 650°C revealed shearing of secondary precipitates by APB couple dislocation pairs, as shown in Figure 5.4. Substantial dislocation debris was observed inside the primary γ' precipitates after 2.5% deformation at room temperature as shown in Figure 5.5 (Sinharoy et al., 2001; Milligan, 2004). Shearing of the primary γ' precipitates by dislocation pairs was also observed at 650°C (Sinharoy et al., 2001); therefore, deformation is assumed to primarily take place by precipitate shearing by dislocation pairs in the primary γ' precipitates as opposed to the dislocation looping mechanism observed by Heilmeier and co-workers (2001). While this might seem contradictory to the observations by Heilmeier and co-workers, it should be noted that their tests were based on a unimodel distribution of precipitates. Furthermore the volume fraction of these overaged precipitates was much higher ($\approx 60\%$). It is noted that dislocation looping terms could be introduced as limiting value of threshold stress, particularly at high temperatures.

A non-linear summation is assumed in the general form for the contributions to the CRSS from the precipitates based on Nitz and Nembach (1998). The exponent n_κ is usually between 1-1.2. The non-Schmid stress dependence of the octahedral slip systems is given by (Shenoy et al., 2005)

$$\tau_{ns}^{\alpha} = h_{pe}\tau_{pe}^{\alpha} + h_{cb}\left|\tau_{cb}^{\alpha}\right| + h_{se}\tau_{se}^{\alpha} \tag{5.8}$$

where τ_{pe}^{α}, τ_{cb}^{α} and τ_{se}^{α} are the resolved shear stresses on the primary, cube and secondary slip systems respectively and h_{pe}, $h_{cb,}$ h_{se} are constants and f_{p_ref} is a normalizing parameter for the precipitate volume fraction. The non-Schmid stresses are not included in the threshold stress for the cube slip systems.

5.5.4 Dislocation Density

The hardening behavior of the flow stress results from nucleation, multiplication and interactions of dislocations under applied loading. The interaction with the forest dislocations is considered for both octahedral and cubic slip systems. In addition, hardening is controlled by a competition between dislocation storage and annihilation (dynamic recovery) mechanisms (Mecking and Kocks, 1981; Estrin and Mecking, 1984). Dislocation storage is regarded as an athermal process and includes storage of both statistically stored dislocations (SSDs) and geometrically necessary dislocations (GNDs). Storage of SSDs arises from dislocations becoming immobilized by forest dislocation interactions upon traveling a mean free path proportional to the square root of the dislocation density, $\sqrt{\rho^{\alpha}}$, SSDs have no net Burgers vector. Dynamic recovery is associated with dislocation annihilation and rearrangement, which is directly proportional to the dislocation density ρ^{α} (Feaugas and Haddou, 2003). The mean free path of dislocations in the matrix channels is also dictated by the size and spacing of γ' precipitates and/or grain boundaries. The size effects due to the grain size and the

precipitate spacing can be included in the model through the first term in Eq. (5.9), Z_o, which may be viewed as the contribution from the geometrically necessary dislocation density. However, only the primary and secondary precipitate spacing effects are included in the model based on experimental observations by Milligan (2004), who showed that the primary and secondary precipitates played a more dominant role in the stress-strain response in the inelastic regime. The grain size influences the inelastic behavior only during the initial part of the inelastic regime ($\varepsilon^{in} < 0.2\%$) and does not significantly influence the stress-strain response at higher inelastic strains (Feaugas and Haddou, 2003). The evolution equation for the dislocation density is given by

$$\dot{\rho}_{\lambda}^{(\alpha)} = \sum_{\beta} h^{(\alpha\beta)} \left\{ Z_o + k_1 \sqrt{\rho_{\lambda}^{(\beta)}} - k_2 \rho_{\lambda}^{(\beta)} \right\} \left| \dot{\gamma}^{(\beta)} \right| \tag{5.9}$$

where

$$Z_o = \frac{k_{\delta}}{b d_{\delta eff}} \qquad \text{and} \qquad \frac{1}{d_{\delta eff}} = \left(\frac{1}{d_{1\delta}} + \frac{1}{d_{2\delta}} \right) \tag{5.10}$$

and k_1, k_2, and k_{δ} are constants,$d_{1\delta}$ and $d_{2\delta}$ represent the primary and secondary precipitate spacing and $d_{\delta eff}$ is an equivalent precipitate spacing. The hardening coefficients for the evaluation of average dislocation densities can be described by many forms(Franciosi, 1985). As a first order approximation,

$$h^{\alpha\beta} = h_o \, q^{\alpha\beta} \quad \Rightarrow \quad \begin{cases} h^{\alpha\beta} = h_o, & \text{for } \alpha = \beta \text{ , self-hardening} \\ h^{\alpha\beta} = h_o \, q, & \text{for } \alpha \neq \beta \text{ , latent-hardening} \end{cases} \tag{5.11}$$

where q is the latent hardening factor and h_o is self-hardening rate. Simple Taylor hardening (same hardening rate on all slip systems) is assumed, i.e., q =1.

5.5.5 Backstress Evolution

A backstress term (χ^{α}) is included in the model to capture the Bauschinger effect associated with the heterogeneous distribution of dislocations at the γ' precipitate interfaces since the two-phase microstructure is not modeled explicitly. The backstress evolution is given by

$$\dot{\chi}_{\lambda}^{(\alpha)} = C_{\chi}\left\{\eta\mu_{s}b\sqrt{\rho_{\lambda}^{(\alpha)}}\,\mathrm{sgn}\left(\tau^{(\alpha)}-\chi_{\lambda}^{(\alpha)}\right)-\chi_{\lambda}^{(\alpha)}\right\}\left|\dot{\gamma}^{(\alpha)}\right| \tag{5.12}$$

$$\eta = \frac{\eta_{o}Z_{o}}{Z_{o}+k_{1}\sqrt{\rho_{\lambda}^{(\alpha)}}} \tag{5.13}$$

where C_{χ} is a fitting parameter, the coefficient η establishes the ratio of backstress amplitude relative to the cyclic flow stress for various slip systems, and η_o is describes the contribution from the GNDs. This phenomenological form essentially assumes η as the fraction of rate of generation of GNDs to the total dislocation density rate. Note that both octahedral and cube slip systems are included, although backstress is primarily anticipated to play a role in affecting slip on the octahedral slip systems.

The set of equations for the constitutive model are summarized in Table 5.2.

Table 0.2 Set of equations for the crystal plasticity based microstructure dependent model.

Flow Rule

$$\dot{\gamma}^{\alpha}=\left[\dot{\gamma}_{o}\left\langle\frac{\left|\tau^{\alpha}-\chi^{\alpha}\right|-\kappa_{\lambda}^{\alpha}}{D^{\alpha}}\right\rangle^{n_1}+\dot{\gamma}_{1}\left\langle\frac{\left|\tau^{\alpha}-\chi^{\alpha}\right|}{D^{\alpha}}\right\rangle^{n_2}\right]\operatorname{sgn}\left(\tau^{\alpha}-\chi^{\alpha}\right)$$

where

$$\kappa_{\lambda}^{\alpha}=\kappa_{o,\lambda}^{\alpha}+\alpha\mu_{mix}b\sqrt{\rho_{\lambda}^{\alpha}} \qquad \lambda=\text{oct, cub}$$

$$\kappa_{o,oct}^{\alpha}=\left[\left(\tau_{o,\gamma}^{\alpha}\right)^{n_\kappa}+\psi_{oct}\left(f_{p1},d_2,f_{p2},d_3,f_{p3}\right)^{n_\kappa}\right]^{1/n_\kappa}+\frac{\left(f'_{p1}+f'_{p2}\right)}{f_{p\_ref}}\tau_{ns}^{\alpha}$$

$$\kappa_{o,cub}^{\alpha}=\left[\left(\tau_{o,\gamma}^{\alpha}\right)^{n_\kappa}+\psi_{cub}\left(f_{p1},d_2,f_{p2},d_3,f_{p3}\right)^{n_\kappa}\right]^{1/n_\kappa}$$

$$\tau_{ns}^{\alpha}=h_{pe}\tau_{pe}^{\alpha}+h_{cb}\left|\tau_{cb}^{\alpha}\right|+h_{se}\tau_{se}^{\alpha}$$

$$\psi_{oct}=\psi_{cub}=c_{p1}\sqrt{0.81wf'_{p1}\mu_{\gamma'}\frac{\Gamma_{APB}}{d_1}}+c_{p2}\sqrt{0.81wf'_{p2}\mu_{\gamma'}\frac{\Gamma_{APB}}{d_2}}+$$

$$c_{p3}\sqrt{\mu_{\gamma'}\frac{d_3}{d_{3ref}}f'_{p3}\frac{\Gamma_{APB}}{b}}+c_{gr}d_{gr}^{-0.5}$$

$$f'_{p1}=\frac{f_{p1}}{f_{p1}+f_m},f'_{p2}=\frac{f_{p2}}{f_{p2}+f_m},f'_{p3}=\frac{f_{p3}}{f_{p3}+f_m}$$

Internal State Variable

a) Dislocation Density

$$\dot{\rho}_{\lambda}^{(\alpha)}=\sum_{\beta}h^{(\alpha\beta)}\left\{Z_o+k_1\sqrt{\rho_{\lambda}^{(\beta)}}-k_2\rho_{\lambda}^{(\beta)}\right\}\left|\dot{\gamma}^{(\beta)}\right| \qquad h^{\alpha\beta}=1$$

$$Z_o=\frac{k_\delta}{bd_{\delta eff}} \qquad d_{\delta eff}=\left(\frac{1}{d_{1\delta}}+\frac{1}{d_{2\delta}}\right)^{-1}$$

b) Backstress

$$\dot{\chi}_{\lambda}^{(\alpha)}=C_\chi\left\{\eta\mu_s b\sqrt{\rho_{\lambda}^{(\alpha)}}\operatorname{sgn}\left(\tau^{(\alpha)}-\chi_{\lambda}^{(\alpha)}\right)-\chi_{\lambda}^{(\alpha)}\right\}\left|\dot{\gamma}^{(\alpha)}\right|$$

$$\eta=\frac{\eta_o Z_o}{Z_o+k_1\sqrt{\rho_{\lambda}^{(\alpha)}}}$$

5.6 Finite Element Model

The constitutive equations formulated in the previous section are implemented as a User MATerial (UMAT) in ABAQUS(ABAQUS, 2005). A full 3D finite element mesh is subjected to both types of strain histories (with and without strain hold periods at maximum or minimum strain peaks before strain reversal) to generate the stress response. Twenty five grains with random orientations are used to represent the polycrystal as shown in Figure 5.6 and the average stress is calculated. A total of 100 elements are used with each grain modeled as a cube comprising four 8-noded brick elements. The choice of the number of elements and shape of grains is dictated by the large computational time required for the analyses. Random 3D periodic boundary conditions are employed.

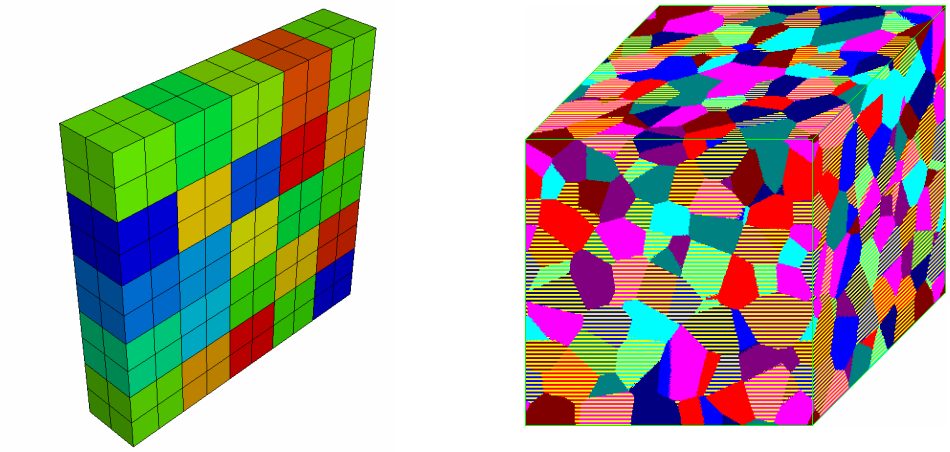

(a) (b)

Figure 0.6 The 25 grain model with cubic grains (left) and the 512 grain SVE with more realistic grains (right).

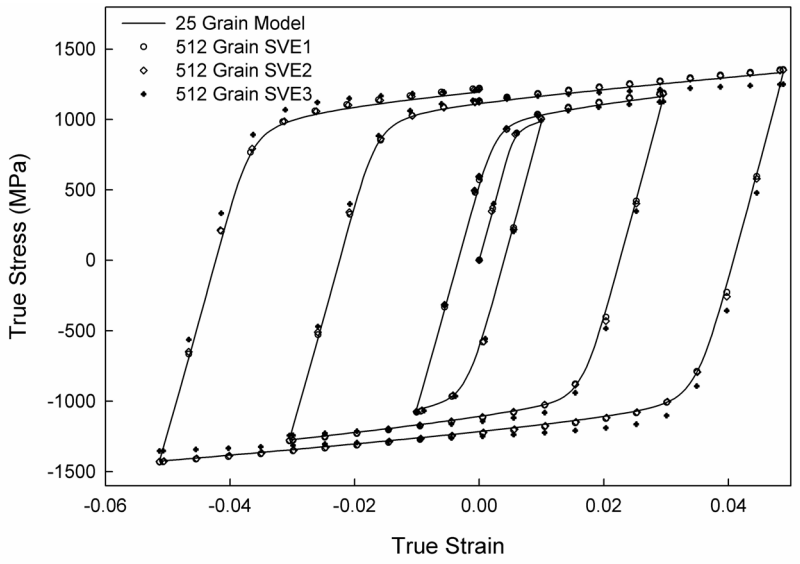

Figure 0.7 Comparison of macroscopic stress-strain response for three SVEs and the 25 grain model.

Ideally, an averaged response is desired from a number of statistical volume elements (SVEs) with more realistic representation of the grain shape (e.g. voronoi tessellated grains) and size distribution (Kanit et al., 2003) for any given microstructure. However, as a first step, the response from one simulation using the 25 cube shaped grain model is used for computational efficiency. To test the accuracy of this model, 3 SVE's were modeled containing 512 grains with realistic representation of shape using a voronoi tessellation scheme. Details on the SVE will be explained in Chapter VII. As seen from Figure 5.7, the stress response from the 25 grain model is in between the responses from the SVEs, therefore, the 25 grain model does an adequate job in correlating the stress-strain response.

5.7 Parameter Estimation

The constants for the constitutive model are obtained by fitting the stress responses for both types of strain histories discussed before for the microstructures listed in Table 5.1. The constants c_{p1}, c_{p2}, c_{p3} and c_{gr} are based on a best-fit of the experimentally obtained critical resolved shear strength, which was determined by converting the 0.2% yield strength, applying the appropriate Taylor factor for a fcc polycrystal with random orientation distribution (M=3.06). Physically reasonable values are used for the material parameters Γ_{APB}, w, D^{α} and b, which are obtained from literature (Wang et al., 2005). The value of $\dot{\gamma}_o$ is based on literature and is kept constant for all microstructures while $\dot{\gamma}_1$ is determined from experimental data. Parameter $\dot{\gamma}_1$ is observed to be very weakly dependent on the microstructure as seen in Table 5.3.

Single crystals are not available for this material, therefore, the slip resistance for the cube slip systems is arbitrarily fixed to be two times the values for the octahedral slip systems (Wang et al., 2005). The parameters h_{pe}, $h_{cb,}$ h_{se} are chosen such that they are in the range of values suggested by Vitek et al. (1996). The initial dislocation density for all slip systems is fixed at 10^5 mm^{-2} which is considered reasonable for this class of alloys (Busso et al., 2000; Feaugas and Haddou, 2003). The ratio of the parameters in the dislocation density evolution equations, k_1/k_2, is maintained constant such that the dislocation density saturates at 10^9 mm^{-2} (Feaugas and Haddou, 2003), while k_1 is determined from the experimental data. The value for k_δ is obtained from Wang et al. (2005). The other material parameters in the model are allowed to vary such that a best fit is obtained for the experimental fatigue data. The microstructures without the primary γ'

precipitates are fitted first and then those containing the primary precipitates are fitted. The fits for the different microstructures are shown in Figures 5.8-5.14 for both the strain histories. Based on these fits, k_1 is observed to be relatively insensitive to the microstructure and is kept constant for all microstructures. The parameter α does not show a strong correlation with the microstructure when no primary γ' precipitates are present; however, it decreases substantially for microstructures containing the primary γ' precipitates. The value of α to first order depends only on the equivalent volume fraction of the primary precipitates, i.e.,

$$\alpha = \left\langle 0.1 + 1.1 f_{p1}'^{2} - 0.68 f_{p1}' \right\rangle \tag{5.14}$$

It should be noted that only two microstructures containing the primary precipitates are available; therefore, the exact functional dependence of this variable in between those data points cannot be determined without additional experimental data. A quadratic dependence of α on the primary precipitate volume fraction is motivated from the study by Busso et al. (2000). The value for C_χ is observed to be very small, indicating that there is very little backstress recovery and there is almost linear hardening. Therefore, the backstress evolution equation (Eq.(5.12)) can be modified with the recovery term removed, i.e.

$$\dot{\chi}^{\alpha} = \left(C_\chi \eta \mu_s b \sqrt{\rho_\lambda^{\alpha}} \right) \dot{\gamma}^{\alpha} = \left(C_\chi \eta_o \right) \frac{Z_o \mu_s b \sqrt{\rho_\lambda^{\alpha}}}{Z_o + k_1 \sqrt{\rho_\lambda^{(\alpha)}}} \dot{\gamma}^{\alpha} \tag{5.15}$$

It is noted that the actual value of η_o cannot be determined uniquely since it acts as a multiplier to C_χ ; the microstructure dependence is embedded in C_χ . Parameter C_χ correlates best with the secondary precipitate volume fraction, f'_{p2}. A polynomial fit is used to determine the functional dependence of C_χ on f'_{p2}, given as

$$C_\chi = 384.06 f'^2_{p2} - 433.98 f'_{p2} + 123.93 \qquad (5.16)$$

where f'_{p2} is the equivalent volume fraction of the secondary γ' precipitates It should be noted that the functional forms in Eqs. (5.14) and (5.16), which are based on best fitting the experimental data, are not physically motivated and therefore these are expected to give good predictions only for those microstructures within the range of the experimentally tested data. The material properties for the model are given in Table 5.3.

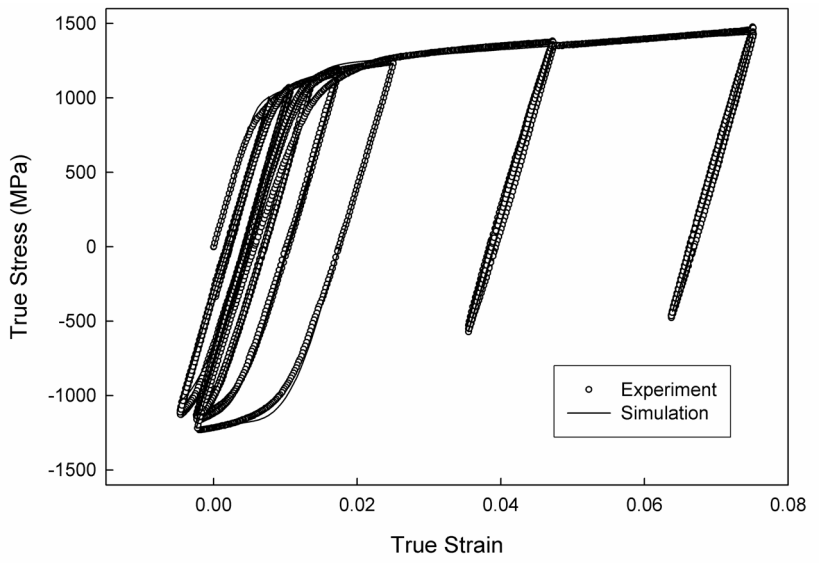

Figure 0.8 Fit for the stress response of Matrix1 microstructure using the 25 grain model at 650ºC for complex strain history without hold period at peak strain before strain reversal.

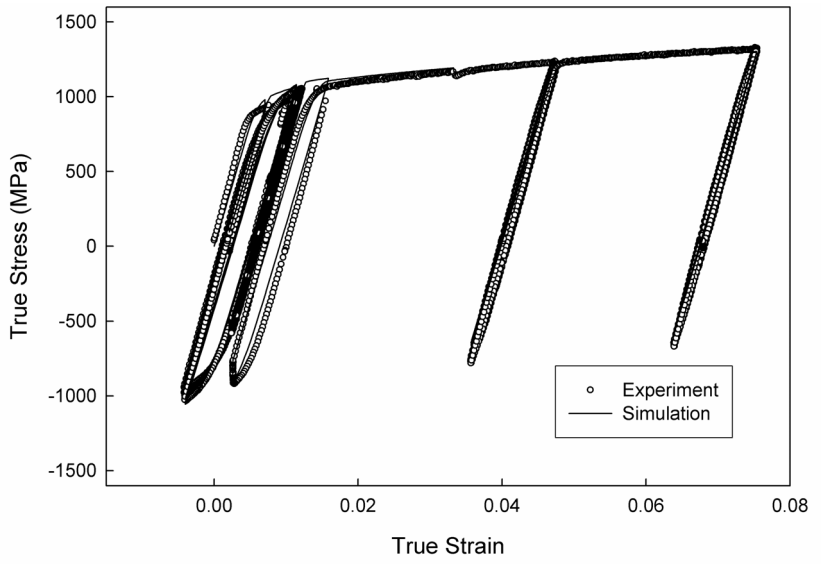

Figure 0.9 Fit for the stress response of Matrix2 microstructure using the 25 grain model at 650ºC for complex strain history with hold period at peak strain before strain reversal.

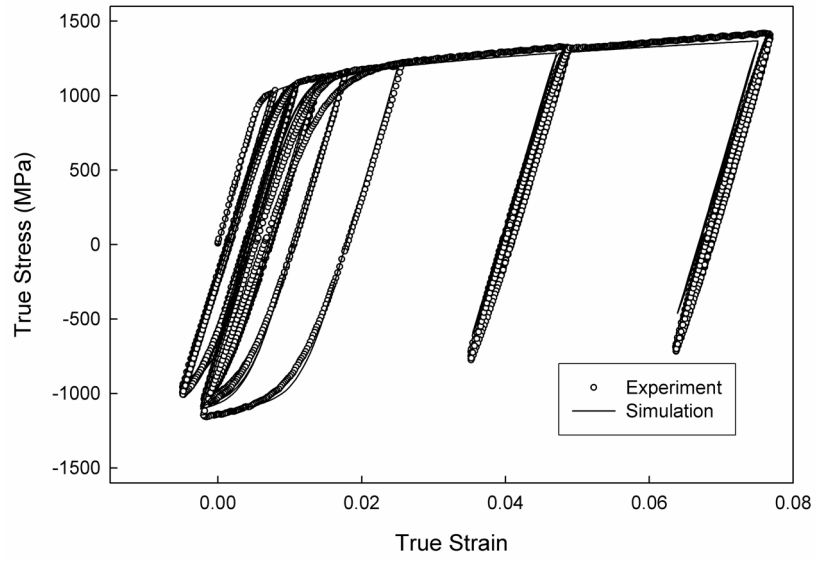

Figure 0.10 Fit for the stress response of Matrix3 microstructure using the 25 grain model at 650ºC for complex strain history without hold period at peak strain before strain reversal.

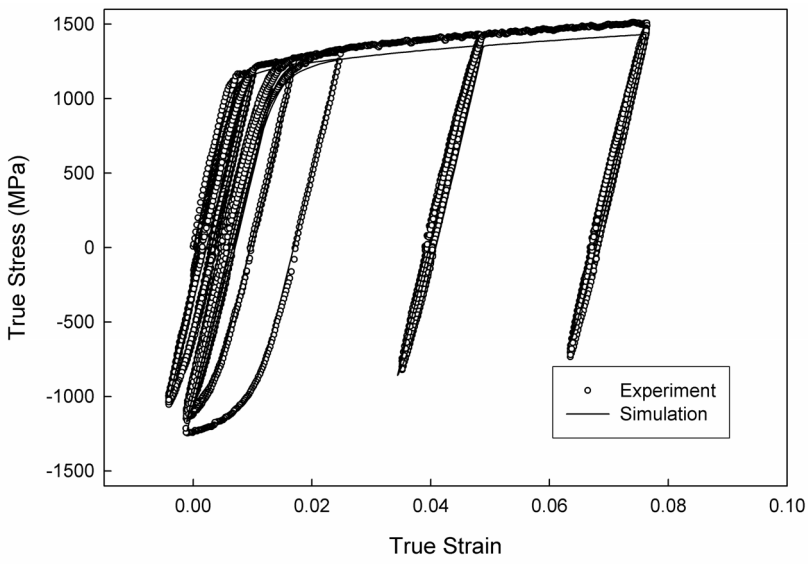

Figure 0.11 Fit for the stress response of Sister Disk microstructure using the 25 grain model at 650ºC for complex strain history without hold period at peak strain before strain reversal.

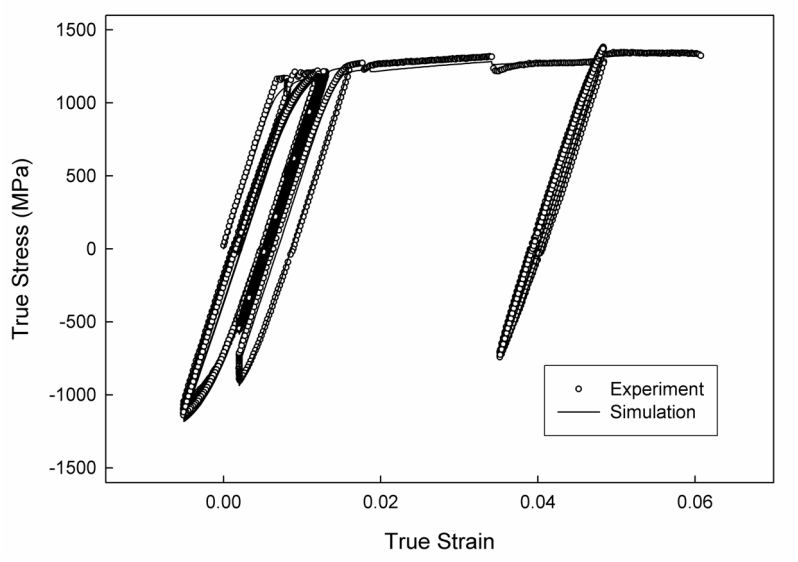

Figure 0.12 Fit for the stress response of Sister Disk microstructure using the 25 grain model at 650ºC for complex strain history with hold period at peak strain before strain reversal.

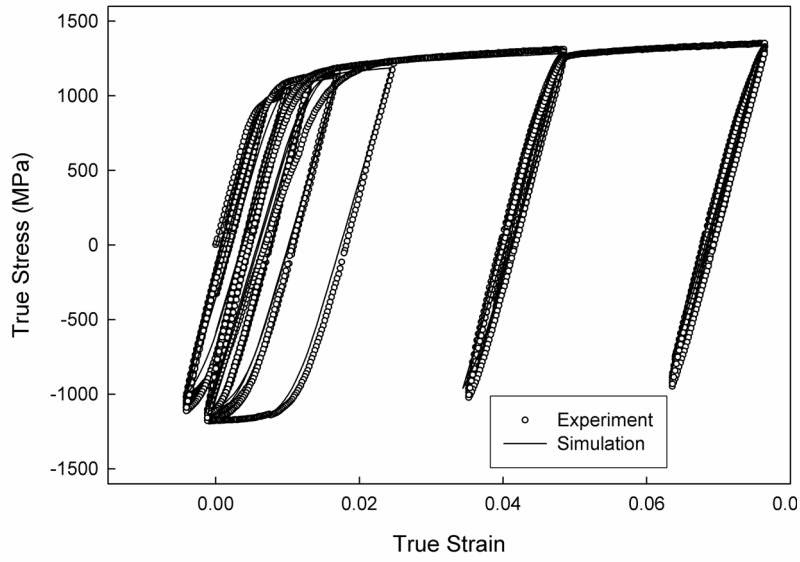

Figure 0.13 Fit for the stress response of Super Weak microstructure using the 25 grain model at 650ºC for complex strain history without hold period at peak strain before strain reversal.

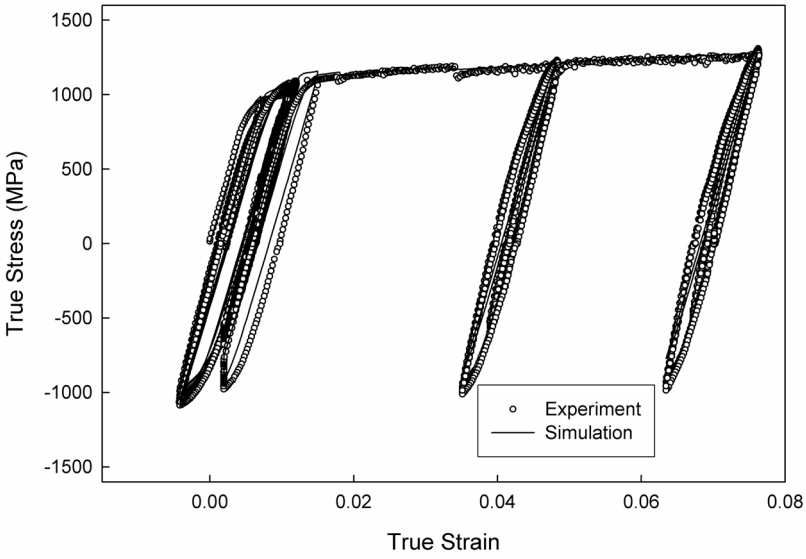

Figure 0.14 Fit for the stress response of Super Weak microstructure using the 25 grain model at 650ºC for complex strain history with hold period at peak strain before strain reversal.

Table 0.3 Material properties for the microstructure dependent model at 650ºC.

Material	α	C_χ	$d_{1\delta}$ (nm)	$d_{2\delta}$ (nm)	$\dot{\gamma}_1$ ($*10^{-10}$ s^{-1})
Matrix1	0.1	3	-	8.2	0.157
Matrix2	0.1	7	92.7	24.7	0.3
Matrix3	0.03	14	35.8	23.9	0.157
Super Weak	0.0	8	-	19.4	0.157
Sister Disk	0.1	2	-	15	0.417

$\tau^{\alpha}_{o,oct}$ (MPa)	$\tau^{\alpha}_{o,cub}$ (Mpa)	c_{p1}	c_{p2}	c_{p3}	c_{gr} (Mpa$\sqrt{mm}$)	k_δ
85.1	170.2	0.225	0.225	16.685	7.2	$5x10^{-3}$

$b_{\gamma'}$ (nm)	b_γ (nm)	$\mu_{\gamma'}$ (Mpa)	μ_γ (Mpa)	k_1 (mm^{-1})	k_2 (mm^{-1})	D^α (Mpa)
0.25	0.41	81515	130150	$2.6x10^5$	8.2	150

h_{pe}	h_{cb}	h_{se}	η_o	w	Γ_{APB} (J/m^{-2})	$\dot{\gamma}_o$ (s^{-1})
0.32	0.0	-0.16	2.82	3.34	$164x10^{-3}$	8.6

$C_{11\gamma'}$ (Mpa)	$C_{12\gamma'}$ (Mpa)	$C_{44\gamma'}$ (Mpa)	$C_{11\gamma}$ (Mpa)	$C_{12\gamma}$ (Mpa)	$C_{44\gamma}$ (Mpa)	n_κ
135000	59210	81515	158860	73910	130150	1

n_1	n_2	f_{p_ref}	d_{3ref} (nm)
9	15	0.4	1

5.8 Results and Discussion

Based on the parameters obtained from the fitting exercise, α and C_χ are observed to be the most microstructurally sensitive parameters at higher inelastic strains, which might be viewed as work hardening parameters for the threshold stress and backstress, respectively; α decreases with increasing the primary precipitate volume fraction, while C_χ decreases with increasing secondary precipitate volume fraction. Single-phase Ni_3Al has a very rapid work hardening rate, which might imply that the presence of large, single crystalline primary γ' particles might lead to increased hardening instead of the observed

decrease in hardening. Further, as the secondary γ' volume fraction increases, one might imagine a greater likelihood of Kear-Wilsdorf (KW) cross-slip locks inside the secondary γ' particles, which would lead to increased strain hardening. It is possible that both the primary γ' particles and larger secondary γ' particles reduce strain hardening by promoting slip heterogeneity. Generally, more heterogeneous and planar dislocation processes lead to reduced strain hardening (Milligan, 2004).

Furthermore, the backstress displayed almost linear hardening with almost no recovery even at high strains ($\varepsilon = 10\%$). However, it should be noted that the differential yielding of the grains leads to an instantaneous kinematic hardening response on load reversal even if no backstress is used in the constitutive model. In Figure 5.15, the backstress term in the constitutive model is not evolved ($\chi = 0$) but a kinematic (backstress) hardening response is observed due to differential yielding of the grains.

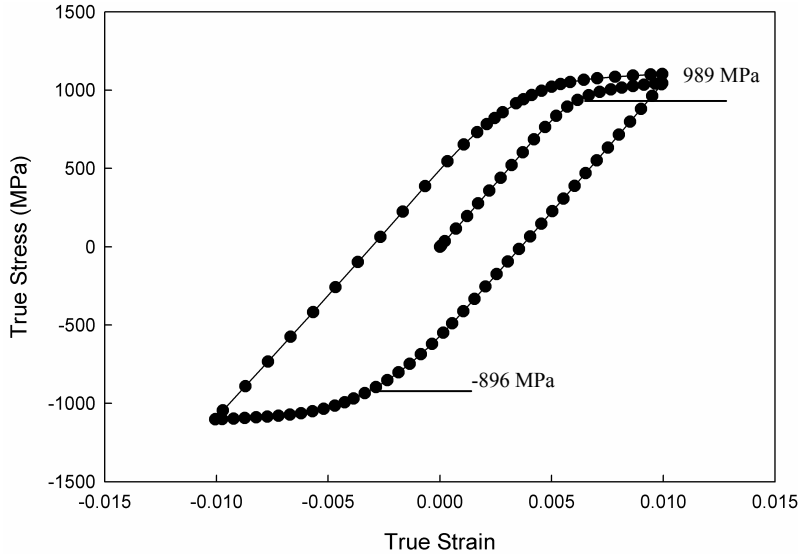

Figure 0.15 Intergranular 'backstress' is obtained from differential yielding (inelastic strain incompatibility) at grain boundary even when backstress variable is not evolved in the constitutive model, i.e., χ=0.

Based on the work of Feaugas and co-workers (Feaugas and Haddou, 2003; Haddou et al., 2004) on pure polycrystalline Ni and Cu, the backstress can be split mainly into two parts: an intergranular backstress and an intragranular backstress. The intergranular backstress saturates very fast at strains less than 0.1% and depends on the grain size while the intragranular backstress is independent of the grain size and is significant only at the higher inelastic strains as shown in Figure 5.16. The backstress due to the differential yielding of grains may is analogous to the intergranular backstress and the explicit backstress term in the constitutive formulation is analogous to the intragranular backstress. It should be noted, however, that the intergranular backstress will also contain contributions from the increase in dislocation density at the precipitate interfaces in the two-phase superalloy.

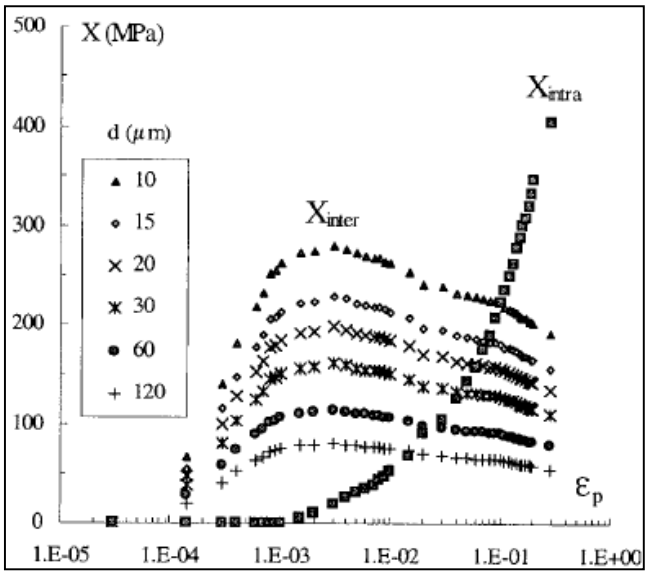

Figure 0.16 Dependence of backstress on grain size and plastic strain in polycrystalline Ni in tension at room temperature (Feaugas and Haddou, 2003).

5.8 Explicit modeling of precipitates

Explicit modeling of precipitates could be very useful in determining physically justifiable functional forms for Eqs.(5.14) and (5.16). The most exhaustive analyses on explicit modeling of precipitates have been carried out by Busso and co-workers (Busso et al., 2000; Busso and Cheong, 2001; Busso and Cailletaud, 2005) and some other researchers (Nouailhas and Cailletaud, 1996; Kumar et al., 2006) on Ni-base superalloys. However, all these analyses were carried out on Ni-base superalloys with a uni-modal distribution of precipitates for monotonic loading conditions at high temperatures (>950°C) at which precipitate shearing does not occur. Cube slip was not considered in these analyses, which should play a prominent role in dictating the orientation dependence of the stress-strain response at high temperatures. It is noted that these analyses are very computationally demanding and the main focus is to study the effect of strain gradient hardening at the precipitate interfaces and grain boundaries.

Explicit modeling of precipitates is not considered in these analyses due to the following reasons:

- IN100 contains a tri-modal distribution of precipitate sizes, which might lead to very complex interactions between these phases. TEM analysis of IN100 (Sinharoy et al., 2001; Milligan, 2004) have led to a better qualitative understanding of the deformation process but more experimental details are needed to develop constitutive models at the precipitate scale to yield any useful results.

- Strain gradient effects are important at the precipitate interfaces and grain boundaries but their effect is most pronounced at the lower plastic strains (just after yielding), which cannot be captured by Busso and co-workers (Busso et al., 2000; Cheong et al., 2005). Furthermore, it was easier to quantify this effect since the precipitates were assumed to be non-shearable, which is not true for the relatively low homologous temperature used in this study. Strain gradient evolution is dealt with in an average sense as defined in Eq. (5.9) and a lower resolution to study this effect is not warranted at this time.
- One of the primary objectives of this model is to study the variability of the fatigue crack incubation life based on the microstructural features. A literature review of existing data on Ni-base superalloys (Findley, 2005) indicates that the crack initiation life is mainly correlated to the grain size and/or inclusion size distribution. Even though the inelastic strain distribution within the grains depends on the precipitate shape and size distribution, a scale lower than the grain size might not be needed. This will be addressed in detail in Chapter VII.

5.9 Limitations

Limitations are discussed next:

- Due to the limited data available on selected microstructures, the model predictions are assumed to hold true only for interpolated microstructures since not all functional forms for the material parameters (e.g. C_{χ}, α) are strictly physically-based.

- Experimental data are not available to validate the model predictions. The contribution in this chapter is to provide a framework to embed the 'first order' microstructural dependencies in a constitutive model is based largely on literature and experimental results.

5.10 Summary

A physically-based rate dependent crystallographic constitutive theory is formulated for predicting the mechanical behavior in a commercial polycrystalline Ni-base superalloy. The microstructural dependence of the stress-strain response is embedded in this model based on experimental cyclic stress-strain data for different microstructures with various γ' precipitate and grain size distributions. The true work hardening rate of both the backstress and threshold stress decreases as a function of the γ' precipitate size. The backstress is interpreted as consisting of two parts: an intergranular backstress due to differential yielding of the grains, and a long range backstress due to the backstress evolution in the constitutive model, which is substantial only at higher inelastic strains. This model is useful in studying microstructural effects on low cycle fatigue behavior and to assist in providing a link of microstructure attributes to macroscopic model parameters, as discussed in Chapter VI. It should also be useful in studying the microstructure dependent variability in fatigue crack formation driving forces in Chapter VII.

CHAPTER VI

Methodology for Informing Microstructure-Dependent Parameters in Macroscopic ISV Model

Abstract

Macroscopic constitutive models for Ni-base superalloys typically do not contain an explicit dependence on the underlying microstructure. Microstructure dependent models are of great importance since the microstructure can vary within a component, depending on the alloy chemistry and the thermomechanical process history. A microstructure dependent macroscopic model is attractive in terms of offering more accurate estimates of component lives for which microstructure is known, and from a design perspective in terms of tailoring more fatigue resistant components. Microstructure features at different scales can affect the stress-strain response in Ni-base superalloys including size, orientation and distribution of grains and γ' precipitates, as well as grain orientation and misorientation distributions.

A physically-based crystal plasticity model with the microstructural dependence embedded in the model was formulated in Chapter V. This chapter focuses on embedding microstructural dependence into parameters of a macroscopic ISV model which is

computationally feasible for industry component analyses. A hierarchical methodology is outlined to embed this microstructural dependence in the macroscale model.

6.1 Introduction

Constitutive models that are formulated to capture material cyclic stress-strain response typically comprise a number of nonlinear equations, each containing a set of material parameters that must be determined experimentally. Therefore, it is highly desirable to use computational microstructure-sensitive models to reduce the experimental load. Microstructural features such as the grain size and the γ' precipitate size and spacing play a very important role in dictating the stress-strain response of Ni-base superalloys. Considerable work has been done in modeling the multiaxial cyclic stress-strain response of Ni-base superalloys using macroscopic viscoelastoplastic models (Nouailhas and Cailletaud, 1996; Busso et al., 2000; Fedelich, 2002; Shenoy et al., 2005; Shenoy et al., 2005; Wang et al., 2005). These models, however, do not contain an explicit dependence of the parameters on the microstructural features. An extensive experimental database is required to determine the functional microstructural dependence of the parameters in the constitutive equations. It might not be always possible to conduct the extensive experimental tests required to uniquely and accurately determine these parameters owing to time, feasibility and/or monetary constraints. Therefore, it is highly desirable to use computational simulations to reduce the number of experiments. A viable strategy for using computational micromechanics as "virtual experiments" is based on:

(i) the use of physically-based micromechanical models that explicitly address key microstructure features,

(ii) calibration of this model to a range of microstructures, and

(iii) simulations of "virtual microstructures" that are interpolated between experimentally calibrated ones.

Accordingly, the model developed in Chapter V is employed to embed microstructural dependence into a macroscale model using the results from the microstructure-dependent physically-based crystal plasticity model.

6.2 Motivation

Phenomenological continuum cyclic plasticity based models that are currently used in the industry serve well for many problems at the macroscopic scale but most of these models do not contain explicit dependence on the material microstructure. A microstructure dependent macroscopic model is attractive from the perspective of prognosis in giving more accurate estimates of component lives for which microstructure is known, and from a design perspective in terms of tailoring fatigue resistance of components.

In metals, plastic deformation can be represented at various length scales. Relevant processes range from the atomic scale at which the atomic arrangement and individual defect properties of a material are of crucial importance for the deformation properties, up to the macroscopic scale where the actual material microstructure is not resolved and plasticity is described on phenomenological grounds. Constitutive equations can be formulated at different length scales. A schematic of the length scales and associated plasticity models in metals was outlined in Figure 1.1, which shows the four distinct length scales at which plasticity may be addressed: nanometer scale (atomistic), the

microscopic scale, the mesoscopic scale and the macroscopic scale. Currently one of the most interesting issues in the computational mechanics of materials community is how to make a smooth and clear connection between plasticity related processes going on at the atomic scale and the plastic material behavior at the macroscale. A solution to this issue would, in principle, lead to the development of a consistent, unified plasticity theory based on a multiscale modeling strategy. There is, of course, no single unique solution.

Microstructural features at different length scales such as the grain size and the γ' precipitate size and spacing play a very important role in dictating the stress-strain response of Ni-base superalloys. An appreciable amount of work has been done at each of these scales; however, linking of the results across the different length scales is relatively still in the nascent stages. Aspects of the material response at some scales may be better understood than at others. A hierarchical scheme would be useful in this sense, since the relevant information in literature across these different scales can be utilized. A computational framework is also desirable since it can express the coupled effects of the microstructural attributes more adequately than isolated models for individual mechanisms, as long as the physics of the mechanisms are adequately incorporated in the constitutive equations.

6.3 Macroscale Model

The difficulty in macroscale characterization of plastic deformation of metals is the formulation of hardening laws that realistically represent hardening behavior for completely general loading histories. A modified form of an already existing Walker-type

macroscale model is used to describe the cyclic behavior of the IN100 microstructures (Chaboche, 1989; Freed and Walker, 1989; Ohno and Wang, 1993).

A uniaxial (1D) form of the macroscale model is formulated since only uniaxial loading histories are investigated in this work. The uniaxial rate of deformation (true strain rate) D is divided into the elastic and inelastic components, i.e.,

$$D = D^e + D^n \tag{6.1}$$

In the isothermal uniaxial case, the stress-strain response is related to the material time derivative of the Cauchy (true) stress since there is no net underlying substructure spin in an initial randomly oriented polycrystal aggregate under this stress state, i.e.,

$$\dot{\sigma} = E\left(D - D^n\right) \tag{6.2}$$

A two-term potential flow rule is employed which is similar to the microscale crystal plasticity model, i.e.,

$$D^n = f_u\left(\left|\sigma - \tilde{\Omega}\right|\right)\mathrm{sgn}\left(\sigma - \tilde{\Omega}\right) = f_u\left(\sigma_v\right)\mathrm{sgn}\left(\sigma - \tilde{\Omega}\right) \tag{6.3}$$

where σ_v is the viscous overstress and the general form for the function f_u is

$$f_u\left(\sigma^v\right) = A_1'(\theta)\left\langle\frac{\sigma^v-\kappa}{K_1}\right\rangle^{p_1}\exp\left\{B_{o1}\left\langle\frac{\sigma^v-\kappa}{K_1}\right\rangle^{p_1+1}\right\} + A_2'(\theta)\left\langle\frac{\sigma^v}{K_2}\right\rangle^{p_2}\exp\left\{B_{o2}\left\langle\frac{\sigma^v}{K_2}\right\rangle^{p_2+1}\right\} \tag{6.4}$$

Here, $\tilde{\Omega}$ is the uniaxial macroscale backstress and κ is the macroscale threshold stress. The flow exponents p_1 and p_2 in Eq. (6.4) are assigned such that $p_1 > p_2$ and $B_{01} = B_{02} = 0$ so as to exclude the effect of the exponential modifier terms; the two term potential may in itself be regarded as an approximation of the power law breakdown regime at higher strain rates (Chaboche, 1989), thereby rendering the exponential terms nonessential. Constants K_1 and K_2 represent drag stresses. $A_1'(\theta)$ and $A_2'(\theta)$ are material parameters which are temperature dependent, however, the temperature dependence of these parameters are not embedded since only one temperature (650°C) is considered.

The backstress, $\tilde{\Omega}$, is decomposed into N components and the following threshold stress (κ) and backstress expressions are employed (Chaboche, 1989):

$$\begin{aligned}\kappa &= \kappa_o + \left[Q_h\left\{1-\exp\left(-b_h p\right)\right\}\right] \\ p &= \int\left|D^n\right|dt\end{aligned} \tag{6.5}$$

$$\dot{\tilde{\Omega}}^i = \frac{A^i}{{\Omega_{lim}}^i}\left({\Omega_{lim}}^i D^n - g\left(\frac{\tilde{\Omega}^i}{{\Omega_{lim}}^i}\right)\tilde{\Omega}^i\dot{p}\right), \quad \dot{\tilde{\Omega}} = \sum_{i=1}^{N}\dot{\tilde{\Omega}}^i \tag{6.6}$$

The second term in Eq. (6.5) corresponds to the isotropic hardening of the material. The total backstress variable $\tilde{\Omega}$ is obtained as the sum of multiple components, $\tilde{\Omega}^i$. Here, Ω^i_{lim} is the backstress norm denoting the asymptotic maximum value of backstress (a constant) in the hardening rule. Setting $g\left(\frac{\tilde{\Omega}^i}{\Omega^i_{\text{lim}}}\right) = 1$ gives the Armstrong-Frederick (1966) kinematic hardening rule with linear dynamic recovery, which is known to be inaccurate for complex histories as it overpredicts ratcheting effects. Based on the work by Ohno & Wang (1993) and further developments in modeling the ratcheting effects under combined states of stress, an option for $g\left(\frac{\tilde{\Omega}^i}{\Omega^i_{\text{lim}}}\right)$ is given by

$$g\left(\frac{\tilde{\Omega}^i}{\Omega^i_{\text{lim}}}\right) = \left\langle \frac{\tilde{\Omega}^i}{\left|\tilde{\Omega}^i\right|}\frac{\dot{\varepsilon}^n}{\left|\dot{\varepsilon}^n\right|} \right\rangle^{\chi_i+1} \left(\frac{\left|\tilde{\Omega}^i\right|}{\Omega^i_{\text{lim}}}\right)^{m^i_g} \tag{6.7}$$

It should be noted that the Macauley bracketed term $\left\langle \frac{\tilde{\Omega}^i}{\left|\tilde{\Omega}^i\right|}\frac{\dot{\varepsilon}^n}{\left|\dot{\varepsilon}^n\right|} \right\rangle$ is either 0 or 1 in the uniaxial case.

The constitutive equations are implemented as a Fortran subroutine termed as 'material point simulator (MPS)' which can generate the stress response for any input strain-time history. A forward Euler scheme is used to integrate the constitutive equations; therefore the time step for each increment is maintained sufficiently small for convergence. The flowchart for the MPS is given in Figure 6.1.

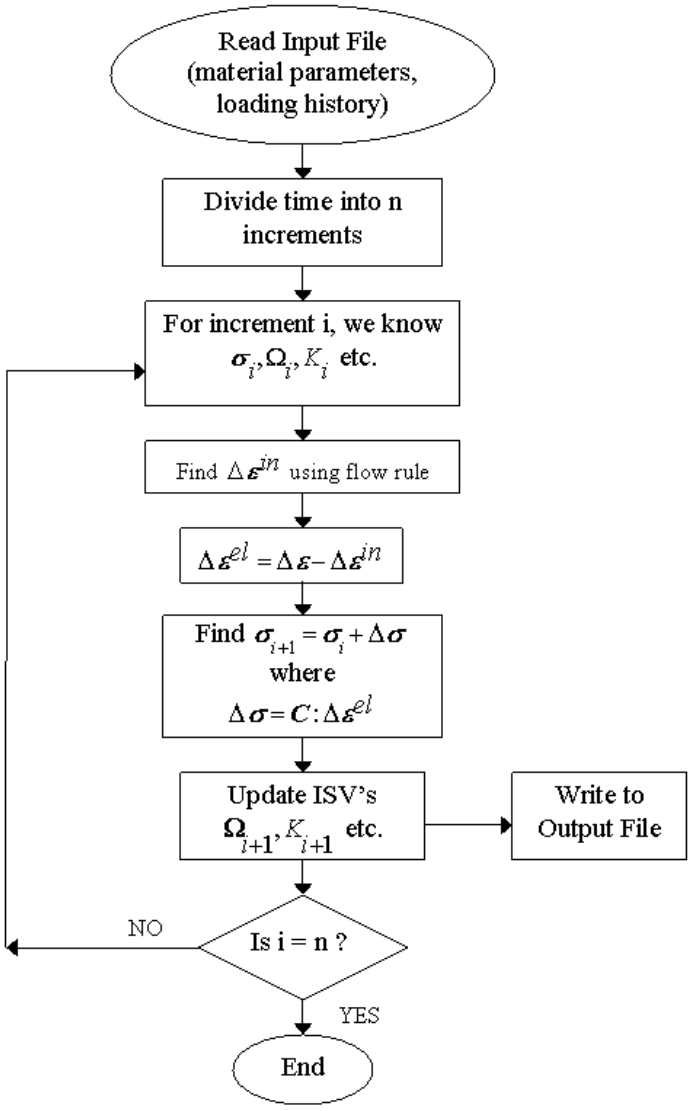

Figure 0.1 Flowchart for the Material Point Simulator (MPS).

6.4 Methodology

Ideally, the microstructure-dependence of the macroscale model (**termed 'macro' model hereafter**) parameters should be determined using an extensive experimental database. In the absence of such data, the crystal plasticity model (**termed 'micro' model hereafter**) is used to determine the microstructure dependence of the 'macro' model. The rationale in using such a scheme is the hypothesis that the 'micro' model is physically-based and should provide representative predictions for the macroscale response. As shown in Figure 6.2, there are mainly three steps involved:

- Step 1 - A stress-strain database is generated for different strain histories using the crystal plasticity 'micro' model for a range of microstructures that are intermediate to the calibrated actual microstructures.
- Step 2 - Macroscopic ISV model parameters are determined for the stress-strain data for each microstructure in the database, including virtual microstructures intermediate to those experimentally characterized, using an optimization scheme.
- Step 3 - An artificial neural network (ANN) is trained to relate the parameters in the 'macro' model to the corresponding microstructural parameters.

Once the ANN is trained, it can be used to predict the material parameters for the macroscopic ISV model for any given microstructure. The ANN is not computationally intensive and results in significant savings of analysis time.

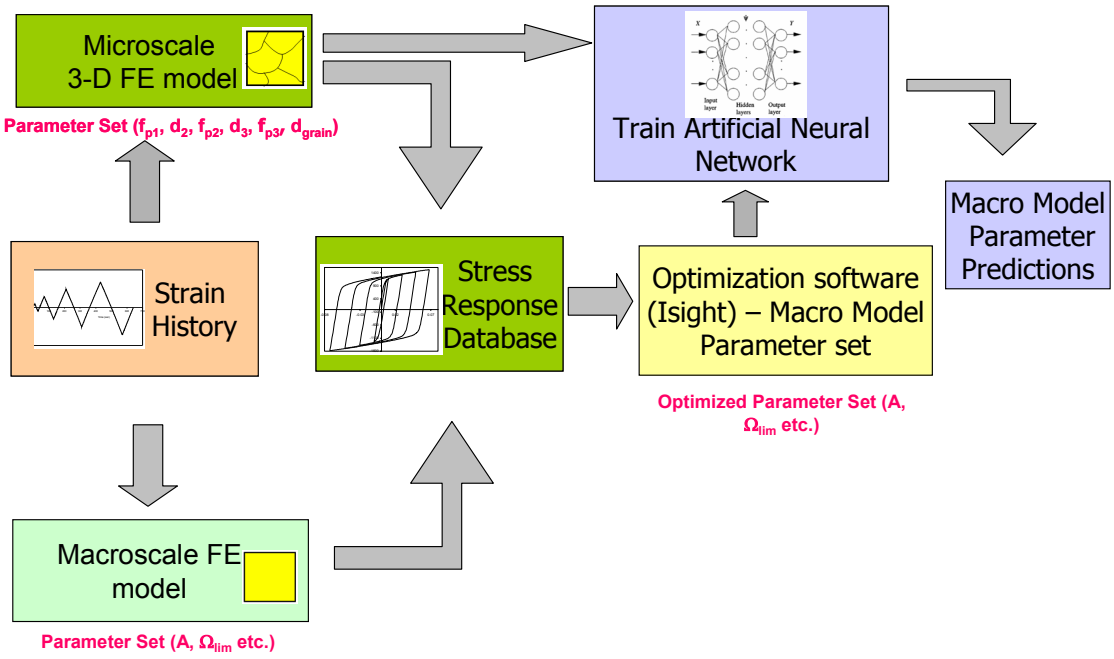

Figure 0.2 Framework for linking the 'micro' model to the 'macro' model.

6.4.1 Step 1: Stress-Strain Database

The strain history that should be used to generate the database depends on the material response that is most crucial to the application, e.g. the cyclic response might be more important than the monotonic response in practical applications. This particular superalloy is used in turbine disks, which are subjected to complex thermal-mechanical loading. Therefore, the rate dependent nature of the material response should be captured accurately for both monotonic and cyclic multiaxial loading histories. However, as a first step, uniaxial strain-controlled loading histories are used to demonstrate this linking framework. This framework can be easily extended for more complex loading histories subject to limits on the rather extensive computational time required for the cyclic crystal plasticity calculations.

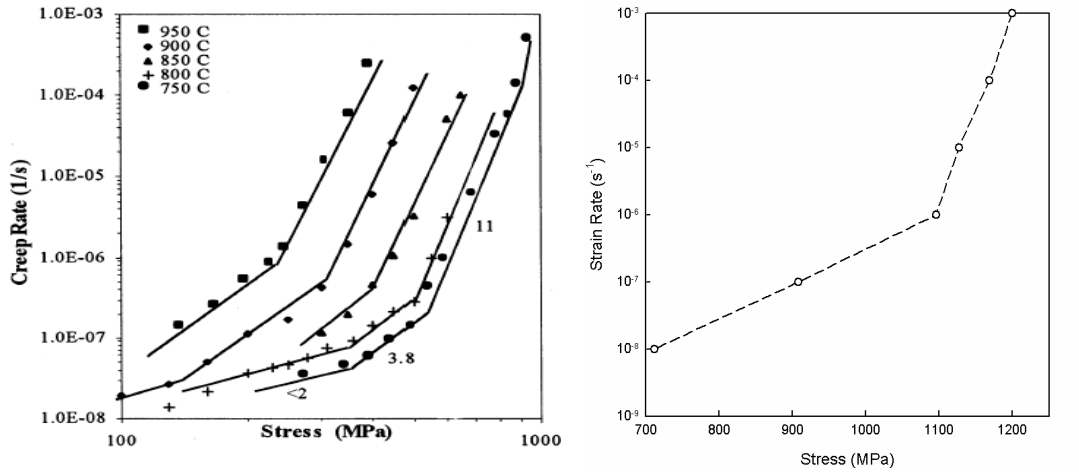

(a) (b)

Figure 0.3 (a) Strain Rate dependence in polycrystalline Ni-base superalloy, GTD111, (Sajjadi and Nategh, 2001) and (b) Strain rate dependence for Sister Disk as a function of stress from the 'micro' model simulations (stress measured at 3% strain) at 650ºC.

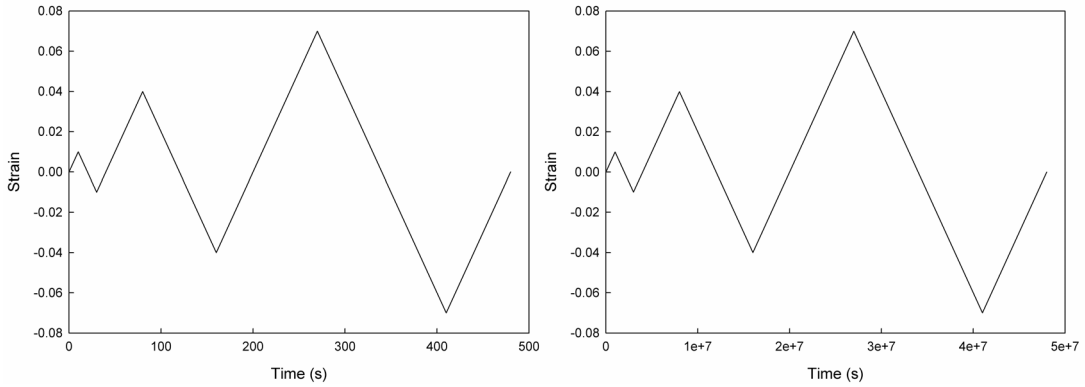

(a) (b)

Figure 0.4 Strain history used to generate the database using the 'micro' crystal plasticity model (a) Strain rate = 10^{-3} s^{-1} and (b) Strain Rate 10^{-8} s^{-1}.

The dependence of stress as a function of strain rate based on the 'micro' model simulations for Sister Disk is plotted in Figure 6.3b. The experimentally observed stress dependence of the strain rate for another Ni-base superalloy, GTD111 is shown in Figure 6.3a for comparison (Sajjadi and Nategh, 2001). The stress at which the power law breakdown takes place are different; however, it should be noted that the yield strength for GTD111 ($\approx$800 MPa) is much lower than Sister Disk (1140 MPa) at 650ºC. It is essential to capture the power law breakdown of the stress response at higher strain rates at which the response is nearly rate independent. Two strain rates are used to calibrate the rate dependence of the 'macro' model: a relatively high strain rate of 10^{-3} s^{-1} and a relatively low strain rate of 10^{-8} s^{-1}. Three uniaxial completely reversed strain cycles are used at each strain rate with strain amplitude of 1, 4 and 7%, respectively, as shown in Figure 6.4. All analyses are conducted at 650ºC.

The microstructure features are varied randomly within the range of the experimental microstructures, as shown in Table 5.1. It is noted that this kind of random assignment does not recognize thermodynamic or kinetic constraints on admissible microstructures. One hundred fifty microstructures are used and the stress response is obtained using the strain history given in Figure 6.4 which is assumed to be enough to train the ANN. More simulations can be run if desired but 150 simulations adequately capture the microstructure dependence of the parameters as will be shown later.

6.4.2 Step 2: 'Macro' Fit

The 'macro' model is subjected to the cyclic strain histories and the material parameters are determined for each microstructure. Optimization software (Epogy, 2004)

is used to minimize the objective function (error), which is based on the L_2 norm of the error between the simulation results (magnitude of stress error between simulations at each strain point) from the 'micro' and 'macro' model. The microstructural dependence is assumed to be entirely embedded in the internal state variables (ISVs) of the 'macro' model. Hence average values are used for the other material parameters, e.g. A_1', p_1, p_2 etc. which are maintained constant for all microstructures; these are given in Table 6.1.

Table 0.1 Material parameters for the macroscale model.

A_1' (s^{-1})	B_{o1}	p_1	$K_1\ (=K_2)$ (MPa)	$\Omega^i(0)$ (MPa)	Ω^2_{lim} (MPa)	B_{o2}	p_2	b_h (MPa)	m^i_g
0.00125	0.	95.	250	0	400	0	7	6.5.	0

The microstructure-dependent parameters are fit using the high strain rate and the low strain rate stress data sequentially. The parameters in the first term in Eq. (6.4) are calibrated using the high strain rate data while the second term is 'tuned off'. Next, the second part of the flow rule is activated and parameters are optimized while the optimized parameters (from the first fit) in the first term are maintained constant. The first term accounts for the high strain rate dependence while the second term accounts for the low strain rate regime.

The L_2 norm of the error between the simulation results from the 'micro' and 'macro' model is calculated as

$$\text{Error} = \sum_i W_i \left(\sigma_{\text{micro}} - \sigma_{\text{macro}}\right)_i \tag{6.8}$$

where W_i is the weight, σ_{micro} is the stress from the 'micro' model and σ_{macro} is the stress from the 'macro' model. An automated algorithm is developed to identify the inelastic region and a differential weighting scheme is used.

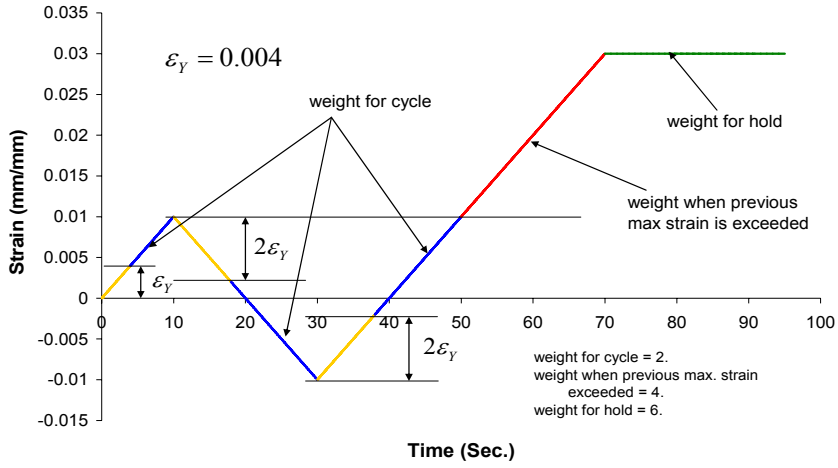

Figure 0.5 Weighting scheme for a given strain history (Tjiptowidjojo, 2006).

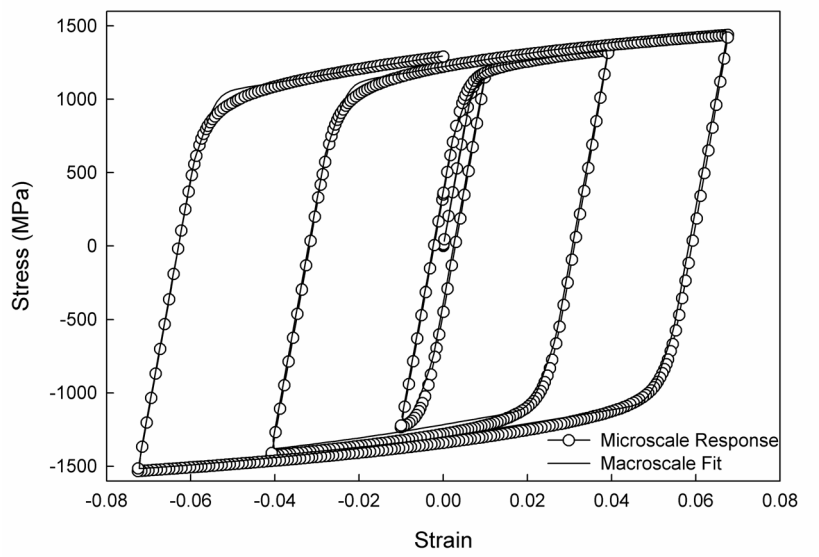

Figure 0.6 Representative fits for the 'macro' model with two backstresses using the optimization scheme (T=650ºC, strain rate = 10^{-3} s^{-1}).

The assignments of the weights are described in Figure 6.5. Using this weighting scheme, more weight is given to the hardening and the stress relaxation behavior by assigning appropriate weights; the weight of the elastic parts is set to zero. It is important to note that the assignment of weights is made by considering the strain-time history prior to integrating the model, which is highly desirable. Representative fits for the 'micro' and 'macro' model data using the optimization scheme are shown in Figure 6.6.

6.4.3 Step 3: Artificial Neural Network (ANN)

Artificial neural networks are often used to identify cause-and-effect patterns for complex nonlinear systems in the field of computational mechanics(Okuda et al., 1994; Sumpter and Noid, 1996; Yagawa and Okuda, 1996; Huber and Tsakmakis, 2001). Some of the advantages of using an ANN are as follows (Yagawa and Okuda, 1996):

- One can automatically construct a nonlinear mapping from multiple input data to multiple output data in the network through a learning process of some sample input versus output relations
- The network has a capability of the so-called 'generalization' such that the trained network can predict the output data satisfactorily even for unlearned input data, provided the training data is sufficiently extensive.
- The trained network operates very quickly and requires minimal computational resources

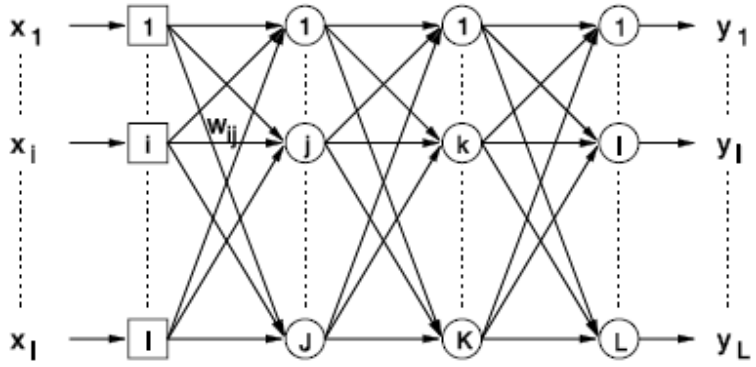

Figure 0.7 Schematic of an artificial neural network containing an input layer, two hidden layers and an output layer (Huber and Tsakmakis, 2001).

A sketch of a hierarchical neural network is shown in Figure 6.7. It consists of neurons connected with links to a highly parallel structure. Each neuron possesses a local memory and can carry out localized processing information processing operations. In general, each neuron has multiple inputs (x_i) and a single output value (y_i) to mimic the biological brain neuron (Huber and Tsakmakis, 2001). The inputs are operated and transformed into the output by the state transition rule, i.e.,

$$\begin{aligned} \upsilon_j &= \sum w_{ij} y_i + \Theta_j \\ y_j &= f(\upsilon_j) \end{aligned} \qquad (6.9)$$

where y_i and y_j in Eq. (6.9) denote the output from a neuron *i* acting as an input on neuron j and the output of neuron j respectively. Also, w_{ij} is the synaptic weight, Θ_j is the bias and υ_j is the state variable of the synaptic weights, which gives the connection strength of the neurons. The weighted signals are summed up in υ_j and transformed into the

output signal through an activation function. An error function is calculated based on the desired output, d_ℓ and the calculated error, y_ℓ. The weights are updated based on the training data such that the error function is minimized.

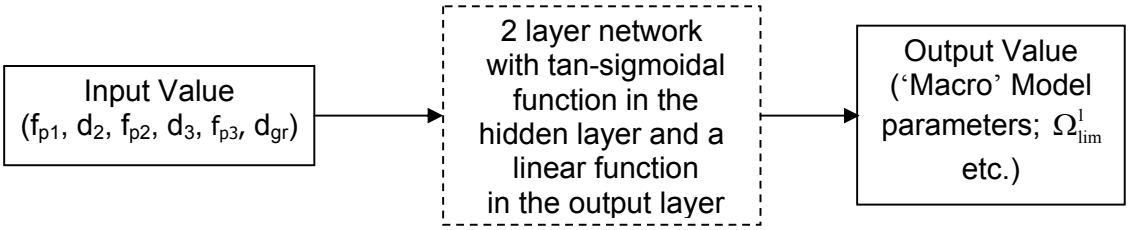

Figure 0.8 The 2 layer ANN with the microstructural variables as input and the 'macro' model parameters as output.

The Neural Network Toolbox in MATLAB is used to perform the training using 150 simulation dataset. In this particular ANN only two layers are used, a hidden layer and an output layer. The microstructural parameters are used as the input parameters and the 'macro' model parameters are used as the output variables, as shown in Figure 6.8. A tan-sigmoidal function is used in the hidden layer given as

$$f\left(\upsilon_j\right)=\frac{2}{1+e^{-\upsilon_j}} \tag{6.10}$$

which varies from -1 to 1. The number of neurons in the hidden layer is varied such that the error is minimized. A linear function is used in the output layer. The backpropagation method is used with the Levenberg-Marquardt training algorithm for the optimization.

For a quick evaluation of the quality of the neural network during training, an error measure denoted by 'mse' is used which is employed, defined by

$$\text{mse} = \frac{1}{\text{L}} \sum_{\ell=1}^{\text{L}} \left(\text{d}_\ell - \text{y}_\ell \right)^2 \tag{6.11}$$

where d_ℓ is the desired output, and y_ℓ is the calculated error. As explained before the material parameters for the 'macro' model are available for 150 microstructures. The overall dataset is divided into three subsets; training data, validation data, and test data. The first subset is the training set, which is used for computing the gradient and updating the network weights and biases. The second subset is the validation set. The error on the validation set is monitored during the training process. The validation error normally decreases during the initial phase of training, as does the training set error. However, when the network begins to overfit the data, the error on the validation set typically begins to rise. When the validation error increases for a specified number of iterations, the training is stopped, and the weights and biases at the minimum of the validation error are returned. The test set error is not used during the training, but it is used to compare different models. Overall 1/2 of the data are used for the training set, 1/4 for the validation set, and 1/4 for the test set.

6.5 Uniqueness versus Accuracy

The 'macro' model can potentially have multiple kinematic (or backstress) components as given in Eq. (6.6).

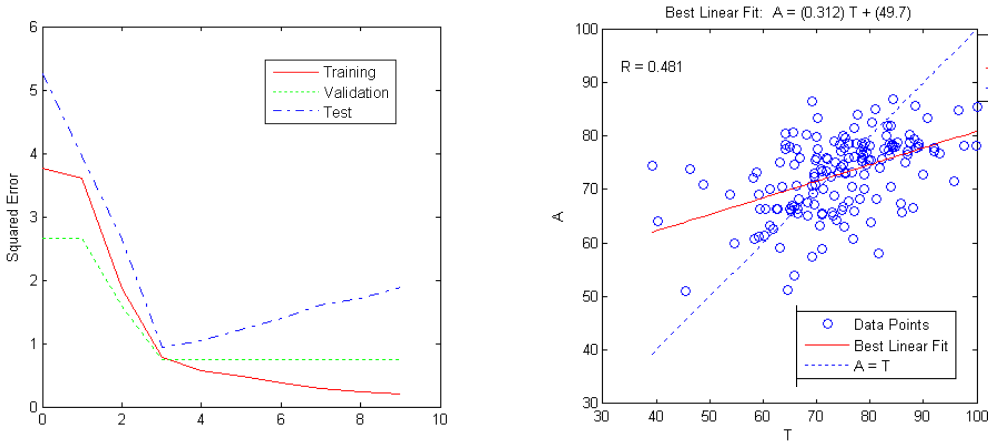

Figure 0.9 The error in Ω^{l}_{lim} for the training, validation and test data sets (left) and the predicted values (A) and target values (T) (right), for the three backstress component model.

The accuracy in capturing the stress response increases with the number of internal state variables (ISVs) that are used; however, this is at the cost of uniqueness of some of these parameters. The challenge is to obtain the minimum number of ISVs, which can capture the stress response adequately. As a first guess, N=3 backstress components were used. The ANN was trained for the three backstress component model using the scheme explained before. Constraints were set on the range of values of the backstress hardening parameters (A^{i}) for the short, intermediate and large range backstress components. The errors in the predicted values from the trained network for the backstress parameters were observed to be very high. For example, the error and predictions for Ω^{l}_{lim} are shown in Figure 6.9. This is seen to be the case despite having very good fits for the stress data. This shows that the ANN struggles in capturing the microstructural dependence of the material parameters in the 'macro' model due to lack of uniqueness in the material parameters.

Based on the previous results, it is concluded that the three backstress component model exhibits substantial non-uniqueness in modeling the cyclic stress-strain response. In other words, multiple parameter sets can effectively describe the same response; this renders the prospect of relating parameters to microstructure variation, and then to physical microstructure attributes, very difficult. Accordingly, a model with two backstress components is used and the material parameters for the 150 microstructures are determined for the 'macro' model. Constraints are set on the range of values for the backstress hardening terms (A^i) to render more consistent trends of short and long range backstress components with microstructure. The two backstress model can be justified based on the literature in terms of intergranular and intragranular backstress in single phase polycrystalline alloys (Feaugas and Haddou, 2003; Haddou et al., 2004), referred to in earlier discussion (Chapter V).

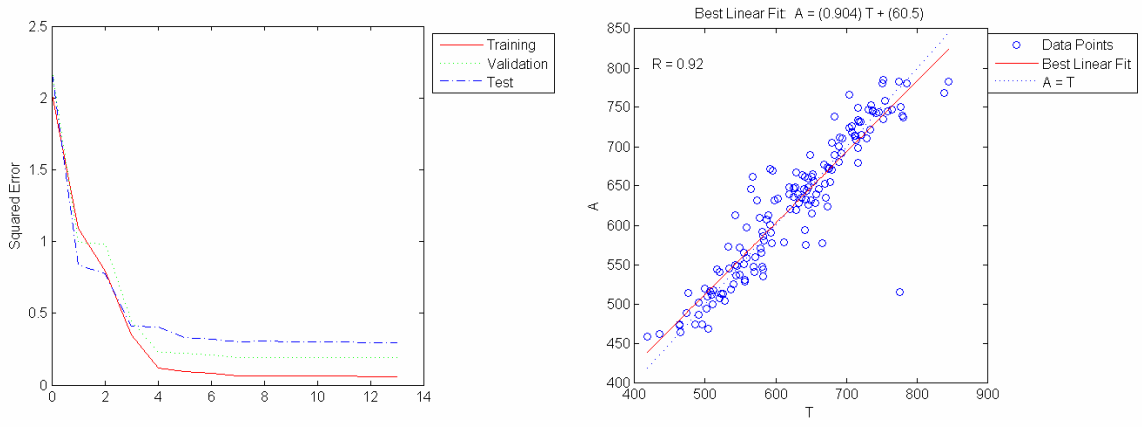

Figure 0.10 The error in κ_o for the training, validation and test sets (left) and the predicted values (A) and target values (T) (right), for the two backstress model.

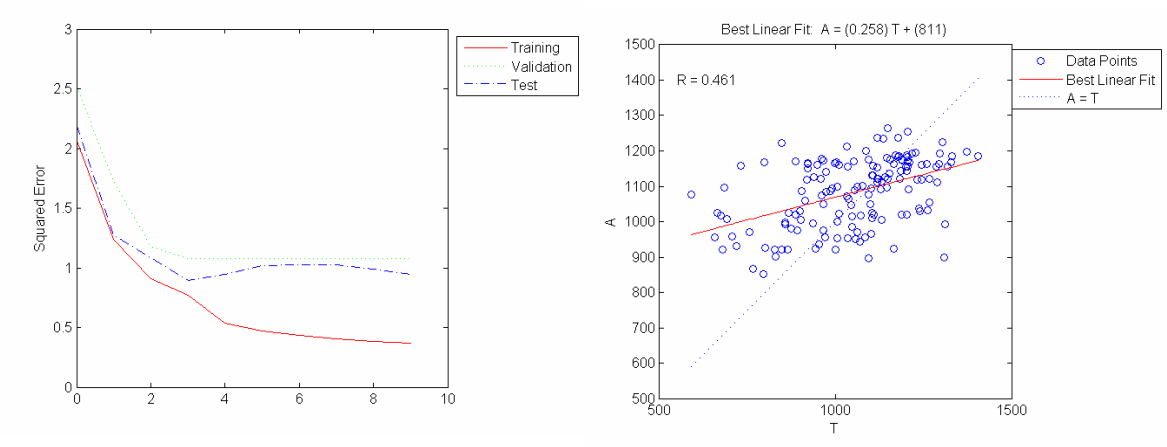

Figure 0.11 The error in A^1 / Ω^1_{lim} for the training, validation and test sets (left) and the predicted values (A) and target values (T) (right), for the two backstress model.

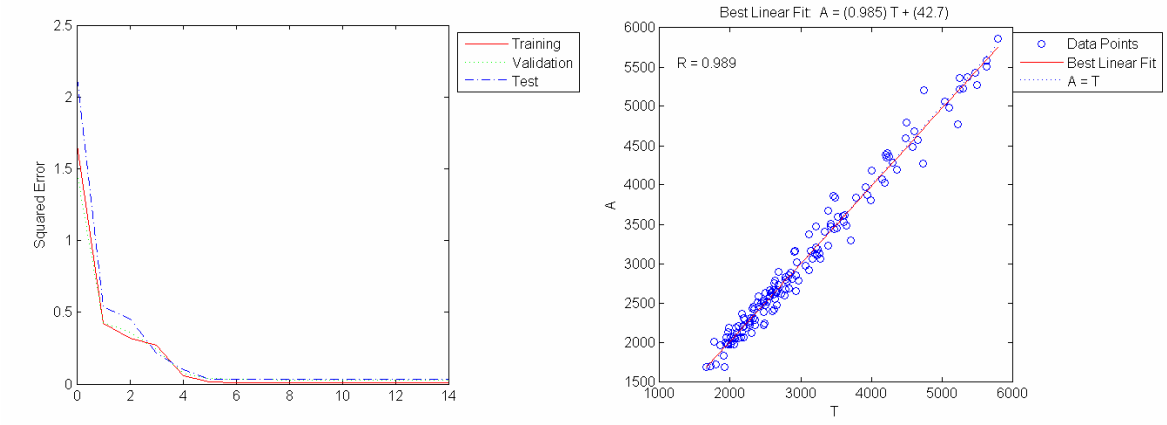

Figure 0.12 The error in A^2 for the training, validation and test sets (left) and the predicted values (A) and target values (T) (right), for the two backstress model.

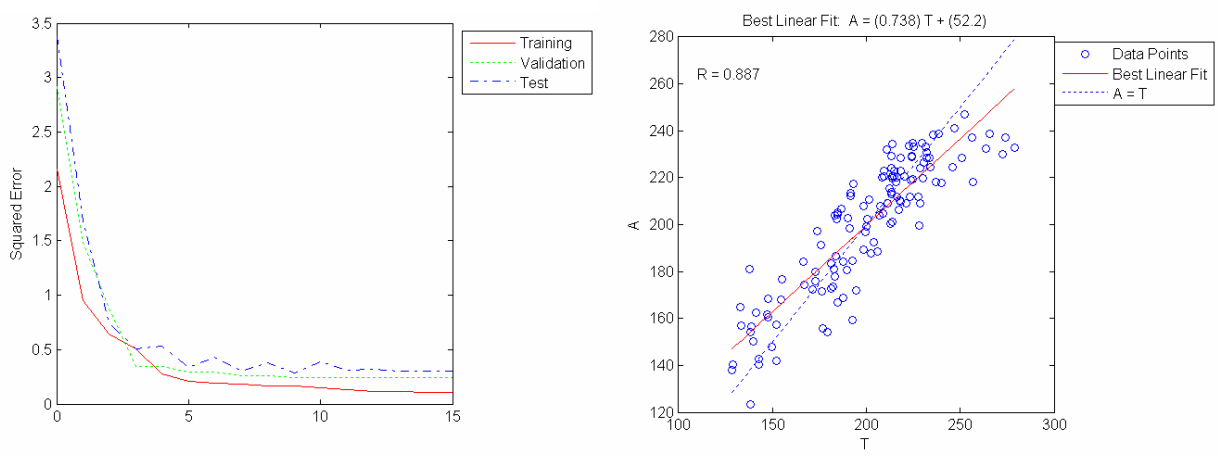

Figure 0.13 The error in Ω^{1}_{lim} for the training, validation and test sets (left) and the predicted values (A) and target values (T) (right), for the two backstress model.

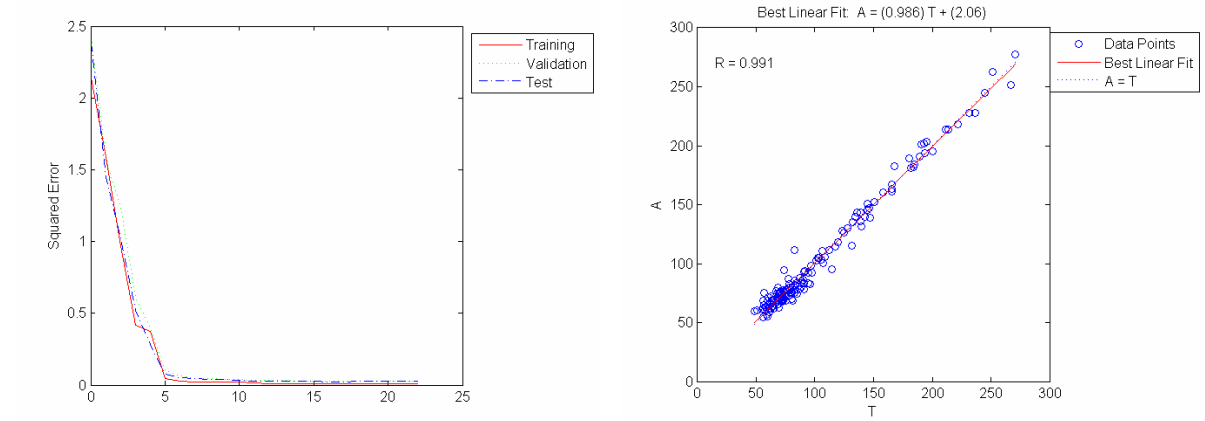

Figure 0.14 The error in Q_h for the training, validation and test sets (left) and the predicted values (A) and target values (T) (right), for the two backstress model.

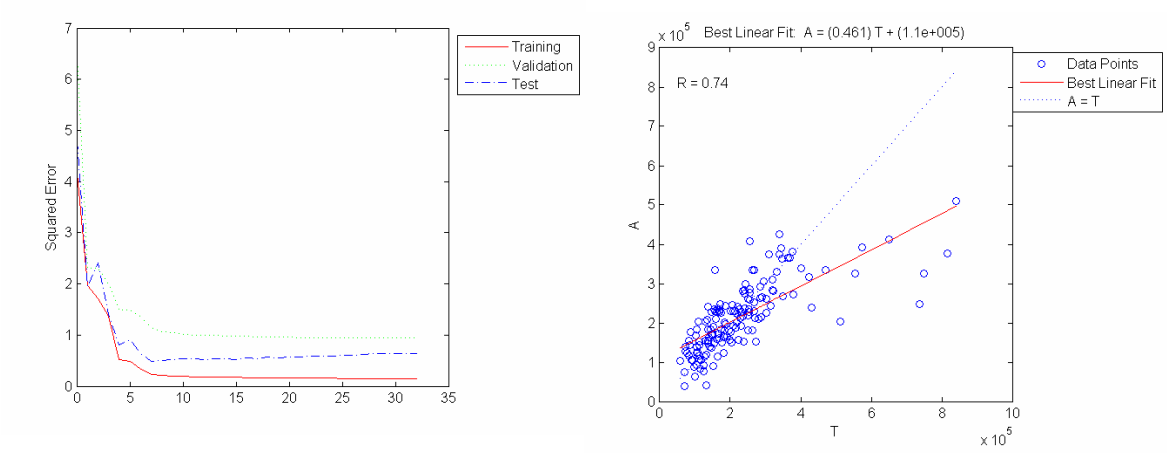

Figure 0.15 The error in A_2' for the training, validation and test sets (left) and the predicted values (A) and target values (T) (right), for the two backstress model.

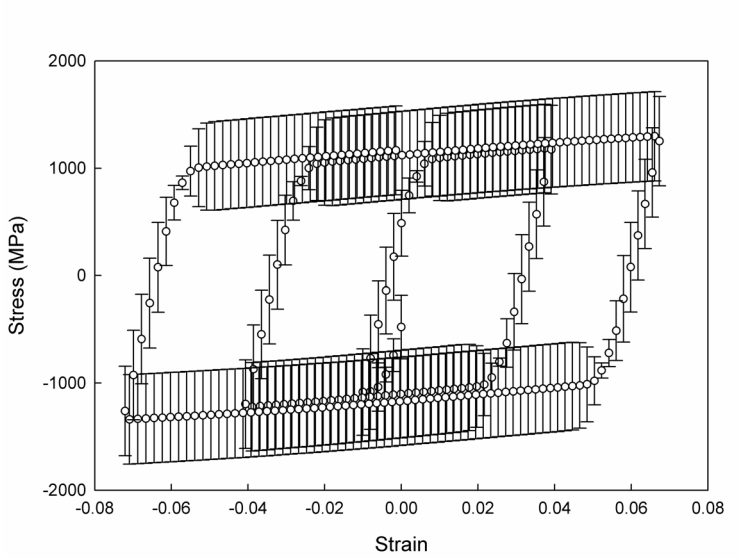

Figure 0.16 The sensitivity of the stress response to κ_o (strain rate = 10^{-3} s^{-1}).

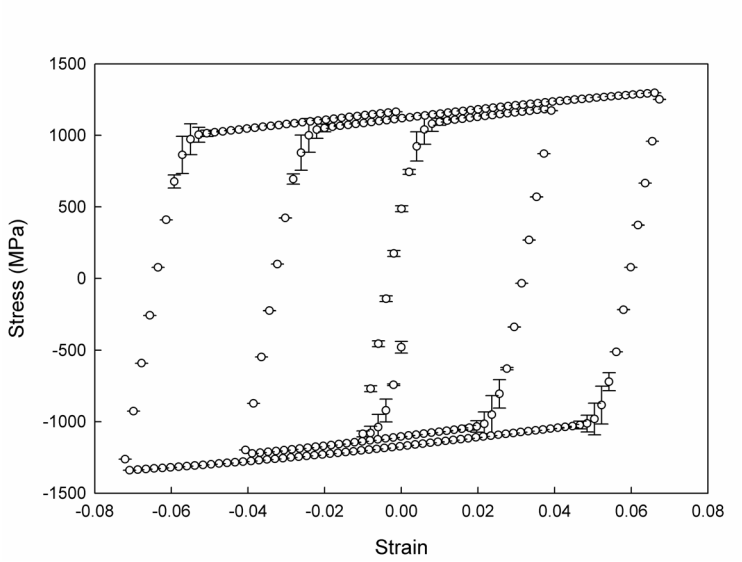

Figure 0.17 The sensitivity of the stress response to A^1 (strain rate = 10^{-3} s^{-1}).

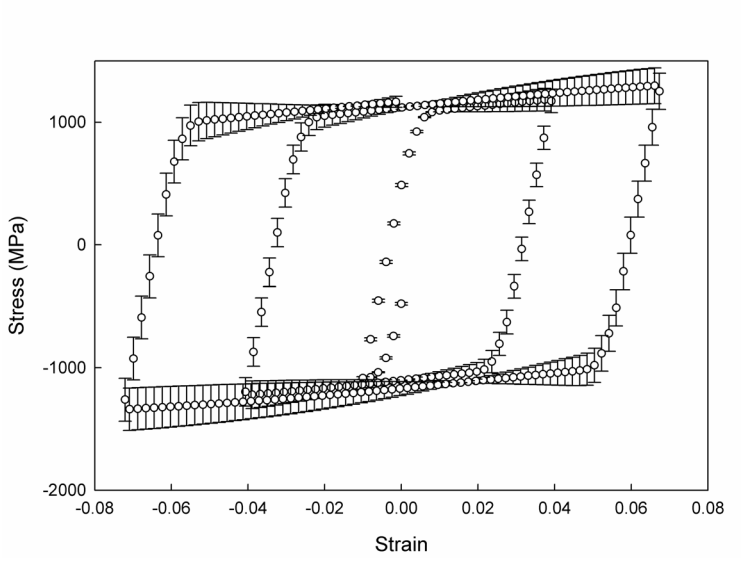

Figure 0.18 The sensitivity of the stress response to A^2 (strain rate = 10^{-3} s^{-1}).

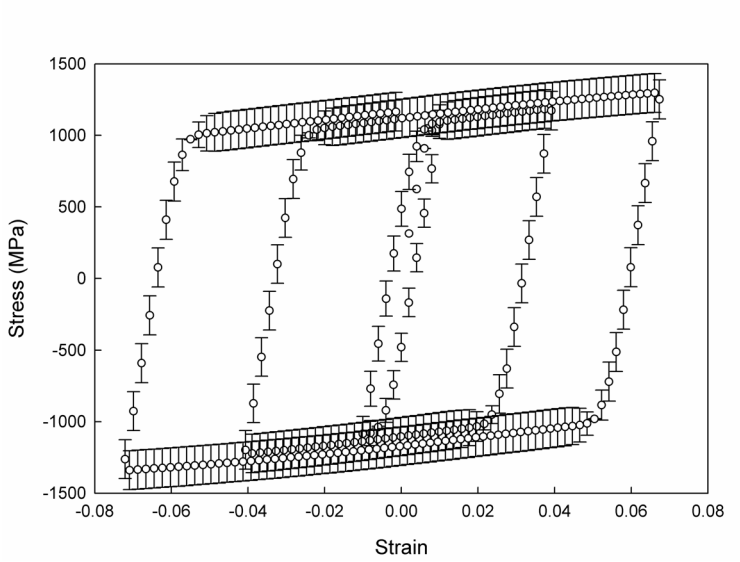

Figure 0.19 The sensitivity of the stress response to Ω^{l}_{lim} (strain rate = 10^{-3} s^{-1}).

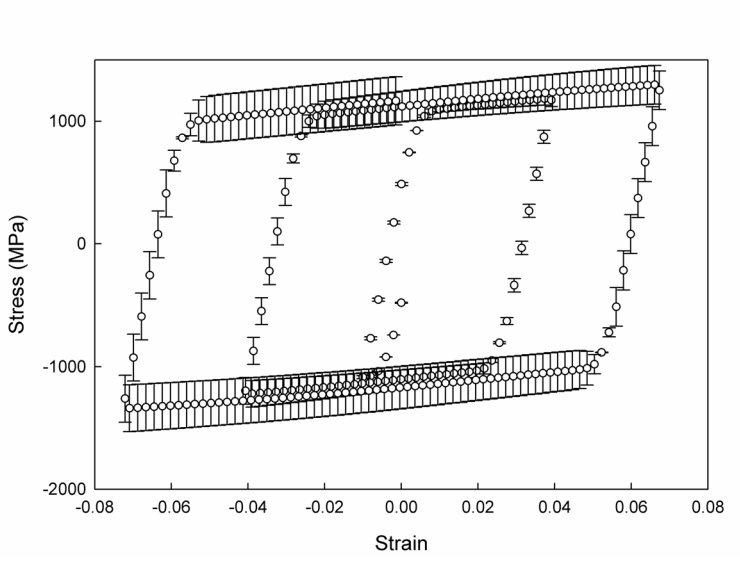

Figure 0.20 The sensitivity of the stress response to Q_h (strain rate = 10^{-3} s^{-1}).

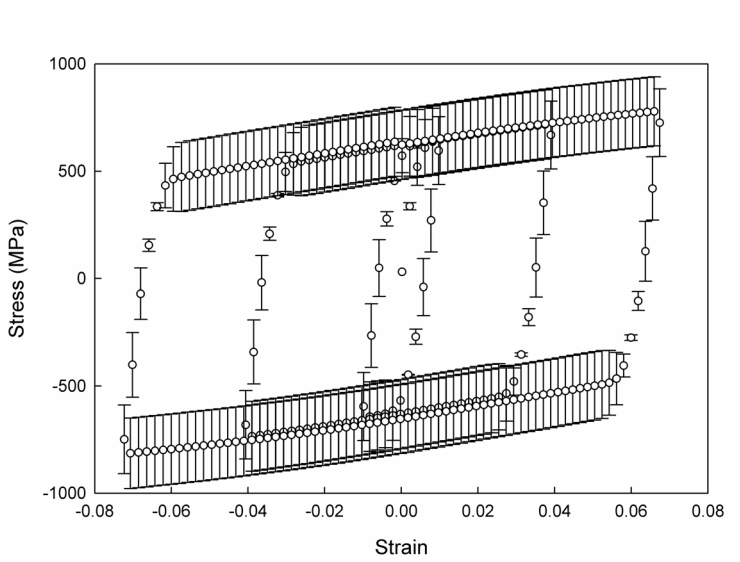

Figure 0.21 The sensitivity of the stress response to A_2' (strain rate = 10^{-8} s^{-1}).

The ANN again is trained for the two backstress component model. The errors and predictions for the macroscale parameters are shown in Figures 6.10-6.15. The errors and predictions for the two backstress component model offer a significant improvement in correlation relative to the three backstress component model, for example compare correlations for Ω_{lim}^{l} in Figure 6.9 and 6.13. All parameters display good correlation except for A^1. A sensitivity study of the stress response with regard to these parameters is conducted. Extremal values of these 'macro' model parameters (for the 150 microstructures) are used to obtain the range of the stress response. These are denoted by the vertical bars for the average stress at each strain value as shown in Figures 6.16 -6.21. From Figures 6.16 -6.21, the stress response is observed to be most sensitive to κ_o and is least sensitive to A^1. Therefore, even though good correlations are not obtained for A^1, it does not lead to significant errors in the stress prediction. Furthermore, it is noted that the

stress response is insensitive to A^2 at higher strain rates, but it is very sensitive at low strain rates, as seen in Figure 6.21.

6.6 ANN Prediction

6.6.1 New Microstructure Predictions

The trained ANN is used to predict the macroscale parameters for several uncorrelated microstructures. The macroscale stress response is compared to stress response obtained from the 'micro' model simulations. Three representative stress strain response predictions for randomly chosen microstructure and different strain-time histories are shown in Figure 6.22-6.24, which shows that the trained ANN does an adequate job in capturing the microstructural dependence of the macroscale parameters. It is acknowledged that better correlations can be obtained with a larger training dataset, if desired.

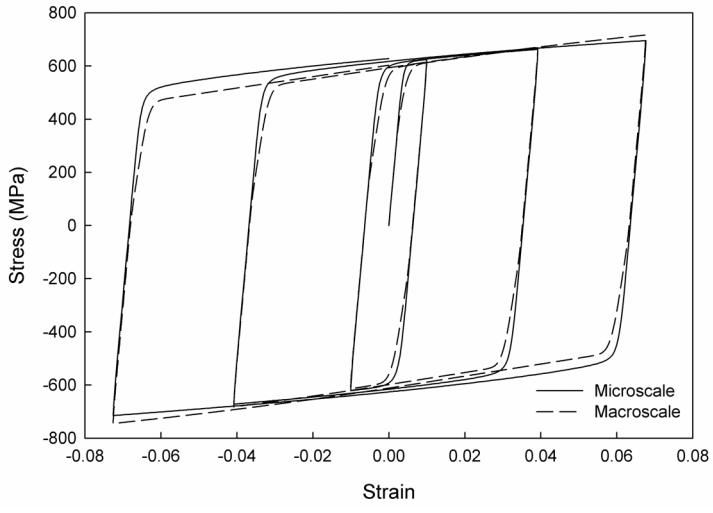

Figure 0.22 Stress response prediction from the trained neural network (strain rate = 10^{-8} s^{-1}, $f_{p1} = 0.07$, $f_{p2} = 0.436$, $d_2 = 332$ nm, $d_3 = 13$ nm, $f_{p3} = 0.053$, $d_{gr} = 17.7$ μm).

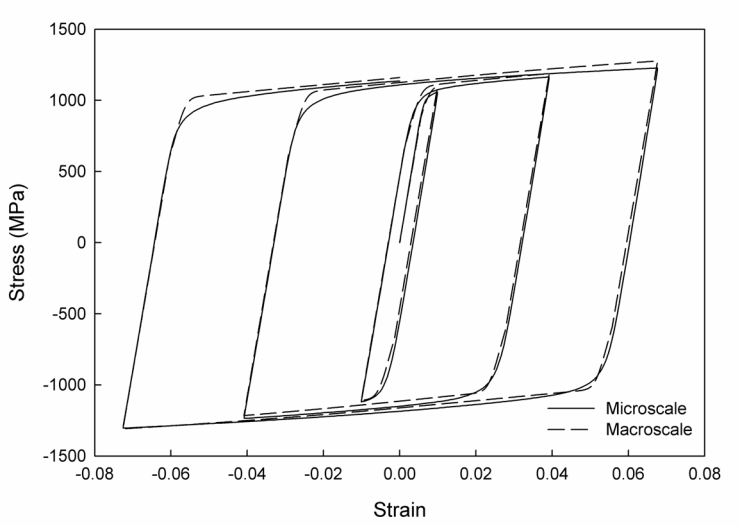

Figure 0.23 Stress response prediction from the trained neural network (strain rate = 10^{-8} s^{-1}, $f_{p1} = 0.108$, $f_{p2} = 0.386$, $d_2 = 261$ nm, $d_3 = 17.9$ nm, $f_{p3} = 0.078$, $d_{gr} = 24$ μm).

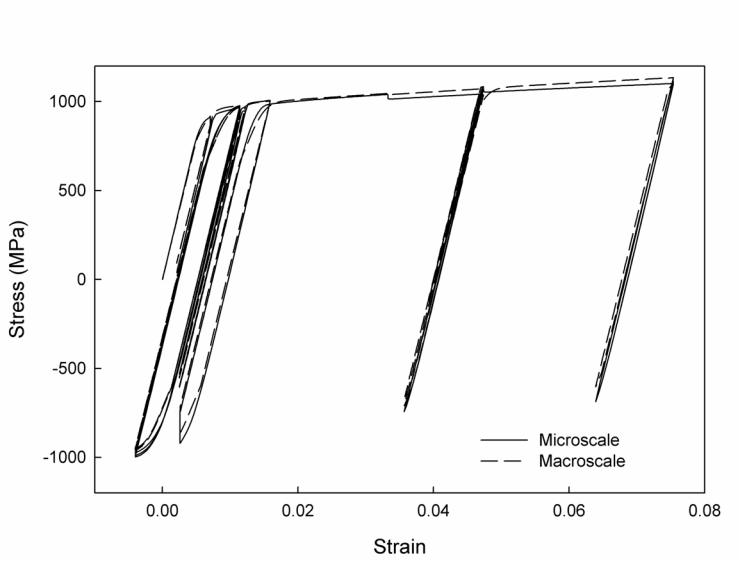

Figure 0.24 Stress response prediction from the trained neural network (variable strain rate, $f_{p1} = 0.166$, $f_{p2} = 0.362$, $d_2 = 209$ nm, $d_3 = 11.6$ nm, $f_{p3} = 0.047$, $d_{gr} = 22$ μm).

6.6.2 Microstructure Dependence

The trained ANN is used to study the dependence of the 'macro' material parameters on the microstructural features. The dependence of the material parameters are studied with regard to the grain size, secondary and tertiary γ' precipitate size, secondary precipitate volume fraction, and the primary γ' precipitate volume fraction.

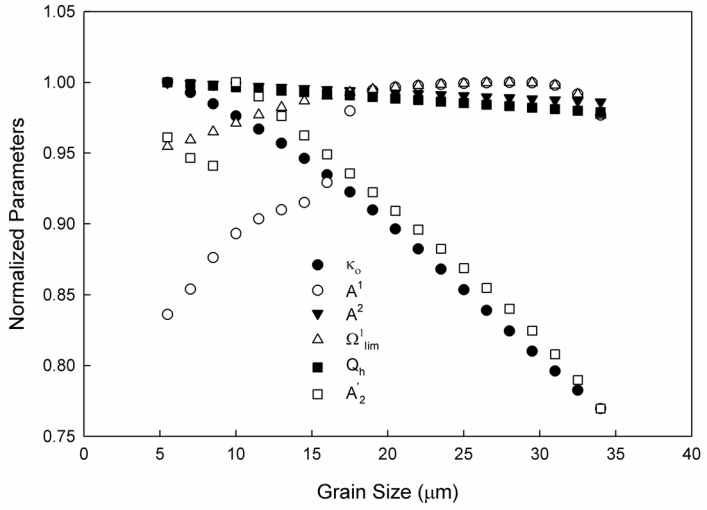

Figure 0.25 Dependence of the 'macro' model parameters on the grain size ($\kappa_{o\max} = 742.8$ Mpa , $\Omega^1_{\lim\max} = 214.3$ Mpa , $A^1_{\max} = 237780\ s^{-1}$, $A^2_{\max} = 3163.7\ s^{-1}$, $Q_{h\max} = 275.8$ MPa , $A'_{2\max} = 379986\ s^{-1}$).

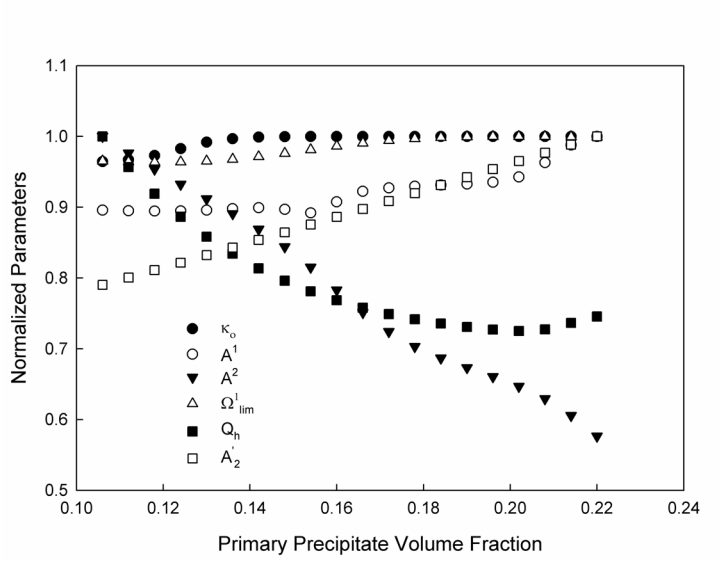

Figure 0.26 Dependence of the 'macro' model parameters on the primary γ′ precipitate volume fraction. ($\kappa_{omax} = 661.4$ Mpa , $\Omega^1_{limmax} = 203.1$ Mpa , $A^1_{max} = 225000\ s^{-1}$, $A^2_{max} = 3596\ s^{-1}$, $Q_{hmax} = 94.1$ MPa , $A'_{2max} = 238287\ s^{-1}$).

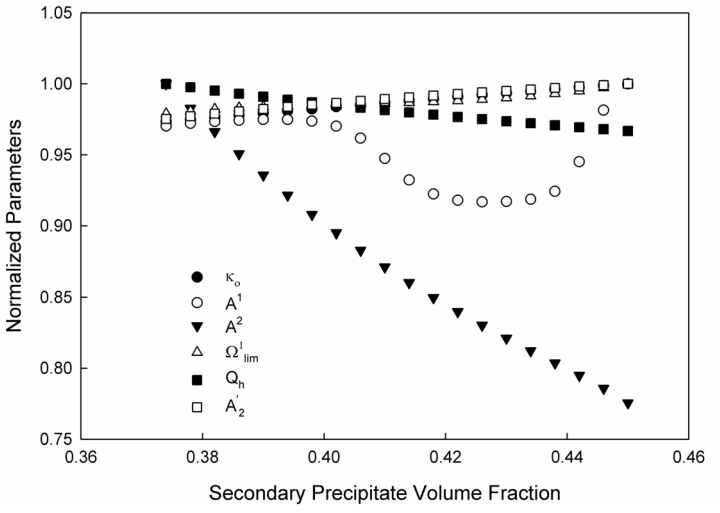

Figure 0.27 Dependence of the 'macro' model parameters on the secondary γ′ precipitate volume fraction. ($\kappa_{omax} = 733.3$ Mpa , $\Omega^1_{limmax} = 220.04$ Mpa , $A^1_{max} = 228317.3\ s^{-1}$, $A^2_{max} = 3389.7\ s^{-1}$, $Q_{hmax} = 275.9$ MPa , $A'_{2max} = 390067\ s^{-1}$).

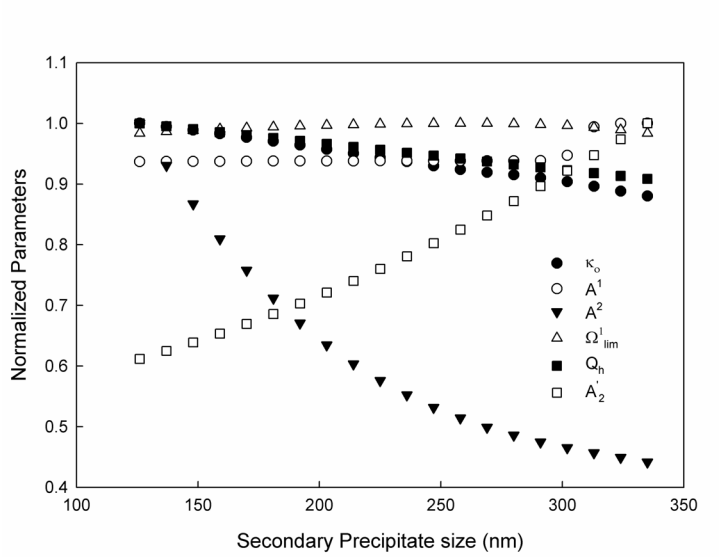

Figure 0.28 Dependence of the 'macro' model parameters on the secondary γ' precipitate size. ($\kappa_{o\max} = 716.12$ Mpa , $\Omega^1_{\lim\max} = 213.5$ Mpa , $A^1_{\max} = 249229\ s^{-1}$, $A^2_{\max} = 5457.6\ s^{-1}$, $Q_{h\max} = 285.5$ MPa , $A'_{2\max} = 461199.7\ s^{-1}$).

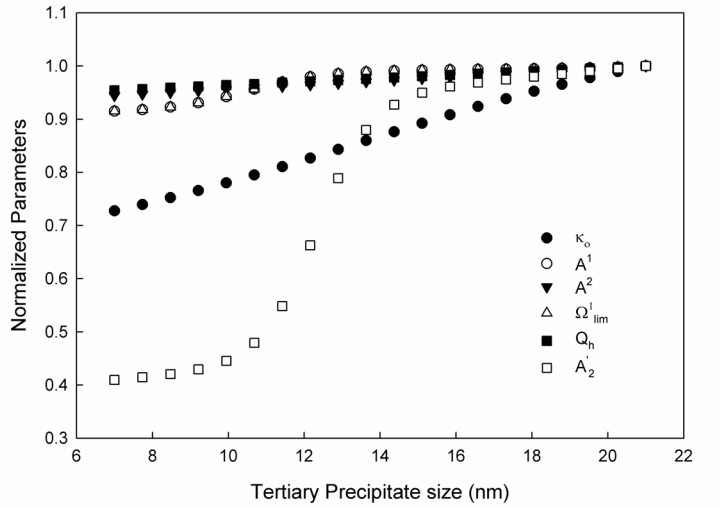

Figure 0.29 Dependence of the 'macro' model parameters on the tertiary γ' precipitate size ($\kappa_{o\max} = 723$ Mpa , $\Omega^1_{\lim\max} = 198.6$ Mpa , $A^1_{\max} = 204252.4\ s^{-1}$, $A^2_{\max} = 6186.3\ s^{-1}$, $Q_{h\max} = 306.7$ MPa , $A'_{2\max} = 327025\ s^{-1}$).

The microstructural dependence of these parameters is shown in Figures 6.25-6.29. The values for these parameters are normalized by the maximum value for each parameter. The functional dependence looks reasonable. For example from Figure 6.25, the initial threshold strength, κ_o, decreases as a function of the grain size and the secondary γ' precipitate size and increases as a function of the tertiary γ' precipitate size, which would be expected based on literature. However, the dependence of the macroscale parameters on the microstructural features is mostly non-intuitive.

6.7 Limitations

Limitations of this methodology are discussed next:

- This chapter offers a simple yet effective framework to relate parameters in a higher scale constitutive model to microstructure features, which should be very useful in hierarchical multiscale modeling. The computational burdens, however, could be significant since the ANN predictions are only as good as the data used for training.
- Only uniaxial loading histories are considered in this chapter to demonstrate the framework; however, it could be easily extended to multiaxial loading histories.

6.8 Summary

A methodology is laid out to embed the microstructure-dependence in a macroscale constitutive model using a lower scale crystal plasticity model. The ability of an artificial neural network (ANN) to identify the microstructure-dependence of the macroscale

model parameters is demonstrated for complex cyclic uniaxial strain-time histories. This methodology could be easily extended for more complex loading histories. The microstructural dependencies of the macroscale model parameters are plotted using predictions from the neural network. This provides the first-ever such systematic linkage of macro-model parameters to microstructure known to the author for such complex microstructures, and offers the potential to incorporate microstructure detail into component level analyses.

CHAPTER VII

Estimating Fatigue Sensitivity to Microstructure in Polycrystalline Ni-base Superalloys using a Computational Framework

Abstract

Microstructure features at various length scales affect the fatigue life of polycrystalline Ni- base superalloys. A computational study is conducted to determine the influence of microstructure attributes and properties on driving forces for fatigue crack formation and microstructurally small crack growth in a polycrystalline Ni-base superalloy IN100, a turbine disk alloy. A principal objective is to obtain quantitative estimates of the effect of variability of microstructure features on scatter in fatigue lives or fatigue strength for a given life by considering variation of first order driving forces for crack formation and microstructurally small crack growth. Understanding is sought regarding sensitivity of driving forces to various microstructure attributes that may guide selection of process route to enhance fatigue resistance or tailor microstructures in specific parts. The microstructure-dependent crystal plasticity model developed in

Chapter V is used to explicitly model individual grains and polycrystals. The model is then used to explore effects of different: (a) grain size distributions, and (b) secondary and tertiary γ' precipitate size distributions and volume fractions. The grains are explicitly modeled using a Voronoi tessellation scheme to address the grain shape and size distributions. The effect of varying microstructure on the cyclic inelastic strain distribution is studied using multiple statistical volume elements (SVE) subjected to random periodic boundary conditions to build up statistically significant measures of distributions of cyclic microplasticity. Multiaxial fatigue criteria with critical plane approaches have been successfully used previously to correlate the crack initiation life. Methods are developed for assessing relative probability of crack formation and microstructurally small crack growth as a function of microstructure for a given loading condition.

7.1 Literature Review

The fatigue life of a polycrystalline Ni-base superalloy is determined by the number of cycles required to incubate a crack, the number of cycles to propagate an existing crack, or a combination of these fatigue stages. Experimental studies on polycrystalline Ni-base superalloy Rene′88 (Chen et al., 1997) have shown that the crack formation and microstructurally small crack growth regimes can comprise a major portion (as high as 70%) of the total fatigue crack initiation life. This fraction further increases for applied stress amplitudes well below the yield strength. Fatigue failure takes place either by propagation of a dominant crack at long lives or by linkage of distributed small cracks to form a rapidly growing critical crack at low lives. A good probabilistic description of

small crack distribution data would be very useful in conducting a statistical analysis to guide a microcrack based reliability inspection scheduling or in-situ diagnostics strategies for small crack detection.

Fatigue crack initiation life is controlled by three primary factors: microstructure, temperature/environment, and loading history. Microstructure features at different scales may affect the fatigue crack initiation life and depend on the alloy composition and processing history. IN100 is a powder metallurgy alloy; therefore, inclusions and pores in the microstructure are often sites for crack formation. In addition, grains that are oriented favorably for slip are prone to slip band cracking; therefore, the incubation of a dominant crack is a competition between initiation from slip band cracking and initiation from defects such as inclusions or pores (Alexandre et al., 2004). It is noted that intergranular cracking could also be a mechanism for crack initiation but this is observed mainly at higher temperatures ($\geq 760\ ^{\circ}\mathrm{C}$) and at lower cycling frequencies (Hyzak and Bernstein, 1982).

The dominant initiation mechanism also depends on the temperature and applied strain amplitude. Crack initiation at inclusions is more likely to occur at very low applied strain amplitudes, at which the inelastic strains maybe highly localized (Hyzak and Bernstein, 1982). Recent studies of a polycrystalline Ni-base superalloy, IN718, (T=350ºC-650ºC, $R_{\varepsilon} = 0, -1$) have shown that the crack initiation life depends on the relative sizes of the grains and inclusions (Alexandre et al., 2004; Findley, 2005). In the small grain size material, the initiation sites were consistently associated with second phase particles; however, in the largest grain size material, cracks formed purely at intense slip bands (Alexandre et al., 2004) . A cracked ceramic inclusion with diameter less than or equal to

the grain size was no more detrimental than a stage I crack originating in persistent slip bands (Jablonski, 1981). Similar conclusions were made by Findley (2005) who conducted fatigue crack initiation tests on Rene′88 DT (T=650ºC, R_{ε}=0, R_{ε}=-1), for two different grain sizes, $d_{gr} = 6$ μm and 20 μm. Findley (2005) observed slip band based crack formation took place even at very low strain amplitudes ($\varepsilon_a = 0.5\varepsilon_y$) in the large grain materials. Caton et al. (2004) performed fatigue tests on Rene′88 DT at 593ºC (R_{ε}=0) at various stress amplitudes. Analysis of the fracture surfaces indicated that the critical cracks formed in the subsurface of the specimens, mainly along slip bands inside grains or crystallographic facets interacting with inclusions, or at the surface at slip bands. They asserted that the variability in fatigue life is not due to crack growth mechanisms; it is dictated by the crack incubation life (defined as the number of cycles required for a crack to form and propagate to the grain scale in slip band based crack initiation, and the number of cycles required for a crack to nucleate and propagate outside the influence of the notch in inclusion based crack initiation) and the initial size of the incubated crack, which is consistent with other alloy systems (Chan and Enright, 2005). The variability of fatigue life increased as the applied stress amplitude decreased. Based on these observations, it is important to study the crack incubation and small crack growth life in polycrystalline Ni-base superalloys.

The γ′ attributes, including volume fraction, shape, and size distribution, can strongly influence the strength and inelastic strain localization inside the grains. However, the dependence of the fatigue life on the precipitate size and volume fraction is not very well documented in literature. Albrecht (1999) performed LCF experiments on Udimet 720 LI with varying microstructures at 600°C and concluded that the variation of the γ′ size

distribution among different microstructures tested had little influence on LCF lives. However, their tests were conducted at stresses well above the yield strength, at which a large number of slip systems are available to help propagate the microcrack, which might make it more difficult to identify the role of microstructure in crack initiation life. Short crack growth tests on Astroloy performed by Brown et al. (1984) showed that the γ' precipitate morphology and volume fraction had no noticeable effect on the short crack growth behavior. For a given volume fraction of the γ' precipitates, the precipitate morphology displays a negligible influence on the fatigue crack initiation life (Ai et al., 1993; Findley, 2005). Long crack growth tests by Antolovich and co-workers (1983; Antolovich, 1987) on Waspaloy showed a dependence of the long fatigue crack growth rates on the γ' precipitate volume fraction, the anti-phase boundary energy, and the $\gamma - \gamma'$ mismatch. Factors tending to promote more planar, inhomogeneous slip lowered the long crack FCP rate. Long fatigue crack growth rates become more dependent on microstructure as temperature increases (Gessinger, 1984).

7.2 Motivation

Most of the variation of fatigue crack initiation life appears to originate, either directly or indirectly, from a statistical range of microstructural features. Defects in the form of pores and inclusions play a dominant role in dictating the incubation of small fatigue cracks in polycrystalline Ni-base superalloys. Recent efforts have been made to reduce the inclusion size distribution and volume fraction in Ni-base superalloys (Moll and McTiernan, 1998). This has been accomplished by decreasing the powder particle size, thus decreasing the size of possible inclusions; and also by changing processing

techniques to decrease the number of inclusions mixed in with the superalloy powder. Therefore, the frequency of failure associated with inclusions has significantly decreased over the past twenty year period, as shown in Figure 7.1.

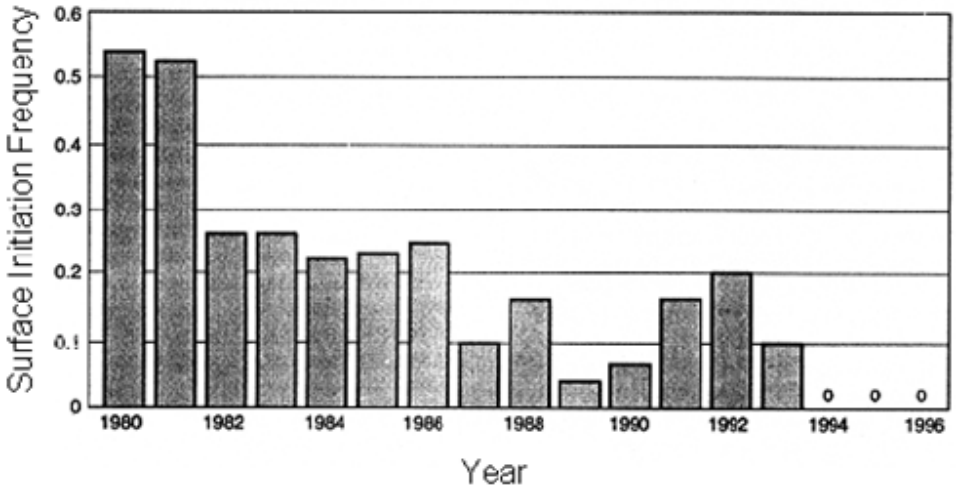

Figure 0.1 Frequency of failure associated with inclusions in LCF tests at 540ºC (Moll and McTiernan, 1998).

Consequently, it is important to understand the effect of variation of intrinsic microstructural features such as grain size, precipitate size, and volume fraction on the fatigue crack initiation life. Accurate prediction of fatigue life variability requires (a) a microstructure-based fatigue crack initiation model, and (b) a probabilistic framework for addressing material-specific randomness (e.g. grain size, orientation). A good understanding of the influence of various microstructure features on fatigue crack initiation life could be used to guide selection of process route to enhance fatigue resistance or tailor microstructures in specific parts. In this study, the focus will be on cyclic plasticity in the microstructure, which governs early stages of crack formation and microstructurally small crack growth.

7.3 Approach

The distribution of cyclic plasticity among grains is important in fatigue crack incubation, which often constitutes a significant part of the total fatigue life. Wei et al (1991) investigated low cycle fatigue in IN100 and showed that crack incubation and small crack growth life dominate the total life when the completely reversed strain amplitude is less than $0.8\,\varepsilon_y$ (where ε_y is defined as 0.1% yield strain). Furthermore, the crack incubation and small crack growth life is mainly responsible for the variability in the crack initiation life, particularly at low applied stress or strain amplitudes. While the growth of long cracks can be approximately described using the Paris-Erdogan equation, microcrack incubation and growth is not well characterized when linear elastic fracture mechanics (LEFM) is directly applied.

Mononukul et al. (2004) correlated the crack incubation life in a polycrystalline Ni-base superalloy, C263, using the maximum accumulated plastic strain (P_{cyc}) in a representative volume element as the driving force for crack initiation at slip bands, i.e.,

$$P_{cyc} = \int_{cyc} \dot{p}\,dt = \int_{cyc} \left(\frac{2}{3} \mathbf{D}^p : \mathbf{D}^p \right)^{1/2} dt \qquad (7.1)$$

where $\mathbf{D}^p$ is the plastic rate of deformation tensor. The accumulated plastic strain, P_{cyc}, was then related to the crack incubation life (N_{inc}) using a critical value of the accumulated plastic strain, p_{crit}, over the number of cycles for crack incubation, i.e.,

$$P_{cyc} N_{inc} = p_{crit} \tag{7.2}$$

Such ductility exhaustion mechanisms were considered in terms of macroscopic plastic strain in the 1950s-1960s, prior to introduction of the Coffin-Manson relation, and were largely determined to be ineffective in correlating the fatigue life. However, Eqs. (7.1)-(7.2) are defined in terms of microscale plasticity, which differs from the macroscale level. It is noted that slip band decohesion models of micromechanical character (cf. (Venkataraman et al., 1990)) do not shed light on the viability of p_{cyc} as a driving force parameter.

Impingement of slip on grain boundaries or other intense slip bands is a physically viable mechanism for fatigue crack formation. This is correlated with build-up of dislocations of like-sign (i.e., pile-ups), reflected on the continuum level by the cumulative plastic shear strain measure, P_r, i.e.

$$P_r = \max\left(\int_{cycle} \dot{\varepsilon}^p_{ij} n_i t_j dt \right) \tag{7.3}$$

where $\mathbf{t}$ is the direction along any given plane with normal $\mathbf{n}$. The maximum value of this parameter is obtained along all possible slip directions over all possible planes for one cycle. Crack incubation associated with slip band cracking and shear-dominated microstructurally small crack growth in polycrystalline Ni-base superalloys has also been successfully correlated using the Fatemi-Socie parameter, P_{FS}, (Fatemi and Socie, 1988; Kurath and Fatemi, 1990; Findley, 2005), given by

$$P_{FS} = \frac{\Delta\gamma^{p}_{max}}{2}\left[1 + k^{*}\frac{\sigma_{n}^{max}}{\sigma_{y}}\right] \tag{7.4}$$

where $\Delta\gamma^{p}_{max}$ is the range of maximum plastic shear strain, σ_{n}^{max} is the peak tensile stress normal to the plane of maximum plastic shear strain amplitude, and σ_{y} is the yield strength. Parameter k^{*} could be a function of the material properties in addition to the multiaxial loading conditions (McDowell and Berard, 1992); however, a constant value of this parameter for any given alloy system usually gives good correlation with fatigue crack initiation life (Socie and Bannantine, 1988; Findley, 2005). A value of $k^{*} = 0.5$ was used by Findley for Rene′88 (2005). The P_{FS} parameter also demonstrated very strong correlative capabilities for fatigue crack initiation life under multiaxial loading conditions (McDowell, 1996a). When the incubation life is completely controlled by to and fro irreversible motion of the dislocations, $k^{*} = 0$ is used in Eq. (7.4) and the parameter P_{mps} is used defined as

$$P_{mps} = \frac{\Delta\gamma^{p}_{max}}{2} \tag{7.5}$$

Unlike P_{FS}, P_{mps} has no normal stress effect. The microstructure dependent 3-D crystal plasticity model developed in Chapter V is used to study the distribution of the fatigue parameters (FPs) i.e. P_{cyc}, P_{r}, P_{mps} and P_{FS}, in IN100 for a polycrystal ensemble. The

secondary and tertiary γ′ precipitates sizes are one to two orders of magnitude smaller than the grain size, and they are uniformly distributed throughout the grains. Because of their size, it is argued that their effect on the local stress fields within the grains is at a length scale too small to influence grain-level stress and strain inhomogeneity similar to Manonukul et al. (2004).

The primary γ′ precipitates have a relatively low volume fraction in most of the microstructures under consideration; therefore, only microstructures without primary precipitates are considered. Furthermore, these large precipitates may potentially be treated like inclusions since they are comparable to the grain size. The influence of these microstructure features on the driving forces for fatigue crack incubation is obtained through the constitutive model.

7.4 Statistical Volume Elements

The Voronoi tessellation method is a good candidate to generate random polycrystals based on geometric considerations, since it provides planar boundaries separating grains and because it reproduces some morphogenetic processes, where germs grow with a constant and isotropic growth rate from random seeds (Barbe et al., 2001). A log-normal grain size distribution can be used, which is typically observed in polycrystalline Ni-base superalloys (Findley, 2005).

7.4.1 Voronoi Polyhedral Model - Implementation

The input data for the model includes the grain size distribution, the number of total grains, and the grain orientation distribution in Rodriguez space. The orientation distribution and misorientation angle distribution can be extracted using electron back scatter diffraction (EBSD); however, random grain orientation and misorientation distributions are used as a first order approximation. A cubic box with an edge size (L) is used to represent the polycrystal aggregate with

$$L = \frac{\sqrt[3]{n_{gr}}\, d_{gr}}{0.7} \tag{7.6}$$

n_{gr} is the number of grains and d_{gr} is the average grain size (Horalek, 1990). It should be noted that the average grain size measured on a section using line intercept method, $\langle d_{gr} \rangle$, and average volume, <V> , follows the relation (Horalek, 1990)

$$\langle d_{gr} \rangle = 0.7 \langle V \rangle^{1/3} \tag{7.7}$$

A set of nuclei is randomly distributed in the cubic box with periodic boundary conditions. The distance between two neighboring grains should be larger than a critical value; this critical distance can influence the initial grain size distribution. The nuclei grow simultaneously at a constant rate until mutual contact prevents further expansion. The Voronoi tessellations divide a space into an array of convex, spacing-filling

polyhedra having planar faces. The grain size distribution is fitted using a simulated annealing algorithm (Recipes, 1992; Gross and Li, 2002). If $f^s(d_i)$ is the simulated frequency of grain size distribution, and $f^t(d_i)$ is the target frequency of grain size distribution. The error function, λ, is defined by the expression

$$\lambda = \sum_{i=1}^{N} [f^s(d_i) - f^t(d_i)]^2 \tag{7.8}$$

where N is the number of grain size categories. A grain is selected randomly and the centers of the neighboring grains are modeled outwards with respect to the center of the selected grain. The change in the error function, Δλ,caused by the operation is recorded and a decision on whether to accept or reject this operation is based on a probability criterion

$$p(\Delta\lambda) = \begin{cases} 1 & \Delta\lambda < 0 \\ \exp(-\Delta\lambda / T) & \Delta\lambda > 0 \end{cases} \tag{7.9}$$

where T is a control parameter (analog of temperature) to define an annealing schedule.

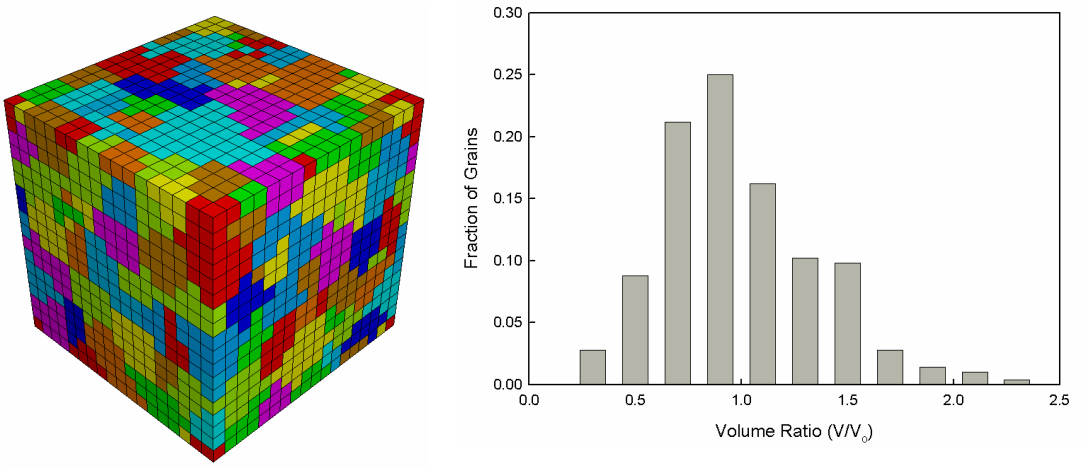

(a) (b)

Figure 0.2 (a) A representative mesh and (b) the corresponding grain size distribution where V is the grain volume and V_o is the average grain volume.

An operation is accepted if it reduces the error function or if it increases the error function with $\exp(-\Delta\lambda / T) \geq \rho$, where ρ is a random number. If an operation is not accepted, the centers of the neighboring grains are moved inwards. If this operation is not accepted, another grain is selected randomly, and the operation is repeated. This operation is continued until the error function is less than a preset tolerance ($\lambda \leq 0.00001$) or until a prescribed (very large) number of reconfigurations have been examined. In this algorithm, there is a good chance for the system to move out of a local minimum of the error function so as to find the global minimum. The cubic box of polycrystalline is meshed with small regular cubic elements (C3D8R). The number of nodes on each edge of the model is controlled by the mesh density. The corresponding grain for any element is determined by the distance between the element integration point and the grain

centroid. A polycrystal aggregate and the corresponding grain size distribution are shown in Figure 7.2.

7.4.2 Model Details

The number of grains modeled and the number of elements in each grain can have a considerable effect on the plastic strain heterogeneity. Recent studies by Barbie et al. (2001) suggest that around 200 grains with 27 (i.e. 3x3x3) 20-noded elements give good results. In this study 216 (i.e., 6x6x6) grains are used to represent the polycrystal aggregate with an average of 27 linear brick elements per grain. It is noted that this is not a representative volume element (RVE) and different realizations termed as 'statistical volume elements (SVEs)' can be obtained for any given microstructure; multiple realizations of SVEs are necessary to build up statistics over representative volumes (Kanit et al., 2003) for the fatigue parameter distribution. Therefore, the variability in the parameter distribution based on the SVEs is analyzed; different randomly assigned grain orientation distribution and different initial random nuclei (seeds) for the Voronoi cells are used. The same grain size distribution is maintained for a given realization (SVE) of any selected microstructure; the grain size (d_{gr}) is varied such that $0.4d_{gr} \le d_{gr} \le 2.5d_{gr}$. Random 3D periodic boundary conditions are used for the SVE analyses in cyclic uniaxial tension-compression. The grain size dependence of the constitutive response is obtained using the Hall-Petch relation in Eq. 5.6.

7.5 Averaging Volume

The volume over which the fatigue crack incubation parameters (P_{cyc}, P_r, P_{mps} and P_{FS}) are averaged should be representative of the physical scale. The slip band width can vary as a function of the microstructure and stress state. The slip band width varies from 0.2-10 μm depending on the grain and precipitate size in polycrystalline Ni-base superalloys (Manonukul and Dunne, 2004; Xiao et al., 2005). It is observed to be relatively independent of the inelastic strain in a polycrystalline Ni-base superalloy, IN718 (Xiao et al., 2005), but increases with the grain size.

The element size used in these analyses varies from 2-6 μm, which is of the same order as that of the slip band width. The fatigue crack formation parameters are evaluated for each element at the element centroid and are therefore averaged over the element scale. The maximum values of P_{cyc}, P_r, P_{mps}, and P_{FS} among all elements within the grain are determined to represent the potency of the slip band to incubate a crack within that grain. It is noted that such a scheme will naturally capture the localized inelastic concentration at the triple point grain boundaries, which are potential sites for crack formation (Manonukul and Dunne, 2004).

In addition to the maximum values, the average values of the FPs over all elements in each grain are also determined. The grain size is a natural averaging scale which can be physically justified based on the dislocation model for crack incubation proposed by Tanaka and Mura (1981).

7.6 Experimental Data

Distribution data for microstructurally small cracks are not available for IN100, however, data are available for a similar Ni-base superalloy, Rene′88, which has a bi-modal distribution of secondary (200 nm diameter) and tertiary precipitates (10 nm diameter) and an average grain size (d_{gr}) of 21 μm (Chen et al., 1997). Rene′88 is hypothesized to give similar qualitative trends for the microcrack incubation, growth and distribution characteristics to IN100.

In Rene′88, the majority of the fatigue cracks formed at slip bands while the others formed at grain or twin boundaries. A large number of cracks (~ 100 μm) were observed which coalesced particularly late in the fatigue life. The evolution of the crack length as a function of number of loading cycles normalized by the fatigue life of a given specimen is shown in Figure 7.3 and the distribution of microcracks is shown in Figure 7.4. The microcracks dominated the fatigue life up to 70% of the failure life after which crack coalescence and long crack growth took place. Microcracks as small as 50 μm could exhibit the Paris law for long crack growth which further emphasizes the need for a study of the crack incubation and small crack growth parameters (Chen et al., 1997).

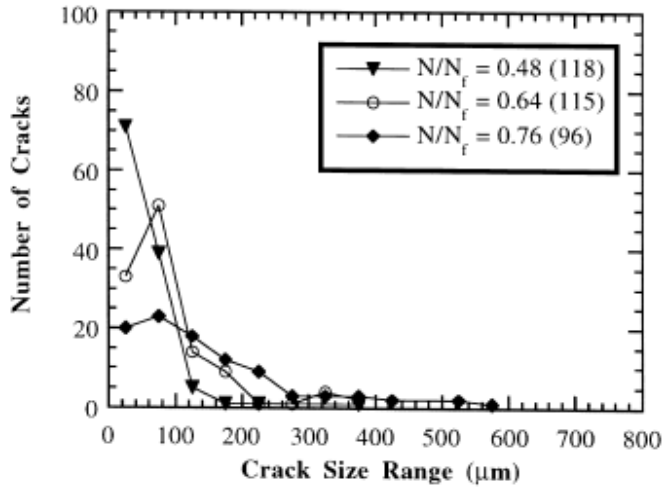

Figure 0.3 Microcrack length distributions in Rene′88 **as a function of the fatigue life,** $R_\varepsilon = -1$, **T = room temperature,** $\sigma_a = 0.9\sigma_y$, $\nu = 1$ Hz (Chen et al., 1997) for a single specimen.

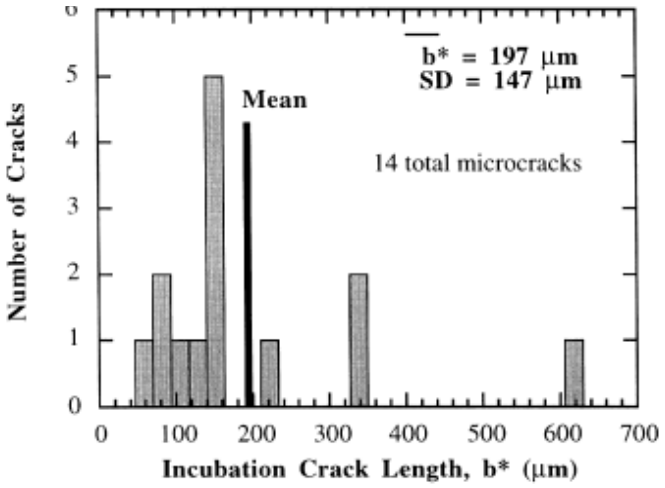

Figure 0.4 Microcrack length distributions in Rene′88 as a function of the fatigue life, $R_\varepsilon = -1$, T = room temperature, $\sigma_a = 0.9\sigma_y$, $\nu = 1$ Hz (Chen et al., 1997).

7.7 Fatigue Incubation Parameters (FP)

The variation of the FPs is studied for statistical volume elements at strain amplitudes varying from $0.5\varepsilon_y$ to ε_y at 650ºC for $R_\varepsilon = -1$ (ε_y=0.77% is the 0.1% yield strain for IN100 with a grain size of 16 μm at 650ºC at $\dot{\varepsilon} = 10^{-3}$ s^{-1}). The maximum (max) and average (av) FPs are calculated for each grain and their distributions among grains are shown in Figure 7.5 at a strain amplitude of ε_y. The distribution of the maximum P_{FS} and P_r is shown in Figure 7.6 and the scatter band gives the variation of this parameter for three SVEs. In these analyses, the base properties are that for Matrix 2 (refer to Table 5.1) with an average grain size of 16 μm at 650ºC. The equivalent plastic strain contours for two strain amplitudes, $0.9\varepsilon_y$ and $0.6\varepsilon_y$ at 650ºC with $R_\varepsilon = -1$ are shown in Figure 7.7.

The FPs display a log normal distribution and roughly display similar trends. The first peak is due to the number of grains that have a relatively low value of the FP. The initial peak decreases as a function of the strain amplitude since plasticity is more uniformly distributed at higher applied strains, as shown in Figure 7.7. This is consistent with the larger number of cracks observed at higher applied strain amplitudes due to the larger number of potential crack incubation sites. The value of the FPs are computed to be very low ($\leq$ 1.e-8) at a strain amplitude of $0.4\varepsilon_y$ suggesting that subsurface inclusions and/or pores might act as the crack initiation sites and slip band based cracking might not occur at all. Figure 7.6 shows the variation of the maximum P_{FS} and P_r parameters for 3 statistical volume elements at strain amplitude=$0.6\varepsilon_y$; the qualitative trends are similar for the 3 SVEs and the scatter band is relatively small.

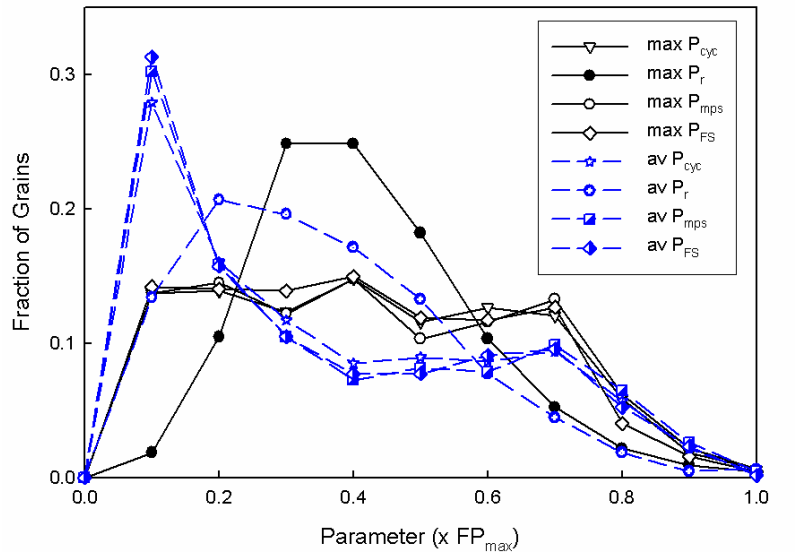

Figure 0.5 Distribution of the FPs among grains at a strain amplitude of ε_y (T=650ºC, $R_{\varepsilon} = -1$, $\dot{\varepsilon} = 10^{-3}$ s^{-1}, max $P_{cyc,max}$ = 0.0242, max $P_{r,max}$ = 0.0011, max $P_{mps,max}$ = 0.0097, max $P_{FS,max}$ = 0.0126, av $P_{cyc,max}$ = 0.0168, av $P_{r,max}$ = 0.00046, av $P_{mps,max}$ = 0.0065, av $P_{FS,max}$ = 0.00843).

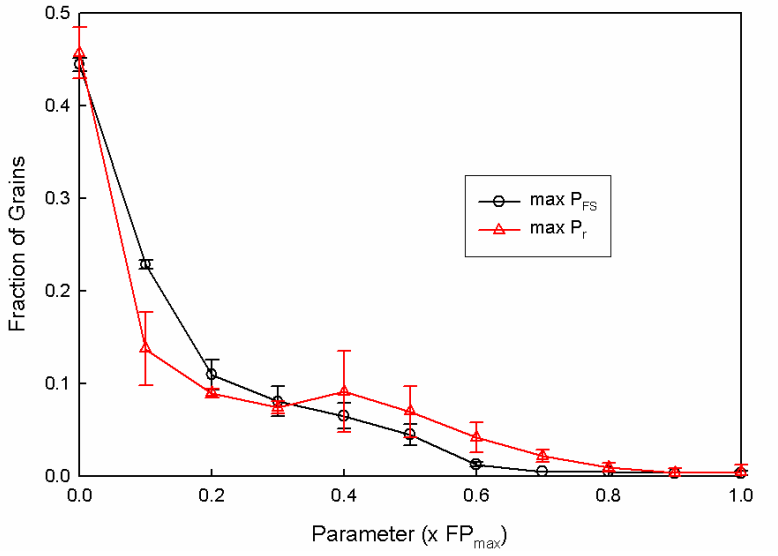

Figure 0.6 Distribution of max P_{FS} and max P_r among grains at strain amplitude of $0.6\,\varepsilon_y$ for 3 SVEs (T=650ºC, $R_{\varepsilon} = -1$, $\dot{\varepsilon} = 10^{-3}$ s^{-1}, max $P_{FS,max}$ = 0.00443, max $P_{r,max}$ =0.00014).

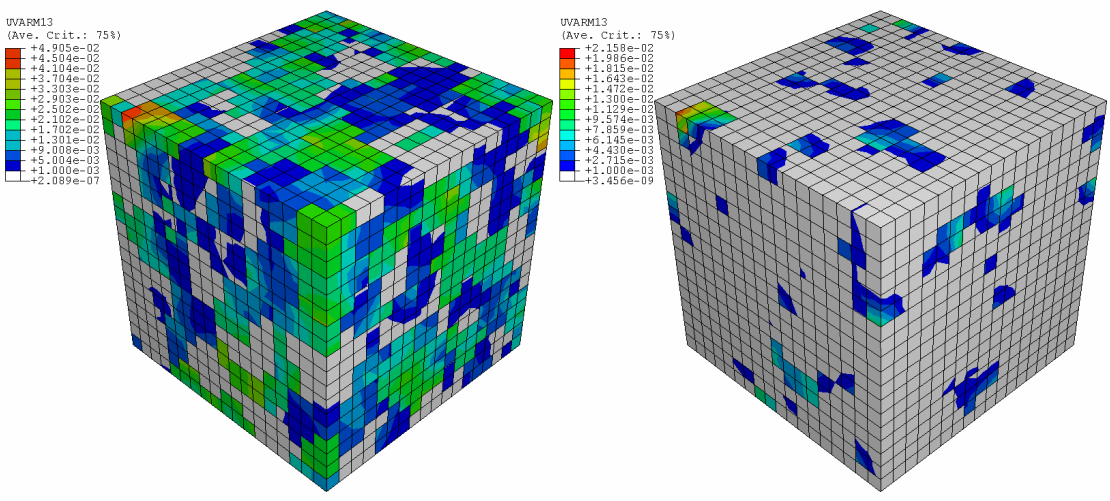

(a) (b)

Figure 0.7 Contours for the equivalent plastic strain distribution for a SVE at (a) $\boldsymbol{\varepsilon}_a = 0.9\,\varepsilon_y$ and (b) $\boldsymbol{\varepsilon}_a = 0.6\,\varepsilon_y$ (T=650ºC, $R_{\boldsymbol{\varepsilon}} = -1, \dot{\boldsymbol{\varepsilon}} = 10^{-3}\ s^{-1}$).

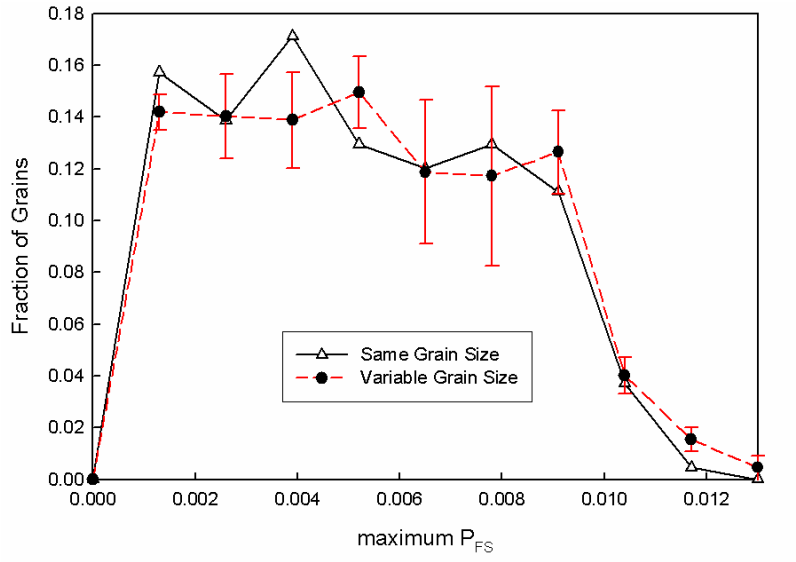

Figure 0.8 Analysis of the effect of grain size distribution on the maximum P_{FS} ($\boldsymbol{\varepsilon}_a = \varepsilon_y$, average d_{gr} =16 μm, T=650ºC, $R_{\boldsymbol{\varepsilon}} = -1$, $\dot{\boldsymbol{\varepsilon}} = 10^{-3}\ s^{-1}$).

It is noted that the distribution in Figure 7.8 shows good qualitative correlation with the crack size distribution in Figure 7.4. Based on Figure 7.5, the distribution for P_{cyc}, P_{mps} and P_{FS} are similar while those for P_r are different. However, the trends displayed by P_r are similar to those of the other parameters.

An analysis was conducted for a polycrystal aggregate with the cubic grains of the same size each containing 27 elements with random orientation distribution to understand the effect of the lognormal distribution of grain size on the FP distribution as shown in Figure 7.8. The average values of number of grains and the corresponding variation are plotted as a function of max P_{FS} for 3 SVEs. Even though the nature of the distributions for the SVE analyses and the same grain size analysis are similar, there is a difference in the quantitative values, which should be expected since the FP contains an additional dependence on the grain size which leads to a higher variability of the FP values. The lognormal distribution of grain sizes gives higher fraction of grains (on an average) at the tail end of the distribution (i.e., grains with high value of the FP). This might have important implications for the larger cracks formed in the distribution.

7.8 Grain Size Dependence of FPs

The influence of the grain size on the FPs is studied for three average grain sizes: 8, 16 and 32 μm. All the FPs show similar grain size dependence; the dependence of the maximum value (over all grains) for P_{FS} and P_r in the SVE are plotted in Figure 7.9. Both P_{FS} and P_r increase as a function of the average grain size; however, P_{FS} displays a much lower dependence on the grain size as compared to P_r. The validity of the

appropriate parameter can only be experimentally corroborated for the corresponding microstructures, but the trend of grain size dependence of the crack initiation life is similar to that observed in other Ni-base superalloys, as shown in Figure 7.10. It is noted that the FPs cannot account for the large variation in the crack initiation life seen in Figure 7.10 for this grain size range. This may be because the contribution from the microstructurally small crack growth life is not accounted for. Also, the temperature and loading conditions are different.

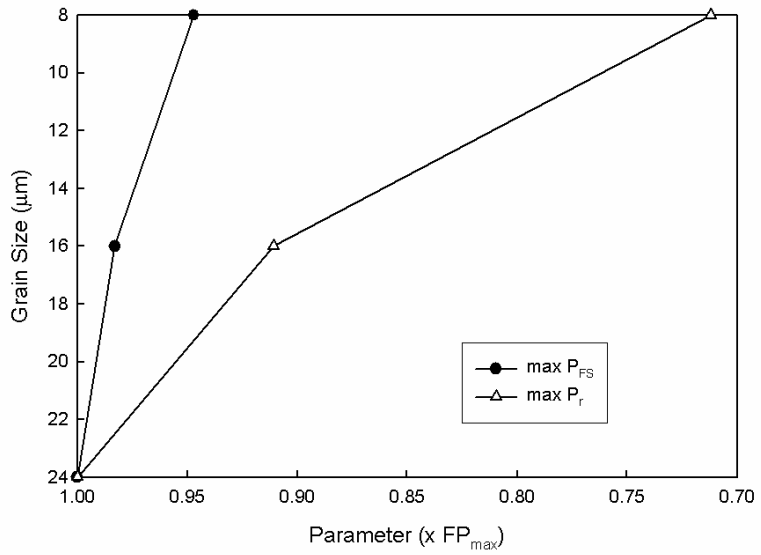

Figure 0.9 Dependence of the maximum P_{FS} and P_r on the average grain size ($\boldsymbol{\varepsilon}_a$ =0.9 ε_y, T=650ºC, $R_{\boldsymbol{\varepsilon}} = -1$, $\dot{\boldsymbol{\varepsilon}} = 10^{-3}$ s^{-1}, max $P_{FS,max} = 0.00832$, max $P_{r,max} = 0.00067$).

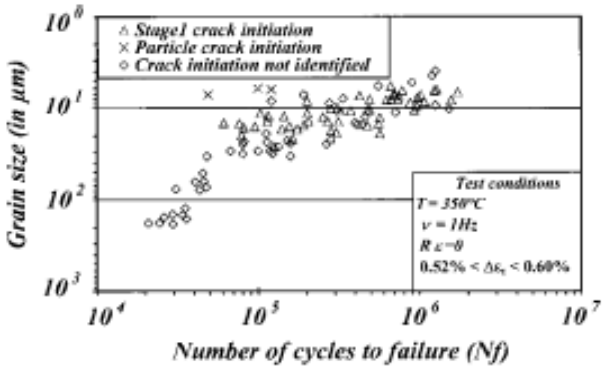

Figure 0.10 Dependence of the fatigue life on the grain size in IN718 (Alexandre et al., 2004).

7.9 Crack Initiation Life Evaluation

The crack initiation life is typically composed of the following stages in polycrystalline Ni-base superalloys (when slip band based crack formation takes place): (i) crack incubation at the favorably oriented grains (ii) microstructure crack growth (up to 100 μm) and (iii) crack coalescence and long crack growth until specimen failure. In this section a qualitative attempt is made to evaluate the crack initiation life distribution using only the FPs. Only the first two stages of crack initiation are considered; long crack growth and crack coalescence are not considered.

7.9.1 Crack Incubation

The model used to evaluate the Stage I crack incubation life based on the dislocation theory proposed by Tanaka and Mura (1981); the incubation life for a Stage I crack to the order of the grain size (N_{inc}) is related to the plastic strain range according to

$$N_{inc}\left(\Delta\varepsilon^{p}\right)^{2} = \frac{\alpha}{d_{gr}} \tag{7.10}$$

The macroscale maximum cyclic plastic shear strain can be related to the uniaxial cyclic plastic strain range by the equation

$$\left(\frac{\Delta\gamma^{p}_{max}}{2}\right)_{macro} = \frac{3}{2}\left(\frac{\Delta\varepsilon^{p}}{2}\right) \tag{7.11}$$

Therefore, Eq. (7.10) is given as

$$N_{inc}\left(\frac{av\ \Delta\gamma^{p}_{max}}{2}\right)^{2} = \frac{\alpha_{g}}{d_{gr}} \tag{7.12}$$

The averaged maximum cyclic plastic shear strain averaged over the grain ($av\ P_{mps}$) is used as the driving force to incubate a crack to the order of the grain size (Alexandre et al., 2004). Experimental fatigue life data are not available for IN100; therefore $\alpha_g = 0.056$ μm^{-1} is used based on Alexandre et al.(2004).

7.9.2 Microstructurally Small Crack Growth

Fatemi and Socie (1988) and Fatemi and Kurath (1988) have demonstrated robust correlation of fatigue crack propagation life under various stress states both with and without mean stress, based on the assumption that the peak normal stress to the plane of maximum range of shear strain directly affects the shear-dominated propagation of small cracks. The grain size averaged Fatemi-Socie parameter ($\text{av}\, P_{FS}$) gives an indication of the microstructurally small crack (MSC) growth rate, once the crack is incubated. Here, a modified form of the MSC growth law is used with $\text{av}\, P_{FS}$ as the driving force, i.e.,

$$\left.\frac{da}{dN}\right|_{msc} = A_{FS}\tau_y(\text{av}\, P_{FS})a \qquad (7.13)$$

where A_{FS} is a constant and τ_y is the resolved shear stress given by $\tau_y = \sigma_y/M$ where M=3.06 is the Taylor factor for a texture free polycrystalline aggregate. The form of Eq. (7.13) is consistent with the ΔJ based approach to address the growth of small cracks along critical planes (Berard and McDowell, 1992). The MSC life is defined as the number of cycles for the incubated crack to grow to $3\,d_{gr}$. The value of A_{FS} is calibrated such that $N_{inc} = N_{msc}$ at an applied strain amplitude$=\varepsilon_y$, using mean values for $\text{av}\, P_{mps}$ and $\text{av}\, P_{FS}$, and is determined to be $A_{FS} = 8.1\text{x}10^{-4}\,\text{MPa}^{-1}$ (Alexandre et al., 2004). The total life (N) for a crack length = $3\,d_{gr}$ is

$$N = N_{inc} + N_{msc} \qquad (7.14)$$

The advantage of using such an approach is that the effect of plastic strain distribution in the neighboring grains is also incorporated; for example, a crack might form at a critically oriented grain but might not have enough driving force to grow. Beyond the MSC life, the long crack growth and/or crack coalescence are assumed to take place, which is not accounted for in this thesis. It is noted that Eq. (7.14) neglects the actual crack tip fields and also neglects the stress redistribution due to crack advance. Ideally 5-6 grains should be included in the MSC regime; however, the small SVE size (6x6x6 grains) limits the number of grains that can be included in these analyses.

7.9.3 Crack Initiation Life Distribution

The incubation lives are calculated for the cracks at each grain using Eq. (7.12). The incubated cracks are assumed to grow along the neighboring grains with the highest values of av P_{FS} and the MSC life is the number of cycles for the crack to grow to a length of 40 μm using Eq. (7.13) and the total initiation life ($N = N_{inc} + N_{msc}$) is calculated. The distribution of the number of cracks as a function of the total life is plotted in Figures 7.11-7.16 for strain amplitudes ranging from $0.5\varepsilon_y$ to ε_y. Cracks with an initiation life greater than 10 times the lowest initiation life, at any given strain amplitude, are not shown in the distribution plots for clarity.

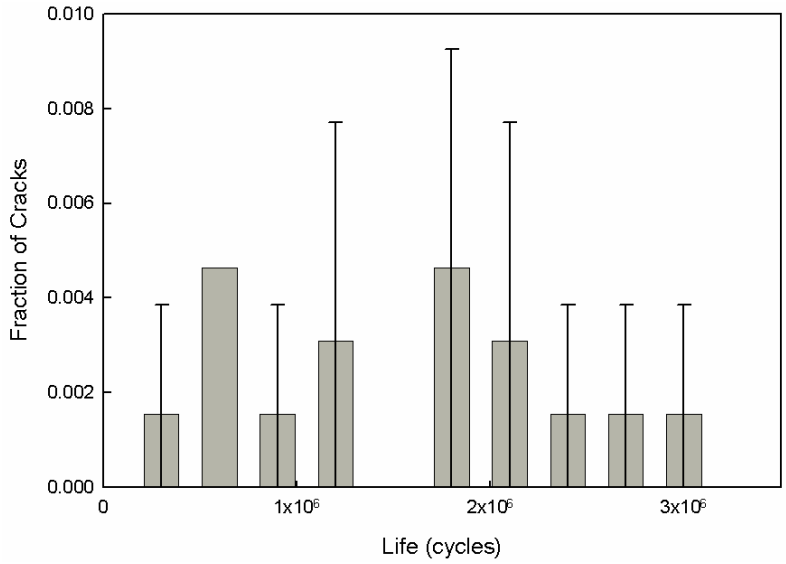

Figure 0.11 Distribution of fraction of cracks versus the crack initiation life at $\varepsilon_a = 0.5\varepsilon_y$, T=650ºC, $R_\varepsilon = -1$, $\dot{\varepsilon}$=10^{-3} s^{-1}.

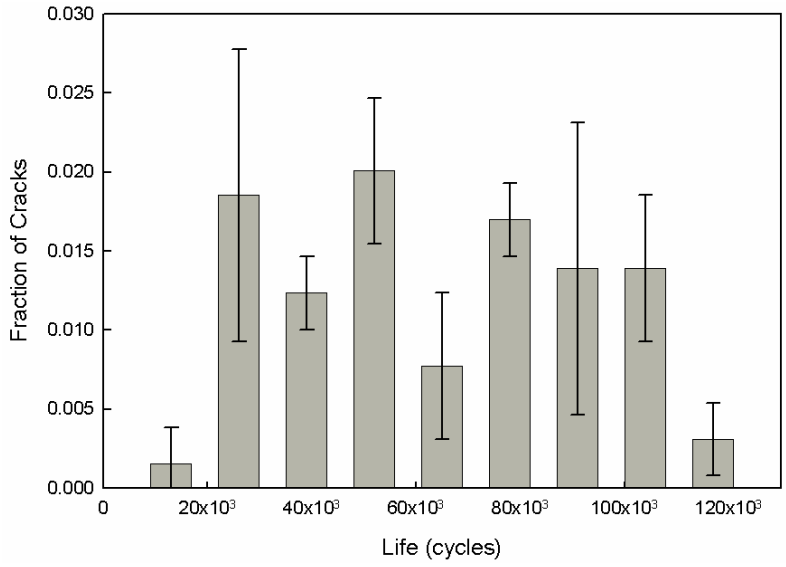

Figure 0.12 Distribution of fraction of cracks versus the crack initiation life at $\varepsilon_a = 0.6\varepsilon_y$, T=650ºC, $R_\varepsilon = -1$, $\dot{\varepsilon}$=10^{-3} s^{-1}.

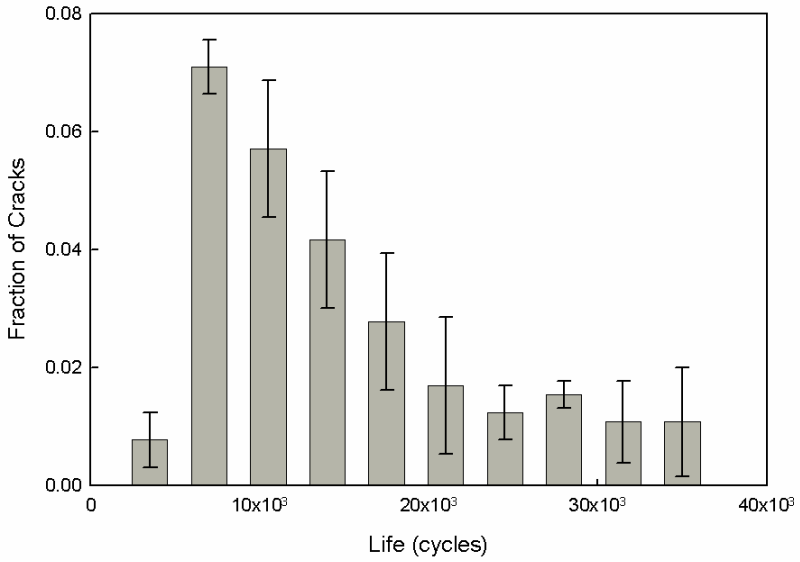

Figure 0.13 Distribution of fraction of cracks versus the crack initiation life at $\varepsilon_a = 0.7\varepsilon_y$, T=650ºC, $R_\varepsilon = -1$, $\dot{\varepsilon}$=10^{-3} s^{-1}.

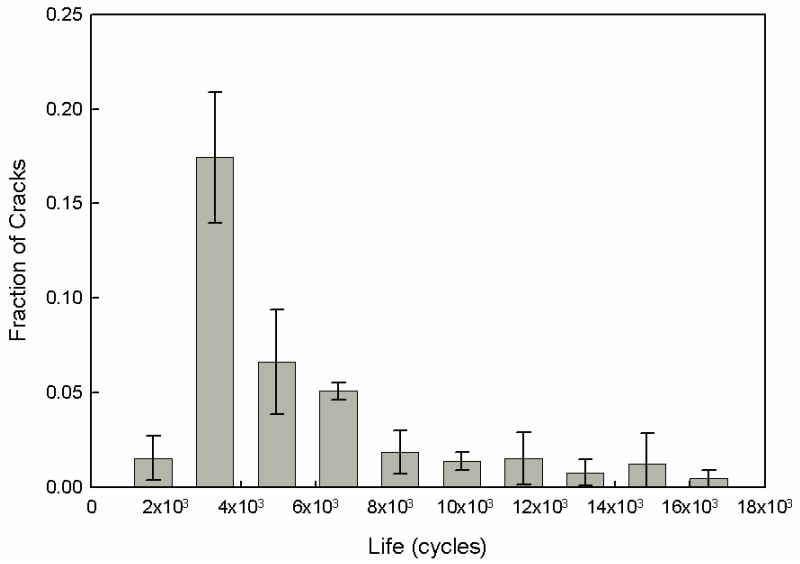

Figure 0.14 Distribution of fraction of cracks versus the crack initiation life at $\varepsilon_a = 0.8\varepsilon_y$, T=650ºC, $R_\varepsilon = -1$, $\dot{\varepsilon}$=10^{-3} s^{-1}.

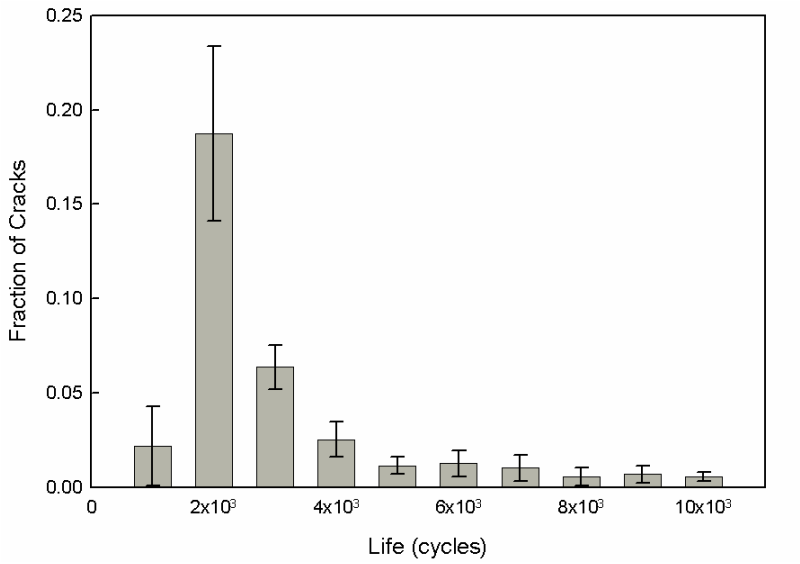

Figure 0.15 Distribution of fraction of cracks versus the crack initiation life at $\varepsilon_a = 0.9\varepsilon_y$, T=650ºC, $R_\varepsilon = -1$, $\dot{\varepsilon}$=10^{-3} s^{-1}.

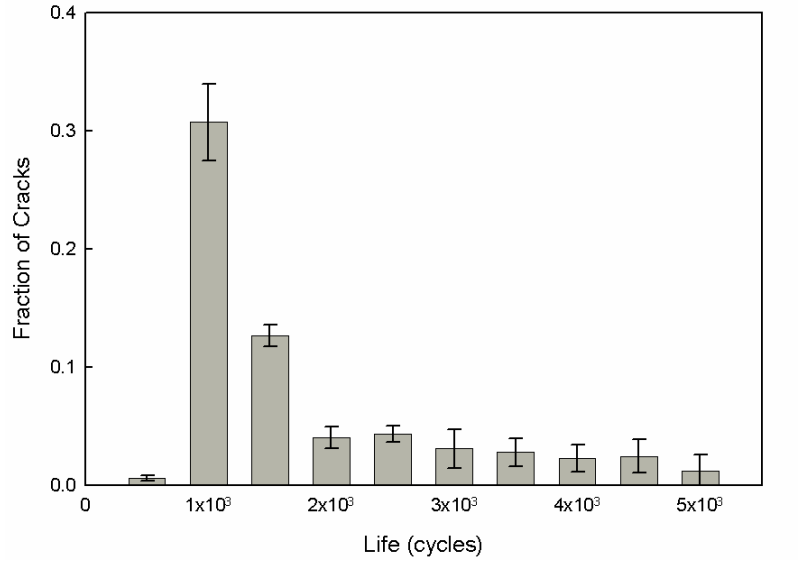

Figure 0.16 Distribution of fraction of cracks versus the crack initiation life at $\varepsilon_a = \varepsilon_y$, T=650ºC, $R_\varepsilon = -1$, $\dot{\varepsilon}$=10^{-3} s^{-1}.

The number of cracks increases as a function of the applied strain amplitude as seen in Figures 7.11-7.16. The fraction of cracks displays higher variability for the 3 SVEs at the lower strain amplitudes ($\leq 0.6\boldsymbol{\varepsilon}_y$). This is expected since the plastic strain is distributed more uniformly at higher strain amplitudes ($\geq 0.7\varepsilon_y$). At lower strain amplitudes, the crack incubates at the favorably oriented grains and grows only if the grains around them have enough driving force for MSC propagation. A dominant crack is formed by crack coalescence of many smaller cracks at higher strain amplitudes while a single dominant crack is observed at lower strain amplitudes, which leads to specimen failure. It is noted that crack coalescence has not been accounted for in this analysis.

It is noted that the driving force is insufficient for slip band-based crack formation at strain amplitudes $\leq 0.4\varepsilon_y$. However, crack incubation might take place at inclusions/hard particles and other defects (e.g. pores) at very low strain amplitudes. A strategy similar to that proposed in Chapter IV can be used to analyze the fatigue life for inclusion based crack initiation. Inclusion based crack incubation might lead to lower crack initiation life estimates even at higher strain amplitudes. Therefore, it is important to use the most conservative fatigue crack initiation life.

7.10 Towards Computational Microstructure Design

Once the physics of the microstructure influence on fatigue crack initiation life is embedded, a computational material design framework could be used in a preliminary design of fatigue resistant microstructures. This is useful since it is may reduce the number of experiments. However, it should be noted that the predictions can only be as good as the models used, so it cannot replace experiments. A computational exercise is

carried out in this section to pursue an example of a preliminary design of a fatigue resistant microstructure that can maximize the crack initiation life ($N_{inc} + N_{msc}$).

Table 0.1 Range for microstructure parameters used for preliminary design.

Material	Secondary γ' d_2 (nm)	Secondary γ' f_{p2}	Tertiary γ' d_3 (nm)	Tertiary γ' f_{p3}
Minimum	110	0.39	7	0.17
Maximum	340	0.46	21	0.024

Design variables include (i) secondary γ' precipitate size (d_2) (ii) secondary γ' precipitate volume fraction (f_{p2}) (iiii) tertiary γ' precipitate size (d_3) and (iv) tertiary γ' precipitate volume fraction (f_{p3}). The design space for these parameters is given in Table 7.1. The ranges in Table 7.1 are set based on the maximum and minimum values of the experimentally tested microstructures. Forty microstructures are generated with different values of d_2, f_{p2}, d_3, f_{p3}. The average grain size is fixed at 16 μm with no primary γ' precipitates for all analyses and a space filling design is used to fill the design space for the other microstructure parameters. The analyses are conducted for completely reversed uniaxial tension-compression loading ($R_\varepsilon = -1$, $\varepsilon_a = \varepsilon_y$, T=650ºC, $\dot{\varepsilon} = 10^{-3}\ s^{-1}$).

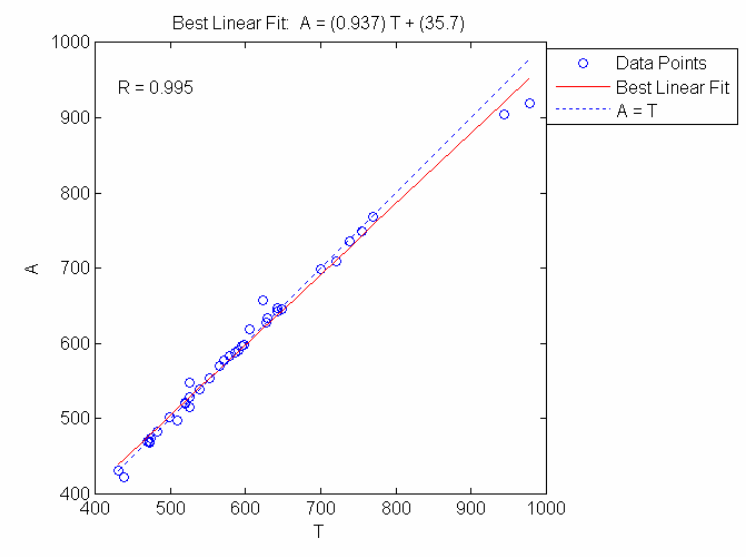

Figure 0.17 The predicted values (A) and target values (T) for the crack initiation life for different microstructures.

The minimum life required for a 40 μm crack to develop is determined for the 40 microstructures. The microstructures and the corresponding life data are used to train an artificial neural network (ANN) using two hidden layers similar to that used in Chapter VI. The ANN captures the microstructure dependence of the fatigue crack initiation life very accurately as shown in Figure 7.17. The trained ANN is used to conduct preliminary design of the microstructure to maximize the crack initiation life.

The crack initiation lives are determined for materials with microstructure features spanning the entire design space using the trained ANN. The microstructure with the maximum crack initiation life has the following features: $d_2 = 110\,\text{nm}$, $f_{p2} = 0.39$, $d_3 = 21$ nm and $f_{p3} = 0.17$. It is noted that the design variables hit the upper or lower boundaries. The values of the tertiary γ' precipitate size (d_3), volume fraction (f_{p3}), and secondary γ'

precipitate size (d_2) are expected since the threshold stress increases with increasing tertiary precipitate sizes (d_3) and volume fractions (f_{p3}), and decreasing secondary precipitate sizes (d_2) based on Eqs. 5.5 and 5.6. Interestingly, maximum crack initiation life is obtained at the minimum volume fraction of the secondary precipitates (f_{p2}). This is due to the reduced strain hardening response of the microstructure with an increase in the secondary γ' precipitate volume fraction (Eq. 5.15), which supersedes the increase in the threshold stress (Eqs. 5.5 and 5.6) and increase in the strain gradient hardening contribution from the geometrically necessary dislocation density (Eqs. 5.9 and 5.10).

7.11 Limitations

Limitations are as follows:

- Experimental crack initiation life data are not available for the IN100 microstructures. However, the framework discussed here is fairly general and the material parameters (α_g, A_{FS}) can be easily modified to capture actual data.
- The Fatemi-Socie parameter has been used as the driving force for microstructurally small crack growth. While this assumption is probably reasonable, crack tip stress fields, interaction with grain boundaries, and redistribution of stresses due to crack advance are neglected.
- Voronoi tessellation is used to represent the grain shape and size distribution, which should be more realistic than modeling cuboidal grains. However, grain shapes from the actual microstructure should be modeled to analyze their effect on crack initiation life.

- Grains are represented by assigning different orientations and the structure of grain boundaries is not modeled, which might influence the stress-strain distribution near grain boundaries.
- The precipitates are not explicitly modeled; the necessity of explicit modeling of the microstructure features smaller than the grain scale is not clear from literature but can be explored in future.

7.12 Summary

A computational study is conducted to determine the influence of microstructure geometry and properties on driving forces for fatigue crack formation in Ni-base superalloy IN100. The effect of varying microstructure on the inelastic strain distribution is studied using statistical volume elements (SVEs). Methods are developed for assessing the relative probability of crack formation and microstructurally small crack growth as a function of microstructure for uniaxial tension-compression loading conditions. The crack initiation life distribution is studied at different strain amplitudes. The methodology captures the qualitative trends of the crack distribution dependence on cyclic strain amplitude. Finally, a computational material design framework is used in preliminary design of a fatigue resistant microstructure.

CHAPTER VIII

Summary and Conclusions

8.1 Overview

This thesis has addressed constitutive modeling and life prediction in Ni-base superalloys subjected to cyclic loading. The subject is of considerable interest in commercial and military sectors and has received considerable attention both in terms of testing and model development. Constitutive models in Ni-base superalloys are predominantly framed at the macroscale in industry; however, there has been no explicit consideration of the microstructure details and the associated deformation mechanisms in these models. Deformation mechanisms take place at a range of length scales during inelastic deformation and incorporation of the relevant length scale dependent mechanisms into the physically-based model is important, especially from the standpoint of predictive capability and design of fatigue resistant microstructures. Even though microscale and mesoscale models have been formulated by recent researchers for Ni-base superalloys, to account for the deformation mechanisms at the grain and precipitate scale (Pollock and Argon, 1992; Nouailhas and Cailletaud, 1996; Probst et al., 1999; Busso et al., 2000; Busso and Cheong, 2001), it is common for each approach to neglect hardening

and deformation mechanisms occurring at length scales other than the primary one addressed by the model. Furthermore, there is no systematic methodology to make a smooth and clear connection between plasticity related processes going on at these different length scales. Fatigue life prediction in Ni-base superalloys is mostly empirical in nature and relies mostly on experiments, which are relatively expensive to conduct. The use of computational tools to aid fatigue life prediction analyses in Ni-base superalloys is still relatively new; most of these analyses are LEFM based and/or are without explicit microstructure consideration (Kruch et al., 1994; Abdul-Latif et al., 1999; Chaboche and Gallerneau, 2001; Manonukul and Dunne, 2004). Microstructure features at different length scales (grain size, inclusion size, precipitates) dictate the crack initiation life in Ni-base superalloys. It is important to understand the most significant microstructure features so that the processing steps might be altered accordingly to enhance fatigue resistance and computational tools should be very useful in this regard.

The work presented here has focused on developing physically-based models that can simultaneously incorporate multiscale microstructure dependent hardening and deformation mechanisms in Ni-base superalloys (DS GTD111 and IN100). This effort necessitated the development and implementation of constitutive models at different length scales and the development of a framework to connect the models. A computational framework was also developed to analyze the microstructure dependent variability in crack initiation life based on both slip band cracking in grains and partially debonded inclusions. Although the models were applied to two specific Ni-base superalloys (DS GTD111 and IN100), it should be noted that the methods presented here are intended to be generic and should serve as a guide for studying other alloy systems.

8.2 Homogeneous crystal plasticity based model for DS GTD111

A homogeneous constitutive model was developed in Chapter II to model fatigue and creep loading histories in a directionally solidified Ni-base superalloy (DS GTD111), in which no explicit distinction was made between the matrix and precipitate phases. A rate dependent crystal plasticity framework was employed to capture the orientation dependent stress-strain response at temperatures ranging from room temperature (RT)-1038ºC. The formulation was then extended to model the stress strain response for in-phase (IP) and out-of-phase (OP) theromomechanical fatigue (TMF) loading histories. Lastly, an existing creep damage model was integrated into the constitutive model to capture tertiary creep behavior. The constitutive model was implemented as a User MATerial subroutine (UMAT) in ABAQUS, by modifying McGinty's UMAT (2001). The model was calibrated using uniaxial isothermal fatigue and creep data for DS GTD111 in both the longitudinal and transverse loading orientations. The model showed good predictive capability for uniaxial fatigue data for different strain rates and (IP and OP) TMF data in both the longitudinal and transverse orientations. The simulation predictions were found to be in good agreement with experimental data.

The conclusions from this chapter are as follows:

1) Crystal plasticity theories can be successfully used in analyzing DS Ni-base superalloys and the deformation response in the transverse orientation can be obtained by using as low as 5-10 grains which are randomly oriented (in the transverse orientation), with their axes perpendicular to the loading direction.

2) The cyclic stress-strain response in DS Ni base superalloys is very stable at any given strain amplitude, therefore the threshold stress can be assumed to be constant and does not evolve with cycling, except at very low temperatures ($\leq$427ºC).

8.3 Transversely Isotropic Viscoplastic model for DS GTD111

Chapter III presented a novel transversely isotropic viscoplastic model to capture the cyclic stress-strain behavior for DS GTD111 and the subsequent implementation of this model as a UMAT subroutine. This model is an extension of the transversely isotropic model introduced by Robinson and colleagues (Robinson, 1983; Robinson and Binienda, 2001). The foundations of the model were presented in a thermodynamically admissible framework with internal variables. The kinematics of isothermal finite elastoplastic deformation were prescribed by the multiplicative decomposition of the deformation gradient and the constitutive equations were formulated in an intermediate isoclinic configuration for finite deformation based on Aravas (1992).

The material parameters for the transversely isotropic model were calibrated using isothermal test data at temperatures ranging from RT-1038ºC. Both IP and OP TMF responses were adequately predicted by this model in both longitudinal and transverse loading orientations.

The conclusions from this chapter are as follows:

1) DS Ni-base superalloys are well-described by the symmetry class of transverse isotropy when sufficient number of grains ($\approx$5-10) are present.

2) Analysis of a plate with a central hole for a model problem in terms of stress concentration and stress distribution show that the stress concentration factor in the

transverse isotropy model correlates well with the crystal plasticity simulations. The stress concentration values in the transverse orientation generally fall in between the values obtained from the single crystal simulations.

3) The transversely isotropic model leads to reduction of the associated computational costs at least by a factor of two when compared to the crystal viscoplasticity model developed in Chapter II for a single crystal simulation. This would be reduced further in cases where more grains are explicitly modeled in the crystal plasticity simulations.

8.4 Effects of Inclusions on Crack Initiation Life in DS Nickel-Base Superalloys

The hierarchical scales of fatigue crack formation and their correspondence to strain-life relations were considered for cast A356-T6 Al in recent work by McDowell and co-workers (2003) using a microstructure-property framework that related cyclic plasticity near debonded silicon particle and large casting pores to formation and early growth of microstructurally and physically small fatigue cracks. The analogous role of carbides or other hard ceramic particles in fatigue crack formation in directionally solidified (DS) Ni-base superalloys were analyzed in Chapter IV. The key difference lies in the additional complexity of microstructure-scale modeling that must consider elastic anisotropy and slip anisotropy, and microstructure heterogeneity.

The conclusions from this chapter are as follows:

1) The simple construct employed in this chapter can be used to address crystal orientation, viscoplasticity, and explicit microstructure features that can enhance fatigue crack formation with the goals of estimation of variability in fatigue and rank order microstructures and inclusions with regard to potency in fatigue.

2) The grain misorientation angle significantly influences the plastic strain intensification at the inclusion notch when the inclusion lies at the proximity of a grain boundary. Effects of orientation (misorientation) distribution of grains on $\Delta\gamma^{P*}_{max}/2$ should be characterized for polycrystals with and without inclusions.

8.5 Microstructurally Dependent Crystal Plasticity Based Model for a polycrystalline Nickel-Base Superalloy

Chapter V was focused on embedding the microstructure dependence of the stress-strain response into a viscoplastic crystal plasticity framework in a polycrystalline Ni-base superalloy, IN100. Dependence of the stress-strain response on the grain size, volume fraction and size distribution of the primary, secondary and tertiary γ' precipitates were considered. The model material parameters were calibrated using experimental cyclic stress-strain data for different microstructures with various γ' precipitate and grain size distributions.

The conclusions from this chapter are as follows:

1) IN100 contains a tri-modal distribution of precipitate sizes, which leads to complex interactions of the microstructural features at different length scales that cannot be modeled using a simple mixture rule. Even though this model contains the first order effects of the microstructure features on the deformation response, more experimental data are required to gather higher confidence in the model parameters.

2) Based on the model parameters obtained from the fitting exercise, α and C_χ were observed to be the most microstructure-sensitive parameters at higher inelastic strains, which might be viewed as work hardening parameters for the threshold stress and backstress, respectively. The parameter α decreased with an increase in the primary precipitate volume fraction, while C_χ decreased with an increase in the secondary

precipitate volume fraction. It is possible that both the primary γ′ particles and larger secondary γ′ particles reduce strain hardening by promoting slip heterogeneity.

3) Based on the model and the simulation results, the backstress can be interpreted as being composed of two parts; a backstress due to the differential yielding of grains which is analogous to the intergranular backstress and the explicit backstress term in the constitutive formulation which is analogous to the intragranular backstress. It should be noted, however, that the intergranular backstress will also contain contributions from the increase in dislocation density at the precipitate interfaces in the two-phase superalloy.

8.6 Methodology for informing Microstructure Dependent parameters in Macroscale Model

Chapter VI presented a novel framework to inform the microstructure-dependence of the material parameters in a macroscale constitutive model based on the microstructure dependent crystal plasticity model developed in Chapter V. An artificial neural network (ANN) was trained based on a computational dataset of the cyclic stress-strain response using the crystal plasticity model for different microstructure features (grain size, volume fraction and size of γ′ precipitates). The capability of the ANN to identify the microstructure-dependence of the macroscale model parameters was demonstrated for complex cyclic uniaxial strain-time histories. This provides the first-ever such systematic linkage of macro-model parameters to microstructure known to the author for such complex microstructures, and offers the potential to incorporate microstructure detail into component level analyses.

The conclusions from this chapter are as follows:

1) Artificial neural networks can be effectively used to relate complex non-linear equation parameters when the trends are not very clear. Even though the training dataset required for the ANN may be extensive; once trained, it operates very quickly and requires minimal computational resources.

2) When fitting constitutive equation parameters to cyclic stress-strain datasets, the accuracy in capturing the stress response increases with the number of internal state variables (ISVs) that are used (since the degrees of freedom increase); however, this is at the cost of uniqueness of some of these parameters. The challenge is to obtain the minimum number of ISVs, which can capture the stress response adequately. A two backstress model fitted the cyclic stress-strain data adequately and could capture the microstructure dependence of the parameters in IN100.

3) The framework introduced in this chapter is fairly general and can be easily extended to more complex stress-strain histories. This chapter lays out a methodology for hierarchical constitutive modeling which can be used even for other alloy systems.

8.7 Estimating Fatigue Sensitivity to Microstructure

A framework was laid out in Chapter VII for analyzing the effect of the microstructural attributes (grain size, volume fraction and size distribution of the secondary and tertiary γ' precipitates) on crack incubation and microstructurally small crack growth lives in IN100, which is a significant extension of the work by Bennett and McDowell (2003b). Various fatigue parameters for crack incubation were analyzed and their sensitivity with respect to the microstructure features was analyzed. The fatigue parameters were then used to determine the fraction of initiated cracks as a function of the crack initiation life. Finally, a computational material design framework was used in the preliminary design of a fatigue resistant microstructure.

The conclusions from this chapter are as follows:

1) This chapter provides a computational micromechanics framework which can be used to study the effects of microstructural variability on fatigue crack initiation life. It affords the ability to explore effects of variations of single features of microstructure holding other features fixed. The effects of extreme variations of microstructure on crack

initiation life can also be studied. Such studies using experimental methods would be very costly, if indeed feasible. However, experiments are needed to calibrate and validate such frameworks since the model predictions are only as good as the experimental data used to calibrate them.

2) Even though a very preliminary framework for design of a fatigue resistant microstructure is shown in this chapter it has important implications for future research. Experiments are very expensive and computations can help reduce the experimental burden to design materials with microstructure attributes for maximum fatigue life.

8.8 Recommendations for Future Work

A large number of topics relating to Ni-base superalloys have been investigated in this thesis and while considerable amount of work has been done, many of these topics are new and it would not be prudent to classify this research as complete in all respects. There are many avenues for future work which are listed as follows:

1) Experiments

- Multiaxial loading and off-axis loading conditions

  Even though the primary axis of DS GTD111 turbine blade materials is designed to be aligned along the stress axis, conditions might exist when crack initiation occurs at skew orientations. Off-axis fatigue and creep tests would shed some light on the relationship between grain orientation and crack initiation life. Multi-axial fatigue and creep tests should also be conducted on both DS GTD111 and IN100 to understand the behavior of grain boundaries under mixed mode conditions. These tests would also be useful to validate/calibrate the stress-strain constitutive model predictions.

- Tests for different microstructures

Crack initiation life prediction models for cyclic loading conditions have been developed in this thesis that are sensitive to microstructure features (inclusions in DS GTD111 and the γ' precipitate size and volume fractions in IN100). Experimental fatigue and creep tests should be conducted for materials with different microstructure features to validate the crack initiation life prediction models. The stress-strain data obtained for these materials could also be used to validate the microstructure sensitive constitutive model for predicting the stress-strain response in IN100. Transmission electron microscopy (TEM) could be conducted to get a better understanding of the complex dislocation interaction and other deformation mechanisms in IN100 which contains a tri-modal distribution of γ' precipitate sizes and volume fractions.

2) Service Conditions and Actual Microstructures

- Actual operating conditions

The aim of this study was to develop life prediction models for predominantly fatigue-dominated loading conditions and the effect of environment (e.g. oxidation, hydrogen embrittlement, sulfidizing) was not considered. Turbine components are subjected to very harsh environments at very high temperatures, therefore, environment induced degradation might play an important role in dictating the crack initiation life and should be included in the model. Crystal plasticity provides a convenient framework for explicitly modeling the grains and grain boundaries, which could be coupled with a diffusion-based model to study effect of surface grain boundary embrittlement on the crack initiation life.

- Actual microstructure features

DS GTD111 and IN100 contain microstructure features with different attributes: carbide inclusion shape and aspect ratio in DS GTD111, distribution of size and

volume fraction of primary, secondary and tertiary γ' precipitates. In addition to this, the precipitate morphology might evolve with loading, especially at higher temperatures. Idealized shapes and distributions (or mean values) have been used in the stress-strain and crack initiation life prediction models which have been formulated in this thesis. It might be important to study the effects of the variability in these microstructure attributes on the crack initiation life.

3) Hierarchical Modeling

- Multiscale modeling to guide microstructure-sensitive models

The functional dependence of the microstructure-based constitutive model parameters for IN100 in this work are determined using experimental data. Therefore the functional forms are not strictly physically-based and the model predictions should be valid only for the interpolated microstructures. A multiscale scheme could be potentially used to determine physically motivated forms for the material model parameters. Explicit modeling of the primary and secondary γ' precipitates could be used to study the effect of slip heterogeneity on the macroscale stress-strain response. However, one significant bottleneck is the lack of complete understanding of the complex deformation processes in Ni-base superalloys with tri-modal distribution of precipitates. Dislocation dynamics could be potentially used to get a better understanding of the dislocation interactions at the matrix-precipitate interfaces.

- Towards computational materials design

Experiments are expensive and sometimes infeasible to conduct; computational resources could be potentially very useful in this regard to guide experiments towards materials design for fatigue resistant microstructures. Material microstructure attributes at different scales could be optimized to give maximum fatigue resistance using microstructure-sensitive computational models.

References

ABAQUS (2003). Hibbitt, Karlsson, and Sorensen, Inc, Providence, RI, v6.3.

ABAQUS (2004). Hibbitt, Karlsson, and Sorensen, Inc, Providence, RI, v6.4.

ABAQUS (2005). Version 6.5, Abaqus, Inc., Providence, RI.

Abdul-Latif, A., Ferney, V. and Saanouni, K. (1999). Fatigue damage initiation in Waspaloy under complex cyclic loading. ASME Journal of Engineering Materials and Technology 121: 278-285.

Ai, S., Lupinc, V. and Onofrio, G. (1993). Influence of precipitate morphology of high temperature fatigue crack growth of a single crystal Ni-base superalloy. Scripta Materialia 29: 1385-1390.

Albrecht, J. (1999). Comparing Fatigue Behavior of Titanium and Nickel-Based Alloys. Materials Science and Engineering A A263: 176-186.

Alexandre, F., Deyber, S. and Pineau, A. (2004). Modelling the Optimum Grain Size on the Low Cycle Fatigue Life of a Ni Based Superalloy in the Presence of Two Possible Crack Initiation Sites. Scripta Materialia 50: 25-30.

Altenbach, H., Huang, C. and Naumenko, K. (2002). Creep-damage predictions in thin-walled structures by use of isotropic and anisotropic damage models. Journal of Strain analysis 37(3): 265-275.

Antolovich, B. (1996). Fatigue and fracture of Ni-base superalloys. Superalloys, 1996.

Antolovich, S. (1983). The Effect of Microstructure on the Fatigue behavior of Nickel Base Superalloys Fatigue and Fracture of Engineering Materials and Sructures: 119-143.

Antolovich, S. (1987). The Effect of Microstructure on the Fatigue Crack Growth Resistance of Nickel Base Superalloys.

Antolovich, S. (2003). Lecture Series, Georgia Institute of Technology.

Aravas, N. (1992). Finite elastoplastic transformations of transversely isotropic metals. International Journal of Solids and Structures 29(17): 2137-2157.

Argon, A. (1995). Mechanical properties of single phase crystalline media: deformation at low temperatures. Physical Metallurgy, elsevier, Amsterdam.

Arnold, S., Robinson, D. and Barlotta, P. (1992). Unified viscoplastic behavior of metal matrix composites. Nasa Technical Memo, No. 105819.

Asaro, A. (1983a). Crystal Plasticity. ASME J, Appl. Mech. 50: 921-934.

Asaro, A. (1983b). Micromechanics of crystals and polycrystals. Adv. Appl. Mech. 23: 1-115.

Asaro, A. and Needleman, A. (1985). Texture development and strain hardening in rate dependent polycrystals. Acta Materialia 33: 923-953.

Balasubramanian, S. and Anand, L. (2002). Elasto-viscoplastic constitutive equations for polycrystalline fcc materials at low homologous temperatures. Journal of the Mechanics and Physics of Solids 50(1): 101-126.

Barbe, F., Decker, L., Dominique, J. and Cailletaud, G. (2001). Intergranular and intragranular behavior of polycrystalline aggregates. Part 1: FE Model. International Journal of Plasticity 17: 513-536.

Bennett, V. (1999a). A study of microscale phenomena in small crack propgation under multiaxial fatigue. Ph.D. Thesis, Georgia Institute of Technology.

Bennett, V. and McDowell, D. (2003a). Crack Tip Displacements of Microstructurally Small Surface Cracks in Single Phase Ductile Polycrystals. Engineering Fracture Mechanics 70: 185-207.

Bennett, V. and McDowell, D. (2003b). Polycrystal Orientation Distribution Effects on Microslip in High Cycle Fatigue. International Journal of Fatigue 25: 27-39

Berard, J. and McDowell, D. (1992). A ΔJ based approach to bi-axial low cycle fatigue of shear damaged materials. Fatigue Fracture Eng. Mater. Struc. 15(8): 719-741.

Betten, J. (1983). Damage tensors in continuum mechanics. J. Mec. Theorique Appliquee 2: 13-32.

Bettge, D. and Osterle, W. (1999). Cube slip in near-[111] oriented speciments of a single-crystal nickel-base superalloy. Scripta Materialia (USA) 40(4): 389-395.

Bilby, B., Bullough, R. and Smith, E. (1955). Continuous Distributions of Dislocations: A New Application of the Methods of Non-Riemannian Geometry. Proc. Royal Society A231: 263-273.

Bodner, S. and Partom, Y. (1975). Constitutive equations for elastic-viscoplastic strain hardening materials. ASME 42: 385.

Brown, C., King, J. and Hicks, M. (1984). Effects of microstructure on long and short crack growth in Ni-base superalloys.

Busso, E. and Cailletaud, G. (2005). On the selection of active slip systems in crystal plasticity. International Journal of Plasticity 21: 2212-2231.

Busso, E. and Cheong, K. (2001). Length scale effects on the macroscopic behaviour of single and polycrystalline FCC crystals. Journal de Physique IV 11(5): Pr5-161-70.

Busso, E., Meissonier, F. and O'Dowd, N. (2000). Gradient dependent deformation of two phase single crystals. Journal of Mechanics and Physics of Solids 48: 2333-2361.

Castelli, M. and Ellis, J. (1993). Improved techniques for thermomechanical testing in support of deformation modeling. Symposium on Thermomechanical Fatigue Behavior of Materials (STP 1186); H. Sehitoglu. Ed., San Diego, CA, ASTM: 195-211.

Caton, M., Jha, S., Rosenberger, A. and Larsen, J. (2004). Divergence of Mechanisms and the Effect on the Fatigue Life Variability of Rene 88DT. Superalloys 2004: 305-312.

Chaboche, J. and Gallerneau, F. (2001). An overview of the damage approach of durability modelling at elevated temperature. Fatigue and Fracture of Engineering Materials and Sructures 24: 405-418.

Chaboche, J. L. (1989). Constitutive Equations for Cyclic Plasticity and Cyclic Viscoplasticity. Int. J. Plast. 5(3): 247-302.

Chan, K. and Enright, M. (2005). Probabilistic micromechanical modeling of fatigue-life variability in an μ-b Ti alloy. Metallurgical and Materials Transactions A (Physical Metallurgy and Materials Science) 36A: 2621-2631.

Chateau, E. and Remy, L. (1998). Creep and creep-fatigue behaviour of Udimet 720 at 850 degrees C. ECF12. ESIS. Fracture from Defects. Proceedings of the 12th Biennial Conference on Fracture. 1: 339-344.

Chen, E., Sauer, S., Meshii, M. and Tucker, W. (1997). Fatigue microcrack distribution and reliability of a Ni-base superalloy. International Journal of Fatigue 19(1): S75-S82.

Cheng, A. and Laird, C. (1978). Fatigue life behavior of copper single crystals. II. Model for crack nucleation in persistent slip bands. Fatigue and Frature of Engineering Materials and structures 4: 343-353.

Cheong, K., Busso, E. and Arsenlis, A. (2005). A study of microstructural length scale effects on the behaviour of FCC polycrystals using strain gradient concepts. International Journal of Plasticity 21(9): 1797-1814.

Coffin, L. (1974). Fatigue at High Temperature - Prediction and Interpretation. Proc. Inst. Mech. Eng.: 188.

Conrad, H. (1964). Thermally activated deformation of metals. J. Metals 16: 582-588.

Dafalius, Y. (1998). Plastic Spin: Necessity or Redundancy. International Journal of Plasticity 14(9): 909-931.

Daleo, J. and Wilson, J. (1998). GTD-111 Alloy material study. J. engineering for gas turbines and power 120: 375-382.

DeBartolo, E. and Hillberry, B. (1998). Effects of constituent particle clusters on fatigue behavior of 2024-T3 aluminum alloy. International Journal of Fatigue 20(10): 727-735.

Ding, Z., Liu, Y., Yin, Z., Yang, Z. and Cheng, X. (2004). Study of elastoplastic constitutive model for single crystal nickel-based superalloy. Hangkong Dongli Xuebao/Journal of Aerospace Power 19(6): 755-761

Donahue, R., Clark, H., Atanmo, P., Kumble, R. and McEvily, A. (1972). Crack opening displacement and the rate of fatigue crack growth. International journal of Fracture Mechanics 8(2): 209.

Epogy (2004). Synaps Inc., Atlanta, GA, USA, v2004A.

Estrin, Y. and Mecking, H. (1984). A unified phenomenological description of work hardening and creep based on one-parameter models. Acta Metallurgica 32: 57-70.

Fan, J., McDowell, D., Horstemeyer, M. and Gall, K. (1999). Computational micromechanics analysis and model development for fatigue behavior of microstructurally small crack growth behavior in dual phase materials. Engineering Fracture Mechanics 68(15): 1687-1706.

Fatemi, A. and Kurath, P. (1988). Multiaxial fatigue life predictions under the influence of mean stress. ASME J.Eng. Mater. Tech. 110: 380-388.

Fatemi, A. and Socie, D. (1988). A critical plane approach to multiaxial fatugue damage including out-of-phase loading. Fatigue Fracture Eng. Mater. Struc. 11(3): 145-165.

Feaugas, X. and Haddou, H. (2003). Grain size effects on tensile behavior of Ni and AISI 316L stainless steel. Metallutgical and Materials Transactions 34A(10): 2329.

Fedelich, B. (2002). A microstructural model for the monotonic and the cyclic mechanical behavior of single crystals of superalloys at high temperatures. International Journal of Plasticity 18: 1-49.

Feng, L., Ke-shi, Z., Guang, Z. and Hai-dong, Y. (2002). Anisotropic damage model under continuum slip crystal plasticity theory for single crystals International Journal of Solids and structures 39: 5279-5293.

Ferney, V., Hautefeuille, M. and Clavel, M. (1991). Multiaxial cyclic behavior in two precipitates strengthened alloys: Influence of the loading path and microstructure. Memoires et Etudes Scientifiques de la Revue de Metallurgie 88: 441-451.

Findley, K. (2005). Physically-Based model for elevated temperature low cycle fatigue crack initiation and growth in Rene 88DT. Ph.D. Thesis, Georgia Institute of Technology.

Fleury, E. and Remy, L. (1993). Low cycle fatigue damage in nickel base superalloys at elevated temperatures. Materials Science and Engineering A A167: 23-30.

Fleury, E. and Remy, L. (1994). Behavior of nickel-base superalloy single crystals under thermal-mechanical fatigue. Metallurgical and Materials Transactions A (Physical Metallurgy and Materials Science) 25A(1): 99-109.

Franciosi, P. (1985). The concepts of latent hardening and strain hardening in metallic single crystals. Acta Metallurgica 33: 1601-1612.

Frederick, C. and Armstrong, P. (1966). Convergent internal stresses and steady cyclic states of stress. Journal of Strain Analysis 1(2): 154-159.

Freed, A. and Walker, K. (1989). Refinements in a viscoplastic model. NASA Technical Memorandom 102338.

Gall, K., Horstemeyer, M., Degner, B., McDowell, D. and Fan, J. (2001). On the driving force for fatique crack formation from inclusion and voids in a cast A356 aluminum alloy. International Journal of Fracture 108(3): 207-233.

Gall, K., Sehitoglu, H. and Kadioglu, Y. (1997). Methodology for predicting variability in microstructurally short fatigue crack growth rates. ASME Journal of Engineering Materials and Technology 119(2): 171-179.

Gallerneau, F. and Chaboche, J. (1999). Fatigue Life Predictions of Single Cystals for Turbine Blade Applications. International Journal of Damage Mechanics 8: 404-427.

Gayda, J. and Miner, R. (1983). Fatigue crack initiation and propagation in several nickel-base superalloys at 650 °C. International Journal of Fatigue 5(3): 135-143.

Gell, M. and Leverant, G. (1968). The fatigue of the Ni base superalloy, MAR-M200 in single crystal and columnar grained forms at room temperature. Transactions of the Metallurgical Society of AIME 242: 1869-1879.

Gessinger, G. (1984). Powder Metallurgy of Superalloys, Butterworth and Company.

Goh, C. (2002). Crystallographic plasticity in fretting of Ti-6Al4V. Ph.D. Thesis, Georgia Institute of Technology.

Gordon, A. (2006). Crack Initiation Modeling of a Directionally-Solidified Ni-base Superalloy. Ph.D. Thesis, Georgia Institute of Technology.

Gross, D. and Li, M. (2002). Constructing microstructures of poly and nanocrystalline materials for numerical modeling and simulation. Applied Physics Letters 80(5): 746-748.

Haddou, H., Risbet, M., Marichal, G. and Feaugas, X. (2004). the effects of grain size on the cyclic deformation behavior of polycrystalline Ni. Material Science and Engineering A379: 102-111.

Hasebe, T., Sakane, M. and Ohnami, M. (1992a). High Temperature low cycle fatigue and cyclic constitutive relation of MAR-M247 directionally solidified superalloy. Transactions of the ASME 114: 162-167.

Hasebe, T., Sakane, M. and Ohnami, M. (1992b). Elastic anisotropy of directionally solidified superalloy. Journal of Engineering Materials and Technology (Transactions of the ASME) 114: 141-146.

Heilmaier, M., Leetz, U. and Reppich, U. (2001). Order strengthening in the cast nickel-based superalloy IN 100 at room temperature. Material Science and Engineering 319-321: 375-378

Hill, R. and Rice, J. (1972). Constitutive analysis of elastoplastic crystals at arbitrary strain. Journal of the Mechanics and Physics of Solids 20: 401-413.

Hirsch, P. (1992). A new theory of the anomalous yield stress in LI2 alloys. Philosophical Magazine A 62(3): 569-612.

Horalek, R. (1990). ASTM Grain–Size Model and Related Random Tessellation Models. Materials Characterization 25: 263-284.

Horstemeyer, M. and Ramaswamy, S. (2000). Factors affecting localization and void growth in ductile metals: A parametric study International Journal of Damage Mechanics 9(1): 5-28.

Hoshide, T. and Socie, D. (1988). Crack nucleation and growth modeling in biaxial fatigue. Engineering Fracture Mechanics 29(3): 287-299.

Huber, N. and Tsakmakis, C. (2001). A neural network tool for identifying the material parameters of a finite deformation viscoplasticity model with static recovery. Comput. Methods Appl. Mech. Engg. 191: 353-384.

Hyzak, J. and Bernstein, I. (1982). The Effect of Defects on the Fatigue Crack Initiation Process in Two P/M Superalloys. Metallurgical Transactions A 13A: 33-52.

Ibanez, A. (2003). Modeling creep behavior in a Directionally Solidified Ni-base superalloy. PhD Thesis, Georgia Institute of Technology.

Jablonski, D. (1981). The effect of ceramic inclusions on the low cycle fatigue life of low carbon Astroloy subjected to hot isostatic pressing. Materials Science and Engineering A 48: 189 -198.

Jiao, F., Bettge, D., Osterle, W. and Ziebs, J. (1996). Tension-compression asymmetry of the (001) single crystal nickel base superalloy SC16 under cyclic loading at elevated temperatures. Acta Materialia 44(10): 3933-3942.

Kachanov, L. (1958). Time of the rupture process under creep condiitons. Izv. Akad. Nauk. SSR 8: 26-31.

Kakehi, K. (1999a). Influence of precipitate size and crystallographic orientation on strength of a single crystal Ni-base superalloy. Materials Transactions, JIM 40(2): 159 -167.

Kakehi, K. (1999b). Influence of crystallographic orientation on the strength of Ni-base superalloy single crystals at temperatures above the peak temperature Journal of the Japan Institute of Metals (Japan) 63(5): 641-648.

Kanit, T., Forest, S., Galliet, I., Mounoury, V. and Jeulin, D. (2003). Determination of the size of the representative volume element for random composites: Statistical and numerical approaches. International Journal of Solids and structures 40: 3647-3679.

Klepaczko, J. and Chiem, C. (1986). Rate sensitivity of FCC metals instantaneous rate sensitivity and rate sensitivity of strain hardening. Journal of the Mechanics and Physics of Solids 34(1): 29-54.

Kocks, U., Argon, A. and Ashby, M. (1975). Thermodynamics and kinetics of slip. Progress in Material Science, Pergamon Press, London.

Koster, A., Alam, A. and Remy, L. (2002). A physical-base model for life prediction of single crystal turbine blades under creep-fatigue loading and thermal transient conditions. Temperature-Fatigue Interaction: 203-212.

Kozaczek, K., Sinharoy, A., Ruud, C. and McIlree, A. (1995). Micromechanical modelling of microstress fields around carbide precipitates in alloy 600. Modelling Simul. Mater. Sci. Eng. 3(6): 829-843.

Kral, C., Lengauer, W., Rafaja, D. and Ettmayer, P. (1998). Critical review on the elastic properties of transition metal carbides, nitrides and carbonitrides Journal of Alloys and Compounds 265(1-2): 215-233.

Krausz, A. and Eyring, H. (1975). Deformation of Kinetics, Wiley, New York.

Kruch, S., Prigent, P. and Chaboche, J. (1994). A fracture mechanics based fatigue-creep-enviroment crack growth model for high temperature. Int. J. Pre. Ves. and Piping 59: 141-148.

Kumar, R., Wang, A. and McDowell, D. (2006). Effects of microstructure variability on intrinsic fatigue resistance of Ni-base superalloys - A computational micromechanics approach. International Journal of Fracture 137(1-4): 173-210.

Kurath, P. and Fatemi, A. (1990). Cracking mechanisms for mean stress/strain low cycle multiaxial fatigue loading. ASTM Special Technical Publication 1085: 123-143.

Lall, C., Chin, S. and Pope, D. (1979). Metallurgical Transactions A 10A: 1323.

Lankford, J., Davidson, D. and Chan, K. (1984). The influence of crack tip plasticity in the growth of small cracks. Metallurgical Transactions A 4A: 1459-1588.

Latif, A., Clavel, M., Ferney, V. and Saanouni, A. (1994). On the modeling of non-proportional cyclic plasticity of Waspaloy. ASME J. Eng. Mat. Techn. 116: 35-44.

Laz, P. and Hillberry, B. (1998). Fatigue life prediction from inclusion initiated cracks. International Journal of Fatigue 20(4): 263-270.

Leckie, F. and Hayhurst, D. (1977). Acta Metallurgica 25: 1059.

Lee, H. (1969). Elastic plastic deformations at finite strains. Journal of applied mechanics, ASME 36: 1-6.

Lemaitre, J. and Chaboche, J. (1990). Mechanics of Solid Materials, Cambridge University Press.

Lemaitre, J. and Chaboche, J. L. (2000). Mechanics of solid materials. Cambridge University Press.

Leverant, G. and Gell, M. (1969). The elevated temperature fatigue of a Ni-base superalloy, MAR-M200, in conventionally cast and directionally solidified forms. Transactions of the Metallurgical Society of AIME 245(1167).

Li, C. (1990). Vector CTD analysis for crystallographic crack growth. Acta Metallurgica Materialia 38(11): 2129-2134.

Liu, L., Jin, T., Zhao, N., Sun, X., Guan, H. and Hu, Z. (2003). Formation of carbides and their effects on stress rupture of a Ni-base single crystal superalloy. Materials Science and Engineering A A361: 191-197.

Ma, F., Deng, X., Sutton, M. and Newman, J. (1999). A CTOD-based mixed-mode fracture criterion. Mixed Mode Crack Behavior, ASTM STP 1359, Miller KJ, McDowell DL, eds., ASTM, West Conshohocken, PA. (86-110).

Maclachlan, D., Wright, L., Gunturi, S. and Knowles, D. (2001). Constitutive modeling of anisotropic creep in single crystal blade alloys SRR99 and CMSX4. International journal of plasticity 17: 441-467.

Mandel, J. (1971). Plasticite classique et viscoplasticite. Courses and Lectures, ICMS, Udine, Springer, Wien, New York (97).

Mandel, J. (1974). Thermodynamics and plasticity. Proceedings of the international symposium on foundations of continuum thermodynamics, Macmillan, London(283).

Manonukul, A. and Dunne, F. (2004). High- and low-cycle fatigue crack initiation using polycrystal plasticity. Proceedings of the Royal Society of London, Series A (Mathematical, Physical and Engineering Sciences) 460(2047): 1881-1903.

Marin, E. and McDowell, D. (1997). A semi-implicit integration scheme for rate-dependent and rate-independent plasticity. Computers and Structures 63(3): 579-600.

McClintock, F. (1999). Considerations for fatigue crack growth relative to crack tip displacement. Engineering against Fatigue, Eds. J.H. Beynon, M.W. Brown, T.C. Lindley, R.A. Smith and B. Tomkins, Balkema Press, Chapter 24: 227-241.

McDowell, D. (1991). Micromechanical implications for state variable viscoplasticity. American Society of Mechanical Engineers, Materials Division (Publication) MD 26: 103-114.

McDowell, D. (1992). A Nonlinear Kinematic Hardening Theory for Cyclic Thermoplasticity and Thermoviscoplasticity. International Journal of Plasticity (UK) 8(6): 695-728.

McDowell, D. (1996a). Basic Issues in the Mechanics of High Cycle Metal Fatigue. International Journal of Fracture 80: 103-145.

McDowell, D. and Bennett, V. (1997). Micromechanical aspects of small multiaxial fatigue cracks. Proc. 5th Int. Conf. on Biaxial/Multiaxial Fatigue & Fracture, Cracow, Poland: 325-348.

McDowell, D., Fan, J. and Horstemeyer, M. (1999). Multi-Length Scale Analyses of Cyclically Loaded A356 Cast Aluminum Alloy. AFS Transactions.

McDowell, D., Gall, K., Horstemeyer, M. and Fan, J. (2003). Microstructure-Based Fatigue Modeling of Cast A356-T6 Alloy. Engineering Fracture Mechanics 70: 49-80.

McDowell, D., Ho, K. and Moosbrugger, J. (1990). Continuum damage representation of creep-dominated non-proportional cyclic loading. High Temperature Fracture Mechanisms and Mechanics: 51.

McDowell, D. L. and Berard, J. (1992). A delta J approach to biaxial fatigue. Fatigue and Fracture of Engineering Materials and Sructures 15(8): 719-741.

McEvily, A., Endo, M. and Murakami, Y. (2003). On the square root (area) relationship and the short fatigue crack threshold. Fatigue and Fracture of Engineering Materials and Structures 26(3): 269-78.

McGinty, R. (2001). Multiscale representation of polycrystalline inelasticity. Ph.D. thesis, Georgia Institute of Technology.

McGinty, R. and McDowell, D. (1999). Variable Resolution Polycrystal Plasticity: Assignment of Shearing Rates. Constitutive and Damage Modeling of Inelastic Deformation and Phase Transformation, A.S. Khan, ed.: 823-826.

Mecking, H. and Kocks, U. (1981). Kinetics of flow and strain-hardening. Acta Metallurgica 29: 1865-1875.

Melander, A. and Gustavsson, A. (1996). FEM study of driving forces of short cracks at inclusions in hard steels. International Journal of Fatigue 18(6): 389-399.

Meric, L., Poubanne, P. and Cailletaud, G. (1991). Single Crystal Modeling for Structural Calculations. I. Model Presentation. Journal of Engineering Materials and Technology (Transactions of the ASME) 113(1): 162-170.

Merrick, H. and Floreen, S. (1978). Effect of microstructure on levated temperature crack growth in Ni base superalllys. Metallurgical and Materials Transactions A (Physical Metallurgy and Materials Science) 9(A): 231-233.

Miehe, C., Schroder, J. and Schotte, J. (1999). Computational homogenization analysis in analysis in finite platicity simulation of texture development in polycrystalline materials. Comput. Meth. Appl. Mech. Eng. 171: 387-418.

Miehe, E. and Stein, E. (1992). A canonical model of multiplicative elasto-plasticity: Formulation and aspects of the numerical implementation. Eur. J. Mech.. A/Solids 11: 25-43.

Mielek, J., Novak, V., Zarubova, N. and Gemberle, A. (1997). Orientation dependence of plastic deformation in NiAl single crystals. Mater. Sci. Eng. A234-236: 410-413.

Miller, K. (1993a). Materials science perspective of metal fatigue resistance. Materials Science and Technology 9: 453-462.

Miller, K. (1993b). The two thresholds of fatigue behaviour. Fatigue and Fracture of Engineering Materials and Structures 16(9): 931-939.

Miller, M., McDowell, D. and Oehmke, R. (1992). A Creep-Fatigue-Oxidation Microcrack Propagation Model for Thermomechanical Fatigue. Journal of Engineering Materials and Technology (Transactions of the ASME) 114: 282-288.

Milligan, W. (2004). Effects of Microstructure on High Temperature Constitutive Behavior of IN100. Superalloys 2004.

Milligan, W. and Antolovich, S. (1989). Deformation modeling and constitutive modeling for anisotropic superalloys. NASA Report 4215.

Moll, J. and McTiernan, B. (1998). Powder Metallurgy Superalloys, in ASM Handbook Powder Metal Technologies and Applications. 887-902.

Moosbrugger, J. and McDowell, D. (1989). On a class of kinematic hardening rules for non-proportional cyclic plasticity. ASME J. Eng. Mat. Tech. 111: 87.

Morrissey, R., Goh, C.-H. and McDowell, D. (2003). Microstructure-Scale Modeling of HCF Deformation. Mechanics of Materials 35(3-6): 295-311.

Mughrabi, H., Ott, M. and Tetzlaff, U. (1997). New microstructural concepts to optimize the high temperature strength of hardened monocrystalline Ni-base superalloys. Mat. Sci. Eng. A 234-236: 434-437.

Mukherji, D. and Wahi, R. (1996). Some implications of the particle and climb geometry on the climb resistance in nickel-base superalloys. Acta Mater. 44: 1529-1539.

Murakami, S., Kawai, M. and Rong, H. (1988). Finite element analysis of creep crack growth by a local approach. Int. Journal Mech. Sci. 30: 491-502.

Murakami, S. and Ohno, N. (1981). A continuum theory of creep and creep damage 3rd IUTAM symposium on creep in structures, Springer-Verlag, Berlin: 422-444.

Murakami, Y. and Endo, M. (1994). Effect of defects, inclusions, and inhomogeneities on fatigue strength. Fatigue International Journal of Fatigue 16: 163-182.

Nan, M. and Krempl, E. (1991). Thermoviscoplasticity based on overstress applied to the analysis of fibrous metal matrix composites. Journal of composite materials 26(7): 969-990.

Navarro, A. and de los Rios, E. (1987). A model for short fatigue crack propagation with an interpretation of the short-long crack transition. Fatigue and Fracture of Engineering Materials and Structures 10(2): 169-186.

Nemat-Nasser, S. and Hori, M. (1999). Micromechanics: Overall Properties of Heterogeneous Solids, Elsevier Science Publishers.

Neu, R. and Sehitoglu, H. (1989). Thermomechanical Fatigue, Oxidation, and Creep: Part II. Life Prediction. Metallurgical Transactions A 20A: 1769-1783.

Newman, J. (1994). A review of modelling small-crack behavior and fatigue-life predictions for aluminum alloys. Fatigue and Fracture of Engineering Materials and Structures 17(4): 429-439.

Nisitani, H. (1987). Behavior of small cracks in fatigue and relating phenomena. Current Research on Fatigue Cracks, T. Tanaka, M. Jono and K. Komai, Eds., Current Japanese Materials Research 1: 1-26.

Nitz, A. and Nembach, E. (1998). The critical resolved shear stress of a superalloy as a combination of its matrix and precipitates. Metallurgical and Materials Transactions A (USA) 29A: 799-807.

Nouailhas, D. (1989). Unified modelling of cyclic vicoplasticity. Int. J. of Plasticity 5: 501.

Nouailhas, D. and Cailletaud, G. (1996). Finite element analysis of the mechanical behavior of two-phase single-crystal superalloys. Scripta Materialia (USA) 34(4): 565-571.

Ohashi, T., Hidaga, K. and Saito, M. (1997). Quantitative study of the plastic slip deformation and formation of internal stresses in Ni-base superalloys. Material Science and Engineering A238: 42-49.

Ohno, N. and Wang, J. (1991). Multisurface and multicomponent forms of nonlinear kinematic hardening: applications to nonthermal plasticity. Proc. third conf. on constitutive laws for engineering materials, Tuscon, AZ, 1991: 219-222.

Ohno, N. and Wang, J. (1993). Kinematic hardening rules with critical state of dynamic recovery. Part I: Formulation and basic features for ratchetting behavior. International Journal of Plasticity 9(3): 375-390.

Okazaki, M., Tabata, T. and Nohmi, S. (1990). Intrinsic Stage I crack growth of directionally solidified Ni-base superalloys during low cycle fatigue at elevated temperatures. Metallurgical Transactions A 21A: 2201-2208.

Okuda, H., Miyazaki, H. and Yagawa, G. (1994). Neural network approach for modeling of viscoplastic material behaviors. American Society of Mechanical Engineers, Pressure Vessels and Piping Division (Publication) PVP, Advanced Computer Applications 274: 141-145.

Orowan, E. (1940). Problems of plastic gliding. Phil. Trans. R. Soc. London A52: 8-22.

Ortiz, M. and Stainier, L. (1999). The variational formulation of viscoplastic constitutive updates. Computer Methods in Applied Mechanics and Engineering 171(3-4): 419-444.

Ostergren, W. (1976). A Damage Function and Associated Failure Equations for Predicting Hold Time and Frequency Effects in Elevated Temperature Low Cycle Fatigue. Journal of Testing and Evaluation 4: 327-339.

Osterle, W., Bettge, D., Fedelich, B. and Klingelhoffer, H. (2000). Modeling the orientation and direction dependence of the critical resolved shear stress of Nickel base superalloy single crystal. Acta Materialia 48: 689-700.

Paidar, V., Pope, D. and Vitek, V. (1984). A theory of the anamolous yield behavior in LI2 ordered alloys. Acta Metallurgica 32(3): 435-448.

Pollock, T. and Argon, A. (1992). Creep resistance of CMSX-3 Ni-base superalloy single crystals. Acta Metallurgica 40: 1-30.

Probst, H., Dlouhy, A. and Eggeler, G. (1999). Interface dislocations in single crystals. Acta Materialia 47: 2497-2510.

Qi, W. and Bertram, A. (1998). Damage modeling of the single crystal superalloy SRR99 under monotonous creep. Comput. Mater. Sci. 13: 132-141.

Qin, Q. and Bassani, J. (1992). Non-Schmid yield behavior in single crystals. J. Mech. Phys. Solids 40(4): 813-833.

Recipes, N. (1992). Numerical Recipes in C: The art of science computation (ISBN 0-521-43108-5), 1992, Cambridge University Press.

Reger, M. and Remy, L. (1988). High temperature, low cycle fatigue of IN-100 superalloy I: Influence of temperature on the lcf behavior. Materials Science and Engineering A 101: 47-54.

Reppich, B. (1982). Some new aspects concerning particle hardenning mechanisms in gamma prime precipitating Ni-base alloys - 2. Experiments. Acta Metallurgica 30(1): 95-104.

Rice, J. (1971). Inelastic constitutive relations for solids: an internal variable theory and its application to metal plasticity. Journal of the mechanics and Physics of Solids 19: 433-455.

Robinson, D. (1983). Constitutive relationships for anisotropic high temperature alloys. NASA Technical Memorandum 83437.

Robinson, D. and Binienda, W. (2001). Model of viscoplasticity for transversely isotropic inelastically compressible solids. Journal of Engineering Mechanics 127(6): 567-573.

Robotnov, Y. (1968). Creep Rupture. Applied Mechanics. Proceedings of the 12th International Congress of Applied Mechanics, Berlin: 342-349.

Roven, H. and Nes, E. (1991). Cyclic deformation of ferritic steel - I. stress-strain response and structure evolution. Acta Metallurgica Materialia 39(8): 1719-1733.

Sajjadi, A. and Nategh, S. (2001). A high temperature deformation mechanism map for high performance Ni-base superalloy, GTD111. Material Science and Engineering A325: 484-489.

Sauzay, M. and Gilormini, P. (2000). Surface and cyclic microplasticity Fatigue and Fracture of Engineering Materials and Structures 23(2): 573-579.

Sheh, M. and Stouffer, D. (1988). Anisotropic constitutive model for Nickel-base Single Crystal Superalloys. NASA Report No. CR-182157.

Sheh, M. and Stouffer, D. (1990). A Crystallographic Model for the Tensile and Fatigue Response for Rene N4 at 982 deg C. J. Appl. Mech. (Trans. ASME) 57(1): 25-31.

Shenoy, M., Gordon, A., McDowell, D. and Neu, R. (2005). Thermomechanical fatigue behavior of a directionally solidified Ni-Base Superalloy. JEMT, Transactions of ASME 127(3): 125-137.

Shin, I., Nho, I. and Yim, S. (1997). A finite element approach to anisotropic damage of ductile materials in large deformations. International Journal of Fracture 84: 261-277.

Shirafuji, N., Kenji, S., Masao, S. and Ohnami, M. (1998). Tension torsion multiaxial low cycle fatigue of MAR-M247 LC directionally solidified superalloy at elevated temperatures. Journal of Engineering Materials and Technology, ASME 120: 57-63.

Shrikanth, A. and Zabaras, N. (1999). A computational model for the finite element analysis of thermoplasticty coupled with ductile damage at finite strains. International Journal for Numerical Methods in Engineering 45: 1569-1605.

Sinharoy, S., Virro-Nic, P. and Milligan, W. (2001). Deformation and strength behavior of two Ni-base turbine disk alloys at 650 C. Metallurgical and Materials Transactions A (Physical Metallurgy and Materials Science) 32A(8): 2021-2032.

Smith, R. and Miller, K. (1977). Fatigue cracks at notches. International Journal of the Mechanical Sciences 19: 11-22.

Smith, R., Watson, P. and Topper, T. (1970). A stress strain parameter for the fatigue of materials. Journal of Fatigue 5: 767-778.

Socie, D. and Bannantine, J. (1988). Bulk deformation fatigue damage models. Mat. Sci. Eng. A 1988: 3-13.

Spencer, A. (1971). Theory of invariants. Continuum Physics 1: 240-253.

Spencer, A. and Rivlin, R. (1962). Isotropy integrity bases for vectors and second order tensors. Arch. Ration. Mech. Anal. 9: 45-63.

Sumpter, B. and Noid, D. (1996). On the use of computational neural networks for the prediction of polymer properties. J. Thermal Analysis 46(833-852).

Sun, Y. and Hazzledine, P. (1996). Geometry of dislocation glide in $L1_2$ - phase: TEM observations. Dislocations in Solids 10: 27-68.

Suresh, S. (1998). Fatigue of materials. Cambridge University Press, 2nd Edition.

Takeuchi, S. and Karamoto, E. (1971). Anomalous temperature dependence of the yield stress in Ni3Ga. J. Phys. Soc. Japan 31: 1282.

Takeuchi, S. and Karamoto, E. (1973). Temperature and Orientation Dependence of the Yield Stress in Ni3Ga Single Crystals. Acta Metallurgica 30: 921.

Tanaka, K. (1987). Short-crack fracture mechanics in fatigue conditions. Current Research on Fatigue Cracks, eds. T. Tanaka, M. Jono and K. Komai. Current Japanese Materials Research, Elsevier 1: 93-117.

Tanaka, K. and Akinawa, Y. (1989). Propagation and non-propagation of small fatigue cracks. Advances in Fracture Research, Proc ICF7, Houston, TX 2: 869-887.

Tanaka, K. and Mura, T. (1981). A dislocation model for fatigue cack initiation. Journal of Applied Mechanics 48: 97-103.

Tanner, A., McGinty, R. and McDowell, D. L. (1999). Modeling Temperature and Strain Rate Sequence Effects on OFHC Copper. Int. J. Plasticity 15: 575-603.

Teodosiu, C. (1970). A dynamic theory of dislocations and its applications to the theory of the elastoplastic continuum. Proceedings of the conference on fundamental aspects of dislocation theory: 837.

Tjiptowidjojo, Y. (2006). Personal Communication, Georgia Institute of Technology.

Trexler, M. (2004). Microstructural effects on fracture and corrosion behavior of a directionally solidified superalloy. PhD Proposal, Georgia Institute of Technology.

Trexler, M. (2005). Personal Communications, Georgia Institute of Technology.

Umakoshi, Y., Pope, D. and Vitek, V. (1984). The asymmetry of the flow stress in Ni3 (Al, Ta) single crystals. Acta Metallurgica vol. 21(4): 415-425.

Venkataraman, G., Chung, Y.-W., Nakasone, Y. and Mura, T. (1990). Free energy formulation of fatigue crack initiation along persistent slip bands: calculation of S-N curves and crack depths. Acta Metallurgica Materialia 38(1): 31-40.

Venkataraman, G., Chung, Y. and Mura, T. (1991). Application of minimum energy formalism in a multiple slip band model for fatigue-II. Crack nucleation and derivation of a generalised Coffin-Manson law. Acta Metallurgica Materialia 39(11): 2631-2638.

Vitek, V., Pope, D. and Bassani, J. (1996). Superalloys (Ni base) and dislocations - An Introduction. Dislocations in Solids 10: 135-186.

Walker, K. and Jordan, E. (1985). Cconstitutive modeling Of superalloy single crystals and directionally solidified materials. NASA Conference Publication: 65-81.

Wang, A., Kumar, R., Shenoy, M. and McDowell, D. (2005). Microstructural Constitutive Models for Cyclic Deformation and LCF in Two Phase Ni-base Superalloys. To be submitted.

Wang, C. and Miller, K. (1992). The effects of mean and alternating shear stresses on short fatigue crack growth rates. Fatigue and Fracture of Engineering Materials and Structures 15(2): 1223-1236.

Wei, W., Floge, H. and Affeldt, E. (1991). Investigation of the low cycle fatigue behaviour of IN100 using a beachmark technique. Scripta Metall. Mat. 25: 1757-1761.

Westbrook, J. (1996). Superalloys (Ni base) and dislocations - An Introduction. Dislocations in Solids 10: 1-26.

Wusatowska-Sarnek, A., Blackburn, M. and Aindow, M. (2003). Techniques for Microstructural Characterization of Powder-Process Nickel-based Superalloys. Material Science and Engineering A 360: 390-395.

Xiao, L., Chen, D. and Chaturvedi, M. (2005). Shearing of γ' precipitates and formation of planar slip bands in Inconel 718 during cyclic deformation. Scripta Materialia 52: 603-607.

Yagawa, G. and Okuda, H. (1996). Neural networks in computational mechanics. Modell. Simulation Mater. Sc. 3: 435-512.

Yaguchi, M., Yamamoto, M. and Ogada, T. (2002a). A viscoplastic constitutive model for Nickel based superalloys - Part 1; Kinematic hardening rule of anisotropic dynamic recovery. International Journal of Plasticity 18: 1083-1109.

Yaguchi, M., Yamamoto, M. and Ogada, T. (2002b). A viscoplastic constitutive model for Nickel based superalloys - Part 2; Kinematic hardening rule of anisotropic dynamic recovery. International Journal of Plasticity 18: 1111-1131.

Yashiro, K., Kurose, F., Nakashima, Y., Kubo, K., Tomita, Y. and Zbib, H. (2005). Discrete dislocation dynamics simulation of cutting of γ' precipitate and interfacial dislocation network in Ni-based superalloys International Journal of Plasticity 22(4): 713-723.

Zhang, J., Halliday, M., Poole, P. and Bowen, P. (1997). Crack closure in small fatigue cracks - a comparison of finite element predictions with in-situ scanning electron microscope measurements. Fatigue and Fracture of Engineering Materials and Structures 20(9): 1279-1293.